An Investigation on the Enhancement of Electromechanical Performance of Polymer Composites using Supercritical Carbon Dioxide for Electroactive Applications

By

Nireeksha S Karode (B.E., M.Sc.)

Submitted in Fulfillment for the Requirements for Doctorate in Engineering Technology

Waterford Institute *of* Technology

School of Engineering

Waterford Institute of Technology

Research Supervisors: Dr Austin Coffey

Dr Laurence Fitzhenry

Dr Philip Walsh

Submitted to Waterford Institute of Technology

June 2018

Declaration of Authorship

I, Nireeksha Karode, certify that this report is all my own work and contains no plagiarism. By submitting this assignment, I agree to the following terms:

- Any text, diagrams or other material copied from other sources (including, but not limited to, books, journals and the internet) have been clearly acknowledged and referenced. These details are then confirmed by a fuller reference in the bibliography.
- I have read the sections on referencing and plagiarism in the handbook or in the WIT Plagiarism policy and I understand that only assignments which are free of plagiarism will be awarded marks. I further understand that WIT has a plagiarism policy which can lead to the suspension or permanent expulsion of students in serious cases.
- I have read the relevant institutional regulations and hereby declare that this thesis is in line with these requirements.

Signed:

_____

Date:

_____

Acknowledgements

I thank Dr Austin Coffey and Waterford Institute of Technology for opening up doors to chase my dream of PhD.

I express my sincere gratitude to Dr Laurence Fitzhenry, who believed in me and consistently pushed me towards successfully acquiring the most prestigious award from Irish Research Council Government of Ireland Postgraduate Scholarship.

I thank Dr Shioban Matthews (SCF Processing Ltd, Drogheda) for her continuous support and mentorship on processing throughout the duration of research.

I would like to thank Trish for your boundless love and support, our trips to Copper coast and beaches always made me stress free. The completion of this study would not have been possible without the support and understand of my husband, Dr Anup Poudel. It is only because of your support that strengthened me to believe in myself and stay calm throughout the study. I thank my mother, brother and entire family from Nepal who encouraged me throughout the period of my research.

Abstract: Electroactive polymers (EAPs), also known as artificial muscles, are a type of polymer which responds to an electric field with structural or mechanical changes. However, current plastic research and manufacturing sectors are still lacking the use of EAP's for smart applications, due to their diverse thermal, mechanical and electrical behavioural changes depending on small variations in their processing conditions. Therefore, this research investigated the effects of novel supercritical carbon dioxide ($scCO_2$) fluid assisted polymer processing techniques on the thermal, mechanical and electrical properties of EAPs. Semi-crystalline polymer Pebax and rubber elastomer Poly(styrene-ethylene-butylene-styrene) - SEBS was chosen as the base polymeric material; and in order to enhance the electroactive properties, graphene-graphene oxide were used as filler material. The research begins with preliminary investigations of the $scCO_2$ processing of polymers at various critical pressures. This initial study indicated that both polymers resulted in increased microphase formation producing a more homogeneous co-polymer base material and decreased the mechanical properties due to the foaming effect. In order to enhance the electroactive properties of the base polymers, graphene-based filler materials at low concentrations (<2.5% wt.) were used, processed with and without $scCO_2$. Clear enhancement with respect to mechanical properties and crystallisation kinetics were observed below 1% filler loading and additional information on the exfoliation and agglomeration effects were drawn. Finally, the effects of reprocessing $scCO_2$ processed composites were investigated. Various crystallisation kinetics theories were used to understand the effects of $scCO_2$ processing on the crystallisation process; these results were validated using X-ray diffraction through crystallite size calculation. An in-depth understanding of results obtained from thermal, mechanical and electrical behaviour were co-related. The thesis concludes that the use of $scCO_2$ processing induced rearrangement of polymer chains into favourable configurations resulting in exfoliation of filler particles with improved homogeneity, mechanical and electrical properties. Bending capabilities were evaluated by sulfonation of the manufactured SEBS graphene oxide composites. The sSEBS graphene oxide composites processed with $scCO_2$ demonstrated a maximum bending actuation of 27 degrees.

Table of Contents

List of Figures

List of Tables

List of Abbreviations

EAP Electroactive Polymer

DSC Differential Scanning Calorimetry

DMA Dynamic Mechanical Thermal Analysis

TGA Thermal Gravimetric Analysis

ATR-FTIR Attenuated Total Reflectance-Fourier Transform Infrared spectroscopy

t Time in sec

Tc Crystallisation temperatures

Tm Melting Temperature

TEM Transmission Electron Microscopy

XRD X-Ray diffraction

n Nucleation dimension

k Crystallisation rate under isothermal condition

k' Crystallisation rate under non-isothermal condition

k* Crystallisation rate under Ozawa Model

K Temperature independent pre-exponential factor

IPMC Ionic polymer-metal composites

SCF Supercritical Fluid

$scCO_2$ Supercritical Carbon Dioxide

Pebax Polyether block amide

SEBS Poly(styrene ethylene butylene styrene copolymer)

sSEBS Sulfonated Poly(styrene ethylene butylene styrene copolymer)

TPEs Thermoplastic Elastomers

AC Alternating Current

DC Direct Current

1 Introduction

During the last decade, polymeric materials have garnered attention for applications ranging from simple plastic artefacts to sophisticated products, such as electronic chips or biomedical devices. The ability to control the behavioural properties, such as the mechanical, thermal or electrical behaviour of polymeric material has attracted scientific researchers and industry to investigate new approaches, in applications such as drug delivery, artificial muscle or stress/strain sensors, in order to develop a stimuli-responsive polymeric matrix. Specifically, thermoplastic elastomers (TPEs), a type of copolymer consisting of a hard thermoplastic and a soft rubbery part, are widely used in commercial products, due to the ability of TPEs to perform as elastic and plastic re-processable polymers. Among TPEs, electroactive polymers (EAPs) are a new class of polymers that have received attention in the field of engineering and material science. EAPs have proven to bring about technological changes in the field of actuation and sensing applications [1]. EAPs are a type of polymer that can change their shape and size, depending on the stimuli applied, such as heat, electrical, light and change in pH. EAPs are considered to possess capabilities that can mimic human muscles, thus emulating biological actuation mechanism. A simple EAP-based actuator consists of a conducting or polarising polymeric membrane sandwiched between two electrodes. The use of additional nanoparticles to improve the performance of EAPs has garnered much attention due to their ability to tailor specific properties (thermal, mechanical or electrical activated/responsive) depending on specific applications. Moreover, such modifications on the addition of nanoparticles not only result in responsive polymer membranes but also become cost-effective polymer composites. However, one of the major challenges encountered in this research is the difficulty in confining the particles to the nano dimension within the polymer. This is usually achieved by overcoming the Van der Waals forces that result in the stacking of the particles, thereby diminishing the inherent mechanical and electrical properties of additives. Common processing techniques used to manufacture such composites include solution casting, melt-extrusion and *in situ* polymerisation. Of these, *in situ* polymerisation is most successful in producing highly dispersed polymer composites due to the lower viscosity of monomers when compared with polymers. Although a plethora of research studies exist on EAPs, the use of EAPs for smart commercial applications is still lacking from scientific research, mainly due to:

a. Their diverse thermal, mechanical and electrical behaviour changes depending on different processing conditions (specifically difference between research lab based solution casting method and industrial standard processing techniques such as extrusion and injection moulding)

b. Need of high voltage to energise/activate EAPs for appropriate actuator or sensing applications (in the case of dielectric EAPs class)

c. Knowledge gap to use standard polymer processing techniques for high volume low-cost production, which in turn, affects the technological performance and price

d. Other concerns such as performance deterioration during EAPs lifetime, recycling issues that impact the ecological and environmental aspect and effects of additives or flame retardants on the health of the factory workers

The ability to process materials at high density (large-scale production) and how these processing conditions affect the performance of the final device are considered as the current knowledge gaps. This is suggested as a probable reason behind the failure of EAP technology to the transition from the research scale into industrial applications. Therefore, manufacturing industries aim to understand the electromechanical behaviour of low-power EAPs and provide engineering solutions for the mass production of such EAPs. One of the most common routes to enhance the electromechanical performance is to use additional fillers or additives. However, issues with respect to uneven dispersion of fillers are persistent, specifically when the additives are in the size ranging from micro to nanoparticles. This knowledge gap forms basic motivation of this thesis, which is to investigate the electromechanical performance of electroactive polymers using a supercritical assisted polymer processing technique.

The work in this thesis focuses on issues that aim to promote the transition of EAPs to practical industrial applications using industry standard polymer processing techniques (such as extrusion and injection moulding). These industry standard processing techniques exhibit simpler, faster, and cost-effective alternatives, with the ability to easily tailor mechanical and electrical properties by using additive/filler particles. In addition, the novelty of this research comes from the use of supercritical fluid technology to enhance the electromechanical properties of EAPs by providing even dispersion and exfoliation of graphene within the polymeric matrix. The aim of this research work is to provide a better understanding of the effects of a supercritical carbon dioxide assisted polymer composite processing technique on the electromechanical performances

of the manufactured polymer composites. Novel processing techniques which exploit supercritical fluids have unique and enormous potential for enhancing the processability of polymers. The ability of supercritical fluids to swell and plasticise polymers is crucial to the modification of polymeric material which results in reducing the viscosity of the polymer melt and changing the mechanical and physical properties of the polymer. In the case of polymer composite manufacturing, the supercritical fluid can enhance the even dispersion of nanoparticles by separating the tightly stacked layers apart, thereby enhancing the electromechanical performance of the polymer. The manufactured composites are evaluated as bending actuators on the application of low electric (6-8 V) stimuli.

1.1 Organisation of Thesis

The objectives of the research work are divided into a number of chapters.

Chapter 1 of the thesis gives a brief introduction and defines the aims and objectives, materials selected and methodology for this research work.

Chapter 2 provides a literature survey of the materials used, manufacturing processes used and the effects of these on the electromechanical performance of polymeric membranes.

Chapter 3 presents experimental methodologies carried throughout the chapters. Specifically, characterisation techniques such as thermal gravimetric analysis, differential scanning calorimetry, dynamic thermal-mechanical analysis and fourier transform infrared spectra were used to evaluate the thermal properties and understand interactions of the manufactured extrudates. dynamic mechanical thermal analysis, tensile test and conductivity test were carried out to evaluate the mechanical properties and electrical properties of the polymer composites.

Chapter 4 focuses on the effect of supercritical assisted processing of polymers at various critical pressures (800psi, 1000psi and 1200psi) on the thermal and mechanical properties. The effects of such processing conditions were validated using differential scanning calorimetry, dynamic mechanical analysis, Fourier transform spectra and tensile test.

Chapter 5 and Chapter 6 investigated the effect of adding filler particles such as graphene and graphene oxide when processed with assisted supercritical carbon dioxide for Pebax (Ch-5) and SEBS (Ch-6) polymer matrices. Graphene was selected as the additive or filler material due to its ability to be easily tailored providing additional functionality (graphene oxide). These chapters provide a complete insight into how the addition of graphene and graphene oxide particles affect

the thermal mechanical and electrical characteristics of the manufactured porous Pebax and SEBS composites.

Chapter 7 (Pebax composites) and Chapter 8 (SEBS composites) look at the effect of reprocessing the polymer composites that were discussed in Chapter 5 and Chapter 6 in relation to the thermal, mechanical and electrical behaviour. The composites which were produced with assisted supercritical fluid (porous membrane) were reprocessed and the characteristic results were compared against composites which were extruded without supercritical fluid at various filler concentrations. Chapter 8 provides the evaluation of all the processed polymer composites to act as bending actuator.

Finally, Chapter 9 includes the conclusions and suggested future work. Throughout the thesis, an in-depth study of the crystallisation kinetics under the isothermal and non-isothermal condition is presented, specifically for the Pebax composites. Additional X-ray diffraction analysis was carried out to evaluate the effect of filler particles and supercritical processing on the actual crystallite size of the polymer composites.

2 Literature Review

2.1 Introduction

Electroactive polymers (EAPs) are a type of material which changes its shape or size upon external stimuli. EAPs open up new applications in emerging technologies that are low cost, are compatible with various fabrication techniques and are stable at different environmental conditions [2]. EAPs are not only proposed for possible applications in biomedical engineering as actuators or sensors but also in microelectronic mechanical systems (MEMS) and robotic systems [3]. Based on the type of activation mechanism, EAPs are divided into Ionic EAPs, which involve mobility or diffusion of ions and Electronic EAPs, which are driven by an electric field or Maxwell forces [2-4]. Ionic EAPs (carbon nanotubes, conductive polymers, ionic polymer gels, ionic polymer metallic composite) require low voltage and can produce bidirectional activation depending on the voltage polarity.

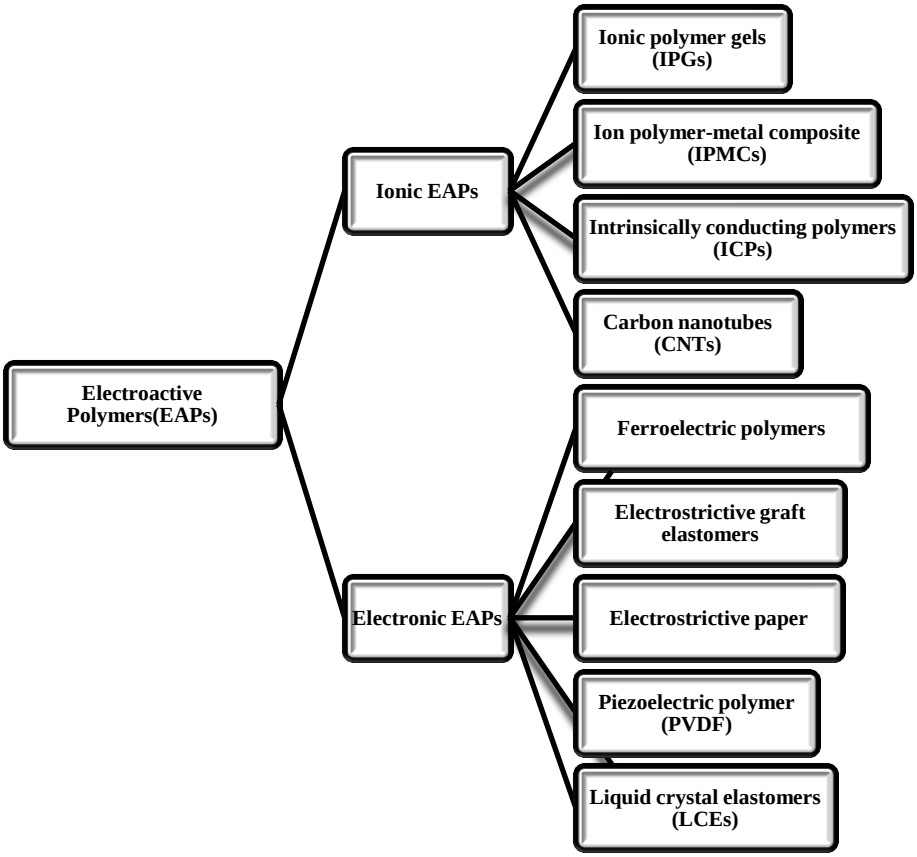

Figure 2.1 Classification of Electronic EAPs (adapted from [1, 5])

On the other hand, electronic EAPs (electrostrictive, electrostatic, piezoelectric, and ferroelectric) exhibit higher mechanical strength requiring high voltage and can hold induced displacement under DC voltage, and are thus suitable for robotic applications [5, 6]. A clear

classification of electroactive polymers is shown in Figure 2.1. Federico [5] reported that the ionic class of EAPs are more suitable for artificial muscle applications because of low voltage requirement, bi-directional actuation depending on voltage polarity and wet/dry state operation Table 2.1.

Table 2.1 Difference between Ionic and Electronic EAPs (adapted from [1, 5])

Ionic EAPs	Electronic EAPs
Mostly bending actuators with strong bending capability	Planar actuators with large in-plane deformation
Actuators may require electrolyte ("wet /dry actuators")	Actuators work also in the dry state ("dry actuators")
Low voltages in the range of a few volts	High activation voltages in the range of several kilovolts
Slow response (tenths of a second) and relaxation(minutes)	Rapid response (milliseconds) and relaxation (seconds)
Strain/stress against an external load is not held under DC activation	Deformed state/stress against an external load maintained under DC activation
Low activation stresses	Large activation stresses
Production of stable material/actuator difficult	Long life under ambient conditions
Expensive, often not commercially available	Cheap, usually commercially available
Hydrolysis in aqueous conditions (> 1.23 V)	Requires compromise between achievable strain and stress

2.2 Working Principles of Ionic Polymer Metal Composites

A type of EAP known as ionic polymer metal composites (IPMC) has brought much attention to the field of actuators and sensor for the biomimetic application. IPMCs consist of an ion-exchange polymer film coated with metal electrodes. IPMCs have large bending capabilities with low applied voltage, simple fabrication processes and beneficial miniaturisation capabilities [7, 8]. Hunter and Oguro et al [9, 10] reported Nafion (ion exchange membrane)-platinum composites which show fast response under low applied voltage. When an electric field is applied, the mobile cations move towards stationary anion groups. The movement of cations and water causes a change in shape of the IPMC depending on the polarity of applied voltage [11, 12]. Thus, the IPMC device can be divided into two stages with respect to their functionality and fabrication process as shown in Figure 2.2: Ion-Exchange Membrane (IEM) and Surface

Electrode. IEMs are characterised by their ionic side groups, allowing ions to be transported through the membrane. Nafion (Dupont) and Flemion (Asahi Glass) are the most commonly used membranes, having sulfonate (SO_3^-) and carboxylate (COO^-) side groups, respectively [11]. Nafion is considered for most of the actuator applications because of its high ion-exchange capacity, thermal and chemical stability, and good mechanical properties, whereas the electrolytes such as H^+, Li^+, and Na^+ play an important role during bending [13, 14].

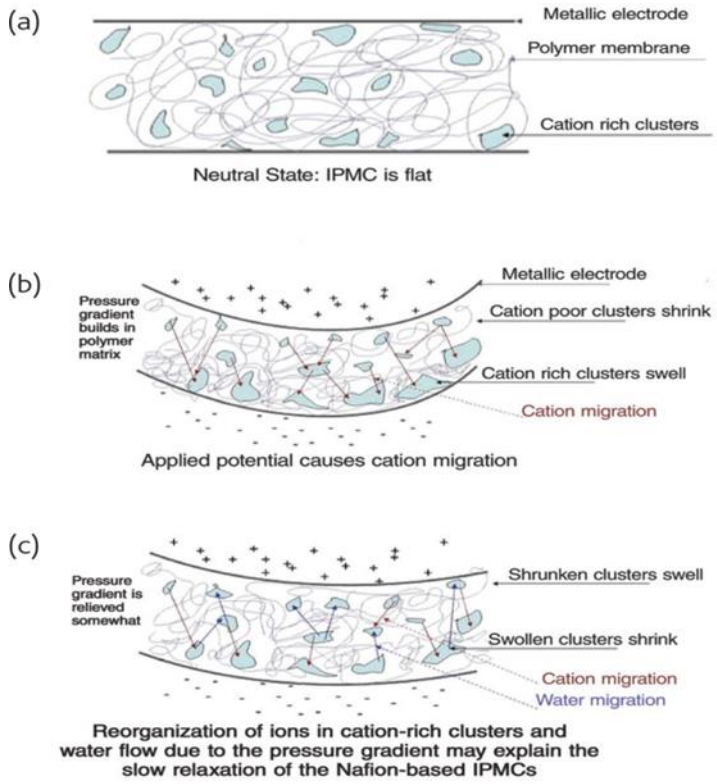

Figure 2.2 IPMCs based Actuator: (a) before the voltage is applied and (b,c) after the application of voltage [14]

Ionic EAP's still face issues due to their inability to tailor the mechanical, electrical or thermal properties of the manufactured polymeric membrane due to use of standard polymers [8, 15, 16]. For example: silicones and acrylics in the case of dielectric EAPs (elastomeric material - good mechanical and fair electrical properties), ferroelectric polymers which maintain permanent electric polarisation such as PVDF (polyvinylidene fluoride) (stiff material- mechanically bad electrically good), and in case of ionic EAPs such as conductive polymers (polypyrrole and polyaniline) and IPMCs (consist of Nafion and Flemion membranes) face difficulties in both mechanical and electrical compliance due to limited knowledge on the available charge transfer sites and motion of ions in and out of the polymeric films [8].

2.3 Characteristic Enhancement using Additives/Fillers Materials

A composite results from of mixing two or more materials and usually enhance the properties of the consequential material. Composites have paved a long way since the ancient Egyptian era with first ever use of mud-straw mixture to construct stronger buildings. Specifically, over the last three decades, materials manufacturers are constantly finding new ways to combine the intrinsic properties of a specific loading material onto the primary carrier material (usually polymers) in order to achieve lightweight yet mechanically strong parts. Although the current material manufacturing industry has achieved huge success in terms of commercialisation and meeting the needs of low volume production of carbon fibre based composite materials; these advancements are limited to the aerospace market only concentrating on how to achieve relatively high strength to weight ratio and an easy yet inexpensive way to manufacture. Unfortunately, researchers/designers fail to foresee the complexities surfacing the carbon-based filler materials in order to meet specific smart applications, where not only mechanical properties but thermal and electrical properties have also become one of the prime design considerations for complete system design. For example, an application like structural health monitoring systems in the case of bridges and wind turbines, artificial muscle applications in the case of robotic systems, construction and rails and/or medical devices, well-established carbon fiber composite technologies have a limited applications compared to their traditional counterpart virgin materials such as polyvinylidene fluoride, nafion, polyaniline and polypyrole. For these reasons, graphene-based additive materials have been chosen for this research, where mechanical, thermal or electrical characteristics can be easily tuned depending on the design specification, in spite of major roadblocks and challenges that arise in terms of scalability, particle dispersion within the polymer matrix and lack of standardised testing methods. Although this research does not focus on how to achieve high scalability at low cost, it investigates how the properties of the graphene-based electroactive polymer composite matrices can be tailored (mechanically, thermally or electrically) depending on specific requirements by using supercritical assisted polymer processing technique to attain even dispersion, exfoliation and maintaining the functionalised properties of graphene filler materials.

2.4 Supercritical Fluid (SCF)

A supercritical fluid is any substance or matter at a temperature and pressure beyond its critical point. Supercritical fluids are characterised by any phase i.e. there is no distinction between gas and liquid beyond the critical point. Supercritical fluids (SCF) has the capabilities to fill up a

container behaving near to gas from one aspect and take the shape of the container acting near to liquid in different aspects [2, 17]. Thus, SCF is characterised by the inability to distinguish if the substance as a liquid or a gas. A phase curve represents the idealised temperature-pressure behaviour on the phase of any material. The phase curve also defines the boundaries of the phase region for a given material [18, 19]. Consider a material which is placed in a closed system along with a gradual increase in temperature and pressure until the characteristic critical point is reached. It can be observed from Figure 2.3, as the temperature and pressure increase, the phase curve between liquid and gas disappears beyond the critical point. This dynamic equilibrium beyond critical points is called a supercritical fluid region [20, 21].

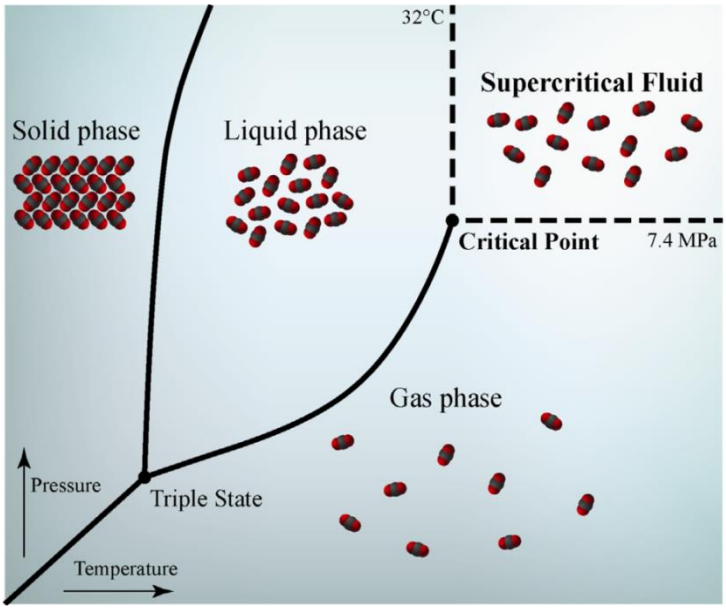

Figure 2.3 Phase diagram representing the supercritical region [21]

A supercritical fluid shows physical and chemical properties intermediate between those of liquids and gases. Supercritical fluids have the following characteristics [13, 20, 22]: (i) solubility approaching the liquid phase, and (ii) diffusivities approaching the gas phase. Therefore, supercritical fluids have densities and diffusivities similar to liquids and viscosities comparable to gases, as outlined in Table 2.2.

Table 2.2 Comparison of phase densities and diffusivities (adapted from [20])

Phase	Density (g/cm^3)	Viscosity (Poise)	Diffusivity (cm^2/s)
Gas	10^{-3}	$0.5\text{-}3.5\times10^{-4}$	0.01-1.0
Supercritical Fluid	0.2-0.9	$0.2\text{-}1.0\times10^{-3}$	$0.1\text{-}3.3\times10^{-4}$
Liquid	0.8-1.0	$0.3\text{-}2.4\times10^{-2}$	$0.5\text{-}2.0\times10^{-5}$

As observed in Table 2.2, the supercritical fluid diffusion coefficient is more than ten times that of a liquid and both the viscosity and diffusivity are dependent on temperature and pressure. In the region of the critical point, viscosity and diffusivity are considerably less than that of a liquid [22-24]. The properties of gas-like diffusivity, gas-like viscosity and liquid-like density have provided the motivation to use supercritical fluid technology to a variety of problems [23, 25]. Kazarian reported that one of the major advantages of a supercritical fluid is that the density can be easily tuned from gas to liquid without changing the molecular structure by simply changing the pressure of the fluid. This tunable property of supercritical fluids makes it advantageous for adjusting many properties of process operation that can be realised through density tuning. The list of compounds used as SCF is presented in Table 2.3

Table 2.3 List of compounds used as supercritical fluid [21, 23, 25]

Solvents	**Tc(°C)**	**Pc(MPa)**	**ρ_c(g cm^{-3})**
N-Methyl-2-pyrrolidone (NMP)	450.9	4.8	0.318
N, N-Dimethylformamide (DMF)	376.5	4.4	0.293
Water	374.0	22.1	0.322
1-Butanol	289.3	4.4	0.270
1-Propanol	263.5	5.2	0.275
Ethanol	240.9	6.1	0.276
Methanol	239.5	8.1	0.272
Isopropanol	234.9	4.8	0.273
Hexane	234.1	3.0	0.233
Ammonia	133.0	11.4	0.244
Carbon dioxide (CO_2)	31.0	7.3	0.469

Although many compounds are available to be used as a supercritical fluid (Table 2.3), supercritical carbon dioxide ($scCO_2$) is most commonly used due to its unique characteristics, such as having a low critical temperature, being non-toxic and non-flammable, it is inexpensive and does not contribute to the net global warming effect [23, 26]. $scCO_2$ is a clean and multipurpose solvent and a promising alternative to noxious organic solvents and chlorofluorocarbons [26]. Therefore, $scCO_2$ saves cost and energy when compared to traditional polymer processing techniques such as drying and solvent removal, as CO_2 is readily available as a gas under ambient conditions. The supercritical condition for carbon dioxide is attained at a low operating pressure and temperature (Tc=304 K/ 31.1 °C, P_c=7.38 MPa / 71.1Bar / 1058 psi) and it can be removed from a system by simple depressurisation [24]. Moreover, polymer

manufacturing processes such as extrusion or injection moulding can readily use the supercritical temperature and pressure range and as such, are cost effective. Many polymers become highly swollen and plasticised in the presence of CO_2, allowing processing at low temperatures [26]. Hyatt et al, Nalawade et al and other researchers [24, 26, 27] have reported that $scCO_2$ has a restricted capability to dissolve in all polymers (except silicones or fluorinated polymers) and high molecular weight polymers, however, it can plasticise thermoplastic polymers with a reduction in the glass transition temperature that could lead to processing with less energy.

2.5 Polymer Processing using Supercritical Fluids

The use of SCF has garnered much attention, not only due to their impressive density tuneability, low environmental effects or lower energy consumption, but SCF has a number of unique properties that can be useful to the present polymer processing techniques. Specifically, the molecular structure of carbon dioxide plays an important role in the processing of polymers. The overall effect of $scCO_2$ on polymers is presented schematically in Figure 2.4.

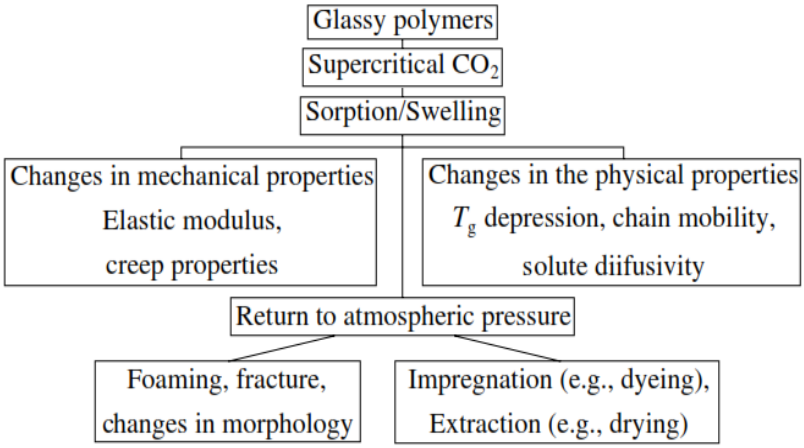

Figure 2.4 Effect of Supercritical carbon dioxide on glassy polymers [17]

Usually, the adsorption of $scCO_2$ into the polymer brings about swelling effects within the polymer matrix, in turn changing the mechanical and physical properties of the polymer. This swelling effect usually results in a reduction of the glass transition temperature due to enhanced segmental and chain mobility. However, upon returning to atmospheric pressure, effects such as foaming, impregnation or even extraction can be obtained accordingly. A review by Kazarian [23], summarised how the use of different methodologies or temperature-pressure conditions results in various outcomes. The following sections concentrate on the specific composite-based processing techniques using $scCO_2$.

2.6 Supercritical Fluid Technology in Processing Graphene Nanoparticles

Graphene is becoming more popular due to its remarkable mechanical strength, elasticity, electrical conductivity and thermal stability. However, one of the crucial challenges that graphene-based materials face for complete industrial transition, is the inability to produce a more stable dispersion of graphene and its derivatives at a large scale. Therefore, methods of graphene production are growing rapidly to meet many applications [28-33]. One of the most simple and common means of graphene production is through solvent exfoliation yielding a graphene oxide (GO) monolayer and further reducing to graphene via thermal treatment. The use of additional reduction and exfoliation step to produce graphene monolayers, often use harsh reducing agents and high temperatures; this, in turn, limits the use of graphene in many applications, such as drug delivery systems or use of graphene in composites. The main disadvantage of this processing technique is that the chemical residue which difficult to remove and it gives a low yield. Another method of producing graphene is the chemical vapour deposition technique, which is an industrial standard technique that incurs the high cost and is difficult to strip off once deposited [30-32, 34, 35]. Figure 2.5 shows the current SCF techniques such as rapid expansion of supercritical solution (RESS), supercritical chemical deposition technique (SFCD) and supercritical anti-solvent technique (SAS) used in the processing of graphene particles.

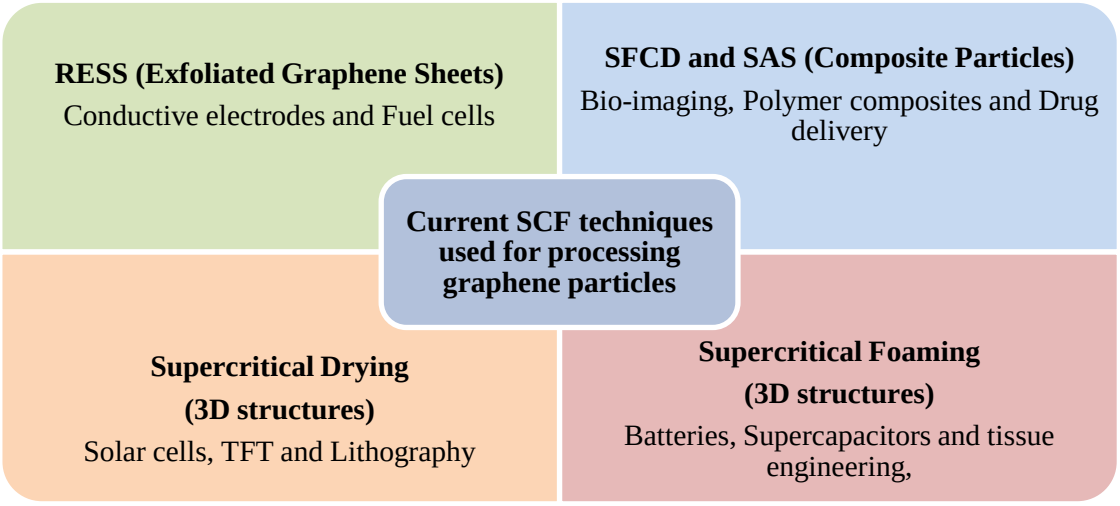

Figure 2.5 General representation of current SCF techniques used in the processing of graphene particles and their respective applications (adapted from [25, 36, 37])

Recently, researchers have reported the use of a supercritical fluid (SCF) for the synthesis of organic and inorganic material for the semiconductor device fabrication industry (as seen (Figure

2.5) [33, 34, 36]. SCF offers potential benefits to tailor specific properties of graphene thereby enhancing the processibility of such graphene and functional graphene materials [30-34, 36-38]. One of the main advantages of using supercritical fluid is that it replaces the long duration ultra-sonication usually used in mechanical exfoliation which results in defective graphene sheets, thereby disturbing the mechanical and electrical properties. A brief introduction is given to the current state of the art techniques used and their application in the context of processing of graphene using SCF.

2.6.1 Rapid Expansion of Supercritical Solution (RESS): In the case of graphene production, this process is mainly used for the exfoliation of graphite to produce graphene [37-40]. In a typical experiment, either CO_2 or organic solvents such as dimethylformamide (DMF) or N-methyl-2-pyrrolidone (NMP) are used. Graphite is immersed in the required solvent and pressurised until the critical temperature and pressure are reached. This process allows SCF to diffuse through the graphite layers. After a specified time, the pressurised cell is depressurised rapidly, where SCF expands the graphite interlayers producing graphene monolayers. Usually, organic solvents are used, where these exfoliated particles do not stack up again in interlayers of graphite. Therefore, the SCF process can completely eliminate the use of harsh chemicals, long ultra-sonication duration and additional reduction processes, which is a common process in the case of the chemical route of graphene synthesis.

2.6.2 Supercritical Anti-Solvent Technique (SAS): This technique is mainly used to synthesise polymer-graphene composites. SAS is one of the industrial standardised micronisation techniques used for pharmaceutical and natural compounds. Typically, a solvent is chosen which has less affinity for CO_2 and is highly mixable with the polymer. The solvent is mixed with a polymer and placed in an autoclave with the gradual introduction of graphene (depending on the wt. or vol. %). This autoclave is further pressurised to reach the critical temperature, where the $scCO_2$ reaches a supersaturation condition due to its insolubility with the polymer molecules. This supersaturation and insolubility of the polymer provides mass transfer and results in the homogenous dispersion of graphene sheets in polymers [36, 41, 42]. A typical SAS technique was reported by Xiaolia et al [43] to produce a high throughput exfoliated graphene-pyrene polymer composite using dimethyl sulfoxide (DMSO) as the anti-solvent. While Rangappa et al [36, 42, 43] reported a one-pot impregnation of pyrene sulfonic acid (PSA) on graphene nanosheets using *in situ* supercritical exfoliation technique for a battery application.

2.6.3 Supercritical Chemical Deposition Technique (SFCD): This technique is similar to conventional CVD processes, except that a supercritical fluid (SCF) is used to deposit metallic nanoparticles on graphene nanosheets. Horibe et al demonstrated a method to deposit TiO_2 nanoparticles on the surface of carbon nanotubes for fuel cell/capacitor applications [43, 44]. A typical experiment consists of two pressure chambers connected to each other by piping and separated by a needle valve. One of the chambers contains the metal precursors and the other container of graphene substrates/ nanotubes. The metal-containing precursor particles are sprayed over the graphene sheets in the reaction chamber and upon depressurisation, the metal molecules impregnate the surface of graphene. This is followed by nucleation and particle growth on the surface of the graphene. Similarly, silver nanoparticle-decorated graphene using supercritical synthesis for engine-oil nanofluids was reported by Yuan Meng et al [42, 45].

2.6.4 Supercritical Drying (SD): In the case of graphene, the SD process is mainly used for drying of graphene-based hydrogels to form aerogels. The ability of hydrogels to retain the porous gel matrix is one of the major drawbacks of using the solvent evaporation process. As such, the evaporation process can result in the creation of an additional liquid-vapour interface, which, in turn, increases the surface tension leading to shrinkage and collapse of pore volume within the hydrogel matrix. In a typical SD process, the hydrogels are immersed in SCF soluble alcohol solvents such as acetone or ethanol and are placed in an autoclave. When pressurised, the $scCO_2$ is completely soluble in acetone or ethanol. When depressurised, the soluble alcohol converts from the liquid to the supercritical state and to the gas state without entering the liquid-vapour state. This retains the porous gel matrix. Tewari et al [46] and De Cicco et al [47] have reported the drying of aerogels using the supercritical drying technique.

2.6.5 Supercritical Fluid Foaming Technique (SF): CO_2 is one of the most abundantly available, environmentally friendly and non-toxic foaming agents. In a typical foaming process, a pre-fabricated graphene-polymer composite, usually prepared by *in situ* polymerisation or solution cast method is placed in an autoclave [48, 49]. It is then filled with $scCO_2$ and the critical points are maintained for the desired duration. Due to the supersaturation of CO_2 within the polymer matrix, the antiplasticisation effect is observed because of the sudden withdrawal of CO_2. This results in nucleation and growth of bubbles within the polymer matrix. Yang et al [50] reported well controlled porous foams of graphene oxide-polypropylene carbonate using the $scCO_2$ foaming technique. This optimisation was controlled by carefully varying critical temperature and pressure to specifically meet the requirements of pore size for tissue engineering applications. Edward et al [51] demonstrated the use of the $scCO_2$ foaming technique to enhance

and control the porosity, mechanical and biocompatibility characteristics for bone grafting application.

2.7 Graphene-based Polymer Nanocomposites using Supercritical Fluid

Graphene-based polymer composites are becoming more attractive due to their exceptional mechanical, electrical and thermal properties. However, one of the major issues with graphene composites is poor dispersion levels due to aggregation of graphene within the polymer matrix [36, 40, 50-52]. Because of these reasons, graphene oxide (GO) (which has an oxygen-rich surface) has replaced graphene fillers particles, due to its inherent ability to uniformly disperse within the polymer matrix [35, 36, 50, 52]. One of the most commonly reported techniques for preparing graphene/GO-based polymer composites is the solution intercalation method (or *in situ* polymerisation). This preparation method usually uses a readily available polymer or monomer mixed with graphene/GO under long ultra-sonication to provide an even dispersion. In addition to producing defective graphene/GO particles, this process also suffers from the poor interaction between the polymer and GO interface (fewer particles interact with the polymer chains). The supercritical fluid (SCF) processing technique produces homogenous composites due to its ability to interact with graphene/GO particles while also swelling the polymers. Therefore, SCF not only provides exfoliation of the graphene interlayer but also enhances the interaction between the polymer chain and the nanoparticle as one step process. Exfoliation of the graphite interlayer occurs when SCF solubilised polymer chains, diffuse and interact with the graphene/GO interlayer surface and in turn push the tightly stacked layers apart upon depressurisation [35, 36, 42, 43]. A proof of this concept is reported by Jang et al and Rangappa et al [43], where graphene sheet modified pyrene sulfonic acid with SCF produced more than 60% of bilayer graphene particles when compared to that produced without utilising the SCF technique. In another case, Zhang et al [53], demonstrated the two-step synthesis process, where GO was first mixed with the polymer (polyethene-b-poly (ethylene oxide - PE-PEO) and then subsequently exposed to $scCO_2$. It was observed that the polymer chain interacted with both the edges and the surface of the GO sheets resulting in a homogenous distribution of PEO crystallites on the surface of GO (similar experiments were also conducted on carbon nanotube PEO composites). However, the same process without SCF resulted in an amorphous PEO graphene composite. The authors (Zhang et al) suggest that the SCF process influences the polymer crystallite size and arrangement. In addition, the anti-solvent technique was also reported by Zheng et al to produce uniformly wrapped poly(vinylidene fluoride) on carbon

nanotubes (CNTs) using three different organic solvents (namely: dimethyl sulfoxide (DMSO), N,N-dimethylformamide (DMF) and N,N-dimethylacetamide (DMAc). It was reported that use of the high-pressure SCF anti-solvent - DMF and DMAc, showed more dispersion and wrapping of PVDF when compared to DMSO [53, 54]. Xu et al [55] and D Gui et al [56] have reported the $scCO_2$ assisted *in situ* polymerisation of graphene oxide/polyaniline nanocomposites for supercapacitor applications [57]. The reported synthesis procedures used various ratios of GO and aniline monomer mixed into a solution with ethanol. This solution was then exposed to $scCO_2$ using the anti-solvent technique, where the diffusivity and mass transfer characteristics of $scCO_2$ help to impregnate polyaniline on the surface of GO. Similar RESS techniques have also been reported by S. Xu et al [56] in the preparation of highly conductive pyrrole graphene nanocomposite films. The authors (S. Xu et al) suggest that SCF technique has a greater advantage in terms of producing graphene monolayer and even dispersion within polymer composites.

2.8 Graphene Polymer Foams using Supercritical Fluid

The use of $scCO_2$ assisted foaming of polymer composites using high-pressure autoclaves are well documented, mainly due to the reason the $scCO_2$ is more environmentally friendly when compared to ozone-depleting conventional blowing agents such as chlorofluorocarbons (CFC) and hydrochlorofluorocarbons (HCFC) [36, 55, 58, 59]. More specifically, one of the major applications of foaming is in the fabrication of scaffolds for tissue engineering [50, 60, 61]. The conventional chemical foaming agents cannot be used for tissue engineering applications due to their toxicity. Such a tissue engineering application, using the $scCO_2$ foaming technique, is reported by G Yang et al [50, 60]. G Yang et al demonstrated enhanced mechanical strength and thermal stability of poly(propylene carbonate) by adding graphene oxide and using $scCO_2$ as the foaming agent. The use of SCF further enhanced the storage modulus by 50% when compared to initial GO composite without SCF. In addition, Gedler et al and M Antunes et al [62-64] also investigated the effect of higher CO_2 critical pressure and critical temperature, which results in smaller denser cells. In addition, SCF not only provides even dispersion of nanoparticles within the matrix but also affects the crystallisation of polycarbonate. Typical experimental procedures consist of the preparation of a polymer composite/membrane, usually using the solution cast method or hot melt extrusion. These composites are then placed inside a high-pressure vessel for a specific duration to initiate the foaming process [62, 63]. In similar work by Tai-Rong Kuang et al [65], the fabrication of poly(lactic acid)/graphene oxide foams with high orientation and

elongated cell structure using $scCO_2$ as blowing agent were reported. C Li et al [66], reported his work on polystyrene functionalised graphene nanocomposite foams prepared using $scCO_2$. Li's study reports the effect of SCF and fillers on the nucleation and thermal stability. It was reported that the GO agglomerated due to the non-polar nature of styrene and thus, reduced the nucleation efficiency. However, the higher GO ratio (more than 3%) improved the foam structure (pore size - 4.3 µm) and increased the glass transition temperature by 5 °C. At the same time, incorporation of reduced GO within the styrene group resulted in a dispersed system with high cell density. Additionally, the GO and reduced GO foams showed better mechanical and thermal stability when compared to virgin PS foams [66]. Recently, a polycarbonate graphene nanocomposite was prepared using a 1-step supercritical carbon dioxide process by G. Gedler et al [64] for electromagnetic shielding applications. The results showed that the shielding effectiveness was increased by 15 times after foaming (30 dB cm^3/g- which is 4 x of copper - 35 times greater than that of non-foamed) and the relative permittivity of polycarbonate increased upon foaming and the addition of graphene. Here the samples were melt-compounded first by physical mixing of graphene into polycarbonate and further saturated in $scCO_2$, up to 120 min at various critical temperatures (200-213 °C) and pressures (12-16MPa) with a rapid depressurisation rate of 0.3MPa/s. This reported work showed that graphene-based polymer foaming using supercritical fluid produces a highly controlled cell size and enhances the thermal, mechanical and electrical properties of the foamed composites. However, potential applications of such foaming techniques using SCF, other than tissue engineering are limited. Such limitations arise mainly due to the poor justification of significant relation between the tunable properties of SCF (specific pressure and temperature used) on the properties of the foamed composites, and lack of investigation on direct one-step foam production using industrial standard polymer processing technique such as extrusion or injection moulding.

2.9 Materials used in this Study

Electroactive Polymers (EAP's): The most common polymer membrane used in the fabrication of actuators is the perfluorinated membrane, such as Nafion (DuPont). Nafion is not environmentally friendly as it is a fluorinated polymer, and it is expensive for practical applications [67]. Although Nafion-based actuators are considered to perform well, they have problems such as the straightening-back phenomenon under a DC electric field [6, 68-72]. Thus, industry and research groups are constantly looking for much cheaper and ecologically acceptable polymer membranes to replace the most widely used Nafion polymer membranes.

This research proposes the use of Pebax and Poly (styrene–ethylene–butylene–styrene) (SEBS) as membrane materials.

Pebax is a registered trade name for a group of polyether block amides manufactured by Arkema. The properties of Pebax such as mechanical stiffness, flexibility, biocompatibility, chemical resistance, ease of sterilisation which makes Pebax, a good choice for biomedical devices such as catheters and haemodialysis membrane tubings. Interest in the use of Pebax for sporting equipment and gas separation membranes has grown, mainly due to its low density, high mechanical performance and reverse selectivity for CO_2 and H_2. The general formula of Pebax is $(A\text{-}B)^n$, and it combines linear chains of rigid polyamide segments (PA hard segment) interspaced with flexible polyether segments (PE soft segment) [33, 73].

Figure 2.6 shows the chemical structure of Pebax. The presence of a polar (NH) amine functional group in the polyamide segment and (CO) carbonyl oxygen forming a polar ester linkage between the PA and PE segments within the copolymer makes Pebax an appropriate material for membrane-based applications, as these functional groups act as suggested charge transfer sites, which may provide mass transfer of charges. Pebax grade 5533 was chosen for this study.

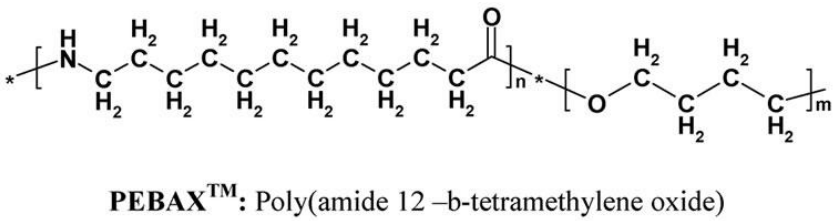

Figure 2.6 Chemical structure of Pebax® [74]

Poly(styrene–ethylene–butylene–styrene) – is a triblock copolymer (SEBS) which is a thermoplastic elastomer with high thermal and mechanical stability. SEBS consists of soft or amorphous ethylene-butylene block in between the hard styrene blocks [75]. Further, they maintain their mechanical properties; have high proton conductivity and high water uptake over a wide temperature range [73, 75-78]. Figure 2.7 shows the chemical structure of SEBS. SEBS has a low production cost with respect to that of Nafion. The styrene blocks of the SEBS can be subsequently sulfonated to provides high ionic conductivity [77-79]. Ehrenberg et al [80, 81] synthesised sulfonated polystyrene-block-poly(ethylene-butylene)-block polystyrene (SEBS) and reported proton conductivity of over 10^{-2} S/cm.

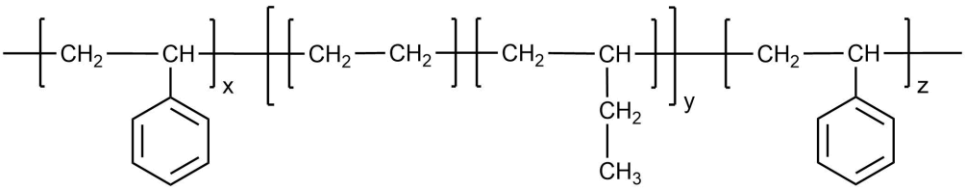

Figure 2.7 Chemical structure of SEBS

Graphene and Graphene Oxide: Graphene is a two-dimensional, highly conjugated single-atom-thick carbon material. It has drawn scientific and commercial interest in various applications in the field of electronics, quantum physics, novel material and chemistry [80-83]. Due to its unique single atom structure of hexagonally arranged sp^2 hybridised carbon atoms [34, 82-90], graphene has been proved to have better electrical, optical, mechanical and thermal properties.

Carbon, the sixth element of the periodic table, has 4 valence electrons and a ground state electron configuration of $1s^2$, $2s^2$, $2p^2$. Every carbon atom in graphene has three covalent σ bonds with its nearest carbon neighbour in the trigonal xy plane forming 120° angles [82-86, 89, 90]. The remaining pz electron orbital forms a π-bond whose electron density lies above and below the nodal xy plane. The valence electron wave functions are sp^2 hybridised. The aromatic π electron cloud [91] and the crystal structure are responsible for the extraordinary electronic and thermal properties of the monolayer, bilayer and few-layer graphene [82-86, 89, 90]. The Schrodinger equation for the electron wave function using the tight binding approximation was calculated by Wallace [92] to estimate the electronic properties of single layer and multilayer graphene structure. The Fermi level lies exactly at the Dirac points in graphene which also separates the bonding and anti-bonding energy states [82-86, 89, 90]. In graphene, a linear (parabolic in metals and semi-metals) energy dispersion is observed at the Dirac points which are responsible for its electronic properties [34, 93]. The electrons in the linear dispersive region behave as massless Dirac fermions [34, 93]. Due to this reason, graphene is considered as a zero bandgap semiconductor or semi-metal. Morozov [87], indicated that up to a few layers of graphene can behave as conductive metals. This shows that as the number of layers is increased, the Dirac points separate from the Fermi level allowing for tuning the band-gap accordingly. The intrinsic Van der Waal force on the surface of graphene results in agglomeration of graphene particles. This, in turn, reduces the conductivity and reinforcement properties of nanocomposites. Therefore, it is crucial to control the thickness of graphene to attain specific electromechanical properties. Graphene particles offer the capability to modify or functionalise the carbon backbone, therefore, the graphene particles can be easily tailored according to specific

conductive or insulator requirements. The functionalisation of graphene can effectively reduce the agglomeration within the polymer matrix. Graphene Oxide (GO) is a thin sheet of graphite that is covalently decorated with oxygen-containing functional groups on the basal plane or at the edges. Graphene oxide acts as an electron insulator while it provides ion conduction due to specific site interaction of sp^2 and sp^3 hybridised carbon atoms [34, 87, 93]. The oxygen-containing functional groups include hydroxyl, epoxide, carboxyl, diols and ketones. The heavy oxidation of graphene makes GO hydrophilic and thereby provides better dispersion in water. Studies have shown that the oxygenated basal plane enhances the interaction between the filler and polymer matrix thereby enhancing the electromechanical performance of the polymer matrix [34, 93].

Methodology: The composites were processed by using twin screw melt extrusion. Hot melt extrusion offers low cost and solvent-free approach to large-scale membrane fabrication. The key advantage of using melt extrusion method is that the degree of molecular alignment and the degree of crystallinity can be easily controlled compared to solvent casting method which in turn leads to improved mechanical strength and durability of polymer membranes [77-79].

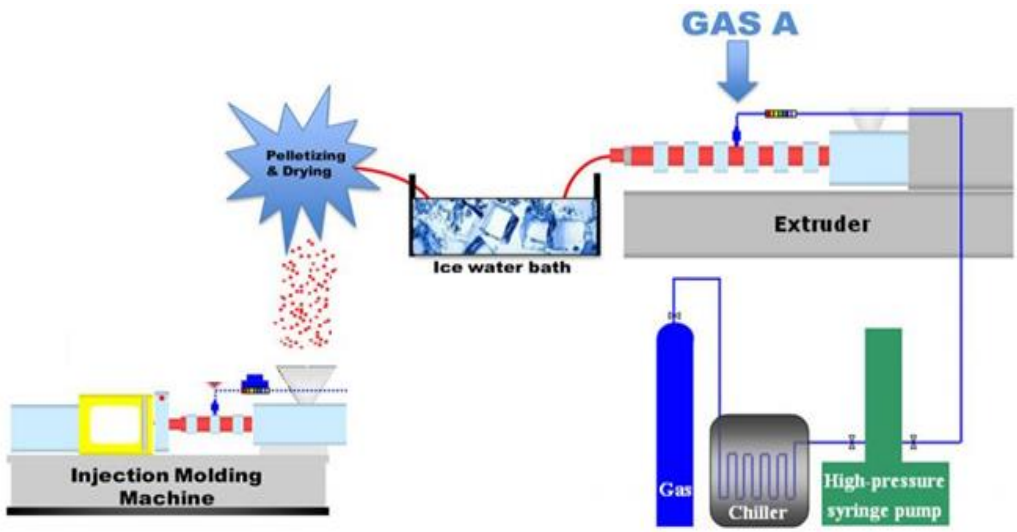

Figure 2.8 Schematic of scCO2 assisted hot-melt extrusion process

The use of high shear screws during the extrusion process promotes mixing of nanoparticles within the polymer matrix (process as shown in Figure 2.8). In addition, an appropriately porous morphology can be obtained by incorporating supercritical carbon dioxide during the process of extrusion. The extruded-calendared membrane is sandblasted to achieve an appropriately rough surface. Kazarian et al [25, 94, 95] reported that use of $scCO_2$ reduces the viscosity with an

increase in the diffusion rate of the polymer. Rangappa et al [41, 43] demonstrated a one-pot supercritical fluid (SCF) assisted the exfoliation process to produce high-quality, large-scale, and processable graphene. The exfoliated sheets were described as 90 to 95% of the exfoliated sheets were < 8 layers with about 6–10% monolayers and the remaining 5–10% is ≥ 10 layers. On the other hand, Gulari et al [96] have reported a supercritical CO_2 assisted technique to exfoliate layered silicates and delaminating graphite structure. Here, supercritical fluid assisted graphene exfoliation is proposed to open the cross-sectional number of graphene layers, thereby producing highly conductive graphene. Graphene oxide was synthesised using Hummer's method [97, 98].

2.10 Aims and Objectives

Although several well-established processes/techniques have been reported to disperse nanofillers within the polymer matrix, solution-based SCF techniques have shown extraordinary results in the exfoliation of graphene-based nanoparticles (bilayers or few-layer graphene can be produced easily). SCF processing technique in the case of composites has shown even dispersion throughout the polymer matrix with short processing duration, which is otherwise difficult to achieve when compared to long duration ultra-sonication. This, in turn, enhances the mechanical, thermal and electrical property of the polymer nanocomposite. It is also unknown to how SCF processing effect the molecules or microphases/crystallite structure and size of the polymer. Therefore, this research hypothesises that SCF processing can play a crucial role not only in terms of exfoliation of graphene, or even dispersion, but also plays a key role in the alignment of crystallites size and the lamellar structure of the polymer. SCF-assisted foaming has also resulted in a more environmentally friendly technique to produce a well-controlled porous composite. Despite the number of SCF techniques available on the scientific research front, industrial standardised processing of polymers composites using supercritical fluid still remains unexplored. In addition to the advantages of SCF in the preparation of composites, there is a lack of sufficient investigation on graphene-polymer foams and their respective effects on the properties. Therefore, this research focuses on the use of supercritical fluid in preparing graphene-based polymeric composites using industrial standard polymer processing techniques. Potential modifications to polymer processing techniques using supercritical fluid in this research work include the following:

a. The proposed study will investigate the electroactive polymer composite properties of nanocomposite based thermoplastic elastomers

b. This research will exploit the high-volume continuous $scCO_2$ assisted polymer extrusion and injection moulding technologies to add value to existing low-volume batch production systems currently employed.

The novelty of this work is in the use of nanofillers, such as graphene and graphene oxide that further improve the electromechanical behaviour of the EAP. The use of supercritical assisted polymer processing technique provides a homogeneous dispersion of nanoparticles and enhances their performance by interfacial interactions between the filler and the polymer matrix. The functionalisation of graphene enhances the interaction between the polymer matrices and enhances the electromechanical performance of the membranes. The ability to tailor the properties of EAPs using supercritical carbon dioxide assisted processing technique helps to provide an industrial solution with respect to the needs of low-powered, lightweight, environment-friendly and easy industrial production of EAPs for use in a broad range of applications.

The aim of this work was to investigate the electromechanical performance of graphene-based electroactive polymer composites using supercritical assisted polymer processing technique. The following objectives were proposed for the study,

1. To investigate and understand the effects of supercritical assisted processing at various critical pressures (sub @ 800 psi, near @ 900 psi and beyond @1200 psi critical pressure) on the thermal and mechanical properties of Pebax and SEBS polymer matrix.

2. To investigate the effect of incorporating graphene-based (graphene and graphene oxide) filler particles (at loading less than equal to 2.5 wt. %) into Pebax and SEBS polymeric matrices when processed with $scCO_2$.

- To understand the effects of various filler loading concentrations on the actual crystallisation kinetics of the manufactured Pebax polymer composites

3. To understand the effects of reprocessing the $scCO_2$ processed graphene-based polymer composites on the thermal and electromechanical performances of the manufactured polymer matrix.

- To understand the effects of various filler loading concentrations on the actual crystallisation kinetics of the manufactured Pebax polymer composites

4. Evaluation of bending actuating mechanism for all the manufactured composites

3 Experimental Methods

3.1 Materials

Poly (ether-block-amide) - Pebax® was procured from Arkema, France. For ease of illustration of the trade name Pebax® throughout the thesis, the word Pebax alone will be used. The received Pebax was stored at room temperature for several months before extrusion and material characterisation. Pebax (refer to Figure 2.6) was dried using a vacuum oven at 75 °C for 5-6 hours to remove the moisture content before the start of any process. The 33 series of Pebax is composed of polyamide 12 (Nylon 12) as the hard segment and poly(tetramethylene oxide) PTMO as the soft segment. Pebax consists of 80% hard segments of polyamide-12 (PA12) and 20% soft segments of poly(tetramethylene oxide) (PTMO) by molecular weight. The density of grade 33 series Pebax is around 1.01g/cm^3 by ISO 1183.

Poly (styrene-b-ethylene butylene-b-styrene)-(SEBS) (Kraton® G1652E Polymer) with linear triblock structure and styrene/rubber ratio of 29/71 was supplied by Kraton Polymer Research, Belgium. The received SEBS (refer to Figure 2.7) was stored at room temperature for several months before extrusion and material characterisation.

Graphene with a thickness of 6-8 nm, a specific surface area of 120 m^2/g and purity of 99.5% was procured from Ionic Liquid Technologies, USA. Graphene was stored at room temperature for several months before any experiment. No additional graphene modification was carried out during the experimental procedure.

3.2 Synthesis of Graphene Oxide using Hummer's Method

Chemicals required: Graphite flakes, Sodium nitrate (98%, Alfa Aesar), Potassium permanganate (99%, Alfa Aesar), Hydrogen peroxide (35% wt. Alfa Aesar), Sulphuric acid (98%, ACS) and Hydrochloric acid (35%, Alfa Aesar)

Graphene oxide was synthesised through oxidation of graphite particles using Hummer's method [98, 99]. The stepwise preparation is as follows:

a. Graphite flakes (5 g) and $NaNO_3$ (2.5 g) were mixed in a 1000 ml volumetric flask and kept in an ice bath (0-5 °C) with continuous stirring for 5 minutes. 110 ml of H_2SO_4 was added and kept stirring for 2 hours at the same temperature.

b. Potassium permanganate (15 g) was slowly added to the continuously stirred suspension under controlled conditions for about 1 hour by keeping the reaction temperature below 15 °C (colour changes from black to green).
c. The ice bath was removed and the mixture was stirred at room temperature for 15 minutes and then the temperature was increased to 35 °C until it was a thick brownish paste or for 30 minutes.
d. Deionized water (230 ml) was slowly added under continuous stirring. The temperature was then increased to 98 °C when effervescence was observed. The colour changes to copper or orange-brown (exothermic reaction – GO production process).
e. The solution was further diluted with 400 ml of water and stirred continuously for 2 hours (golden brown).
f. The solution was treated with 50 ml H_2O_2 to terminate the reaction when the colour changed to yellowish brown.
g. The mixture was allowed to settle overnight, washed with HCl and then with deionized water several times using centrifugation until the pH was 6 or 7.
h. After filtration, the GO cake was dried under vacuum at room temperature for 48 hours and cake was crushed to obtain powdered GO.

3.3 Preparation of Polymer Composites

A co-rotating twin screw extruder with length/diameter (L/D) ratio of 40:1 and/or 25:1 was used for the preparation of polymer composite of Pebax and SEBS combined with graphene and graphene oxide. Table 3.1 provides the details of polymer composite selection made under different conditions.

Pebax and SEBS without $scCO_2$ were extruded in a co-rotating twin screw extruder with L/D ratio of 40:1. Extrusion was carried out at a screw speed of 55 revolutions per minute, torque between 15 to 10 Nm, die pressure was maintained between 5-10 psi and temperature profile as per Table 3.2.

For $scCO_2$ assisted extrusion, an additional $scCO_2$ setup consisting of a CO_2 cylinder, injection pump and controller were installed together using stainless tubes to prevent the fluctuating pressure at the injection point and along the barrel (up and down). Additional kneading blocks were incorporated along the length of the screw to provide better mixing and avoid pressure fluctuation.

Table 3.1 Experimental matrix for extrusion of polymers/composites under different conditions

Exp. No	Polymers used	Additives used (wt. %)	Stage 1 processing – hot melt extrusion		Stage 2 reprocessing without $scCO_2$	Chapters
			With $scCO_2$	**Without $scCO_2$**		
1	a. Pebax	0	√	√	×	4.1
	b. SEBS	0	√	√	×	4.2
2	Pebax	Graphene (0%, 0.25%, 0.5%, 1%, 2.5%)	√	×	×	5
		Graphene Oxide (0%, 0.5%, 1%, 2.5%)	√	×	×	5
3	SEBS	Graphene (0%, 0.25%, 0.5%, 1%, 2.5%)	√	×	×	6
		Graphene Oxide (0%, 0.5%, 1%, 2.5%)	√	×	×	6
4	Pebax	Graphene (0%, 0.25%, 0.5%, 1%, 2.5%)	√	√	√	7
		Graphene Oxide (0%, 0.5%, 1%, 2.5%)	√	√	√	7
5	SEBS	Graphene (0%, 0.25%, 0.5%, 1%, 2.5%)	√	√	√	8
		Graphene Oxide (0%, 0.5%, 1%, 2.5%)	√	√	√	8

Table 3.2 Temperature profile for extrusion of Pebax and SEBS composites

Material	**Temperature profile (Zones) (°C)**									
	1	2	3	4	5	6	7	8	9	Die
Pebax	30	60	110	130	155	155	160	170	180	180
SEBS	40	120	150	180	190	200	210	220	230	240

The critical temperature and pressure of 31 °C and 1200 psi were maintained throughout the extrusion process for all the SCF-assisted samples as designed in experiment number 4 and 5 in Table 3.1. The flow rate was maintained at 2 ml/min and alternatively, the injection pump was refilled to avoid fluctuation in the flow rate (refer to Figure 2.8). All extrudates were then passed through a pelletiser system. The granulated composite material (Step 1) was further divided equally into two parts and where the first part was processed again without $scCO_2$ (Step-2, reprocessed). All the reprocessed extrusion temperature parameters were maintained as described in Table 3.2. The second part was processed using injection moulding (Table 3.3) to attain a homogeneous and evenly dispersed flat polymer matrix (Step 2 Extrusion and Step 2 Injection).

Table 3.3 Temperature profile for Injection Moulded Pebax graphene composites without SCF (Step-2 Injection Moulding without SCF)

Material	**Temperature profile (Zones) (°C)**					
	1	2	3	4	5	Sprue
Pebax	110	130	145	155	165	170
SEBS	170	175	220	230	240	240

The formulation of graphene nanoparticles in the polymer nanocomposites was varied from 0%, 0.25%, 0.5%, 1% and 2.5%. The term "treated" and "untreated" in the context of this Chapter means that the materials were processed with $scCO_2$ (treated) and without $scCO_2$ (untreated). The formulations of GO nanoparticles in polymer nanocomposites were varied from 0%, 0.5% and 2.5%.

Table 3.4 Temperature profile of paraffin oil modified SEBS graphene oxide composite with/ without $scCO_2$

Material	**Temperature profile (Zones) (°C)**					
	1	2	3	4	5	Die
SEBS without $scCO_2$	30	100	120	130	130	130
SEBS with $scCO_2$	30	100	110	120	125	125

When processing the SEBS/GO composites, the GO particles tend to lose their functional group due to the high processing temperatures required to process SEBS. For this reason, a small modification was made to lower the processing temperature of SEBS by using paraffin oil with SEBS in the ratio of 2:1. To start with, SEBS pellets were heated for 4-6 hour at 50 °C in a vacuum oven to remove any moisture. These pellets were immersed in a 2:1 ratio of SEBS to paraffin oil overnight before the day of extrusion. Table 3.4 shows the temperature profile of paraffin oil modified SEBS graphene oxide composite without $scCO_2$ and with $scCO_2$ accordingly.

3.4 Characterisation Methods and Techniques

3.4.1 Thermal Gravimetric Analysis

The degradation and thermal stability of all extrudates were analysed using a TGA Q50, TA Instruments. TGA measures weight changes in a material as a function of temperature under a

controlled atmosphere. TGA measurements are used to determine the thermal stability of the manufactured polymer matrix. Each measurement was carried out using temperature increments of 10 °C/min, from room temperature to 650 °C. All the measurements were done using aluminium pans with sample masses of approximately 6 mg to 7mg.

3.4.2 Heat/Cool/Heat Differential Scanning Calorimetry for Crystallinity Study of Pebax

Chapter 4 and 5: All heat/cool/heat thermal analysis experiments were carried out using TA instruments 2000 DSC. Approximately 8 mg of each sample was hermetically sealed in aluminium pans. Standard heat/cool/heat test method with a ramp rate of 10 °C/min from -85 °C to 200 °C (first and second heating cycle) and cooling rate of 10 °C/min to -85 °C (cooling cycle) was used for each sample. Where required, curve smoothing up the process of 2 - 3 was used.

3.4.3 Study on Crystallisation Kinetics of Pebax Graphene-Based Composites

The characteristic behaviour of semicrystalline polymers or their composites, such as crystallinity and/or homogeneity can be determined not only by their chemical structure, chain conformation and molecular weight distribution but also by the mechanism and kinetics of crystallisation. It is well known that the properties of semicrystalline block copolymers, such as Pebax, depend strongly on the crystallisation mechanism of the hard block and the phase separation of incompatible hard–soft blocks.

In Pebax, the process of crystallisation occurs through the linking of hard-soft segments, by means of hydrogen bonding between the amide and ether groups, respectively [100-102]. When a block copolymer crystallises from its melt, the crystallisation process is comparable to most homopolymers, where crystallites can easily grow to form spherulites without any restriction to the crystal growth. However, in phase-separated melts such as Pebax, the crystallisation process is confined to microdomains which restrict the crystal growth to one-two dimension. The addition of graphene particles (agglomerated or evenly dispersed) and $scCO_2$ processing conditions further restricts/affects the crystal growth to one dimension, resulting in nanoscale crystal structures. These behavioural changes (degree and rate of crystallisation) with respect to the effect of particle dispersion/exfoliation and $scCO_2$ processing conditions can be clearly observed by understanding the crystallisation kinetics.

Therefore, in order to systematically investigate the effect of processing condition (use of $scCO_2$) or the addition of filler particles on the polymer crystallisation process; isothermal and non-

isothermal crystallisation kinetics studies were carried out with the help of differential scanning calorimetry.

3.4.3.1 Isothermal Crystallisation Kinetics of Pebax Graphene-based Composites

DSC thermographs were recorded for each of the Pebax samples using TA instruments 2000 DSC. Each sample was heated from room temperature to 20 °C above melt temperature at the rate of 30 °C/min and was held isothermally for 10 minutes in order to remove all the thermal history or residue of crystallinity. The sample was then cooled to various predetermined crystallisation temperatures (Tc) at a cooling rate of 50 °C/min. A fresh sample was prepared for each of the Tc specific thermograms and the exothermic curves of heat flow as a function of time were recorded. Further processing and acquisition of data were done using Origin and TA universal data analysis software.

Analysis Technique: The Avrami equation was used to describe the crystallisation kinetics of semi-crystalline polymer under isothermal conditions. This model describes the primary nucleation and growth of crystal units until their impingement towards the secondary crystallisation stage under isothermal conditions. A time-dependent relative volumetric crystallinity Xt under isothermal conditions can be expressed as:

$$Xt = 1 - \exp(-kt^n) \qquad \text{Equation 3.1}$$

The above equation can also be written as:

$$\log[-\ln(1 - Xt)] = logk + nlog \qquad \text{Equation 3.2}$$

Where ‘t’ is the time, n is the Avrami exponent and k is the overall crystallisation rate constant which gives information on the mechanism of nucleation and the growth rate. The parameters n and k can be obtained from the slope and the intercept of the Avrami plot of log[-ln(1-Xt)] vs. log t. Lorenzo et al reported that polymers which nucleate sporadically and crystallise in a spherulitic manner usually have an Avrami index of 4. If the nucleation is instantaneous then the Avrami index is 3. The author also describes that the Avrami index of 3 and 2 describes axialitic sporadic and instantaneous crystallisation. In all of the experimental calculations, efforts were made to maintain the coefficient of determination of Avrami plot (r^2) near to unity in order to obtain the best fit between the theoretical and experimental results. The relationship between k and $t_{1/2}$ based on the Kurajica approach is defined as $t_{1/2} = (\ln 2/k)^{1/n}$. The theoretically calculated $t_{1/2}$ and the practically obtained $t_{1/2}$* are compared in the all the tables where the best match provides an indication of analysis correctness between the theory and the experimental value. As

described by Lorenzo et al, the relative crystallinity range of 3% to 20% was chosen for all the samples in order to obtain a good fit between the theoretical and experimental value.

The crystallisation process under isothermal conditions is dependent on the thermal activation energy and the crystallisation rate parameter and can be described by an Arrhenius type equation as:

$$K^{1/n} = K_0 \exp -\frac{\Delta E}{RTc} \qquad \text{Equation 3.3}$$

where K is a temperature independent pre-exponential factor, ΔE is activation energy, R is the gas constant, and T is the absolute temperature. The slope of the plot ln(K). (1/n) vs. 1/Tc determines the ΔE/R. The activation energy was calculated and was tabulated under appropriate sections through specific chapters.

3.4.3.2 Non-Isothermal Crystallisation Kinetics of Pebax Graphene-based Composites

DSC thermographs were recorded for each of the Pebax samples using TA instruments 2000 DSC. Each sample was heated from room temperature to 20 °C above melt temperature at the rate of 30 °C/min and was held isothermally for 10 minutes in order to remove all the thermal history or residue of crystallinity. The sample was then cooled to 0 °C at a various cooling rate starting from 2.5 °C/min, 5 °C/min, 10 °C/min and 20 °C/min. A fresh sample was prepared for each of the cooling rates and the exothermic curves of heat flow as a function of time were recorded.

Analysis Technique: The well-known Avrami analysis was articulated to understand the phase change process, nucleation and growth, of a given material and has most commonly been used to determine the isothermal polymer crystallisation kinetics [103-107]. However, the same can also be used for non-isothermal conditions. The degree of phase conversion is given by Equation 3.1 and can be reduced to Equation 3.2.

The parameters n and k are obtained from the slope and the intercept of the straight line by the plot of Log [-ln (1-X (t)) vs. Log t. The Avrami model has been modified by Jeziorny [108] to describe the non-isothermal crystallisation processes. Jeziorny's analysis describes how the kinetic constants can be determined by using the Avrami equation. However, under non-isothermal conditions, crystallinity/phase change is the function of temperature X(T). Therefore, the corrected kinetic constant (k') as a function of the Avrami kinetic constant (k) and the cooling rate (ϕ) is given as follows:

$$\log k' = \left(\frac{\log k}{\phi}\right) \qquad \text{Equation 3.4}$$

The relative crystallinity was calculated as a function of temperature and transformed to a time scale by using the relationship t = (Tc_{on}- T)/ ϕ, where, Tc_{on} is the crystallisation onset temperature at crystallisation time t = 0, T is the temperature at the crystallisation time t and ϕ is the cooling rate. The reaction half-time ($t_{1/2}$) can be calculated from the corrected kinetic constant (k') from the following equation:

$$t_{\frac{1}{2}} = \left(\frac{\ln 2}{k'}\right)^{1/n} \qquad \text{Equation 3.5}$$

In most polymer non-isothermal studies, the modified Avrami model fails to provide actual information on the phase transition and the structure, therefore the classical Ozawa model or Avrami-Ozawa is most applicable to non-isothermal conditions [109]. The Ozawa model extends the mathematical derivation proposed by Evans to non-isothermal crystallisation at a constant cooling rate with infinite isothermal steps as follows [110]:

$$1 - X(T) = e^{\frac{-K^*}{\phi^m}} \qquad \text{Equation 3.6}$$

where constant m is the Ozawa exponent, which is independent of temperature, and K* is a heating/cooling function. The plot of ln [-ln (1-X (T)] vs. ln ϕ gives a linear fit, where the slope and intercept gives the kinetic parameters m and k*. The Ozawa exponent m provides qualitative information on the nature of the nucleation and growth process, whereas K* provides information related to the overall crystallisation rate and indicates how fast crystallisation occurs [107].

Liu and co-workers [111] further combined the Avrami and Ozawa equations for non-isothermal polymer crystallisation analysis given by the equation:

$$\ln \phi = \ln F(T) - b \ln t \qquad \text{Equation 3.7}$$

where, F (T) = $[K^*(T)/k]^{1/m}$, which defines the cooling rate required to reach a specific degree of crystallinity in a given crystallisation time and b is the ratio between Avrami and Ozawa exponents. A plot of ln ϕ vs. ln t at a specific degree of crystallinity gives a straight line, where the intercept and the slope give the values of F (T) and b.

Kissinger proposed activation energy considering the influence of various cooling rates under non-isothermal crystallisation process as follows [112]:

$$\frac{d[\ln\left(\frac{\phi}{Tc^2}\right)]}{d(\frac{1}{Tc})} = \frac{-\Delta E}{R}$$ Equation 3.8

where R is the universal gas constant and Tc is the peak crystallisation temperature. The plot of ln (ϕ/Tc^2) vs. 1/Tc gives the linear slope determining the ΔE.

3.4.4 Modulated Differential Scanning Calorimetry Analysis

Chapter 4, 6, 7 and 8 – Both in the case of Pebax and SEBS: All experiments were carried out with TA instrument 2000 MDSC. Approximately 10 mg of the sample were encapsulated and sealed in aluminium pans. The sample and reference pans were matched for accurate heat capacity measurements. The heat capacity was calibrated using sapphire, while temperature and baseline were calibrated using indium. An oscillation period of 60 sec and amplitude of ± 0.47 °C were used in modulated heating and cooling experiments. Pebax was subjected to 3 successive thermal regimes, a) Rapid cooling of Pebax to –80 °C followed by heating at 3 °C/min to 200 °C (250 °C in case of SEBS), b) Rapid cooling to -10 °C, and annealing for 0, 30, 120, 180, 240 minutes and, c) Rapid cooling to –80 °C and heating again to 200 °C. At the beginning and end of each heating and cooling cycle, Pebax was held isothermally for 3 min. TA software for MDSC was used for recording, analysis and deconvolution of the signals. The least square method was used to smooth all the curves for better analysis. The level of smoothing was selected within the range of 8-12 to give minimum distortion and no shift of peaks. In all MDSC figures, the exotherm points upwards. An average of three samples was reported (n=3).

3.4.5 Dynamic Mechanical Analysis for Pebax and SEBS

Tensile flat samples were prepared by cutting an extruded sheet along the axis of screw rotation obtained from co-rotating twin screw extrusion. Dynamic mechanical analysis (DMA) was carried out on a TA Instruments DMA 800 to evaluate the viscoelastic properties of Pebax elastomer. The experiment was carried out in a ramp temp/multi-frequency mode from 25 to 120 °C at a frequency of 1 Hz with a heating rate of 3 °C/min. DMA was used to measure transitions of mechanical failure of elastomer, maximum molecular chain movements of the same and glass transition of the samples using data obtained from storage modulus, loss modulus and tan delta, respectively, as the sample deforms at an amplitude of 16 µm under a sinusoidal deformation of 1 Hz. An average of three samples was reported (n=3).

3.4.6 Dynamic Mechanical Rheological Testing for Pebax

Rheological testing was carried out on a TA Instruments AR2000ex to evaluate the viscoelastic properties of Pebax. Frequency sweep test under oscillation procedure of Pebax melts at 172 °C was carried out using a parallel plate with 0.6 grams of the extruded polymer sample. The complex viscosity is the frequency-dependent viscosity function containing both the real and imaginary part, which is determined during the forced harmonic oscillation of shear stress.

3.4.7 Fourier Transform Infrared Spectroscopy for Pebax and SEBS

Infrared spectra were obtained with a Varian 600 spectrometer along with IR microscope of Varian 610 attenuated total reflectance-fourier transform infrared spectroscopy (ATR-FTIR). An ATR attachment was used on the Varian 610 to obtain IR spectra. FTIR spectroscopy was carried out at room temperature on clean solid extruded samples with a resolution of 4 cm^{-1}. All data were collected between 700 cm^{-1} and 4000 cm^{-1} with an average of 32 scans.

3.4.8 Mechanical Testing for Pebax and SEBS

Tensile testing of supercritical assisted extrusion of Pebax and SEBS was performed using Zwick/ Roell Z010 with 2.5 KN load cell with a crosshead speed of 500 mm/min and maximum extension of 500%. The extrudates were cut per ASTM Type I dumbbell shape specimen along the axis of twin screw rotation. An average of five extrudates was calculated and plotted for each type (n=5).

3.4.9 Electrical Conductivity of Pebax and SEBS

The impedance of flat samples of each composite of thickness values between 1-2 mm was carried out using a Solartron 1260 impedance analyser with a 1296 dielectric interface. Electrode setup consisted of two parallel electrodes, both of 40 mm diameter, between which the material was placed and a 3Vrms alternating voltage applied. Impedance was measured for frequencies ranging from 1 Hz to 1 M Hz. An average of 3 samples was taken and standard deviation remained within 5% (n=3).

3.4.10 X-Ray Diffraction for Pebax Composites

X-Ray diffraction (XRD) data were collected using a PANalytical X'Pert MPD PRO with an X'Celerator detector and Copper anode, at 40 kV, 40 mA and a fixed divergence slit of 0.25°. The step size was 0.0167°. A Bruker-AXS Phaser diffractometer equipped with a copper source

and a Lynx eye detector operated at 40 mA, 40 kV was also used on some samples. Similar results were obtained from both instruments. The instrument operated in a Bragg-Brentano (2θ) geometry which was fixed to the goniometer stage comprising 0.25° primary slits and the K-Alpha2/K-Alpha-1 ratio of 0.5. Origin software was used to correct the baseline and calculate the full-width half maximum (FWHM). The well-known Scherrer formula was used to find the crystallite size given by [113, 114]:

$$L = \frac{K\lambda}{\beta . cos\theta} \qquad \text{Equation 3.9}$$

where L is the average crystallite size in nanometre (nm), λ is the X-ray wavelength, β (2θ) is the peak width of the diffracted peak profile at half maximum height (also known as FWHM) in radians and K is a constant related to the crystallite shape normally taken as 0.9.

3.4.11 Polarised Optical Microscopy for Pebax and SEBS

Nikon ShuttlePix P-400Rv Digital microscope with 20x zoom capabilities, attached to a motorised focus stand was used to capture the surface profile of the polymer matrix. The samples were immersed in liquid nitrogen and were cryo-fractured to obtain the cross-sectional surface morphology.

3.4.12 Scanning Electron Microscopy for Pebax and SEBS

The samples were immersed in liquid nitrogen and were cryo-fractured to visualise the distribution of additives in the polymer matrix along the thickness (traverse cross-section area). Morphological studies were carried out in TESCAN scanning electron microscopy (SEM) at 20 kV. Different regions were selected and element mapping was performed to get the information about the filler distribution profile.

3.4.13 Transmission Electron Microscopy for Pebax and SEBS

Different composite samples were carefully sliced and transferred to copper grids of 400 mesh sizes. Then a 200 kV FEI-Tecnai G2 20 S-TWIN High-resolution Transmission Electron Microscope was used for the analysis of additive dispersion. Bright-field transmission electron microscopy (TEM) images of composites were obtained at different magnification from 1.7kx-19kx at 80 kV. ImageJ software was used for further analysis to enhance the desired region of the sample where required.

3.5 Evaluation of Bending Actuation

3.5.1 Sulfonation of SEBS Composites

The extruded membranes (0.5 to 0.6 mm thick) were grafted with sulfonic moieties to make the membrane ionic active using a solution of chlorosulfonic acid ($CISO_3H$) and 1,2-dichloroethane at room temperature. The chlorosulfonic acid concentration was maintained at 0.75M and the sulfonation time of 60 minutes was used for all the samples. After sulfonation, the membranes were neutralised and washed using methanol and distilled water until a pH of 6-7. The membranes were stored in distilled water for 24 hours for further analysis. The water uptake capacity (WUC) was calculated using the following equation:

$$WUC = \frac{W_{wet} - W_{dry}}{W_{dry}} X\ 100 \qquad \text{Equation 3.10}$$

where W_{wet} and W_{dry} are the weight of wetted and dried polymer membranes respectively.

3.5.2 Bending Actuation of SEBS Composites

The dried membranes were sputtered with 150-200nm platinum on both the sides to form electrodes. The samples were then cut into rectangular shapes with a length of 1-1.5 cm and width of 0.2-0.4 cm. The cut membranes were stored in distilled water for actuation. To evaluate the bending actuation ability, the wet membranes were held at one end using copper tape and connected to positive and ground leads of the power supply. The actuation capabilities were noted by varying the input voltage between 0-8 V and current of 40-60 mA.

4 Investigation of the Effect of Supercritical Carbon Dioxide Assisted Processing of Pebax and SEBS at Various Critical Pressures

4.1 Introduction

The supercritical carbon dioxide state comes into existence by means of a change in the physical properties, when carbon dioxide is raised beyond its critical temperature and critical pressure. Beyond such critical condition, carbon dioxide possesses solvating power like a liquid and diffusivity of a gas. Therefore, the supercritical fluid is considered as a good processing medium for a variety of chemicals and polymers. Specifically, supercritical assisted processing helps to obtain one-step foamed polymers with high throughput. Hence, it is important to understand the effects of various processing conditions on the thermal and mechanical properties of the manufactured polymer. This research chapter (Ch-4) focuses to understand effects of supercritical assisted processing at various critical pressures of selected polymers with respect to thermal, mechanical and rheological properties. This investigation will help to identify and choose specific processing conditions that are required for artificial muscle application. Pebax and SEBS were chosen based on the requirement of shape memory properties, thermal stability, polymer polarity and ease of manufacturing. This study investigates the effects of a supercritical assisted extrusion process at various critical pressures (800 psi, 1000 psi and 1200 psi) on the thermal and mechanical properties. This chapter forms the foundation to all the other chapters, where depending on the results obtained from the thermal and mechanical properties, specific processing conditions were selected and these processing parameters were employed for all the other chapters (Ch-5,6,7 and 8). Differential scanning calorimetry, thermal gravimetric analysis, dynamic thermal analysis and tensile testing are major characterisation techniques used to analyse the effects of various critical processing conditions on thermal and mechanical properties.

4.2 Section 1: Supercritical Fluid Assisted Processing of Pebax at Various Pressures

4.2.1 Thermal Gravimetric Analysis of Pebax at Various Critical Pressures

TGA measurements were made for samples that were extruded for virgin Pebax, Pebax at 800 psi, Pebax at 1000 psi and Pebax at 1200 psi. Figure 4.1 shows the weight percentage and derivative weight measurements of supercritical assisted extrusion of Pebax at various critical pressures. It is evident from the TGA measurements that the supercritical assisted extrusion has

not resulted in significant changes in thermal degradation. The maximum degradation temperature remains almost the same as to the virgin Pebax at around 440 °C.

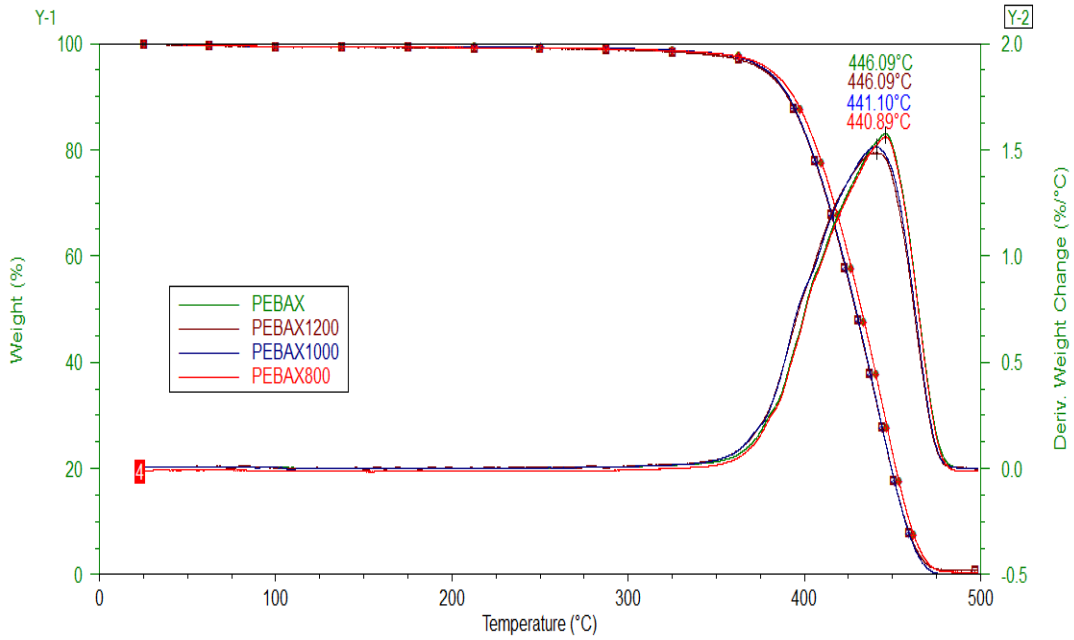

Figure 4.1 TGA measurements of Pebax at various critical pressures

4.2.2 Differential Scanning Calorimetry Analysis of Pebax at Various Critical Pressures

Figure 4.2 shows the DSC thermograms of all the extrudates with its first cycle and gives a very smooth curve and only one endothermic peak at 159 °C, which is associated with the melting temperature (Tm) of the polyamide-12 hard phase. An endotherm (depression) is evident at around 45 °C (Figure 4.2) in all the $scCO_2$ assisted extrudates, mainly due to the orientation of PTMO crystals resulting in a higher melting point (from unclear/hidden 15 °C to evident 45 °C). The melting point of soft PE block (PTMO) is around 15 °C; however, no such observation has been made due to the reason that PMTO composition in Pebax is much smaller when compared to Nylon-12 (crystalline PA-12).

In addition, this melting point lies within the reported equilibrium melting temperature range of 40-90 °C for low molecular weight homogenous PTMO, which can only be created due to the high orientation of the polymer chains [115-118]. The further justification that this evident endotherm at 45 °C is a result of PMTO linkage ordering/crystallisation originates from the second heating cycle, which shows similar behaviour to extruded Pebax with no melting endotherms at 45 °C/90 °C. This difference between the first and second cycle arises due to change in the crystal morphology that was created due to $scCO_2$ (first cycle) and consecutive heating to its melt decreases the PTMO crystallites (second cycle).

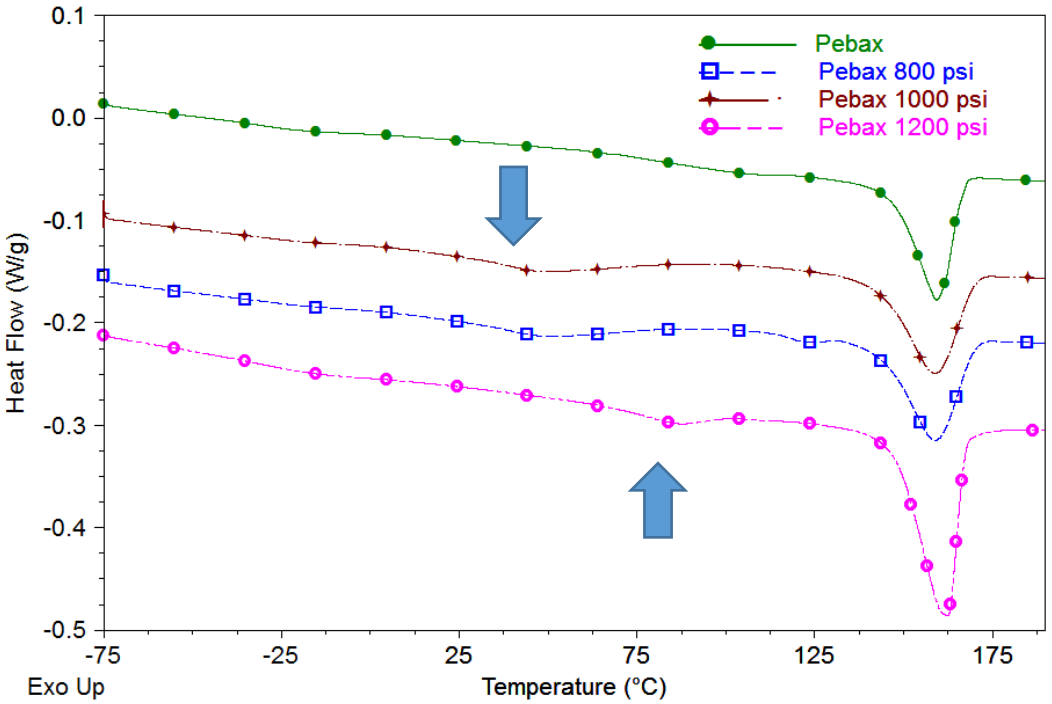

Figure 4.2 DSC thermogram of Pebax at various critical pressures

D.S Kaplan and D.J Hourston [119-121] have described that when the size of two intermixed domains exceeds 15-20 nm, then two peaks representing the phase transitions blend into one. Similarly, the clear and smooth effect on the thermogram may be due to the formation of an additional interphase layer with domain size smaller than 15-20 nm, thereby restricting the creation of additional endotherms/transitions for newly formed intermixed phases. This may also be the reason that no glass transition temperature is ascribed to polyamide block (PA-12 Tg around 50 °C) in block copolymers by many manufacturers and researchers. An ambiguity still remains as to why the depression at 90 °C appears, whether due to the PTMO or nylon (amorphous part of nylon) arrangement, therefore, this depression is ascribed to PTMO/nylon linkage. The degree of crystallinity (X_c) of polyamide 12 hard phase Pebax and $scCO_2$ assisted Pebax was calculated using Equation 4.1 [122] and is presented in Table 4.1.

$$X_c = (\Delta H_f / \Delta H_f^*) \times 100 \qquad \text{Equation 4.1}$$

Where, ΔH_f is the enthalpy of fusion determined from MDSC thermograms and ΔH_f^* is the enthalpy of fusion of perfect crystalline (polyamide-12); ΔH_f^* quoted for polyamide 12 in Pebax is 65 J/g [122, 123].

Table 4.1 suggests that the polyamide segments which participate in consecutive crystallisation cycles have lower molecular weight due to interaction induced by $scCO_2$; this is in agreement with observations made by Bonder et al [124]. An evident decrease in the consecutive cycle is

observed in the degree of crystallinity, especially when Pebax was extruded in the supercritical region (Pebax 1200 psi).

Table 4.1 Degree of crystallinity of PA-12 in Pebax at various heating cycles

Extrudates	**Cycle 1 X_c (%)**	**Cycle 2 X_c (%)**	**Cycle 3 X_c (%)**	**Cycle 4 X_c (%)**	**Cycle 5 X_c (%)**
Pebax	83.03	82.44	82.47	82.76	82.87
800 psi	85.92	83.92	82.16	81.69	81.00
1000 psi	83.33	75.61	76.70	76.41	77.10
1200 psi	65.20	56.24	54.20	54.92	54.21

Another reason for increased (800 psi) crystallinity can be attributed to foaming processes with $scCO_2$, similar to the investigation carried out by Wentao Zhai and his co-workers [125]. He reported that uniaxial or biaxial stretching may have resulted in the development of a crystalline structure in case of amorphous PLA. Similar propositions can be considered, such as exposure to CO_2 induces cell nucleation, resulting in gas supersaturation, followed by cell growth due to a sudden pressure drop.

Pebax, being a semi-crystalline polymer; a crystallisation peak is seen in the cooling cycle of the DSC cooling thermogram (Figure 4.3). It is evident that the crystallisation peak gradually shifts towards lower temperatures for Pebax treated with $scCO_2$. Usually, the process of crystallisation takes place in two steps: a. nucleation and b. crystal growth. The nucleation step is defined as the step of initiation of new crystals or the onset of the formation of a new thermodynamic phase. Usually, nucleation processes are classified as heterogeneous nucleation, when the impurities act as a central nucleus initiator surrounding which atoms become oriented leading to crystal growth; and homogeneous, where a certain degree of supersaturation or supercooling of particles causes the particles to self-assemble to induce nucleation followed by growth. Heterogeneous nucleation occurs on the surface and is typically much faster than the homogeneous nucleation using classical nucleation theory. This demonstrated that supercritical fluid processing (specifically by just increasing the pressure from the sub, near and beyond critical points) makes Pebax a more homogenous material.

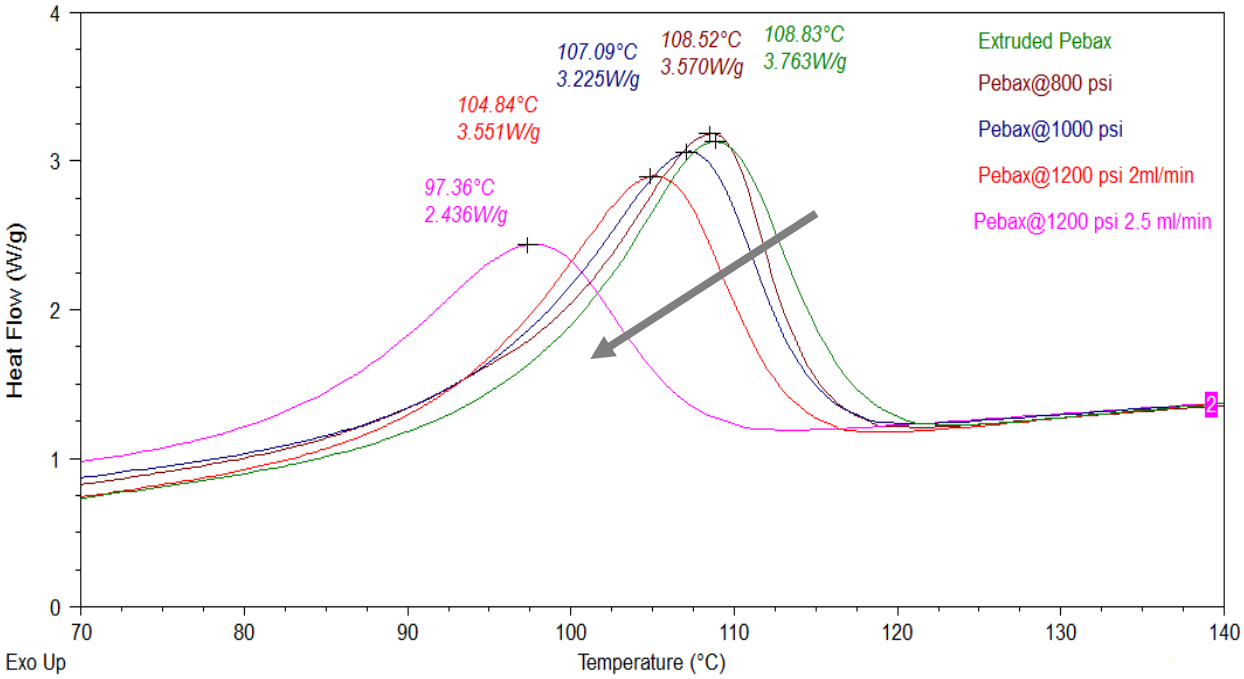

Figure 4.3 Crystallisation peaks for Pebax extruded at various pressures (cooling cycle)

As the flow rate of $scCO_2$ was increased from 2 ml/min to 2.5 ml/min, the onset of crystallisation temperature displaced further towards lower temperatures, only to show that the $scCO_2$ treated samples take more time to initiate density fluctuation and onset of nucleation making the material more homogenous. In addition, the crystallisation peaks continuously broaden, depending on the increase in the $scCO_2$ indicating crystal distortion due to foaming (from the use of $scCO_2$) compared to virgin Pebax. This reveals that $scCO_2$ has induced formation and growth of crystals over a wide range of crystal size (small to big, uneven crystallite size).

This homogenisation process of a copolymer such as Pebax will further diminish the thermodynamic incompatibility between the hard and the soft blocks through the formation of multiple phases (crystallites) with smaller domain size. Such a process is further suggested to enhance the mechanical compliance between the hard blocks and soft blocks, thereby enhancing the ability of Pebax to possess the properties of being a mechanically strong yet flexible material.

4.2.3 Dynamic Mechanical Analysis (DMA) of Pebax at Various Critical Pressures

DMA results for supercritical fluid assisted Pebax are shown in Table 4.2 (storage modulus). Increasing the storage modulus is observed for $scCO_2$ treated Pebax at 800 psi and 1000 psi, however, the storage modulus of Pebax treated at 1200 psi decreases. The broad transition observed at around 62 °C in tan delta curves is the result of viscoelasticity representing the glass transition temperature of the hard PA-12 block. From Figure 4.4 and Table 4.2, the increasing

storage moduli observed for 800 psi and 1000 psi can be attributed to an increased formation of crystallites and alignment of polymer chains due to uniaxial or biaxial stretching; this was also supported by the DSC results. However, the storage modulus of Pebax treated at 1200 psi decreases mainly due to increased nucleation and further cell growth due to a sudden drop in pressure at the die, thereby making Pebax less stiff (SEM results included). The increase in the pore size is associated with the higher probability of cell coalescence because of the rupture of the cell walls upon the quick release of relatively high pressures.

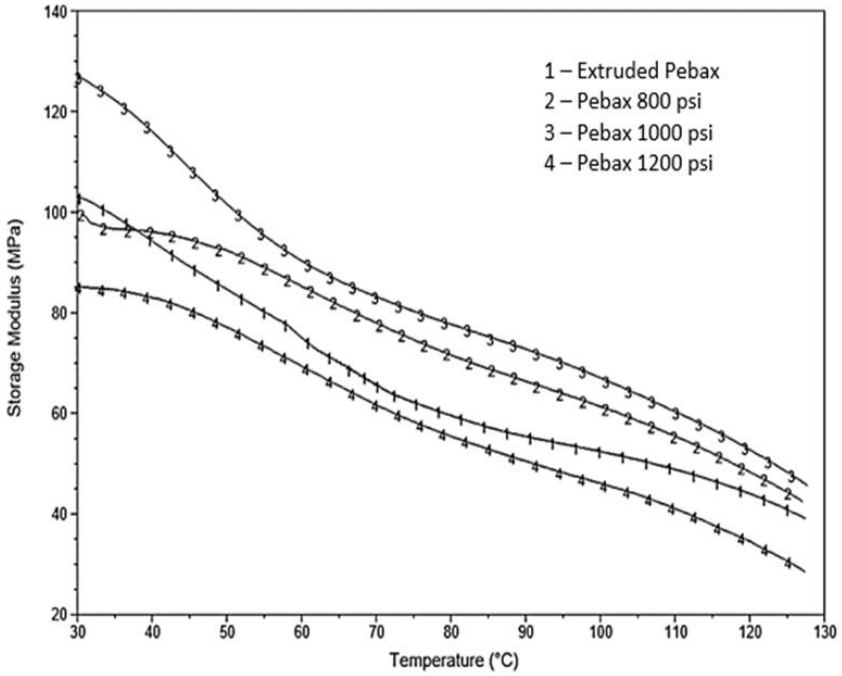

Figure 4.4 Storage modulus of Pebax extruded at sub (800psi), near (1000 psi) and beyond supercritical region (1200 psi)

Tan delta is the ratio of viscous to elastic response of the polymer, representing both elasticity and viscosity (loss factor). Tan delta is considered a good measure of the midpoint between the glass and rubbery state representing the Tg point or the measure of friction at the hard-soft block interface of the polymer. From Figure 4.5, the broad peak observed around 62 °C in tan delta curves is due to the result of viscoelasticity, representing the glass transition temperature of the hard PA-12 block. Reduction in the tan delta for Pebax 1200 psi shows that $scCO_2$ processing has reduced the interfacial friction between the hard and the soft interface.

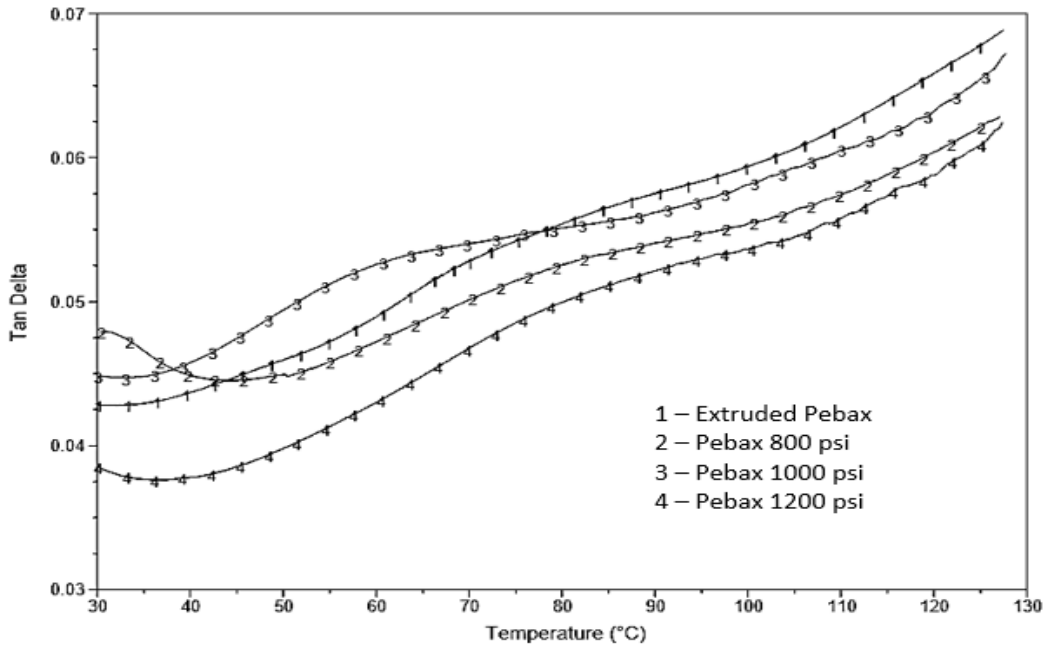

Figure 4.5 Tan Delta of Pebax extruded at the sub, near and beyond the supercritical region

At room temperature (25 °C), the soft block is above its Tg (near to melting) while the hard PA block is in the crystalline phase. This instability between the large sized hard and the soft block provides friction at the interface, therefore virgin Pebax has higher loss factor (tan delta). However, when Pebax is treated with $scCO_2$, the larger domains of the hard block and soft block become smaller (many crystallites–smaller domains as seen on DSC crystallisation peaks), making the material more homogenous thereby reducing the friction at the interface and the loss factor.

Table 4.2 Storage modulus of Pebax extruded at the sub, near and beyond the supercritical region

Samples	Storage modulus measured at 30 °C (MPa)
Extruded Pebax	100.97
Pebax 800 psi	96.88
Pebax 1000 psi	130.33
Pebax 1200 psi	83.98

4.2.4 Tensile Testing of Pebax at Various Critical Pressures

This ability of the material to store energy up to the yield point is termed the modulus of resilience and the total area under the curve up to elongation at break is termed the modulus of toughness. Figure 4.6 and Table 4.3 illustrate the stress versus strain responses exhibited by virgin Pebax, Pebax at extruded 800 psi, Pebax at extruded 1000psi and Pebax at extruded 1200 psi. A sharp yield point and lower elongation at break (less than 500%) are observed for pure

Pebax extrudates, which is mainly due to the higher content of hard PA segment. Here, a clear increase in resilience is observed with Pebax 1000 psi extrudates and slight decrease with Pebax 800 psi when compared to unassisted Pebax extrudates. This increase in the yield strength can be attributed to an increase in the crystallinity/alignment of polymer chains into a more kinetically favourable condition when treated with sub and near $scCO_2$. However, the extrudates at 1200 psi have decreased resilience due to the foaming effect induced by $scCO_2$. In addition, this increase in Young's modulus at 800 and 1000 psi can also be attributed to the alignment of the polymer chains with respect to the cell formation (DMA storage modulus enhancement due to the arrangement of the polymer chains with biaxial and uniaxial stretching of the cell walls). A depression in resilience can also be observed with Pebax 1200 psi extrudates when compared to unassisted Pebax extrudates. A similar pattern was observed in the storage modulus of the DMA results obtained here (Pebax 1000 psi), which means that the ability of a material to absorb energy is increased with higher stress, without suffering damage, thereby increasing materials stiffness, with near supercritical condition under elastic deformation.

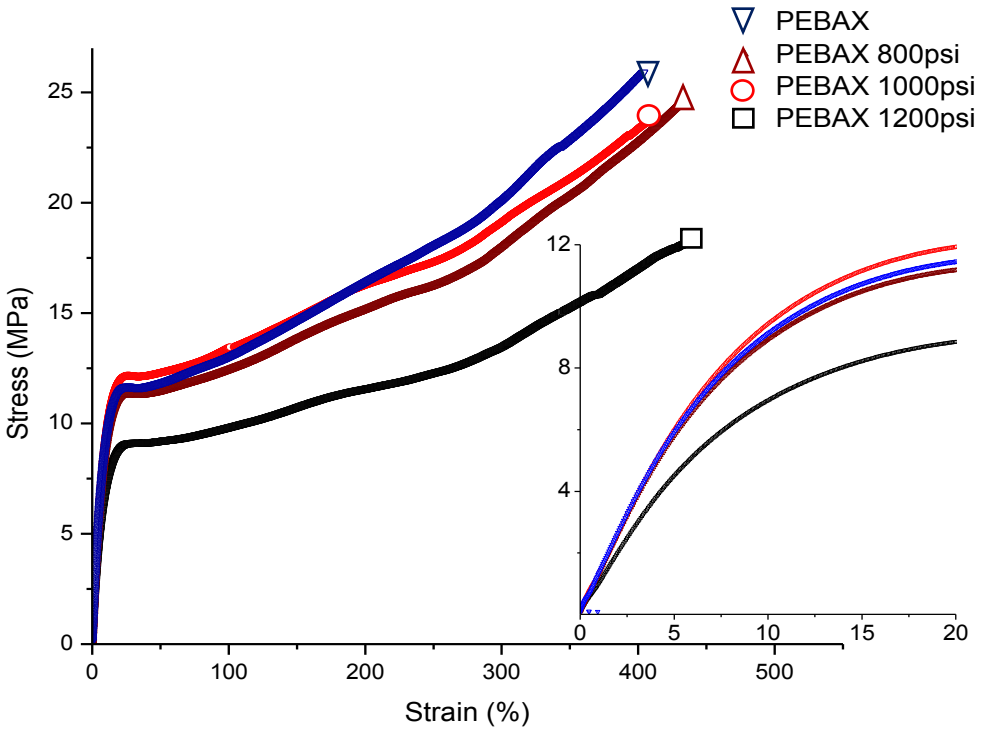

Figure 4.6 Stress-strain response exhibited by pure extruded Pebax, extruded Pebax at 800 psi, extruded Pebax at 1000psi and extruded Pebax at 1200 psi

During the drawing process, the transformation of the material microstructure from spherulitic (containing a lamellar crystalline structure) to lamellar fragments, known as fibrillar microstructure takes place. This is usually followed by a rearrangement of structures to the new equilibrium position. It is clear from the stress-strain graph (both Pebax and Pebax 1000 psi extrudates) that an increase in stress beyond the yield point further promotes the flow of rearranged polymer chains or multiple microstructures slides across each other (dislocation of the polymer chain) due to strain hardening. However, after an elongation of 300%, Pebax 1200 psi extrudates require lower induced stain to undergo the microstructural transformation, thereby reducing the toughness of the material making it almost equivalent to Pebax 800 psi extrudates.

Table 4.3 Average Young's modulus of Pebax extruded at various pressures

Samples	Young Modulus (MPa)
Extruded Pebax	142.56±5.72
Pebax 800 psi	154.65±3.93
Pebax 1000 psi	161.98±4.55
Pebax 1200 psi	101.52±6.96

4.2.5 Fourier Transform Infrared Spectroscopy (FTIR) of Pebax at Various Critical Pressures

The ATR-FTIR spectra (transmittance and absorbance) of Pebax with and without assisted supercritical carbon dioxide recorded at room temperature are given in Figure 4.7 and Figure 4.8. It is clear from the transmittance and absorbance spectra that when Pebax is treated with $scCO_2$, the major characteristic peaks at 1638 cm^{-1} (representing polyamide-12 block) and 1100 cm^{-1} (representing polyether PTMO block) increase peak intensity (area and height). The peaks at 1465 cm^{-1} and 1365 cm^{-1} representing CH_2 vibration and C-N stretching of the amide group, respectively, reduce in absorbance intensity (Figure 4.8). The stretching and bending of the CNH bond present at 1555 cm^{-1} show a reduction in absorbance intensity. From Figure 4.8, the characteristic peaks at 1735 cm^{-1} and 1638 cm^{-1} represent the presence of O-C=O stretching of the carbonyl group of ester linkage and the N-C=O carbonyl vibration of the PA-12 group [126, 127]. The amide carbonyl band at 1638 cm^{-1} is sensitive to hydrogen-bonding distance between the segments [128]. The amorphous amide is usually broader, while the crystalline state has a sharper peak. The peak at 1555 cm^{-1} is ascribed to CNH vibration with NH bending and CN stretching. The peaks at 1465 cm^{-1} and 1365 cm^{-1} represent the CH_2 vibration and C-N stretching of the amide group. The soft PTMO blocks exhibit a stretching vibration of the C-O ether peak at 1100 cm^{-1}. It was clear from the transmittance and absorbance spectra (Figure 4.7 and Figure

4.8) that when Pebax was treated with $scCO_2$, the major characteristic peaks at 1638 cm^{-1} and 1100 cm^{-1} increase in intensity (area and height).

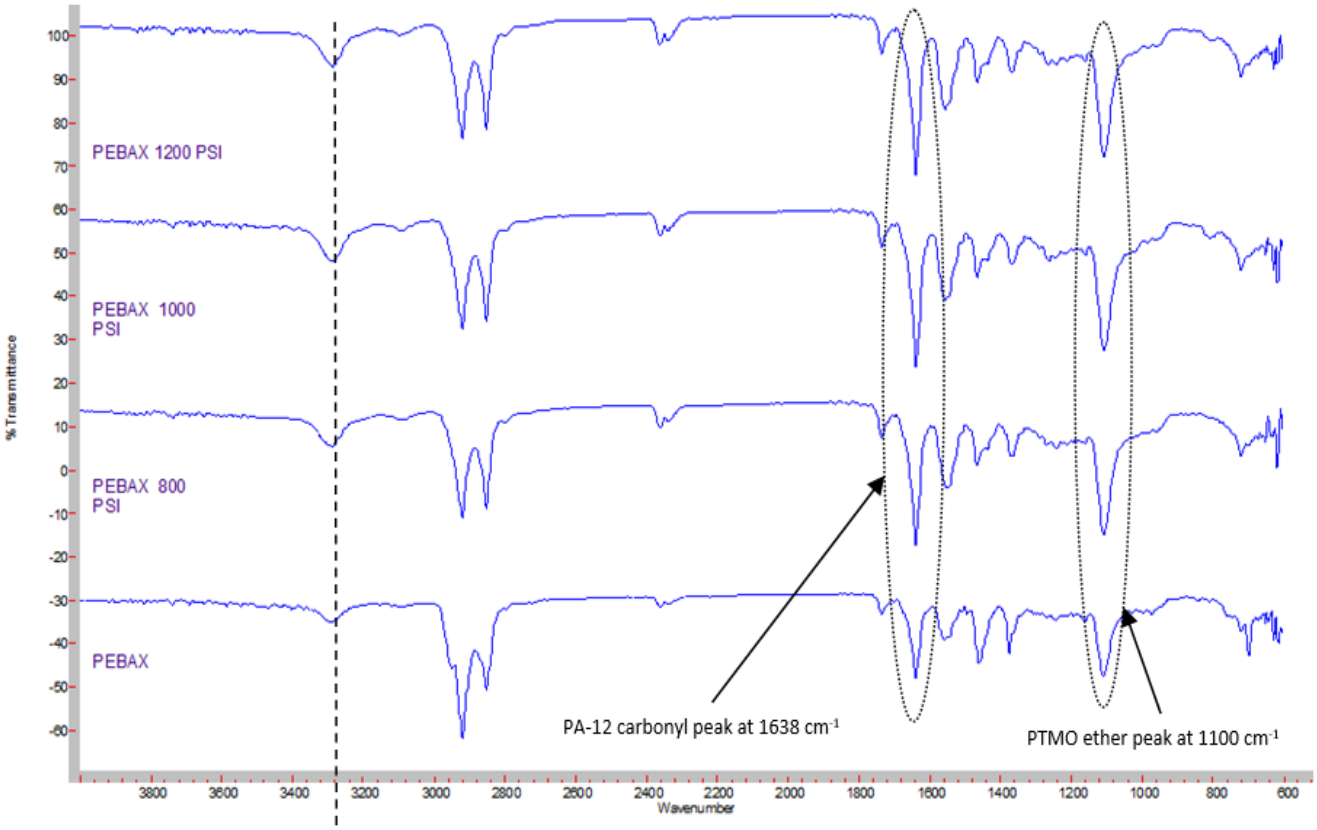

Figure 4.7 FTIR spectra of Pebax extruded at various critical pressures

A carbonyl absorbance peak height at 1638 cm^{-1} is very sensitive to the hydrogen bonding segments within the amide block; this increase in peak height suggests that $scCO_2$ assisted Pebax has reduced/ the hydrogen bonding distance/intensity between the carbonyl segments which in turn may have resulted in the formation of perfect crystallites. Similar intensification of hydrogen bonding between the NH and O=C group has been reported by Hongwei Cao et al [129, 130]. The authors reported that an increase in the area of peaks corresponding to NH and O=C interactions can be ascribed to improved hydrogen bonding within the hard segments of polyurethane. In addition, on hydrogen bonding, the original NH and CN (1555 cm^{-1}) stretching is affected.

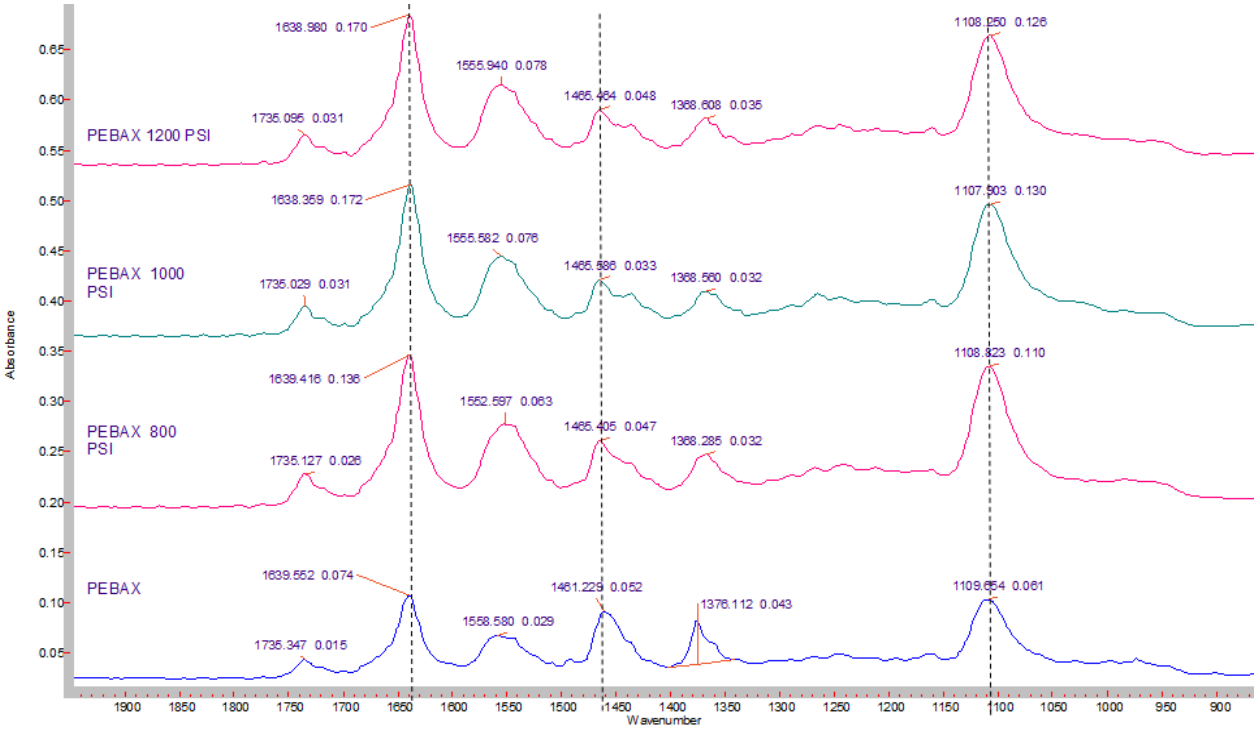

Figure 4.8 Absorbance spectra of Pebax extruded at various supercritical pressures

Specifically, CN stretching is lengthened due to electrostatic attractions between the hydrogen atoms of one molecule and oxygen atom of the other, therefore, the force constant of CN bond is reduced resulting in a decrease in the stretching frequency (1461 cm^{-1} to 1455 cm^{-1}). Usually, the increase in peak intensity is also ascribed to orientation effects; however, the absorption peak in this study also shows the shift in the peak to lower wavenumbers which occurs due to the suggested change in hydrogen bonding length. Table 4.4 shows the values of the area under the characteristic peaks and %PA-12 and %PTMO calculation using the Equation 4.2.

$$\%PA-12 = \frac{h_{1638}}{(h_{1638}+h_{1108})} * 100 \qquad \text{Equation 4.2}$$

Table 4.4 Tabulated area and height for percentage PA-12 calculation of Pebax

Sample Name	1638 cm^{-1} PA-12 Peak Area	1108 cm^{-1} PTMO Peak Area	1638 cm^{-1} PA-12 Peak Height	1108 cm^{-1} PTMO Peak Height	% PA-12	% PTMO
Pebax	1.93	2.14	0.074	0.061	54.81	45.18
Pebax 800	3.62	4.27	0.136	0.110	55.28	44.71
Pebax 1000	4.43	5.28	0.172	0.130	56.96	43.04
Pebax 1200	4.30	4.99	0.170	0.126	57.43	42.56

The gradual increase in calculated PA-12% validates the rearrangement of crystallites into the more favourable manner, where the $scCO_2$ treatment alters/tightens the hydrogen bond thereby pulling the amorphous PTMO block closer into the crystallite.

4.2.6 Rheological Analysis of Pebax at Various Critical Pressures

The complex viscosity is the frequency-dependent viscosity function containing both the real and imaginary parts, which is determined during the forced harmonic oscillation of shear stress. Figure 4.9 represents the complex viscosity vs. angular frequency for Pebax that was extruded at various critical pressures. It can be observed that the complex viscosity, which is the magnitude of the elastic storage modulus and the viscous loss modulus, reduces appropriately as the critical pressure is increased from 800 psi to 1200 psi.

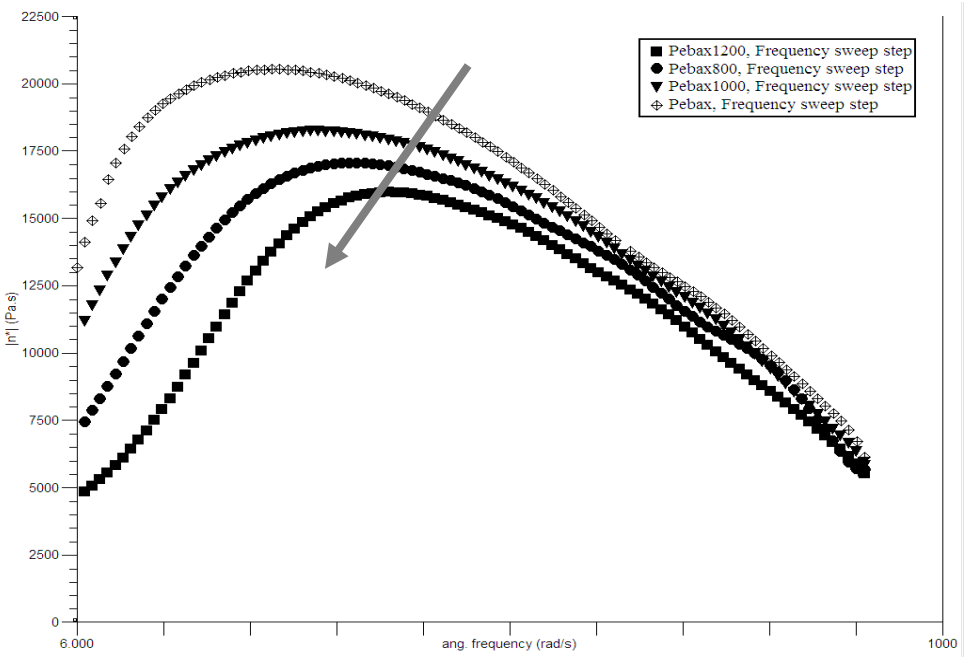

Figure 4.9 Complex viscosity vs. angular frequency for Pebax extruded at various critical pressures

Cogswell and other researchers [131-134] reported that the viscosity of narrow molecular weight distributions of polymers tends to increase when compared to the reduced viscous broad molecular weight distribution (can be observed on the viscosity Vs. angular frequency plot). Therefore, decreasing complex viscosity shows that the molecular weight distribution is broadened when treated with a supercritical fluid. This reduction in the complex viscosity can be attributed to reduced crystallite size as seen on the broadening crystallinity peak from DSC

(Section 4.2.2). This broadening of the peak from DSC has also resulted in a decrease in the mechanical properties of Pebax.

4.2.7 Morphology using Scanning Electron Microscopy of Pebax at Various Critical Pressures

Figure 4.10 presents images obtained from scanning electron microscopy representing the effect of $scCO_2$ processing on Pebax under different pressure conditions. It is clearly evident that the porous nature increases as the critical pressure are increased from 800 psi (Image B) to 1200 psi (Image D). The formation of pores seems to have longitudinal effects which can be attributed to the haul-off system at the output of the extruder. It is suggested that such formation of porous structures may be the reason for the decrease in storage modulus and Young's modulus as discussed in the above sections (4.2.3 and 4.2.4).

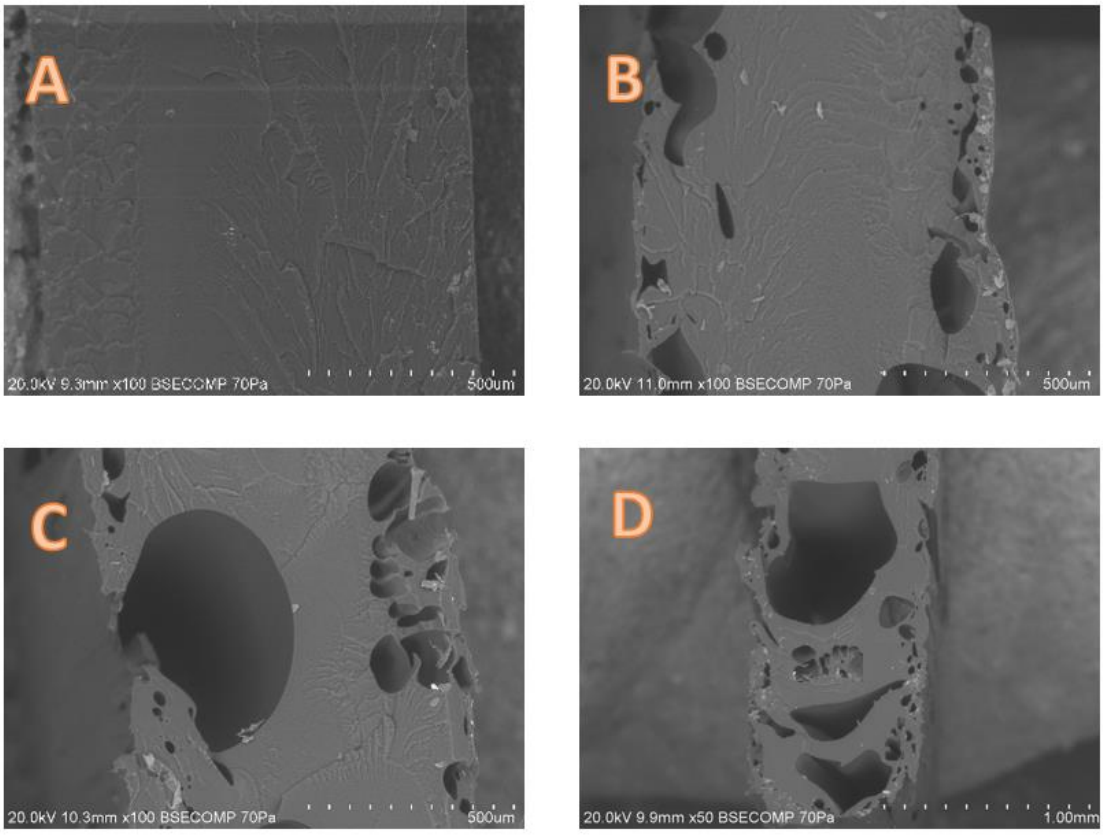

Figure 4.10 Morphology for Pebax extruded at various critical pressures: A - Pebax; B - Pebax @ 800 psi, C - Pebax @ 1000 psi, D - Pebax @ 1200 psi

4.3 Key Points for Pebax Processed at Different Critical Pressures

Thermal and mechanical properties of Pebax with assisted $scCO_2$ extruded at the sub, near and beyond supercritical region were investigated in this study. The following are the key observations:

- Thermal stability and thermal degradation of Pebax remained unchanged throughout the pressure variation from 800 psi to 1200 psi showing no significant difference from the TGA thermograms.
- Homogenisation through break down of larger crystals into smaller crystals between the hard and soft blocks of Pebax is evident from the DSC thermograms as crystallisation peak shifts and broaden to lower temperatures. In addition, the endotherm at 45-90 °C is a result of PMTO-Nylon 12 (PA-12) linkage ordering.
- Increasing storage moduli were observed for $scCO_2$ treated Pebax at 800 psi and 1000 psi, however, the storage modulus of Pebax treated at 1200 psi decreases mainly due to suggested increased nucleation rate and further cell growth due to a sudden drop in pressure. The broad transition observed at around 62 °C in tan delta curves is the result of viscoelasticity representing the glass transition temperature of the hard PA-12 block.
- A similar increase in the yield strength was observed from the tensile test results due to a systematic increase in the crystallinity or rearrangement of molecules into a more kinetically favourable condition, when treated with sub and near $scCO_2$, however, the extrudates at 1200 psi have decreased resilience due to foaming effects induced by $scCO_2$.
- This increase in Young's modulus at 800 and 1000 psi can also be attributed to the alignment of the polymer chains with respect to the cell formation (DMA storage modulus enhancement due to the arrangement of the polymer chain with biaxial and uniaxial stretching of the cell walls).
- The IR bands at 1638 cm^{-1} and 1100 $cm^{-1}$of Pebax when treated with $scCO_2$, increase in intensity (area and height). The carbonyl absorbance peaks height at 1638 cm^{-1} are very sensitive to the hydrogen bonding segments between the amide chains, this increase in peak height suggests that $scCO_2$ assisted Pebax reduced the hydrogen bonding distance between the carbonyl segments which in turn may have resulted in the formation of perfect crystallites.
- The decreasing complex viscosity shows that the molecular weight distribution is broadened when treated with a supercritical fluid. This reduction in the complex viscosity

can be attributed to reduced crystallite size as seen on the broadening crystallinity peak from DSC.

- SEM morphology demonstrates evidence that the porous nature increases as the critical pressure are increased from 800 psi to 1200 psi which is indicative of the foaming effect as pressure is increased.

4.4 Section 2: Supercritical Fluid Assisted Processing of SEBS

4.4.1 Thermal Gravimetric Analysis of SEBS at Various Critical Pressures

The thermal degradation profile of SEBS extruded at different pressures of $scCO_2$ is shown in Figure 4.11. The degradation of SEBS starts at around 350 °C, whereas, the degradation starting temperature shifts to around 445 °C when processed with $scCO_2$. The overall maximum degradation temperature of SEBS has increased from 405.08 °C to 468 °C when treated with $scCO_2$, which are presented in Table 4.5

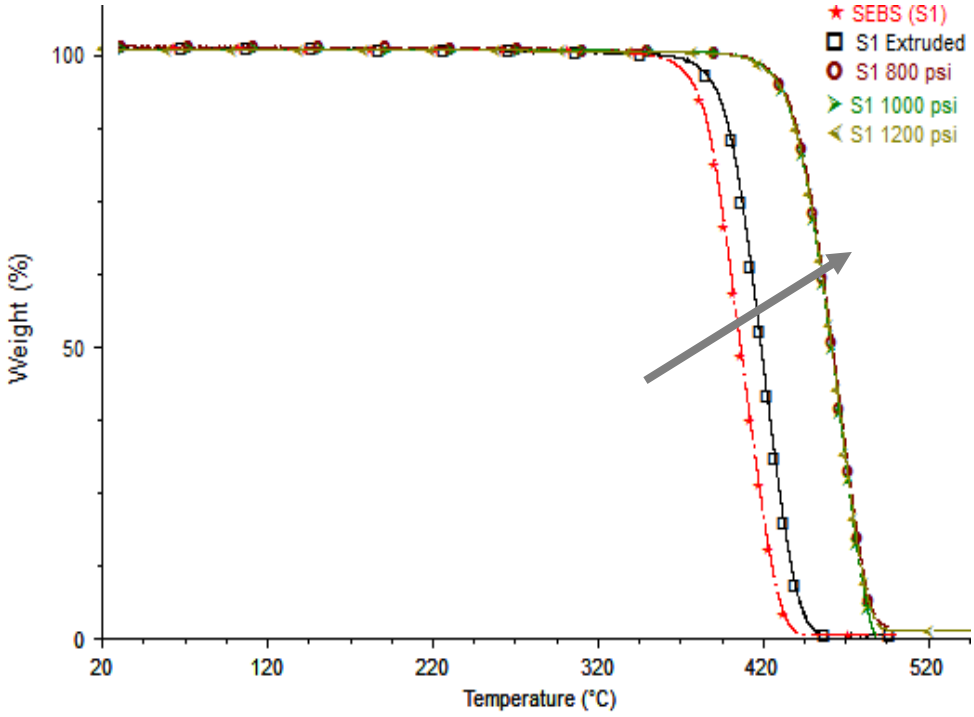

Figure 4.11 Degradation temperature of SEBS extruded under different critical pressure conditions

The shift in degradation temperature was observed due to the fact that extruded samples are thermally more stable than unprocessed materials [135]. Moreover, thermal degradation of a polymer is a complex phenomenon and is dependent on time, temperature, concentration and migration of molecules within a sample. Small changes in these various factors cause changes in the degradation of a polymer [136]. The increase in the degradation profile of thermoplastic elastomers can be suggested to be due to high microdomain formation when extruded at different CO_2 critical pressure. This, in turn, leads to the different structure of SEBS and hence different degradation profiles for the thermoplastic elastomers.

Table 4.5 Degradation temperature of SEBS processed under different critical pressure conditions

Materials	Degradation Temperature (°C)
SEBS	405.08
SEBS extruded	419.81
SEBS 800 psi	467.47
SEBS 1000 psi	467.07
SEBS 1200 psi	468.07

Such structural changes caused due by thermal energy during extrusion leads the material to be more thermally stable than thermally untreated material. Similarly, the onset degradation temperature of SEBS was found highly enhanced by ca. 50 °C when extruded with assisted $scCO_2$.

4.4.2 Modulated Differential Scanning Calorimetry of SEBS at Various Critical Pressures

The Modulated Differential Scanning Calorimetry (MDSC) technique was used to analyse all the complex microscopic transitions of SEBS due to its sensitivity towards thermal transitions. The glass transition of the ethylene-butylene (Tg^{EB}) block can be observed at around -55 °C as heat flows into the sample because of the endothermic process (Figure 4.12).

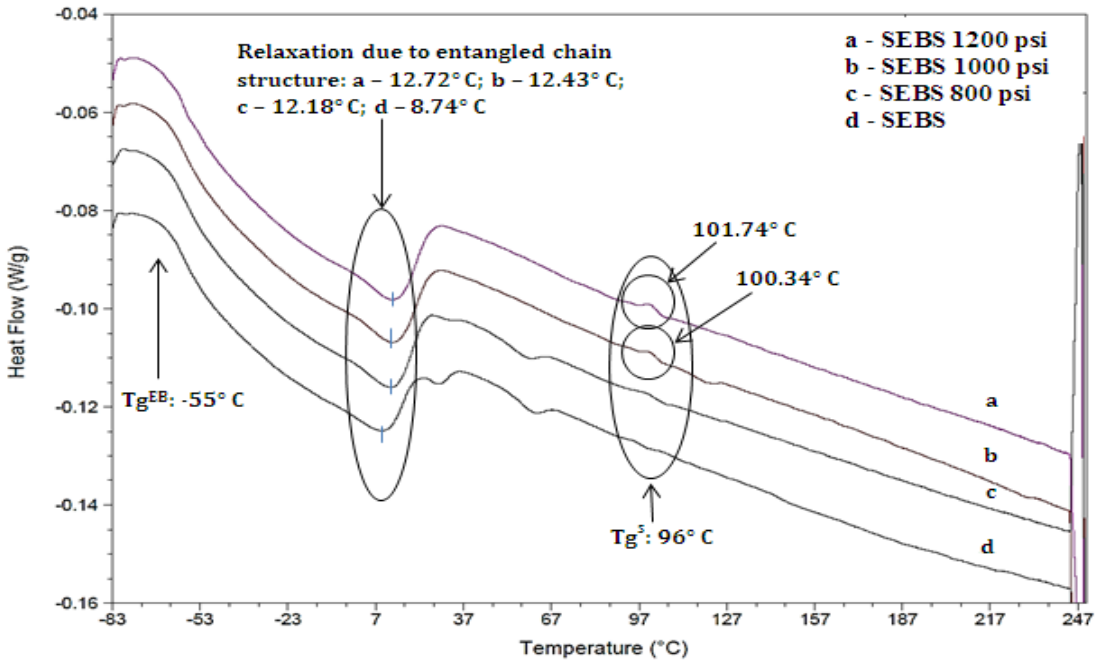

Figure 4.12 Heat flow thermogram of $scCO_2$ assisted extrudates of SEBS for its first cycle

The relaxation due to entanglements can be observed in the heat flow thermogram at 8.74 °C for untreated SEBS and 12.72 °C for SEBS extruded at 1200 psi (shifts to higher temperatures). The Tg of pure styrene (S) rich phase (Tg^S) around 96 °C is not clearly visible in any of the thermograms, however, small exothermic peaks are evident at 101.74 °C and 100.34 °C for extrudates at 1000 psi and 1200 psi showing the formation of microstructures or rearrangement process of pure S phase. A clear and single peak can be observed from Figure 4.13 at around -55 °C, attributed to the Tg of the EB block for untreated, 800 psi, 1000 psi SEBS extrudates, however, divided peaks can be observed at -58.68 °C and -52.59 °C for SEBS extruded at 1200 psi, indicating phase segregation in the EB block. The Tg of the S-rich microphase has a slight shift from 97 °C for untreated SEBS to 102 °C for $scCO_2$ treated SEBS.

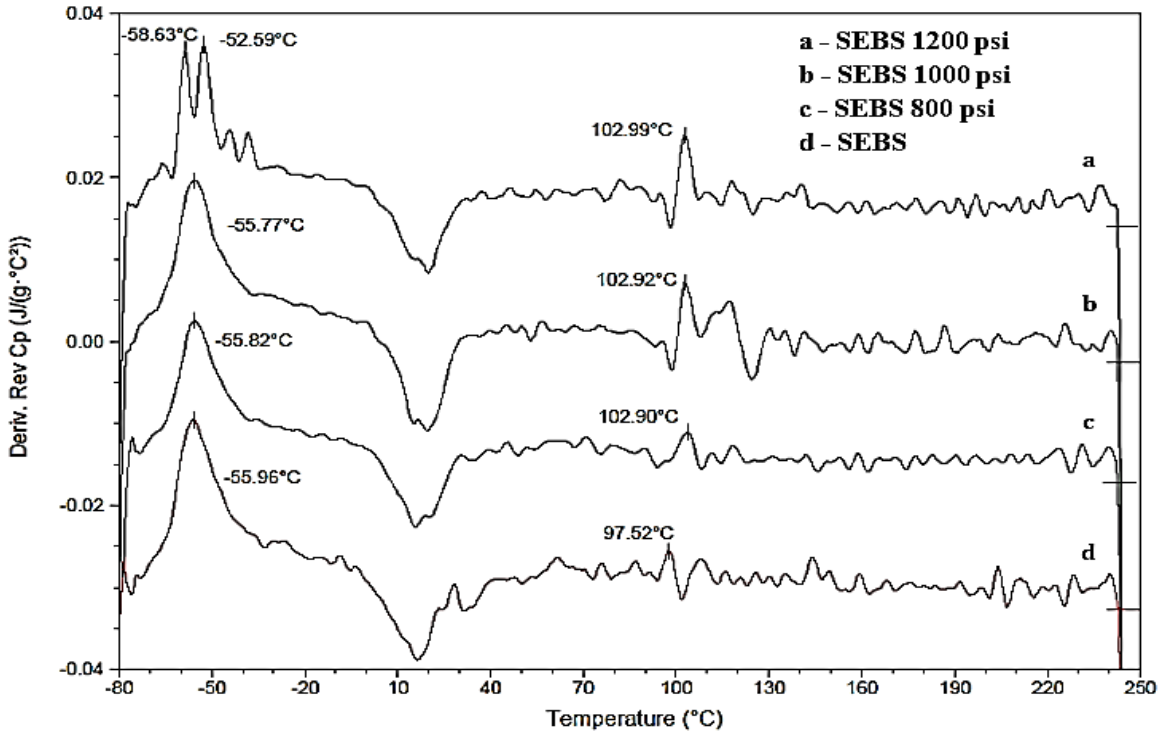

Figure 4.13 Derivative of reversing heat capacity thermogram of $scCO_2$ assisted of SEBS

R.M. Overney et al identified that a non-crystalline polymer behaves in a rubbery fashion just above Tg temperatures consisting of entangled or relatively free to move chain structures, providing partial segmental motion [137]. At higher temperatures (beyond Tg), the entanglements are resolved and most of the chain structures take part in thermal motion via break down of the physical cross-links and rearrangement of the backbone. This relaxation due to entanglements can be observed in the heat flow thermogram at 8.74 °C for untreated SEBS and 12.72 °C for SEBS extruded at 1200 psi. This increasing relaxation, when assisted with $scCO_2$, can be likely attributed to higher temperature requirements to completely resolve the

entanglements/break down of crosslinks and rearrangement of polymer microstructures to behave like a viscous fluid. The Tg of the styrene-rich phase (Tg^S) at around 96 °C is not clearly visible in the thermograms, however, small exothermic peaks are evident at 101.74 °C for extrudate curve at 1000 psi and 100.34 °C for extrudate curve at 1200 psi. Such additional peaks when processed at 1000 and 1200 psi is indicative of the formation of microstructures or rearrangement process of the pure S phase.

A very clear and single peak can be observed from Figure 4.13 (derivative thermogram) at around -55 °C, attributed to the Tg of the ethylene-butylene (EB) block for untreated, 800 psi, 1000 psi SEBS extrudates. In addition, divided peaks can be observed at -58.68 °C and -52.59 °C for SEBS extruded at 1200 psi. Such division of peaks can be likely attributed to the formation of new microstructure and or increase in the microphase separation within the ethylene-butylene (EB) rich phase [138, 139]. Also, the division of the Tg^{EB} suggests that the $scCO_2$ treatment might have resulted in the separation of ethylene and butylene blocks. However, such separation of ethylene and butylene needs additional verification by further processing the SEBS at higher supercritical pressures. The continuous curvature throughout the cycle represents the formation of phase separation/disordered phases of interfacial domains with its own glass transition temperature (Tg). The Tg of styrene (S) rich microphase has a slight shift from 97 °C for untreated SEBS to 102 °C for $scCO_2$ treated SEBS. This also suggests that processing at higher critical pressures will result in altering the microphases of the SEBS structure.

4.4.3 Dynamic Mechanical Analysis of SEBS at Various Critical Pressures

The influence of $scCO_2$ on SEBS under different pressure conditions over temperature on storage modulus, loss modulus and tan delta is presented in Figure 4.15 and Figure 4.15. The influence of $scCO_2$ on loss and storage modulus SEBS was found to be proportional to the pressure of $scCO_2$. Upon reaching the pressure of 1200 psi, the storage modulus reduces to half that of the virgin SEBS due to supersaturation and foaming action.

From Figure 4.14, the introduction of $scCO_2$ during extrusion leads to a decrease in stiffness (represented by storage modulus) as well as the molecular movements between hard and soft block segments (represented by loss modulus) of the elastomers. This decrease in storage modulus suggests that the $scCO_2$ treatment has initiated the rearrangement of structure and breaking up of the large domains into smaller domains. The influence of $scCO_2$ on loss and storage modulus SEBS was found to be proportional to the pressure of $scCO_2$.

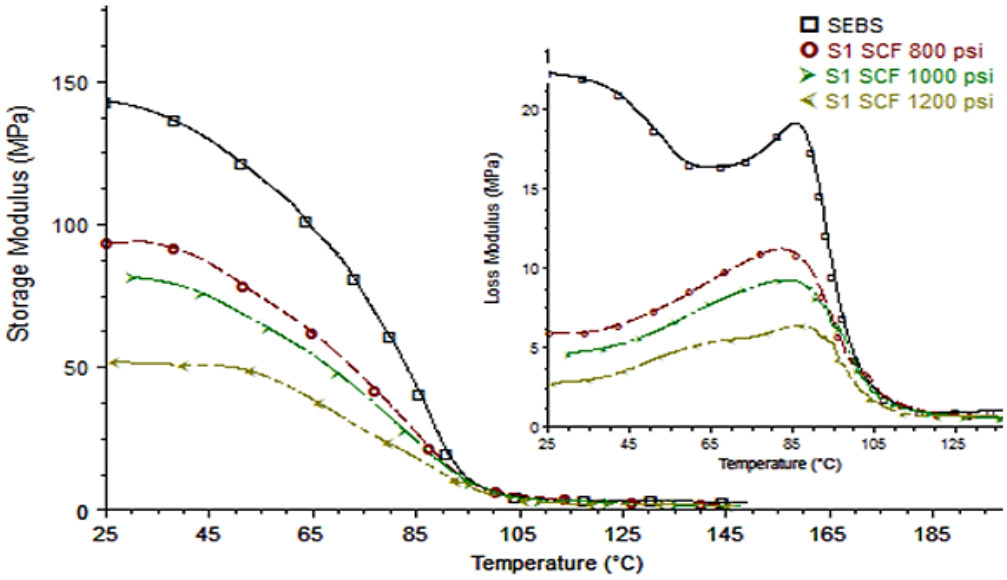

Figure 4.14 Storage and loss moduli of SEBS extruded at various critical pressures

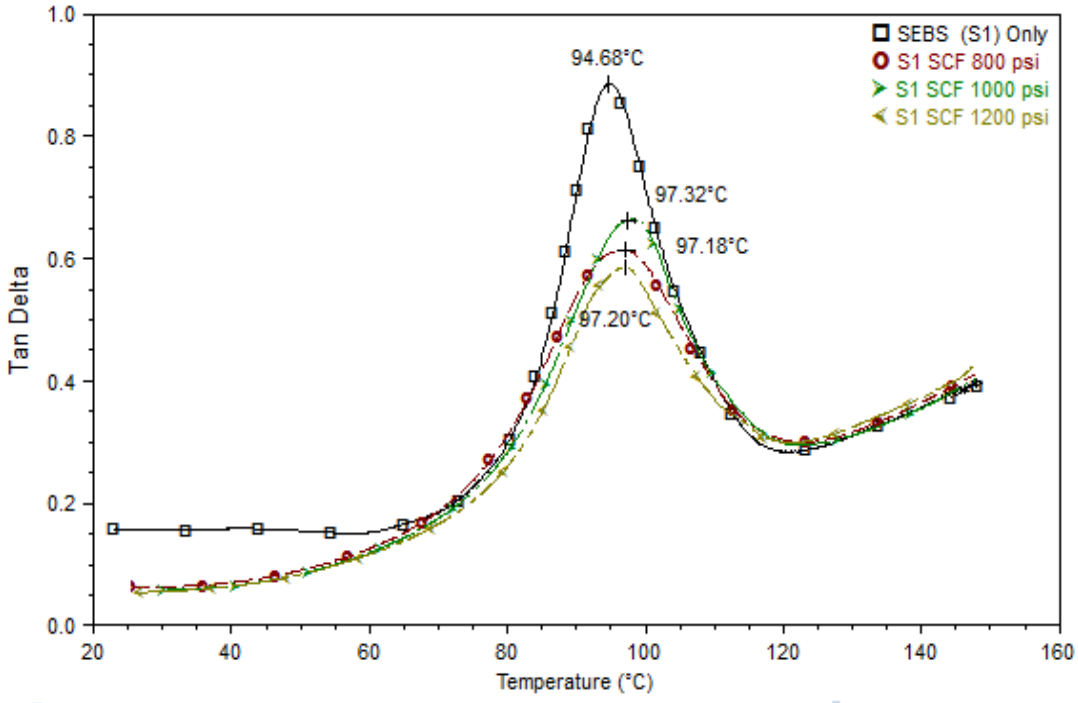

Figure 4.15 Tan Delta of SEBS extruded at the sub, near and beyond the supercritical region

This reduced restriction on the movement of molecules due to the smaller domain size of both hard and the soft phase results in lowering the viscosity of the polymer thereby the loss modulus. The change in relaxation temperature of hard block noted using tan delta (Figure 4.15) was found to be 94.68 °C, whereas, a shift in the tan delta was found to be 97.18 °C, 97.32 °C, and 97.20 °C when extrusion of SEBS was carried out at 800 psi, 1000 psi and 1200 psi,

respectively. The deviation of 2.68 °C, 5.72 °C, 5.62 °C and 5.79 °C was observed for Tg measured from the reverse heat capacity thermogram when compared to the S-rich Tg measured from tan delta for pure SEBS, SEBS with 800psi, SEBS with 1000 psi and SEBS with 1200 psi, respectively.

Although the Tg peak remains constant on the tan delta curve, the height of this peak reduces when SEBS is extruded at 800 psi, 1000 psi and 1200 psi, respectively. This reducing tan delta peak suggests that the reduced frictional and heating loss as well as damping nature of SEBS at the molecular level, as $scCO_2$ breaks down the microdomains, making the material behave like a homogeneous network at the microscale. Analysis of such homogenisation and thermal incompatibility behaviour using DMA has not been reported elsewhere.

4.4.4 Tensile Test of SEBS Extruded at Various Critical Pressures

Figure 4.16 illustrates tensile curves exhibited by pure extruded SEBS, extruded SEBS at 800 psi, extruded SEBS at 1000 psi and extruded SEBS at 1200 psi. When the pressure of $scCO_2$ was increased (from 800 psi to 1200 psi), the resilience decreased. A similar pattern was observed in the storage modulus of the DMA results obtained. Table 4.6 shows Young's modulus of SEBS obtained by regression method from 0.25% - 1% extension extruded under different $scCO_2$ pressures. Similar to storage modulus, Young's modulus of SEBS also was found to decrease with the introduction of $scCO_2$ and was observed was proportional to the pressure used. A slight decrease in Young's modulus of SEBS with 800 psi confirms a decrease in modulus of resilience. This effect of a decrease in modulus of resilience was noted as the pressure of $scCO_2$ was increased to 1000 psi and 1200 psi; similar to the pattern observed in the storage modulus of the DMA results obtained.

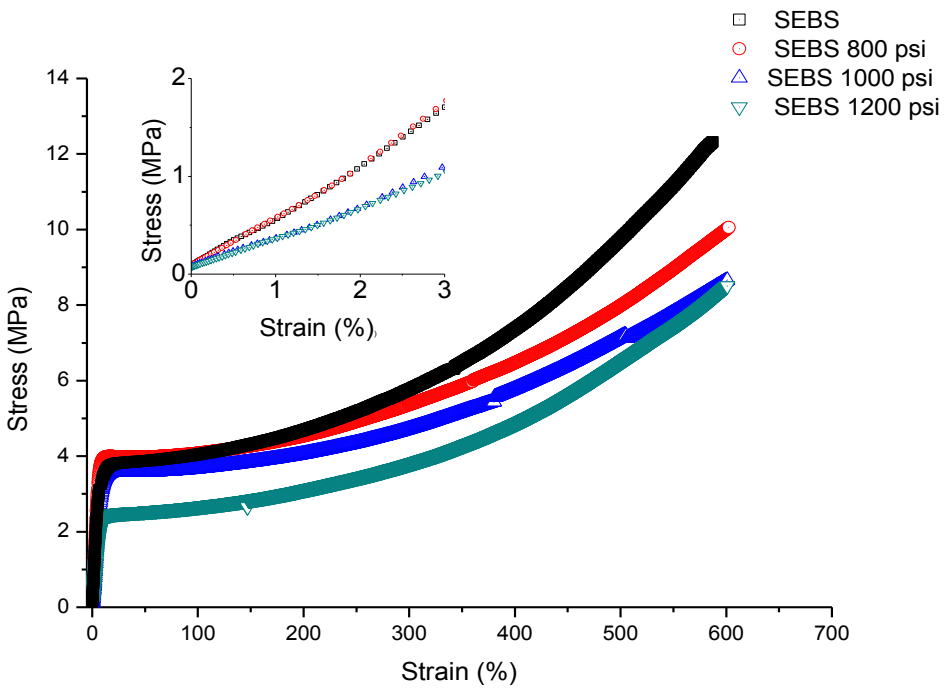

Figure 4.16 Stress-strain response exhibited by pure extruded SEBS, SEBS at 800 psi, SEBS at 1000psi and extruded SEBS at 1200 psi

According to Cantournet et al [140], the extension of elastomers like SEBS occurs with a combination of sliding and non-sliding action between hard and soft blocks. Figure 4.16 shows that the resilience of the SEBS decreased when the critical pressure of $scCO_2$ was increased. A similar pattern was observed in the storage modulus of the DMA results obtained.

Table 4.6 Young's modulus by regression method of SEBS extruded at different pressures

Sample	**Young Modulus (MPa)**
Extruded SEBS	69.45±3.77
SEBS 800 psi	67.53±13.4
SEBS 1000 psi	46.83±6.3
SEBS 1200 psi	44.39± 7.1

The sliding action between the hard blocks and the soft blocks is observed after the elastic limit. The introduction of $scCO_2$ on SEBS has led to high thermal incompatibility between the soft block and hard block as observed in DSC and DMA graphs. This effect shows a direct impact on sliding behaviour of the hard block over soft block making SEBS tri-block less resistant to external forces. The reduced Young's modulus can be attributed to the effect of foaming at higher critical pressures (similar to DMA–1200 psi reduces the storage modulus), rearrangement

and breakdown (as described in DSC-formation of additional Tg's) of original hard and the soft domain of SEBS into smaller domains.

4.4.5 Fourier Transform Infrared Spectroscopy (FTIR) of SEBS at Various Critical Pressures

ATR-FTIR spectra of transmittance and absorbance illustrate the effect of supercritical assisted extrusion on SEBS at various critical pressures (shown in Figure 4.17 and Figure 4.18). Peaks at 2920 cm^{-1} and 2851 cm^{-1} representing the asymmetrical stretching of $–CH_3$ and $–CH_2$ (the ethylene-butylene block) do not show any shift in the position even when treated at higher critical pressures (1200 psi).

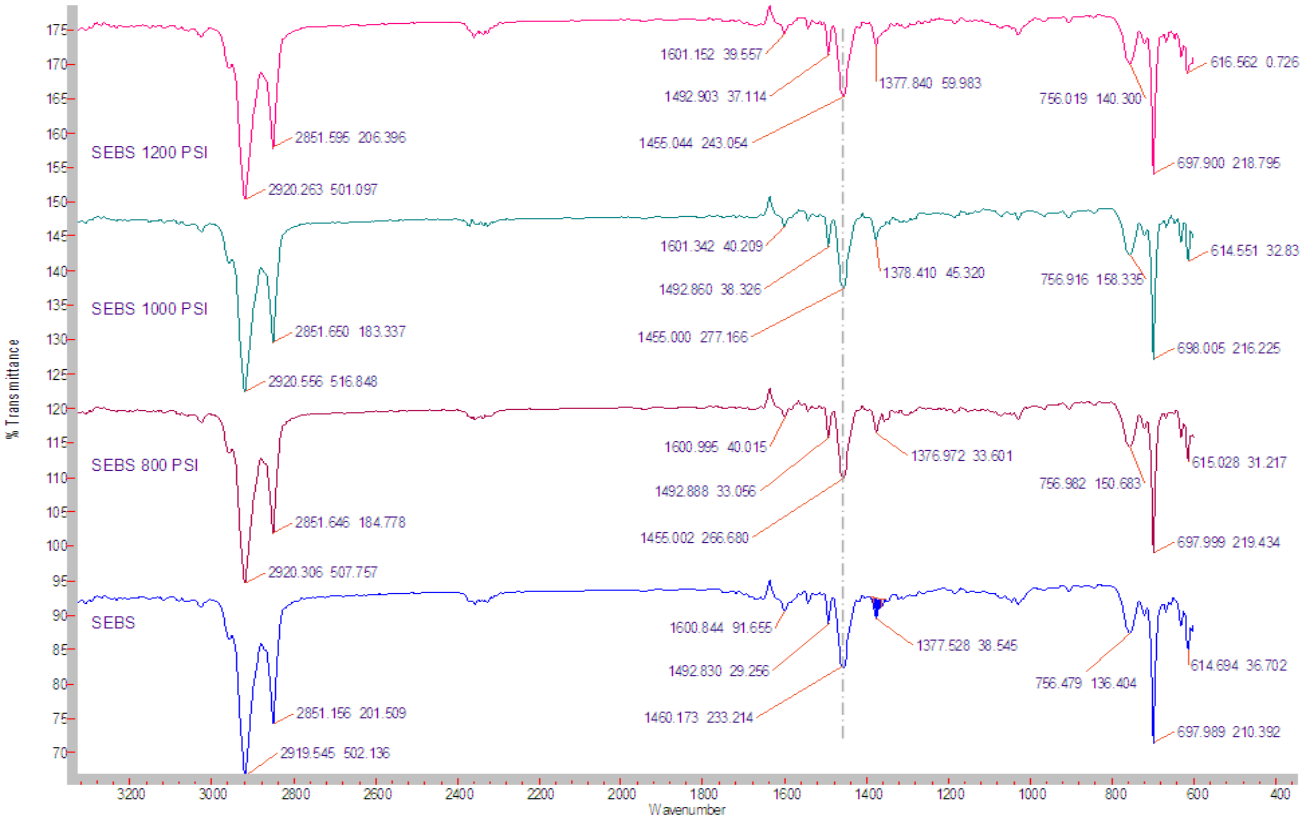

Figure 4.17 ATR-FTIR transmittance spectra of SEBS extruded at various critical pressures

The aromatic C=C stretching of the aromatic system at peak 1600 cm^{-1} and 1492 cm^{-1} remain in their respective positions for extrudates at all the critical pressures. Peaks 756 cm^{-1} and 697 cm^{-1} are attributed to benzene moiety of styrene group. The peak at 1377 cm^{-1} represents the bending of $-CH_3$. It can be observed from the absorbance spectra that the $scCO_2$ has caused a shift in peak from 1460 cm^{-1} to 1455 cm^{-1}, which was attributed to asymmetric $–CH_2$ bending.

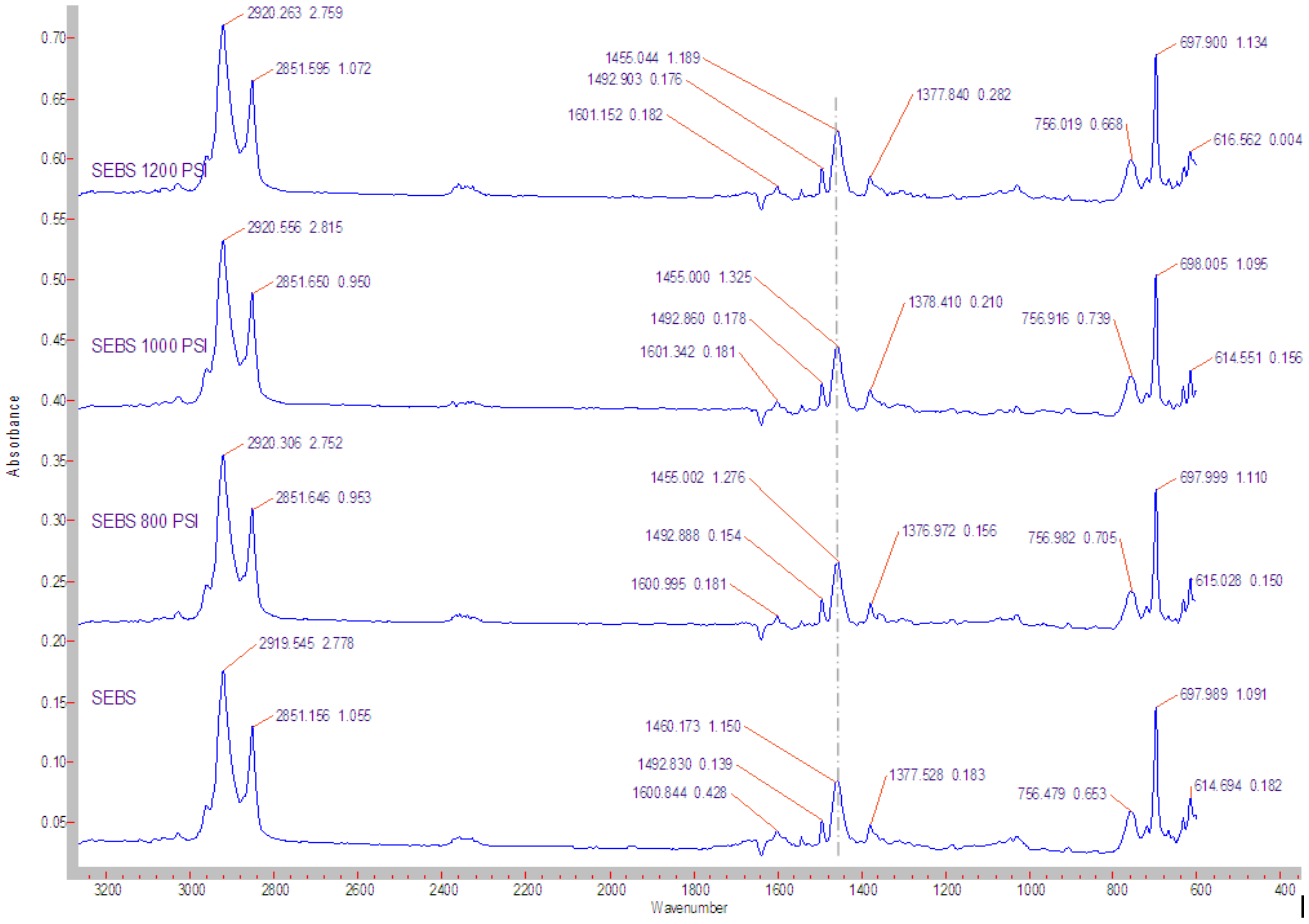

Figure 4.18 ATR-FTIR Absorbance spectra of SEBS extruded at various critical pressures

These bands are also attributed to stretching vibrations of carbons in the aromatic rings [141] (phenyl rings in polystyrene, C=C pi bond interactions with CO_2). The quadrupole moment of CO_2 allows Lewis acid-base interactions between the polymer matrix and CO_2. Many researchers have observed a similar effect of the CO_2 - phenyl ring interaction [25, 94, 95, 142]. Evident differences in the spectra were not observed, due to the reason that SEBS is an amorphous polymer with 29% styrene and mostly consisting of polyethene-butylene.

4.4.6 Scanning Electron Microscopy (SEM) of SEBS Processed at Various Pressures

Figure 4.19 demonstrates the density of pores at the surface is dependent on the critical pressure of carbon dioxide passed through the extruder. The porosity starts to form at the surface at 800 psi as shown in (B), increases at 1000 psi as shown in (C) and becomes intense at 1200 psi as shown in (D). The formation of pores is one of the reasons for the decrease in dielectric permittivity and Young's modulus of SEBS at 1200 psi.

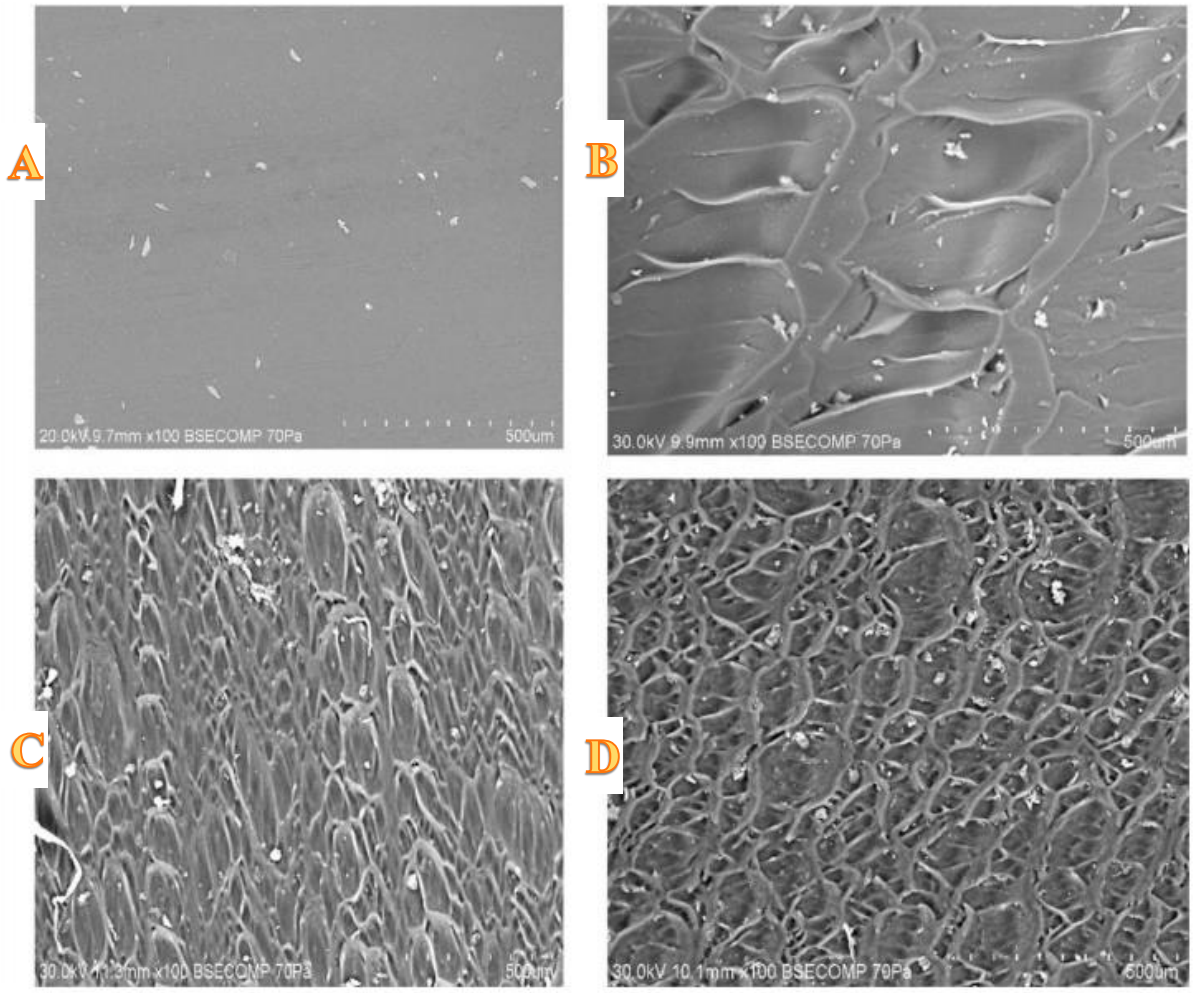

Figure 4.19 Morphology showing the porosity of SEBS extruded under different pressures: A-Virgin SEBS, B-SEBS 800 psi, C-SEBS 1000psi and D-SEBS 1200 psi

4.5 Key Points for SEBS Processed at Different Critical Pressures

SEBS was extruded using $scCO_2$ at various critical pressures (800psi, 1000psi and 1200psi) to investigate its effect on thermal and mechanical performances. The following are the key observations:

- The structural changes caused due to the thermal energy during extrusion has led SEBS to be more thermally stable than untreated material. This increase in degradation temperature occurs due to the amorphous nature that may have resulted in high micro-nucleation formation extruded at different $scCO_2$ which leads to the creation of multi-domains.
- The reversing and non-reversing heat flow gives information on phase size, where $scCO_2$ assisted extrusion of SEBS at various pressures resulted in increased microphases or

formation of new microphases, thus producing more homogenous SEBS. Extrusion of SEBS at various pressures resulted in increased microphase separations or formation of new microphases, thus producing new structure peaks of SEBS (a clear division of Tg EB – separating ethylene and butylene). The appearance of clear Tg of styrene block at 1000 psi and 1200 psi supports the phase separation caused by $scCO_2$.

- DMA analysis demonstrates that the introduction of $scCO_2$ during extrusion leads to a decrease in stiffness (represented by storage modulus) as well as the molecular movements between hard and soft block segments (represented by loss modulus) of the elastomers. A similar decrease in Young's modulus was observed from the tensile test curves. The area under the tan delta curve at 96 °C decreases with increasing $scCO_2$ pressure, suggesting the reduced frictional as well as damping nature of SEBS at the molecular level (happens mainly due to the formation of multiple microphases).
- FTIR analysis presented a significant shift in peak from 1460 cm^{-1} to 1455 cm^{-1} representing the effect of the CO_2 − phenyl ring interaction. Evident differences in the spectra were not observed, due to the reason that SEBS is an amorphous polymer with 29% styrene and mostly consists of polyethene-butylene.
- Porous nature can be observed on the surface at 800 psi, increases at 1000 psi and becomes intense at 1200 psi

4.6 Conclusion for Polymer Processing of EAPs at Different Critical Pressures

This main focus of this chapter was to investigate and understand how a supercritical assisted extrusion polymer processing technique at different pressures affects the thermal and mechanical properties of Pebax and SEBS polymer matrix. The thermal degradation temperature remained constant in Pebax while an increase was observed in SEBS. This increase in degradation temperature of SEBS can be ascribed to the nature of the polymer and its ability to solubilise. Pebax is a semi-crystalline polymer with low sorption capabilities while SEBS is a completely amorphous polymer with high sorption ability. In both, Pebax and SEBS, break down of larger domains to smaller were clearly observed, in terms of DSC thermograms resulting in improved homogenisation between softer and harder blocks (broadening of crystallisation temperature in Pebax and split in glass transition temperature in SEBS). Additional rheology testing also suggested the break down of crystallites by decreasing complex viscosity with increasing critical pressures in case of Pebax. However, at 1200 psi, the mechanical properties (Young's modulus decreased by 28% when processed at 1200 psi compared to virgin Pebax) were lower than of the

virgin Pebax due to the dominance of foaming effects. In the case of SEBS, a gradual decrease in the mechanical properties were observed at 800 psi, 1000 psi and 1200 psi (Young's modulus decreased by 36% when processed at 1200 psi compared to virgin SEBS). A clear understanding can be drawn from the IR spectroscopy (1638 cm^{-1} peak height increase) in terms of Pebax, where $scCO_2$ assisted processing reduced the hydrogen bonding distance/intensity between the carbonyl segments of the hard block which in turn may have resulted in the formation of perfect crystallites. In terms of SEBS, IR spectroscopy does not show any shifts or enhancement in wavenumber peaks, $scCO_2$ interactions with styrene group of SEBS was evident at wavenumber 1460 cm^{-1}. In both the cases, the SEM morphology demonstrated a gradual increase in porous nature as increasing $scCO_2$ pressure acts as a foaming agent as a result of sudden depressurisation at the die of the extruder.

5 Supercritical Fluid Assisted Processing of Pebax Graphene Porous Polymer Composites

5.1 Introduction

One of the most common ways of enhancing the electromechanical performance of polymers is to incorporate additional filler/additive material to form composites. As a continuation of the previous chapter, this chapter investigates the effect of incorporating graphene-based filler particles into Pebax polymeric matrices when processed with $scCO_2$. The Pebax-graphene based composite is processed using supercritical assisted extrusion at critical pressure of 1200 psi or 82.73 Bar (this parameter was selected based on the conclusion made from the previous Chapter 4). Such processing of polymer composites using supercritical carbon dioxide has not been reported elsewhere. A dearth of knowledge exists in understanding the effects of such complex composite processing techniques on the thermal, mechanical and electrical behaviour of the polymer matrix. Therefore, this chapter forms the building block to the following chapters of this thesis, where the novelty of this study is rooted in the amalgamation of two important factors: one is the supercritical processing condition and second is the use of filler particles such as graphene (Section-1) and graphene oxide (Section 2) at various concentrations.

It is well-understood from Chapter 4 that $scCO_2$ assisted extrusion of Pebax results in a porous polymer matrix. Although graphene has excellent mechanical and electrical properties, however, they are relatively hard to process and difficulties to maintain the intrinsic one atom thick physical property. Therefore, graphene oxide was also investigated in the second part of this section. Graphene oxide is a single atomic layer oxidised form of graphene, which is laced with oxygen-containing groups on the surface and edges of the graphene layer. The effects of processing such membranes are characterised for the thermal, mechanical and electrical properties. Differential Scanning Calorimetry (DSC) and Thermal Gravimetric Analysis (TGA) were used to study the thermal characteristics and thermal stability, respectively; a crystallisation kinetics study and X-Ray Diffraction analysis were carried out to relate the effect of $scCO_2$ and graphene-based filler particles on the crystallite size and rate of crystallisation. These analysis techniques were used to draw a conclusion and establish the relationship between the effect of crystallite size on the actual processing conditions and filler loading. Dynamic Thermal Mechanical Analysis (DMA) and tensile test were used to study the mechanical properties; Fourier transform infrared spectroscopy (FTIR) was used to understand the interaction between the polymer-graphene composites, while impedance spectroscopy was used to characterise the electrically conductive property of the manufactured polymer membranes.

5.2 Section 1: Supercritical Fluid assisted Porous Pebax Graphene Composites

5.2.1 Thermal Gravimetric Analysis of Porous Pebax Graphene Composites

Figure 5.1 shows the TGA thermogram of $scCO_2$ assisted extrusion of porous Pebax graphene composites. No major changes can be observed from the derivative of weight change peak, which shows the maximum degradation temperature. The maximum degradation temperature almost remains constant at 460 °C for all the graphene filler content. However, with an increase in the graphene percentage, the total weight percentage of thermograms does not become zero.

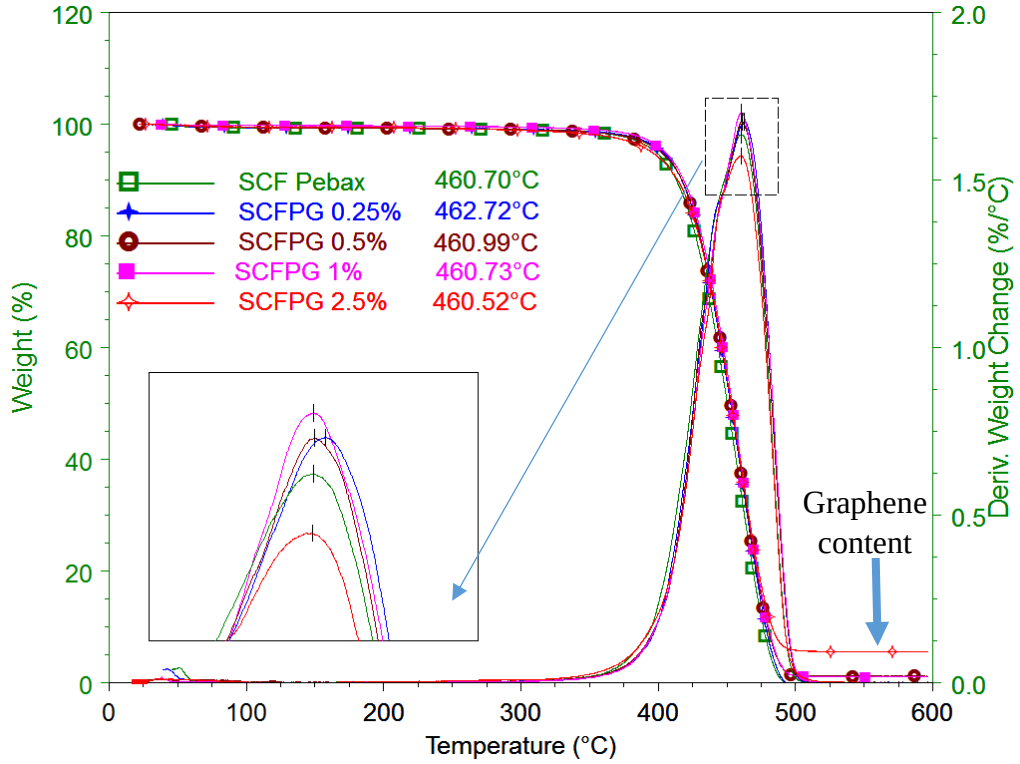

Figure 5.1 TGA thermograms of $scCO_2$ assisted extrusion of porous Pebax graphene composites

This mainly occurs due to the amount of graphene filler content within the composites, whereas the polymer degrades at 460 °C and graphene degrades at a higher temperature (approx. 1000 °C). The zoomed portion of the graph represents the derivative of weight change, where the change in the slope of heat flow is understood more easily. It can be clearly seen that the loss in weight increases for extrudates up to 1% and decreases for 2.5% suggesting that the graphene filler particles restrict the easy movement of polymer chains mainly due to poor dispersion or agglomeration of particles within the polymer matrix.

5.2.2 Differential Scanning Calorimetry of Pebax Graphene Porous Composites

Figure 5.2 shows the heat flow thermogram of $scCO_2$ assisted extrusion of Pebax graphene composites. The peak at 162 °C is attributed to the melting point of Pebax. This melting peak almost remains constant for all the composite matrices. In addition, a small endothermic peak also appears at around 80 °C specifically with the addition of graphene particles. This peak is referred to as the glass transition temperature of the nylon block (caused from $scCO_2$ treatment which aligns the PTMO-Nylon linkage) and usually appears due to the restriction imposed by graphene particles upon polymer-additive interaction, which otherwise is not clearly evident on the virgin Pebax thermogram.

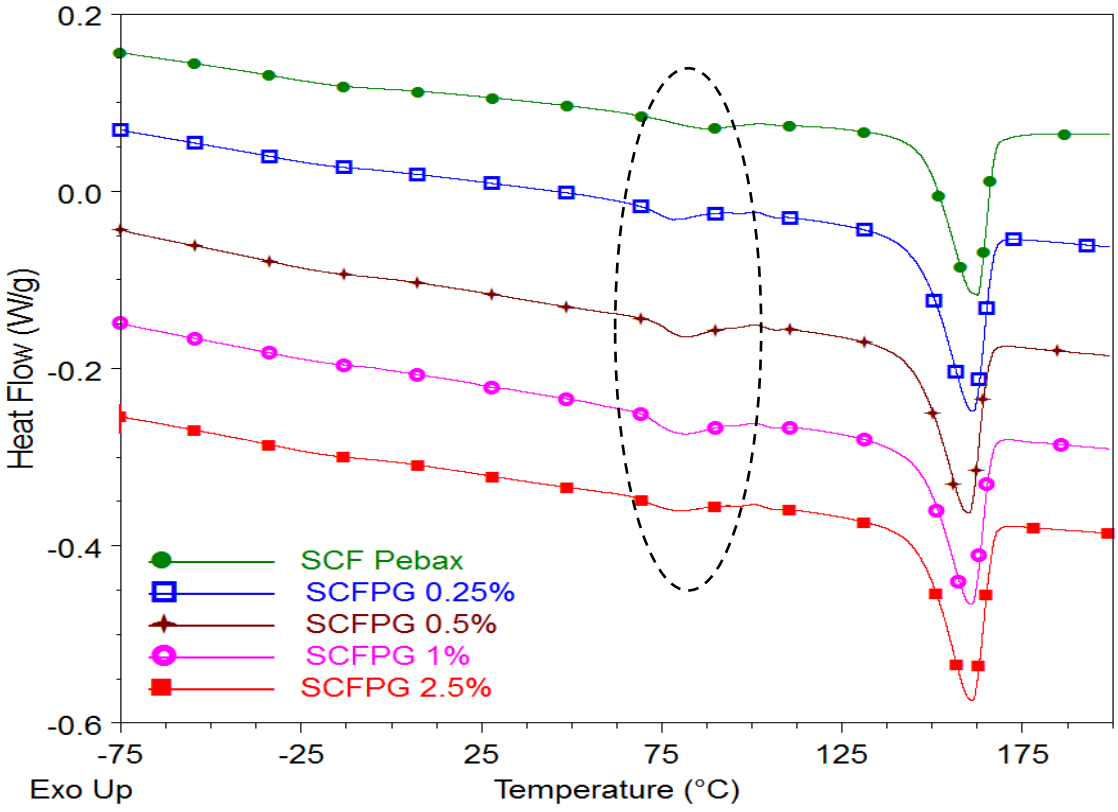

Figure 5.2 Heat flow thermogram of $scCO_2$ assisted extrusion of Pebax graphene composites

When clearly observed, this peak at around 80 °C flattens with the filler concentration of 2.5%, suggesting poor interaction and agglomeration. Figure 5.3 shows the crystallisation peak of all the Pebax graphene composites. The crystallisation peak gradually shifts from 136 °C for virgin Pebax to slightly higher temperatures of 140 °C upon addition of graphene up to 2.5%. In addition, the relative heat flow magnitude also reduces upon increasing graphene content. The shift from peak crystallisation temperature to higher temperatures suggests that the graphene particles are acting as nucleating agents, therefore, the higher the graphene concentration, the

crystallisation peak tends to shift to a higher temperature. The magnitude of the heat flow also decreases upon higher graphene concentration, mainly due to the suggested restriction imposed by graphene particles to initiate easy folding of the polymer chain. In addition, as the number of nucleation sites increase, the crystallites have a tendency to collide with each other, bringing an end to the crystallisation process at a faster rate.

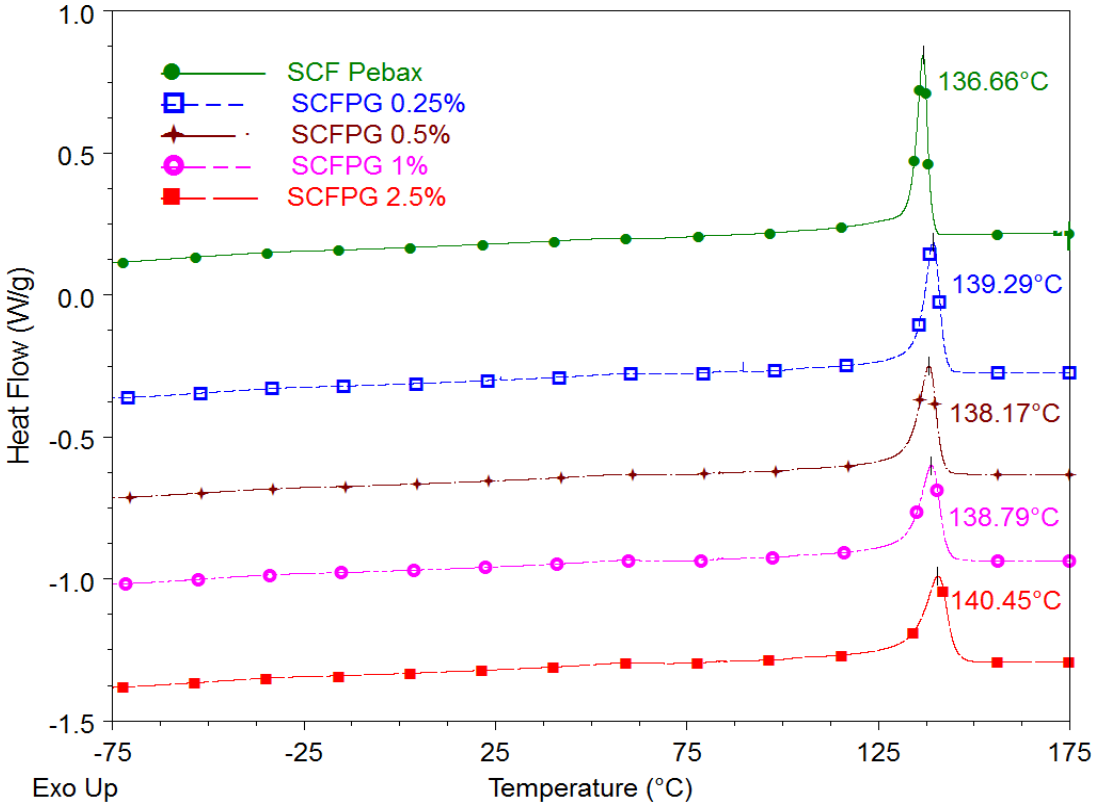

Figure 5.3 Cooling cycle of porous Pebax graphene composites at various filler concentrations

5.2.2.1 Isothermal Crystallisation Kinetics of Porous Pebax Graphene Composites

Isothermal crystallisation studies were conducted to understand the process of crystallisation for porous Pebax–scCO$_2$ treated polymer composites. Isothermal crystallisation using Avrami model is well discussed in Chapter 3 (Refer to 3.4.3.1). Figure 5.4 shows the Avrami plot of log [-ln(1-X(t))] vs. log t and the obtained value from slope and intercept are tabulated in Table 5.1. The Avrami exponent 'n' is in the range from 2 to 3, for all the samples indicating a complex two-dimensional growth phenomenon with branched fibrillar morphology. Such non-integer values of n usually represent a nucleation between instantaneous and sporadic nature as described by Lorenzo [143].

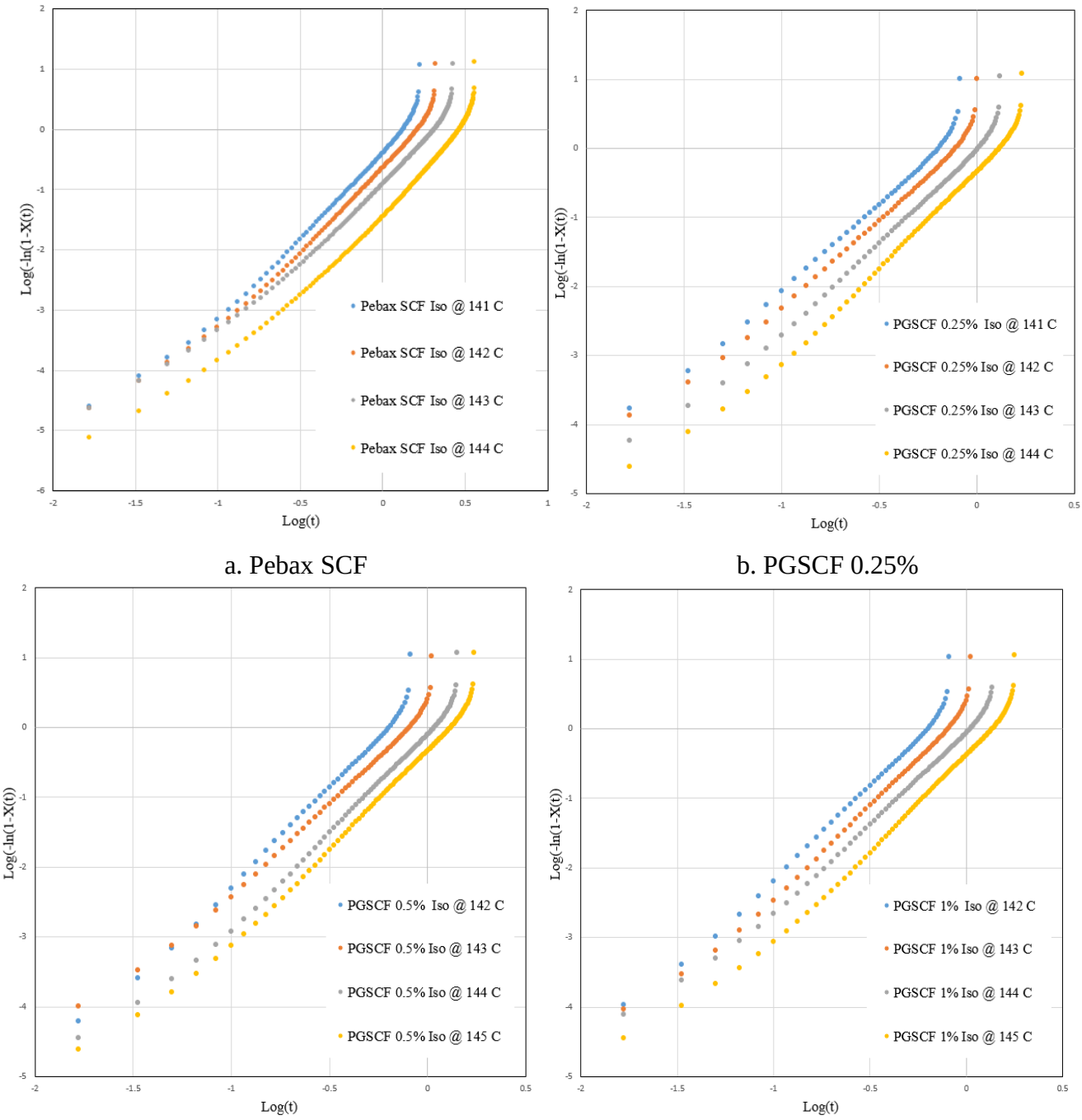

a. Pebax SCF

b. PGSCF 0.25%

c. PGSCF 0.5%

d. PGSCF 1%

Figure 5.4 Avrami plot for porous Pebax graphene composites

A similar Avrami exponent was also reported by N. McFerran for Nylon 12 [144]. Although the addition of graphene particles and $scCO_2$ assisted extrusion did not have a huge effect on the Avrami exponent, a significant drop in the parameter (n and k) can be observed. The Avrami parameters obtained here can be considered as an indication of the dimension or nature of nucleation or crystallisation rate; henceforth these values are not completely compared against each other due to the variability in the selected crystallisation temperatures. Such variability

occurs due to the addition of graphene particles and efforts are made to only consider isothermal samples with a complete baseline match to avoid errors.

Table 5.1 Avrami parameters for porous Pebax graphene composites

Sample Type	Tc (° C)	n	Average N	Log k	K	$t_{1/2}$* (min)	$t_{1/2}$ (min)	G (min^{-1})	R^2
Pebax	141	2.55	2.68	0.50	2.97	0.52	0.54	1.8	0.999
	142	2.65		0.23	1.71	0.69	0.71	1.4	0.999
	143	**2.69**		**-0.07**	**0.85**	**0.88**	**0.92**	**1.0**	**0.999**
	144	2.85		-0.38	0.41	1.16	1.19	0.8	1.000
PebaxSCF	141	2.83	2.87	-0.420	0.38	1.22	1.21	0.82	1.000
	142	2.84		-0.655	0.22	1.49	1.48	0.67	1.000
	143	**2.80**		**-0.922**	**0.11**	**1.87**	**1.86**	**0.53**	**1.000**
	144	3.04		-1.480	0.033	2.70	2.68	0.37	0.999
PGSCF 0.25	141	2.45	2.58	0.417	2.61	0.58	0.56	1.78	1.000
	142	2.50		0.203	1.59	0.70	0.69	1.44	1.000
	143	**2.61**		**-0.063**	**0.86**	**0.91**	**0.90**	**1.11**	**1.000**
	144	2.76		-0.338	0.45	1.16	1.16	0.86	0.999
PGSCF 0.5	142	2.68	2.72	0.489	3.08	0.57	0.57	1.75	0.999
	143	**2.61**		**0.212**	**1.62**	**0.72**	**0.71**	**1.40**	**1.000**
	144	2.78		-0.098	0.79	0.95	0.96	1.04	0.999
	145	2.82		-0.322	0.47	1.14	1.16	0.86	0.999
PGSCF 1	142	2.60	2.67	0.482	3.03	0.56	0.56	1.78	0.999
	143	**2.65**		**0.222**	**1.66**	**0.71**	**0.71**	**1.40**	**0.999**
	144	2.62		-0.065	0.86	0.92	0.92	1.08	1.000
	145	2.81		-0.365	0.43	1.18	1.21	0.82	0.999
	147	2.79		-0.989	0.10	1.95	1.95	0.51	1.000
PGSCF 2.5	**143**	**2.77**	2.90	**-0.468**	**0.34**	**1.29**	**1.28**	**0.78**	**1.000**
	144	2.90		-0.783	0.16	1.64	1.65	0.60	1.000
	145	3.08		-1.232	0.058	2.23	2.25	0.44	1.000
	146	2.87		-1.528	0.029	2.99	2.93	0.34	0.999
	147	2.44		-1.606	0.024	3.91	3.53	0.28	0.999

Note: Values for Tc=143℃ is in bold for ease of comparison between different samples and $t_{1/2}$* represents the practically obtained values

The value of k, which represents the rate of crystallisation tends to decrease as the isothermal crystallisation temperature is increased for all the samples. Such decreases in the k value depending on the isothermal crystallisation temperature are indicative of the actual barrier height in order to initiate the density variation followed by nucleation and crystal growth. The overall value of k tends to increase on the addition of graphene up to 1%. Usually, the addition of filler content enhances the k value where the filler particles act as nucleation sites, thereby accelerating the nucleation process. However, the overall k value reduces for PGSCF 2.5% but

remains higher than virgin PebaxSCF (Tc @ 143 °C having k = 0.11 for virgin PebaxSCF, while Tc @ 143 °C having k =0.34 for PGSCF 2.5%) suggesting that the filler particles do not act as nucleating sites anymore. One probable condition that results in low k value upon higher filler loading can be attributed due to agglomeration of graphene particles. Such lowering of k values upon higher graphene concentration was also reported by Fan Zhang et al [145]. Similar effects such as a reduction in the thermal stability and mechanical properties have been reported in this section with graphene content of 2.5%. The evidence from the crystallisation study confirms possible implication due to agglomeration of graphene particles.

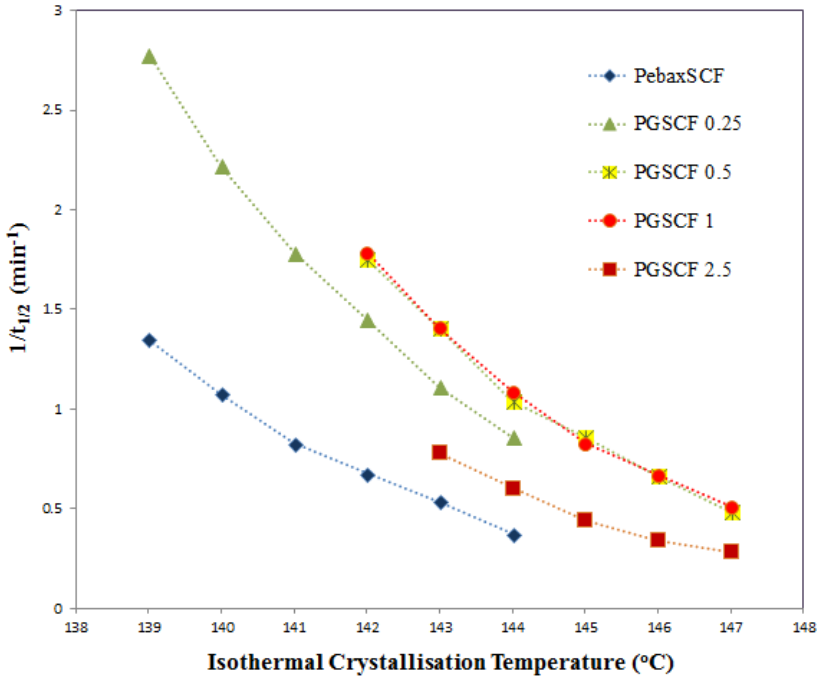

Figure 5.5 Calculated crystallisation rates at different isothermal temperatures for porous Pebax graphene composites

Table 5.1 lists the calculated and practically obtained values of $t_{1/2}$. Halftime crystallisation is defined as the time from the onset of the crystallisation until the crystallisation reaches 50%. The relationship between k and $t_{1/2}$ based on the Kurajica approach is defined as $t_{1/2} = (\ln 2/K)^{1/n}$. The theoretically calculated $t_{1/2}$ and the practically obtained $t_{1/2}$* are compared in Table 5.1. In all the cases the $t_{1/2}$ value increases with increasing T_c. The $t_{1/2}$ is also in agreement with the k value, where the $t_{1/2}$ reduces upon addition of graphene particles indicating faster crystallisation rate, however, $t_{1/2}$ values increase for graphene loading of 2.5% due to uneven dispersion/agglomeration. This can be compared to the value G, which usually determines the rate of crystallisation where G is the reciprocal of $t_{1/2}$ ($G=1/ t_{1/2}$). The value of $1/t_{1/2}$ can be used to describe the crystallisation rate and is plotted in Figure 5.5, as a function of isothermal

crystallisation temperature. It can be clearly seen that the graphene particles act as nucleating agents thereby enhancing the crystallisation rate due to their even dispersion. This can also be confirmed by crystallisation parameter k as listed in the above Table 5.1. Such phenomena of increased G and k value upon addition of graphene up to 1% is usually attributed to heterogeneous nucleation rates as described by Kirkorian et al [146] and W Y Zou et al [147].

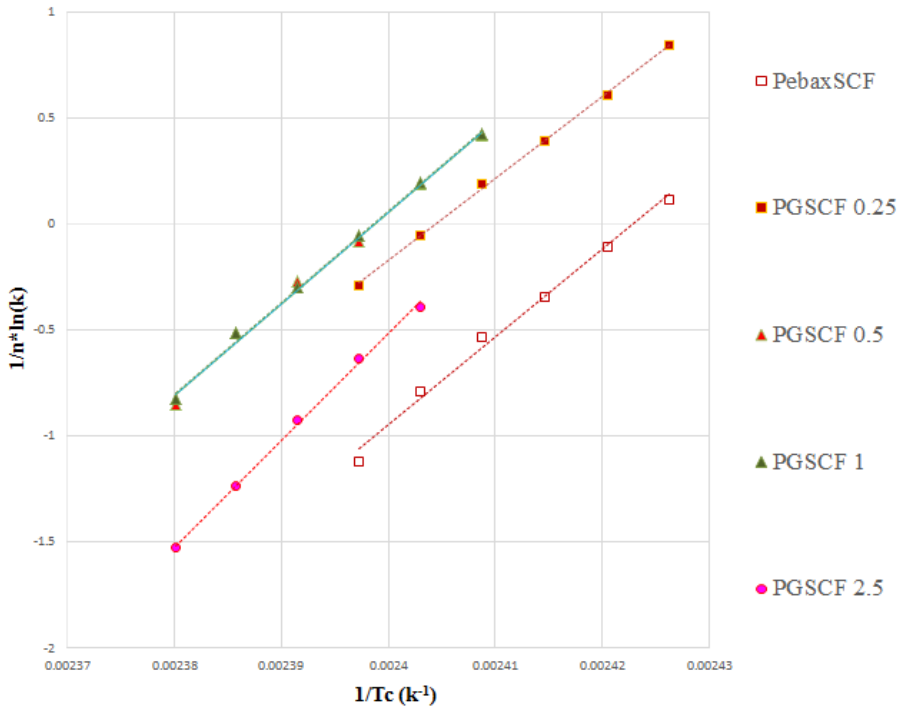

Figure 5.6 Activation energy plot of porous Pebax graphene composite using Arrhenius equation

The crystallisation rate parameter was described by an Arrhenius type equation (refer to 3.4.3.1). The slope of the plot ln (K)*1/n vs 1/Tc as shown in Figure 5.6 determines the ΔE/R. where the activation energy was calculated and is tabulated in Table 5.2.

Table 5.2 Arrhenius activation energy obtained from the slope of the above plot for porous Pebax graphene composites

Samples	Arrhenius Activation Energy (KJ/mol)
PebaxSCF	-342.869
PGSCF 0.25%	-320.089
PGSCF 0.5%	-357.975
PGSCF 1%	-357.202
PGSCF 2.5%	-418.593

The ΔE value decreases for 0.25% loading, almost remains constant for 0.5% and 1% loading with respect to virgin PebaxSCF. However, the activation energy is the highest at 2.5% loading. This shows that the graphene particles in the Pebax matrix up to 0.25% acted as nuclei, again suggesting even dispersion, which decreased the crystallisation free energy barrier, and for 0.5% and 1% loading, the restriction due to graphene polymer interactions might have restricted the free chain movement of polymer phase transformation resulting in a slight increase in the crystallisation activation energy. The effect of uneven dispersion and agglomeration might have resulted in increasing the crystallisation free energy barrier and thus higher activation energy.

5.2.2.2 Non-Isothermal Crystallisation Kinetics of Porous Pebax Graphene Composites

The non-isothermal crystallisation kinetics of Pebax graphene composites with $scCO_2$ was studied under various cooling rates. The thermograms for Pebax graphene composites at various non-isothermal conditions is shown in Figure 5.7 and Table 5.3. It can be clearly observed that the crystallisation onset temperature (Tc_{on}), peak crystallisation temperature (Tc) and crystallisation offset temperature (Tc_{off}) shifts to a lower temperature and becomes broader with an increase in the cooling rate from 2.5 °C/min to 20 °C/min.

Table 5.3 Non-Isothermal parameters recorded form the cooling cycle for porous Pebax graphene composites

Sample Type	Cooling Rate (°C/min)	Tc_{on} (°C)	Tc_{off} (°C)	Tc (°C)	ΔHc (J/g)	Xc (%)
PebaxSCF	2.5	139.70	107.71	136.40	37.20	33.38
	5	135.67	92.80	131.68	38.97	30.58
	10	131.71	85.41	126.38	36.70	32.53
	20	126.68	84.44	120.04	33.68	32.12
PGSCF 0.25%	2.5	144.89	114.80	139.89	35.34	36.33
	5	139.48	101.55	136.24	37.03	31.00
	10	135.55	89.97	132.09	37.25	29.93
	20	131.19	91.33	127.16	34.44	31.03
PGSCF 0.5%	2.5	146.22	115.66	140.67	35.19	32.78
	5	143.40	103.13	137.36	36.61	30.15
	10	137.58	93.11	133.66	36.94	29.37
	20	138.07	91.70	129.32	35.07	30.99
PGSCF 1%	2.5	146.49	110.81	140.63	36.78	31.07
	5	144.22	97.12	137.24	38.76	27.96
	10	140.45	88.00	133.41	37.77	29.15
	20	138.15	86.40	129.15	35.55	31.02
PGSCF 2.5%	2.5	149.96	109.43	139.73	33.62	31.35
	5	144.68	98.03	136.68	34.77	29.91
	10	142.47	90.90	133.26	34.36	29.16
	20	140.33	86.15	129.04	32.97	32.08

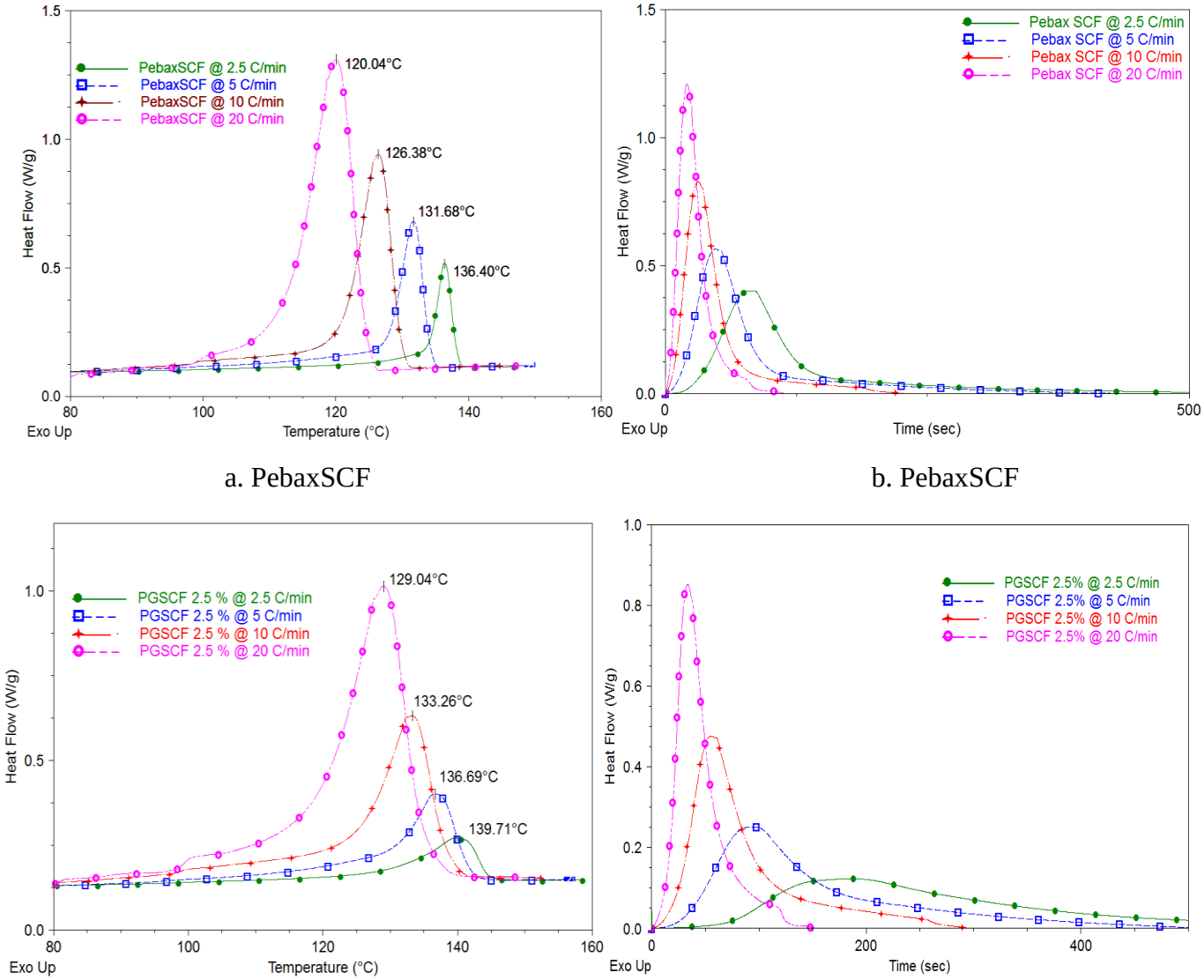

a. PebaxSCF

b. PebaxSCF

c. PebaxSCF 2.5%

d. PebaxSCF 2.5%

Figure 5.7 Heat flow vs. temperature and time for porous Pebax graphene composites

M.C. Kuo et al [148] reported that the addition of inorganic fillers would affect the crystallisation behaviour of the polymer molecules in two possible ways: 1. increases the number of the crystal due to heterogeneous nucleation, or 2. restrict the crystal growth due to mobility hindrance. If heterogeneous nucleation is dominant during the crystallisation process for a given cooling rate, crystallisation temperature will shift to a higher value. Otherwise, the polymer will crystallise at a lower temperature due to the hindrance of mobility of chain segments. Hence, the shifting of Tc Tc peak to higher temperatures with the addition of graphene suggests the dominance of the heterogeneous nucleation process/graphene acting as nucleation sites.

The Avrami model can also be used to analyse the crystallisation kinetics under non-isothermal conditions considering small modification of heating rate. Plots of log (-ln (1 – X(t))) versus log t

are shown in Figure 5.8 for Pebax graphene composites with $scCO_2$. The corresponding Avrami parameters n and k were obtained from the slope and intercept of the plots, $t_{1/2}$ and corresponding R^2 and are listed in Table 5.4.

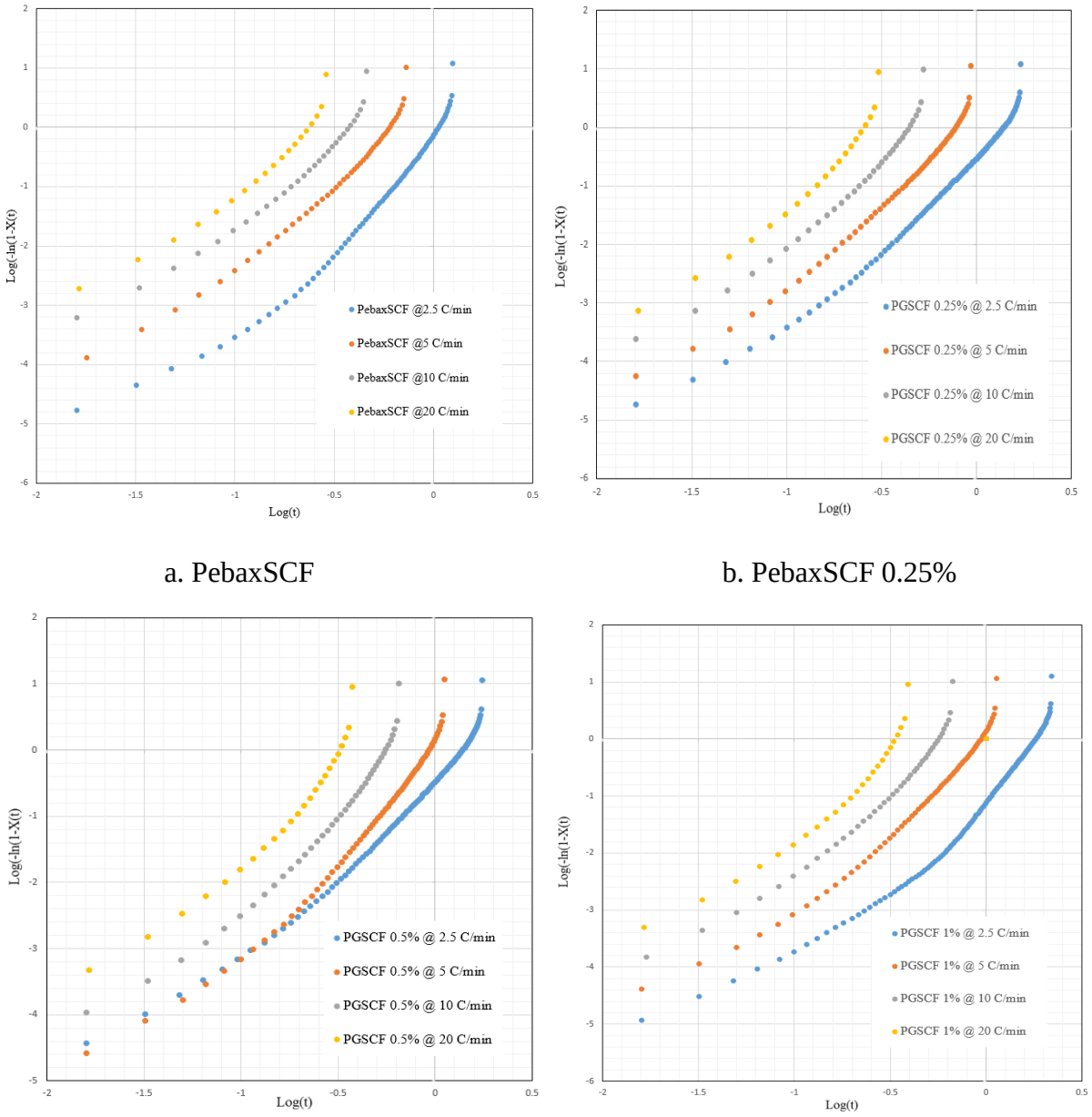

a. PebaxSCF

b. PebaxSCF 0.25%

c. PebaxSCF 0.5%

d. PebaxSCF 1%

Figure 5.8 Avrami plot for porous Pebax graphene composites under non-isothermal conditions

The Avrami exponent n decreases with increasing cooling rate for all the sample types mainly due to less availability of crystallisation time for complete nucleation mechanism. The average n values for all the samples lies between 3 and 4, indicating complex spherulite crystallites having three-dimensional growth. The value of 'n' obtained here under the non-isothermal conditions is much higher than the Avrami 'n' values obtained from isothermal conditions. This may be due to

the fact that under non-isothermal conditions, the samples are given enough time to nucleate and further grow into perfect crystallites, which is not the same under isothermal conditions, where the samples are suddenly cooled to their respective Tc.

Table 5.4 Avrami parameters obtained from the slope and intercept of the Avrami plot for porous Pebax graphene composites under non-isothermal conditions

Sample Type	ϕ (°C/min)	n	Avg n	Log k'	k'	$t_{1/2}$ From Graph (min)	$t_{1/2}$ Calculated (min)	R^2
Pebax	2.5	2.72	2.65	-0.09	0.80	0.95	1.01	0.993
	5	2.66		0.24	1.73	0.56	0.70	0.990
	10	2.70		0.86	7.24	0.32	0.41	0.982
	20	2.53		1.48	30.19	0.17	0.22	0.985
PebaxSCF	2.5	3.94	3.30	-0.21	0.62	0.99	1.03	0.999
	5	3.21		0.58	3.80	0.55	0.59	0.998
	10	3.04		1.19	15.49	0.34	0.36	0.997
	20	3.00		1.78	60.26	0.21	0.23	0.997
PGSCF 0.25	2.5	3.27	3.29	-0.53	0.30	1.27	1.30	1.000
	5	3.21		0.23	1.70	0.72	0.76	0.999
	10	3.30		1.04	10.96	0.44	0.43	0.997
	20	3.40		1.88	75.86	0.23	0.25	0.997
PGSCF 0.5	2.5	3.08	3.47	-0.48	0.33	1.25	1.27	0.999
	5	3.65		0.04	0.85	0.78	0.88	0.999
	10	3.69		0.83	6.76	0.51	0.54	0.996
	20	3.49		1.54	34.67	0.30	0.33	0.993
PGSCF 1	2.5	4.30	3.67	-1.12	0.08	1.68	1.67	0.999
	5	3.50		-0.005	0.99	0.87	0.90	0.999
	10	3.40		0.69	4.90	0.52	0.56	0.997
	20	3.51		1.47	29.51	0.31	0.34	0.994
PGSCF 2.5	2.5	4.46	3.64	-1.82	0.02	2.34	2.36	0.999
	5	3.68		-0.45	0.35	1.17	1.20	0.999
	10	3.22		0.23	1.70	0.69	0.76	0.997
	20	3.22		0.91	8.13	0.42	0.47	0.995

The crystallisation rate value k' increases with higher heating rate, however, this value shows a decreasing trend with the addition of graphene up to 2.5% compared to virgin Pebax. This increasing k' with higher cooling rate indicates a faster nucleation and growth rate, however, these values decrease upon addition of graphene particles which suggests that increasing concentration graphene particles within the polymer matrix can hinder the nucleation and growth rate. The same is observed in the $t_{1/2}$ values, where these values tend to increase up to a loading of 2.5%, suggesting a slow crystallisation rate. A similar decrease in the value of k' was also reported by Zhang et al for nylon6/graphene composites [145]. Such decreasing k' on the

addition of graphene was attributed to a negative effect on crystallisation mainly because graphene particles restrict migration and diffusion of the polymer chains to the surface of the nucleus (slow crystallisation process–longer time). The Avrami model was devised to understand the crystallisation kinetics under isothermal conditions, where the thermal response time is less when compared to the rate of the process.

Table 5.5 Ozawa parameters obtained from the slope and intercept of the Ozawa plot for porous Pebax graphene composites under non-isothermal conditions

Sample Type	T (°C)	M	Log k*	R^2
PebaxSCF	120	-0.90	2.14	0.898
	125	-2.83	4.44	0.764
	128	-2.06	2.91	0.891
	130	-3.98	4.90	0.853
	133	-3.78	3.77	1.000
PGSCF 0.25	120	-0.54	1.94	0.930
	125	-0.69	1.83	0.981
	128	-1.10	2.18	0.905
	130	-1.76	2.92	0.838
	133	-3.87	5.38	0.805
PGSCF 0.5	120	-0.52	1.97	0.882
	125	-0.55	1.66	0.974
	128	-0.71	1.67	0.979
	130	-0.97	1.87	0.937
	133	-1.80	2.67	0.877
	136	-3.13	3.82	0.915
PGSCF 1	120	-0.40	1.58	0.880
	125	-0.48	1.41	0.970
	128	-0.66	1.48	0.969
	130	-0.96	1.73	0.922
	133	-1.82	2.52	0.870
	136	-3.14	3.74	0.915
PGSCF 2.5	120	-0.39	1.50	0.925
	125	-0.48	1.32	0.981
	128	-0.64	1.34	0.973
	130	-0.86	1.47	0.944
	133	-1.40	1.86	0.918
	136	-2.09	2.17	0.954

Therefore, the modified Avrami analysis for non-isothermal conditions was used to understand the crystallisation, where the process begins even before the system reaches the desired the crystallisation temperature [109, 149]. Hence, Avrami can be considered to provide a good insight into the nature of the nucleation and growth process. However, in order to evaluate results from Avrami, the method extended by Ozawa will be discussed, which has been

specifically designed to model non-isothermal crystallisation kinetics [111, 150]. The Avrami equation was extended by Ozawa by modelling the change in the degree of crystallinity (X(T)) as a function of varying cooling rate. The value m depends on the dimensions of the crystal growth and K(T) is a function of cooling rate φ which indicates how fast crystallisation occurs. The heating reaction function Log k* tends to increase with temperature as the nucleation and growth rate is increased for all sample types. In addition, the Ozawa exponent, m, decreases with an increase in temperature. It is evident from the Ozawa plot that a perfect linear fit cannot be achieved, due to the influence of secondary crystallisation (R^2 <<1) (see Table 5.5). This suggests that a mean m and k* value are difficult to achieve and thus the Ozawa method cannot be used to describe the crystallisation kinetics of Pebax graphene composites under non-isothermal conditions. Therefore, a combined Avrami and Ozawa model is used in the next section to describe the kinetics of non-isothermal crystallisation of Pebax graphene composites.

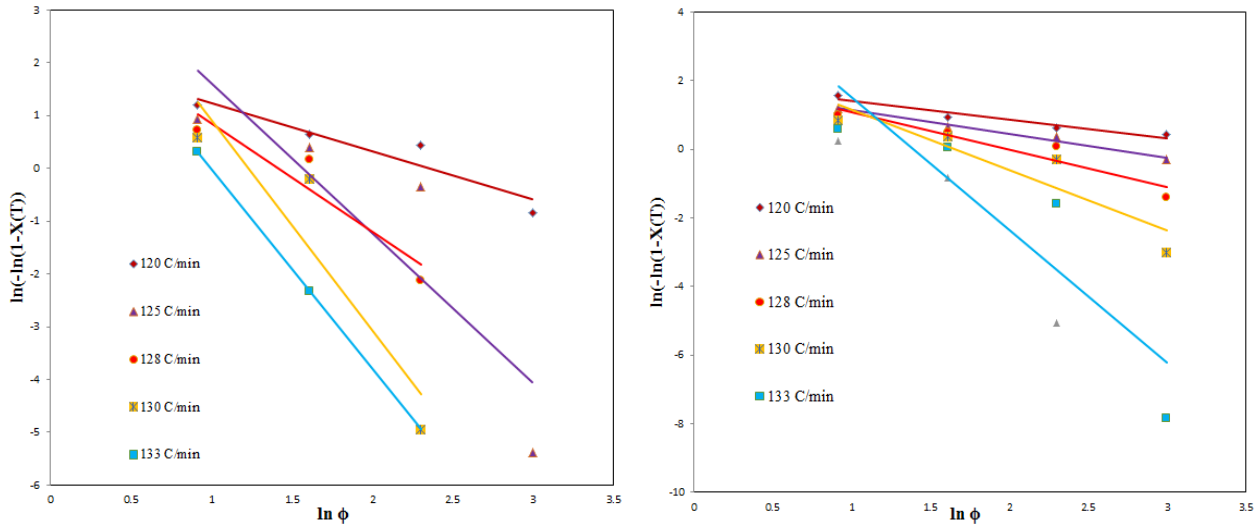

a. PebaxSCF b. PebaxSCF 0.5%

Figure 5.9 Ozawa plot for porous Pebax graphene composites under non-isothermal conditions

Mo et al [111] reported the combined Avrami and Ozawa equation to completely describe the kinetics of non-isothermal crystallisation by plotting the log ϕ vs. log t at a specific value of X(t). The values b and F(T) can be obtained from the slope and intercept of the plot (Figure 5.9). It is evident from the plots and the Table 5.6 that there is a good match between the Mo analysis [111] and the experimental data for all the sample types. In addition, the values of R^2 for each of the plots were nearing unity.

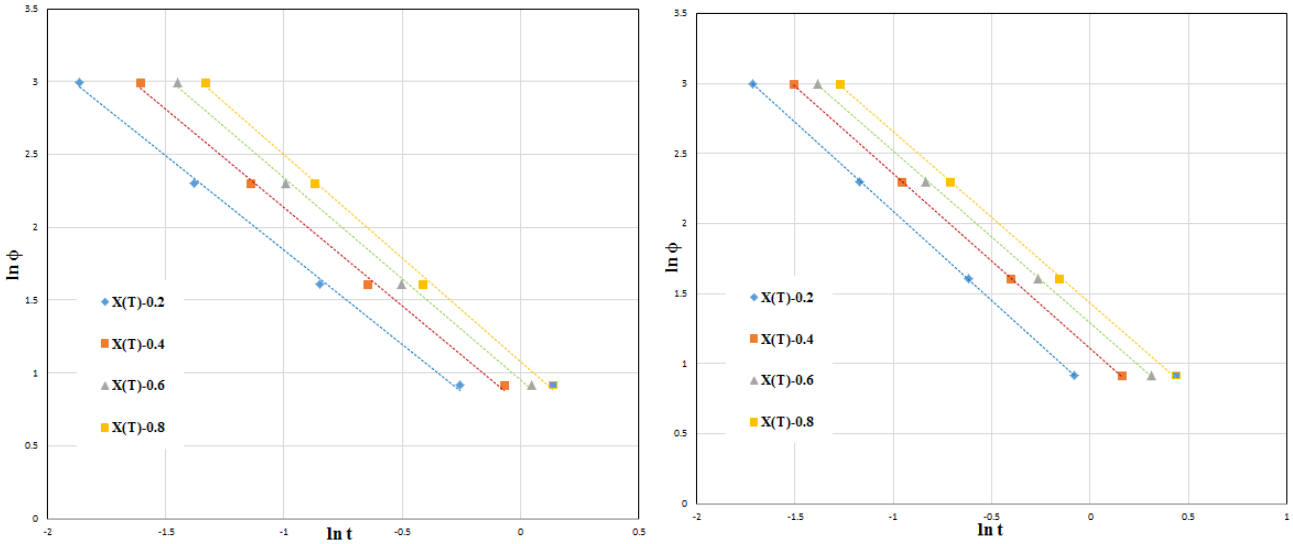

a. Pebax SCF b. PG SCF 0.25%

Figure 5.10 Combined Mo plot for porous Pebax graphene composites under non-isothermal conditions

Figure 5.10 shows lower cooling rates which require a longer time (spreading of the ln t values) for crystallisation, while faster cooling rates require a shorter time for crystallisation (narrow ln t values). This spreading and narrowing of time for crystallisation with increasing cooling rate indicates that the value b is strongly dependent on the cooling rate. On the other hand, the value ln F(T) increases with the relative degree of crystallinity, indicating that longer crystallisation time is required at a higher cooling rate in order to reach unity degree of crystallinity. Huang and Gu et al [151] reported that the value of F(T) can be considered to indicate the polymer crystallisation rate, where lower values suggest a faster crystallisation rate and higher values suggest a slower crystallisation rate. The F(T) values gradually increase with the addition of graphene up to 2.5% meaning that the crystallisation rate decreases upon the addition of graphene (slower crystallisation). A similar trend was also observed with isothermal crystallisation kinetics, with the addition of 2.5% graphene it took a long time to crystallise due to probable agglomeration. All the Pebax graphene composites had a larger ln F(T) when compared to the virgin Pebax for all the relative degree of crystallinity values.

The higher F(T) means a higher cooling rate is necessary within the unit crystallisation time, indicating complex crystallisation behaviour. This suggests that the addition of graphene has lowered the rate of crystallisation compared to virgin Pebax (agreement with the Avrami model and observation made on broader Tc peaks).

Table 5.6 Mo parameters obtained from the slope and intercept of the Mo plot for porous Pebax graphene composites under non-isothermal conditions

Sample Type	X(T)	b	Mean 'n'	ln F(T)	F(T)	R^2
Pebax SCF	0.2	1.29	3.30	0.55	1.73	0.998
	0.4	1.35		0.78	2.18	0.997
	0.6	1.38		0.94	2.55	0.998
	0.8	1.41		1.07	2.91	0.997
PGSCF 0.25	0.2	1.26	3.29	0.81	2.24	1.000
	0.4	1.24		1.11	3.03	1.000
	0.6	1.22		1.29	3.63	0.999
	0.8	1.21		1.43	4.17	0.999
PGSCF 0.5	0.2	1.48	3.47	0.87	2.38	0.997
	0.4	1.47		1.16	3.18	0.999
	0.6	1.42		1.41	4.09	0.999
	0.8	1.38		1.57	4.80	0.997
PG SCF 1	0.2	1.26	3.67	1.20	3.32	0.997
	0.4	1.25		1.43	4.17	0.999
	0.6	1.24		1.60	4.95	0.997
	0.8	1.22		1.73	5.64	0.999
PG SCF 2.5	0.2	1.21	3.64	1.57	4.80	0.991
	0.4	1.19		1.83	6.23	0.998
	0.6	1.20		1.96	7.09	0.997
	0.8	1.19		2.09	8.08	0.998

M.C Kuo et al reported that the addition of nano-sized particles usually results in enhancing the crystallisation rate as each particle acts as a nucleating site. However, in certain cases (as loading is increased), the particles also affect the crystallisation rate, hindering the growth rate [148]. Therefore, as in the case here, the Tc shifts to higher temperatures upon addition of graphene, suggesting increased nucleating sites, but the crystallisation rate from k and F(T) reduces, indicating slower growth rate. It was found that the b value, which is the ratio of n/m, tends to increase upon the addition of graphene for PG 0.5%, suggesting that higher graphene concentration induces a larger number of heterogeneous nucleation sites and limits crystal growth, producing crystals of smaller size. A clear decrease in the n value can be observed for 0.5 (refer to Table 5.4). Considering the influence of various cooling rates under the non-isothermal crystallisation process, the Kissinger activation energy for non-isothermal conditions was used to calculate the activation energy (refer to 3.4.3.2).

Table 5.7 Activation energy obtained from the slope of Kissinger's plot for porous Pebax graphene composites under non-isothermal conditions

Sample Type	Kissinger Activation Energy (KJ/mol)
Pebax SCF	190.48
PG SCF 0.25%	249.25
PG SCF 0.5%	270.25
PG SCF 1%	273.34
PG SCF 2.5%	288.31

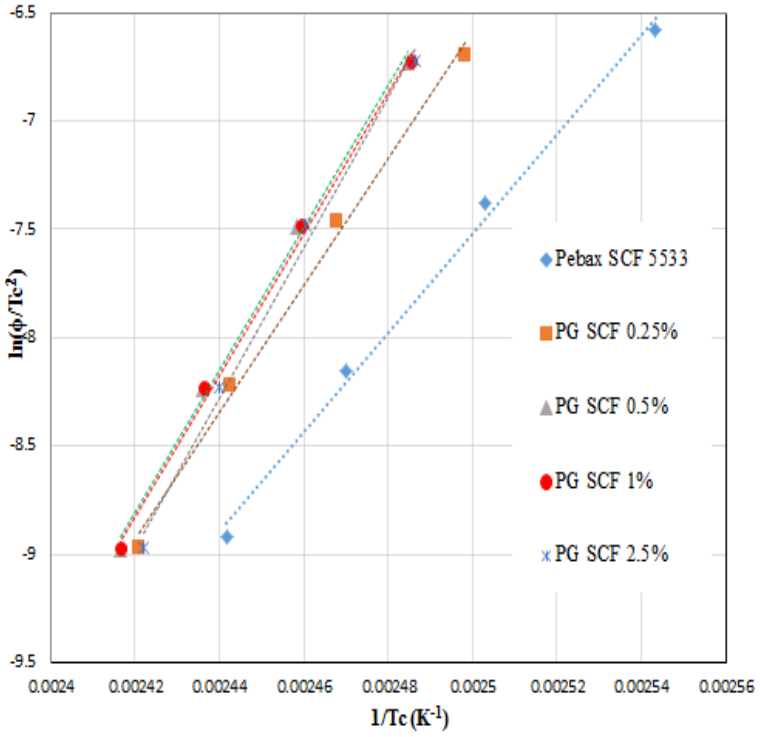

Figure 5.11 Kissinger's plot for porous Pebax graphene composites under non-isothermal conditions

The crystallisation activation energy can be determined from the slope of the plot of ln (heating rate/Tc^2) versus 1/Tc (Figure 5.11 and Table 5.7)). It can be observed that the activation energy increases upon addition of graphene particles. The activation energy was found to be stable for 0.5% and 1% graphene loading, but an increasing trend was observed. Such an increase in activation energy can be attributed to the agglomeration of the graphene particles which hinders the transportation of the molecular segment to the crystalline phase and formation of the nuclei size.

5.2.3 Dynamic Mechanical Analysis of Porous Pebax Graphene Composites

Figure 5.12 and Table 5.8 represents the storage modulus graph in MPa at various temperatures and average storage modulus measured at 30 °C. Figure 5.12 shows that the storage modulus gradually increases from 77 MPa for pure SCF Pebax to 125 MPa upon the addition of graphene filler up to a loading of 1%. However, the storage modulus drops to 108 MPa for 2.5% loading. The loss modulus also follows a similar pattern where the highest value is reflected by a loading of 1% graphene

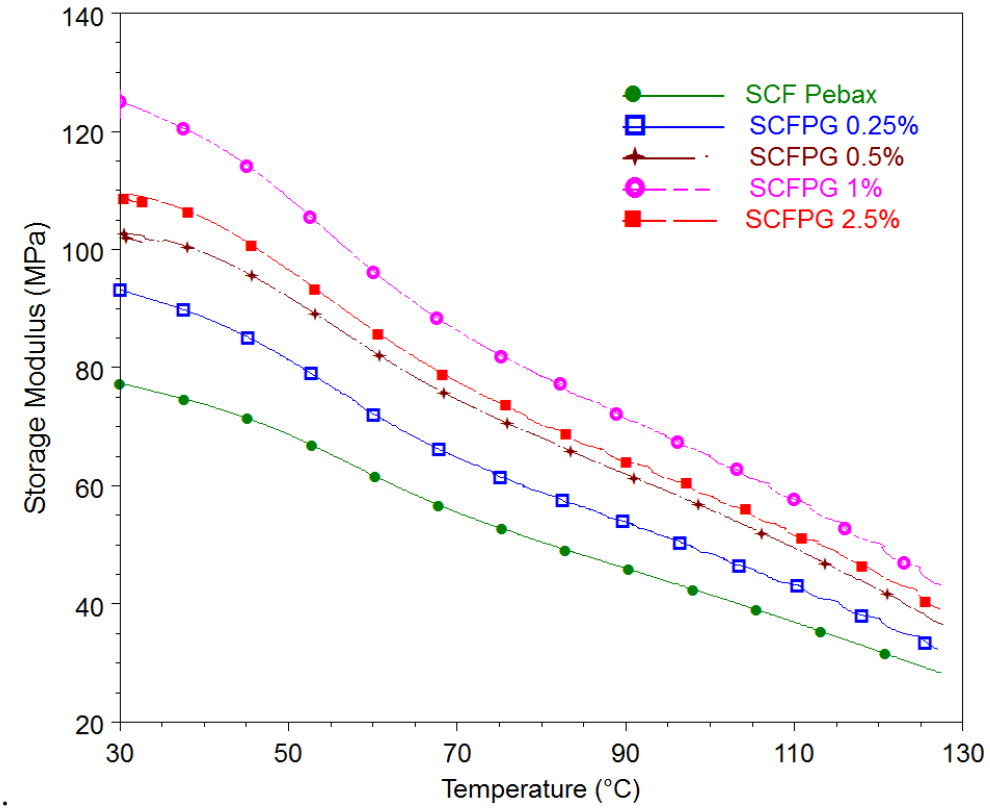

Figure 5.12 Storage modulus for porous Pebax graphene composites

The gradual increase in storage modulus up to 1% gives important information on the effect of concentration of fillers on the mobility of polymers. Similar increases in the rate of crystallisation and activation energy were observed up to 1% graphene loading due to heterogeneous nucleation and restriction imposed by graphene particles during the growth which mainly arises from Pebax-graphene interactions. This significant increase in storage modulus usually occurs due to the interaction between the polymer chain and the graphene particles, which further restricts the free movement of polymer chains resulting in enhancement of the stiffness of the composites.

Table 5.8 Storage, Loss and Tan delta measured at 30 °C for porous Pebax graphene composites under non-isothermal conditions

Sample type	With SCF		
	Storage modulus	Loss Modulus	Tan Delta
	MPa	MPa	NA 10^{-3}
Pebax	77.28 ±6.8	2.77	35.8
SCFPG 0.25%	93.03 ±4.3	3.02	32.4
SCFPG 0.5%	105.10 ±5.2	3.37	32.0
SCFPG 1%	125.30 ±6.6	4.11	32.8
SCFPG 2.5%	108.51 ±7.6	3.93	36.2

However, as the filler concentration reaches 2.5%, the storage modulus decreases, suggesting poor interaction with the polymer chain due to agglomeration of the graphene particles. There are two likely causes for the significant drop observed on increasing the graphene filler concentration. One is the availability of polymer interactive sites and the second probable reason can be attributed to the change in the state of filler particles from being a single layer to agglomerated graphite.

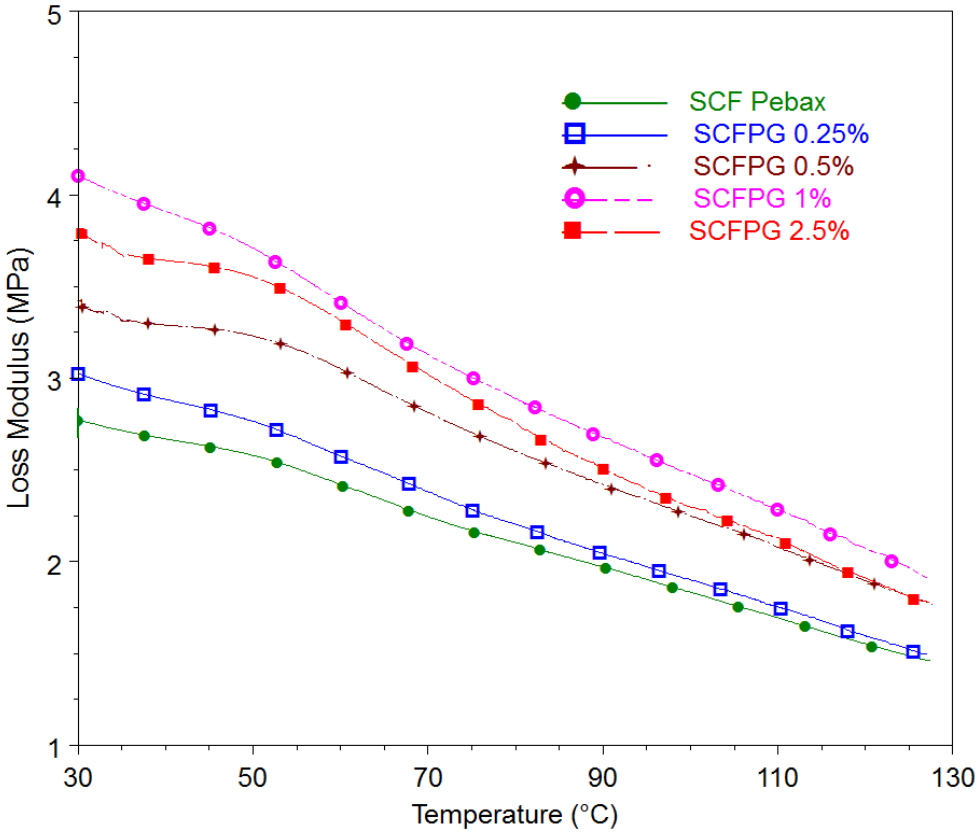

Figure 5.13 Loss modulus for porous Pebax graphene composites

The restriction caused due to graphene polymer chain interaction can be validated by the loss modulus curves, which follow the trends of storage modulus. The loss moduli (Figure 5.13) are highest for graphene concentration of 1%, suggesting an increased viscous nature of the polymer matrix. The evidence of lowering k from the crystallisation study (both isothermal and non-isothermal conditions) confirms possible agglomeration (not evenly dispersed) of graphene particles. Figure 5.14 shows the tan delta curves representing the damping factor/loss factor of porous Pebax graphene-polymer composites. The tan delta curve and the value at 30 °C decreased up to 1% graphene loading, indicating low loss which occurs because of the relatively good interaction between the polymer chain and the filler particles. The loss factor increases with loading concentration of 2.5%, suggesting uneven dispersion or agglomeration of graphene particles. One of the main observations from the tan delta curve is the appearance of the significant wide peak which is spread over the temperature range of 50 °C - 90 °C, which is not clearly visible in the SCF Pebax curve. Similar peaks are also evident in the DSC section around the same range of temperatures. Therefore, the finding of this study suggests that the appearance of a peak upon addition of graphene particles may be due to an interaction between the nylon block and the graphene particles. A similar point has also been discussed in Chapter 4 regarding the actual Tg of the nylon block appearing at around 60 °C when processed with $scCO_2$.

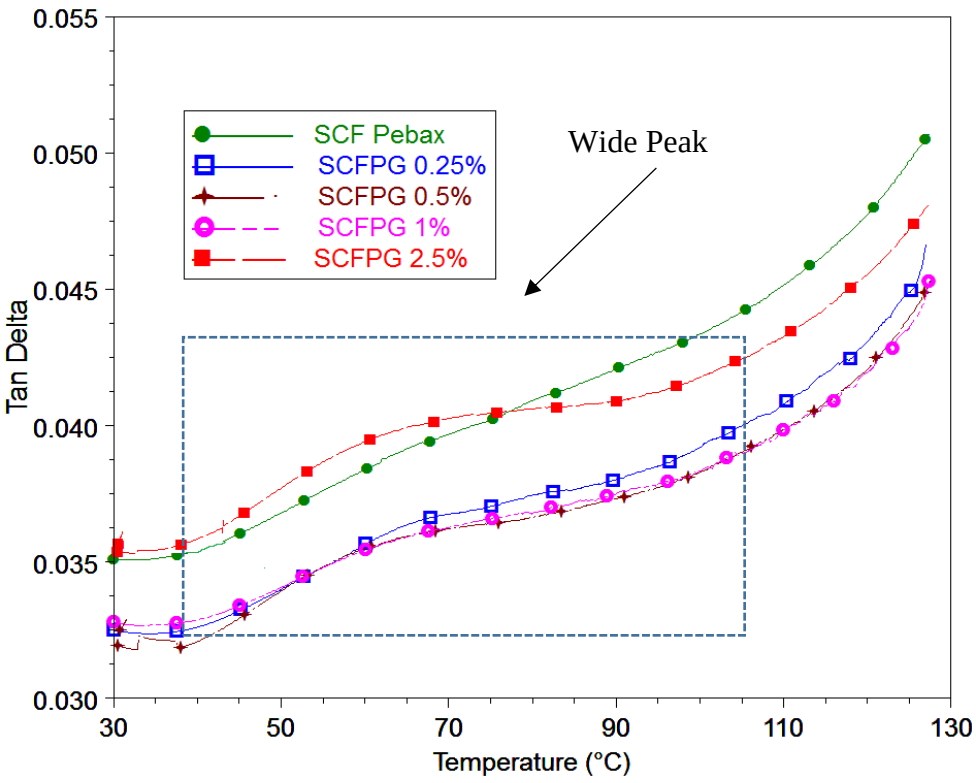

Figure 5.14 Tan Delta for porous Pebax graphene composites

Polarised Optical Microscope of Porous Pebax Graphene Composites

Figure 5.15 presents the 20x magnification images from polarised optical microscopy representing the effect of increased graphene concentration on the extrudates. It is clear that the increase in graphene concentration from 0.5% to 2.5% results in a larger cell structure due to cell coalescence.

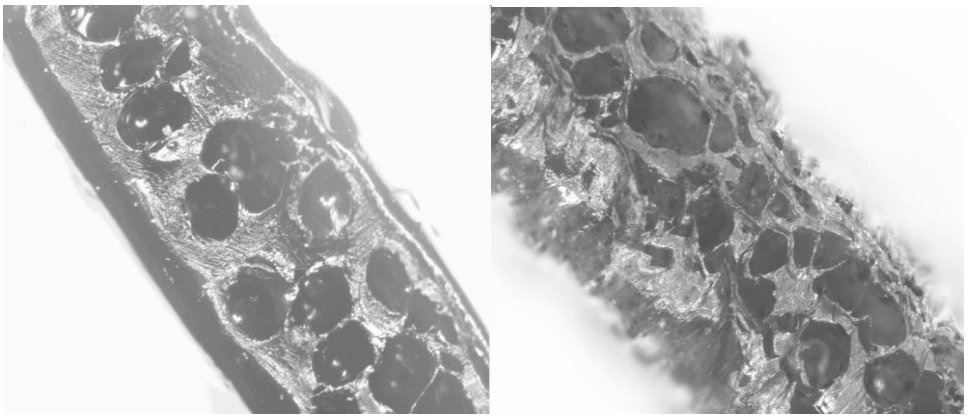

a. PG SCF 0.5% b PG SCF 2.5%

Figure 5.15 Polarised optical microscope images of a. PG SCF 0.5% and b PG SCF 2.5%

Such an increase in cell coalescence is usually the result of increasing $scCO_2$ pressure which is kept constant here at 1200 psi and the only variant is increased graphene concentration. This suggests that increased graphene concentration may have initiated the formation of the viscous plug within the extruder due to exfoliation of graphene. Such changes in the cell structure can be the reason behind the diminished mechanical properties at 2.5% loading.

5.2.4 Fourier Transform Infrared Spectroscopy of Porous Pebax Graphene Composite

The peaks at 1465 cm^{-1} and 1365 cm^{-1} represent CH_2 vibration and C-N stretching of the amide group, respectively. The soft PTMO blocks exhibit stretching vibration of the C-O ether peak at 1100 cm^{-1}. No significant changes were observed with the use of $scCO_2$ Pebax graphene composite (see Figure 5.16). Additional, opportunity to enhance the sensitivity of FTIR by using a focal plane array detector through FTIR imaging approach is recommended.

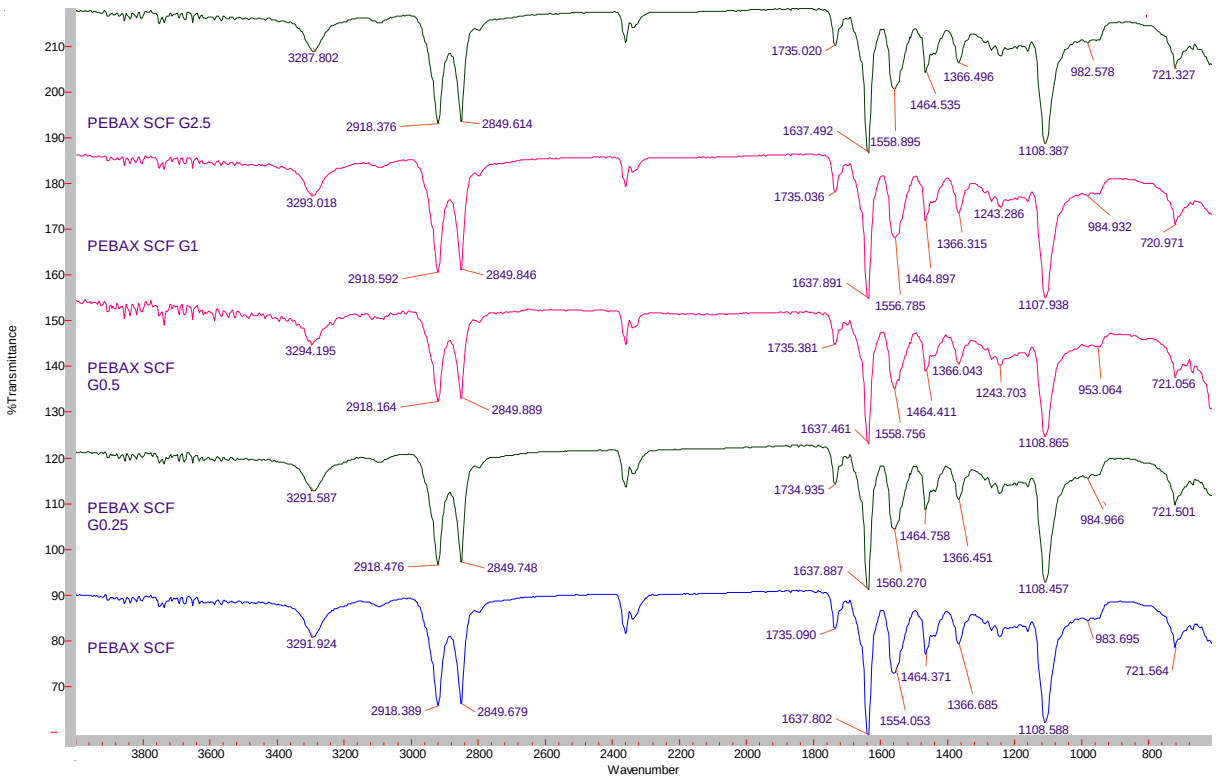

Figure 5.16 Transmittance IR spectroscopy of porous Pebax graphene composites

5.2.5 Tensile Testing of Porous Pebax Graphene Composites

Figure 5.17 presents the stress vs. strain curve for porous Pebax graphene composites. A clear enhancement of the modulus of resilience and modulus of toughness can be observed throughout upon addition of graphene up to 1%. However, as the loading was increased to 2.5%, the modulus of resilience and the toughness reduced. A similar effect has been observed throughout this section on the thermal and dynamic mechanical analysis. Thermal analysis using isothermal and non-isothermal crystallisation kinetics suggests such decreases in thermal and mechanical properties occur due to uneven dispersion or agglomeration of the graphene particles. Another possible reason could be that the graphene particles lose their intrinsic properties upon higher loading as the graphene particles tend to agglomerate or even restack easily due to Van der Waals forces to form graphite.

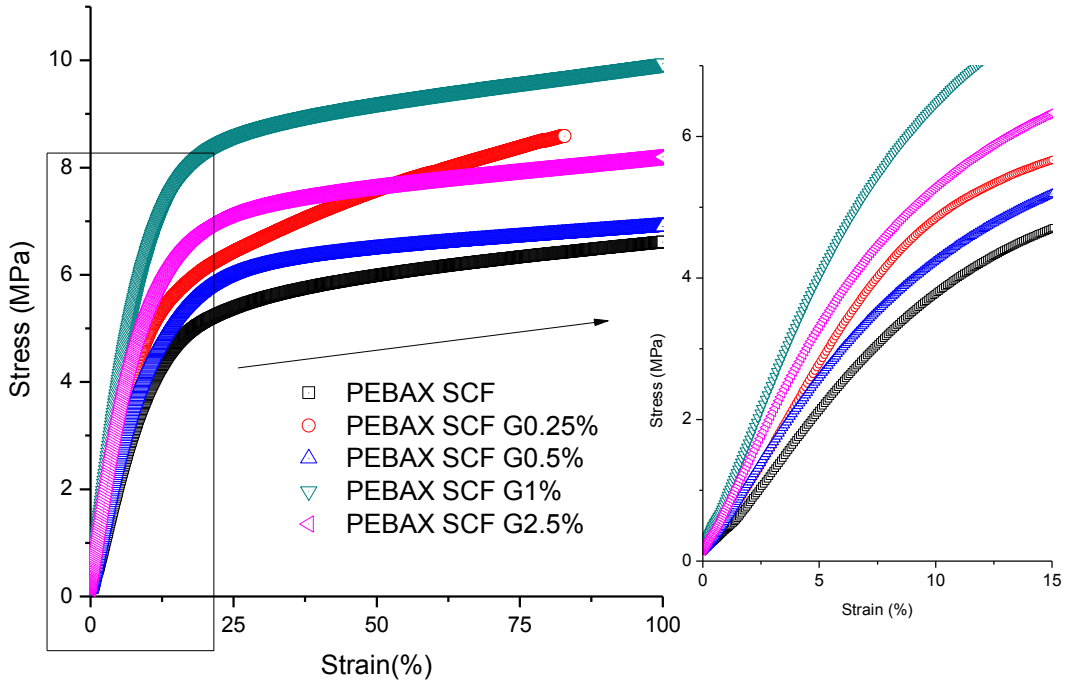

Figure 5.17 Stress vs. strain curves for porous Pebax graphene composites

5.3 Keypoints for Pebax Graphene Composites with $scCO_2$

The aim of this section of Chapter 5 was to investigate the effects of incorporating graphene-based filler materials when processed using $scCO_2$ extrusion. The following are the key observations:

- A peak at 80 °C attributed to the glass transition temperature of the nylon block is clearly visible due to the restriction imposed by graphene particles upon polymer-additive interaction, which otherwise is not as clearly evident on the virgin Pebax thermogram. This peak flattens with a filler concentration of 2.5%, suggesting poor interaction and agglomeration.

- The value of the Avrami exponent n is between 2 and 3 for isothermal conditions indicating a complex two-dimensional axialitic crystallisation process, while n ranges from 3 to 4 for non-isothermal conditions indicating a spherulitic structure. The crystallisation rate k increases up to 1% suggesting that the graphene particle loading up to 1% acts as nucleation sites. However, k decreases for 2.5% loading due to probable agglomeration of graphene particles. The Arrhenius activation energy (ΔE) decreased for 0.25%, further indicating that graphene acts as nucleation sites, while ΔE increased up to

2.5% suggesting a restriction induced by graphene polymer chain interaction due to agglomeration.

- Under non-isothermal conditions the Tc peak shifts to higher temperatures suggesting the dominance of heterogeneous nucleation. However, the value of k decreased upon the addition of graphene compared to virgin PebaxSCF. This suggests that although the graphene particles acted as nucleation sites, they might have restricted the nucleation growth, thus the clear decrease in crystallisation rate.
- The crystallisation rate F(T) value obtained from the combined Avrami-Ozawa model decreases upon addition of graphene up to 2.5% loading indicating slow crystallisation rates. The increase in Kissinger's activation energy (ΔE) upon addition of graphene can be attributed to the agglomeration of the graphene particles which hinder the transportation of the molecular segment to crystallite phase and formation of the nuclei size.
- The storage modulus and loss modulus increase while the tan delta decreases up to 1% graphene loading, similar to the results obtained from the crystallisation kinetics, suggesting good polymer graphene interaction. However, with 2.5% loading, the storage modulus and the loss modulus decrease due to agglomeration; a similar decrease in the crystallisation kinetic parameters was also noted for 2.5% loading.
- A clear enhancement of the modulus of resilience and modulus of toughness can be observed throughout on addition of graphene up to 1%. However, as the loading was increased to 2.5%, the modulus of resilience and the toughness reduced.
- No significant changes were observed in the IR spectroscopy with the use of scCO_2 Pebax graphene composite.
- The outcomes from the crystallisation kinetics and the dynamic mechanical thermal analysis show that the Pebax graphene composites at lower graphene concentrations (up to 1%), results in enhanced the properties of the material, without agglomeration.

5.4 Section 2: Supercritical Fluid Assisted Porous Pebax Graphene Oxide Composites

5.4.1 Thermal Gravimetric Analysis of Porous Pebax GO Composites

Figure 5.18 shows the thermogravimetric analysis (TGA) thermogram of $scCO_2$ assisted extrusion of porous Pebax GO composites. As observed for the graphene composite samples, no major changes can be observed from the derivative of the weight change peak, which shows the maximum degradation temperature. The maximum degradation temperature remains almost constant at 460 °C for all the GO filler levels. With increasing GO percentage, the total weight percentage thermograms almost reach zero. Such effects can be attributed to GO degradation.

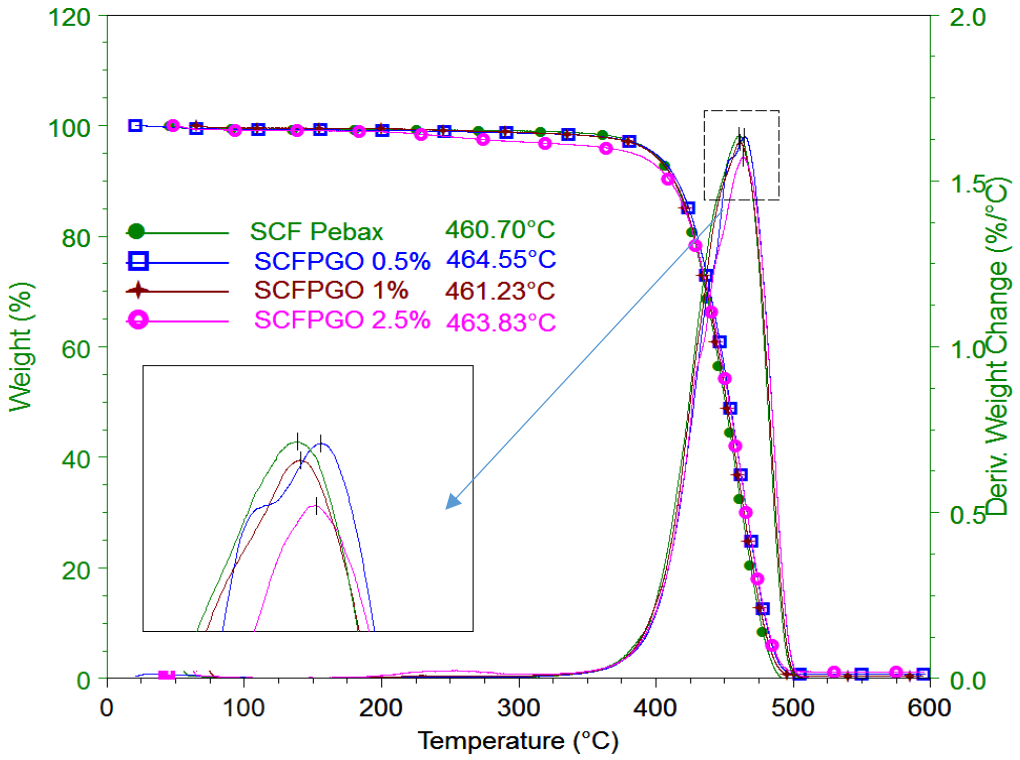

Figure 5.18 TGA thermogram for porous Pebax GO composites

Since GO particles reach about 70% degradation at a much lower temperature (refer to Section 7.4.2), one of the possibilities could be that the GO particles may be degraded at a lower temperature, thus the derivative weight percentage thermogram reaches zero. The zoomed portion of the graph representing the loss in weight decreases with an increase in the GO filler concentration suggesting that the GO interaction restricts the easy movement of the polymer chains.

5.4.2 Differential Scanning Calorimetry of Porous Pebax GO Composites

Figure 5.19 presents the heat flow thermogram of the porous Pebax GO composites. The melting point of Pebax remains constant for the entire Pebax GO matrix. However, an endothermic peak can be seen at 80 °C for virgin SCF Pebax (zoomed section), while the peak can be seen to shift to a lower temperature of around 50 °C. As discussed in Section 4.2, this peak appears to be due to the vibration or movement of the amorphous part of Nylon-12. Such a shift in the Tg from 80 °C to 50 °C upon addition of $scCO_2$ suggests that the oxygen-rich GO particles interact with Pebax.

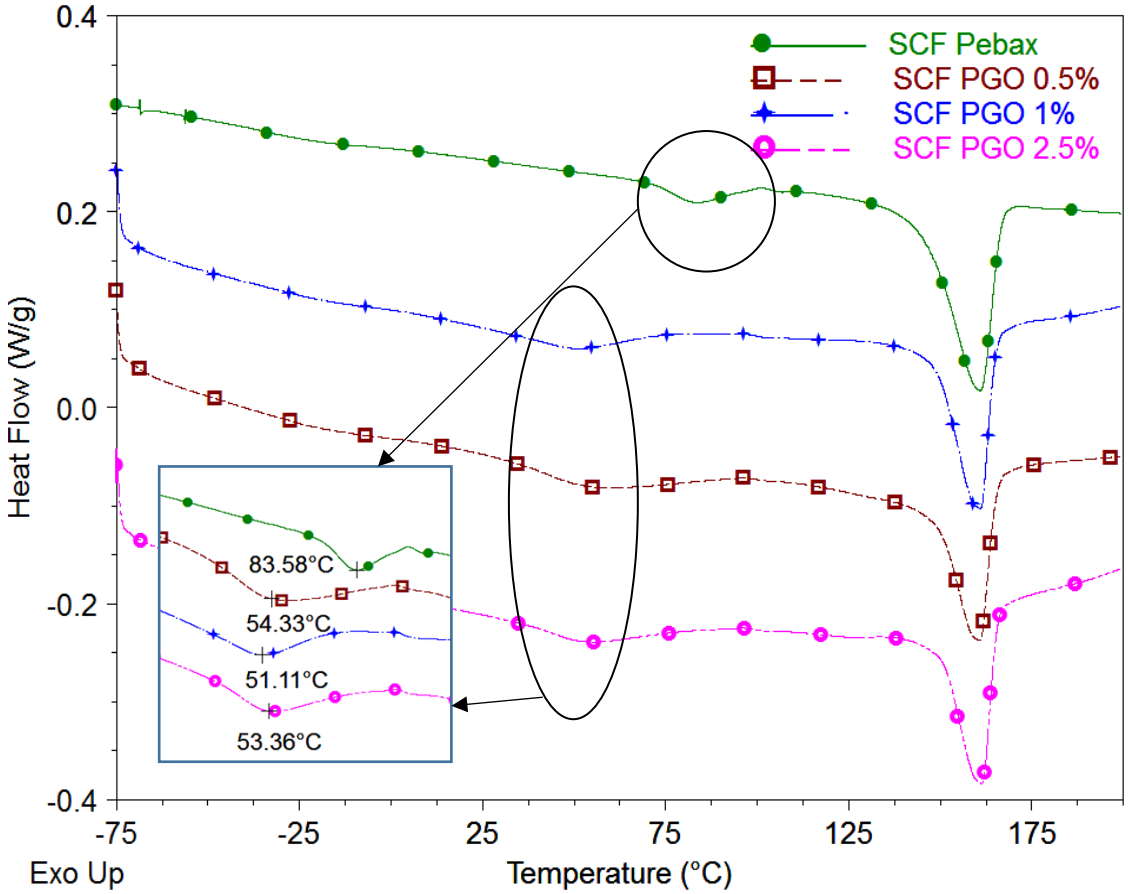

Figure 5.19 Heat flow thermogram of porous Pebax GO composites

Figure 5.20 shows the crystallisation peaks for all the Pebax GO composites. The crystallisation peak of virgin SCF Pebax can be observed at 136 °C. No shift in relative heat flow magnitude was observed with the addition of GO up to 2.5% indicating that GO particles are more compatible or act as one with the polymer Pebax.

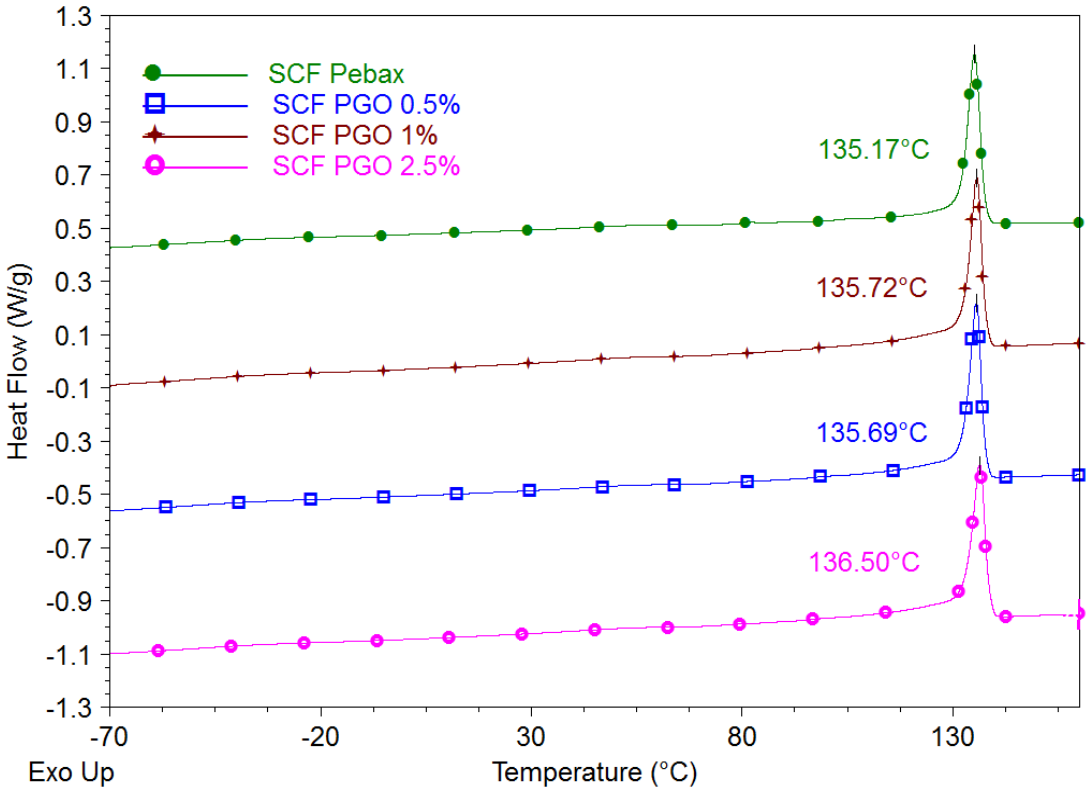

Figure 5.20 Cooling cycles for porous Pebax GO composites

5.4.3 Isothermal Crystallisation Kinetics of Porous Pebax GO Composites

The Avrami equation was used to describe the crystallisation kinetics of semi-crystalline polymers under isothermal conditions (refer to Section 3). The parameters n and k can be obtained from the slope and the intercept of the Avrami plot of log [-ln(1-Xt)] vs. log t. The values of Avrami exponents, calculated and practical obtained values of $t_{1/2}$ are listed in Table 5.9. The value of n, describing the dimension of the crystallite remains between 2 and 3, suggesting complex branched fibrillar morphology. No significant changes can be observed with respect to n, even with the addition of GO up to 2.5%. The value of k, representing the rate of crystallisation, tends to decrease with an increase in the isothermal crystallisation temperature for all the sample type. However, the parameter k tends to increase up to 1% GO loading (faster crystallisation), and remains constant for 2.5% loading (refer to the highlighted section in the Table 5.9, for example, Tc @ 143˚C having k = 0.11 for virgin PebaxSCF, Tc @ 143˚C having k =0.36 for PGOSCF 1% and Tc @ 143˚C having k =0.36 for PGOSCF 2.5%). This suggests that loadings of 1% and above result in agglomeration of particles, thereby restricting the actual nucleation and growth of the crystal. The k values for GO loading does not increase as fast compared to graphene composites (k much higher in case of graphene,for example: Tc @ 143˚C

having k =1.66 for PGSCF 1% (graphene), while k value for PGOSCF 1% (GO) is 0.36 @ Tc =143 ˚C), indicating slower crystallisation rate with GO when compared to graphene. This also suggests that GO particles are more compatible/have superior interaction with Pebax compared to graphene. The $t_{1/2}$ value increases with increasing T_c, however, the values tend to decrease upon addition of GO similar to k, suggesting a lower time to crystallise to 50%, indicating faster crystallisation than the virgin SCF Pebax.

Table 5.9 Avrami parameters for porous Pebax GO composites under isothermal conditions

Sample Type	**Tm (˚C)**	**n**	**Average N**	**Log k**	**K**	**$t_{1/2}$* (min)**	**$t_{1/2}$ Graph (min)**	**G (min^{-1})**	**R^2**
	140	2.72		-0.125	0.74	0.97	0.93	1.07	1.000
	141	2.83		-0.420	0.38	1.22	1.21	0.82	1.000
PebaxSCF	142	2.84	2.84	-0.655	0.22	1.49	1.48	0.67	1.000
	143	**2.80**		**-0.922**	**0.11**	**1.87**	**1.86**	**0.53**	**1.000**
	144	**3.04**		**-1.480**	**0.03**	**2.70**	**2.68**	**0.37**	**0.999**
	142	2.76		-0.343	0.45	1.16	1.15	0.86	1.000
	143	**2.73**		**-0.586**	**0.25**	**1.43**	**1.41**	**0.70**	**1.000**
PGOSCF 0.5	**144**	**2.84**	2.85	**-0.897**	**0.12**	**1.81**	**1.83**	**0.54**	**1.000**
	145	3.07		-1.35	0.04	2.44	2.45	0.40	0.999
	146	2.85		-1.59	0.02	3.17	3.16	0.31	0.999
	142	2.70		-0.156	0.69	0.99	0.98	1.02	1.000
	143	**2.80**		**-0.437**	**0.36**	**1.25**	**1.25**	**0.80**	**1.000**
PGOSCF 1	**144**	**2.83**	2.83	**-0.735**	**0.18**	**1.59**	**1.61**	**0.62**	**1.000**
	145	3.00		-1.186	0.06	2.19	2.21	0.45	1.000
	146	2.85		-1.444	0.03	2.82	2.73	0.36	0.999
	143	**2.70**		**-0.432**	**0.36**	**1.26**	**1.25**	**0.80**	**1.000**
	144	**2.83**		**-0.755**	**0.17**	**1.62**	**1.63**	**0.61**	**1.000**
PGOSCF 2.5	145	2.98	2.75	-1.183	0.06	2.20	2.21	0.45	1.000
	146	2.80		-1.496	0.03	3.00	2.99	0.33	0.999
	147	2.44		-1.606	0.02	3.91	3.80	0.26	0.999

The value of $G=1/t_{1/2}$ can be used to describe the crystallisation rate and is plotted in Figure 5.21 as a function of isothermal crystallisation temperature. It can be clearly seen that the GO particles act as nucleating agents thereby enhancing the crystallisation rate due to even dispersion. The crystallisation rate at various temperatures for 1% and 2.5% loading remains constant, suggesting heterogeneous nucleation for 0.5% and agglomeration or uneven dispersion of 1% and 2.5% loading.

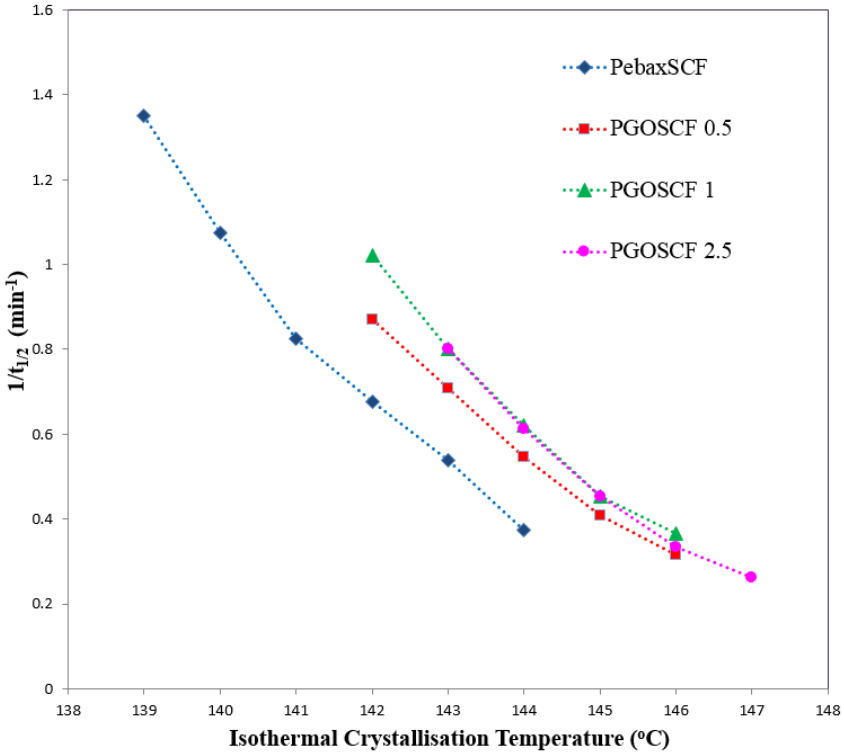

Figure 5.21 Crystallisation rate vs. crystallisation temperature plot for porous Pebax GO composites

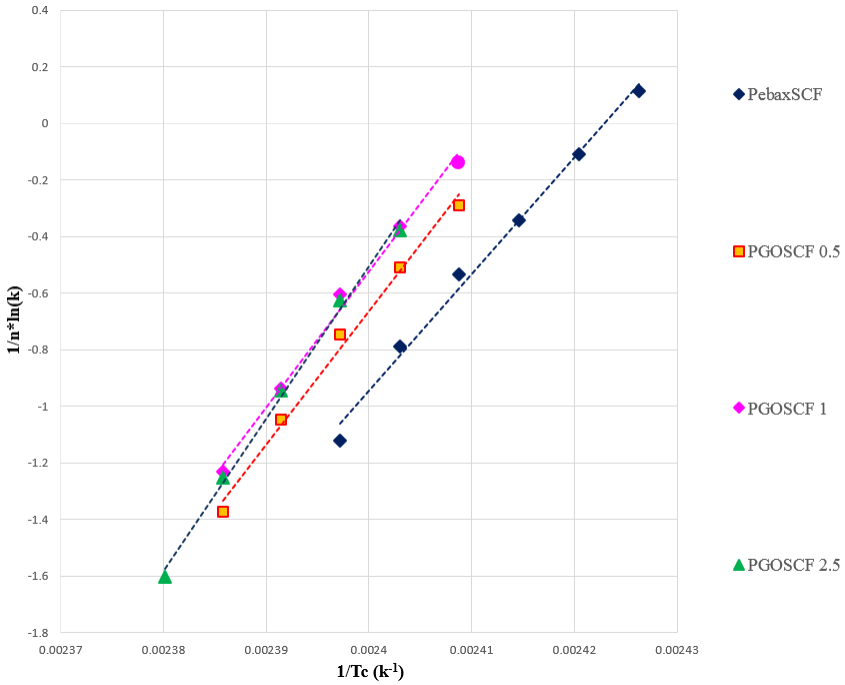

Figure 5.22 Arrhenius activation energy plot for porous Pebax GO composites

The crystallisation rate parameter was described by an Arrhenius type equation (refer to section 3.4.3.1) in order to determine the activation energy under isothermal conditions. The slope of the plot ln (k)*1/n vs. 1/Tc as shown in Figure 5.22 determines the ΔE/R, where the activation energy was calculated and is tabulated in Table 5.10.

Table 5.10 Arrhenius Activation Energy for porous Pebax GO composites under isothermal conditions

Samples	**Arrhenius Activation Energy (ΔE) (KJ/mol)**
PebaxSCF	-342.869
PGOSCF 0.5%	-391.581
PGOSCF 1%	-399.047
PGOSCF 2.5%	-447.077

As seen in Table 5.10, the ΔE value increases with GO loading. However, the activation energy is the highest at 2.5%. This shows that the GO particles in the Pebax matrix restrict the easy movement of the polymer chains in order to process through the crystallisation steps of nucleation and crystal growth. Kuo et al [148] suggested that the activation energy consists of two parts; one is energy required to nucleate and second is the energy required to grow crystallites. If the particles act as nucleating sites as evident from the Avrami k parameter, the activation energy must be reduced. However, in our case, the activation energy gradually increases with increase in the GO loading. This suggests that although a heterogeneous nucleation is evident at lower GO loading, the GO interaction with Pebax chain might hinder the transportation process, thereby increasing the crystallisation free energy barrier.

5.4.4 Non-Isothermal Crystallisation Kinetics of Porous Pebax GO Composites

The non-isothermal crystallisation kinetics of Pebax GO composites with $scCO_2$ was studied under various cooling rates. Figure 5.23 shows the crystallisation thermograms at various heating rates with respect to temperature and time. Important thermal parameters were recorded and tabulated in Table 5.11, from the thermograms for Pebax GO composite at various non-isothermal conditions. It can be clearly seen that the crystallisation Tc_{on}, T_c and Tc_{off} shifts to lower temperatures and becomes broader with an increase in the cooling rate from 2.5 °C/min to 20 °C/min. Such crystallisation temperatures usually shift to a higher value indicating dominant heterogeneous nucleation, which otherwise will shift the Tc to lower temperatures if homogenous nucleation results.

Table 5.11 Tc, Tc_{on}, Tc_{off} parameters obtained from the heat flow thermographs for porous Pebax GO composites under non-isothermal conditions

Sample Type	Cooling Rate (° C/min)	Tc_{on} (° C)	Tc_{off} (°C)	Tc (° C)	ΔHc (J/g)	Xc (%)
PebaxSCF	2.5	139.70	107.71	136.40	37.20	33.38
	5	135.67	92.80	131.68	38.97	30.58
	10	131.71	85.41	126.38	36.70	32.53
	20	126.68	84.44	120.04	33.68	32.12
PGOSCF 0.5%	2.5	142.47	112.31	138.46	36.45	36.56
	5	139.09	93.82	135.41	40.42	28.03
	10	136.86	93.53	131.81	38.30	29.16
	20	132.35	85.41	127.62	37.34	27.26
PGOSCF 1%	2.5	142.45	105.22	138.53	37.61	34.24
	5	139.88	112.47	135.55	33.34	32.63
	10	136.51	95.33	131.99	36.33	34.27
	20	132.99	87.24	127.54	34.66	27.40
PGOSCF 2.5%	2.5	142.76	116.97	138.80	33.33	36.09
	5	139.47	105.76	135.67	34.99	30.58
	10	136.24	95.91	132.00	35.39	27.83
	20	132.64	97.28	127.44	33.62	27.75

The Tc almost remains constant (Tc @ 138 °C/min @ 2.5 °C/min for 0.5%, 1% and 2.5%) irrespective of GO loading concentration, which was not same in case of graphene composites (max Tc-140 @ 2.5 °C/min). This suggests that addition of GO particles up to 2.5% does not add in or act as additional nucleating sites, which is not the case for graphene. The Avrami model as described in Chapter 3, Section 3.4.3.2 was used to understand the crystallisation behaviour under non-isothermal conditions. Plots of log (-ln (1 – X(t))) versus log t is shown in Figure 5.24 for porous Pebax GO composites with $scCO_2$. The corresponding Avrami parameters n and k were obtained from the slope and intercept of the plots, $t_{1/2}$ (calculated from the Equation 3.4) and corresponding R^2 are listed in Table 5.12.

The Avrami exponent n decreases with increasing cooling rate for all the sample types mainly due to less availability of crystallisation time for the complete nucleation mechanism. The average n value for all the samples lies between 3 and 4, indicating that the complex spherulitic crystallites have three-dimensional growth.

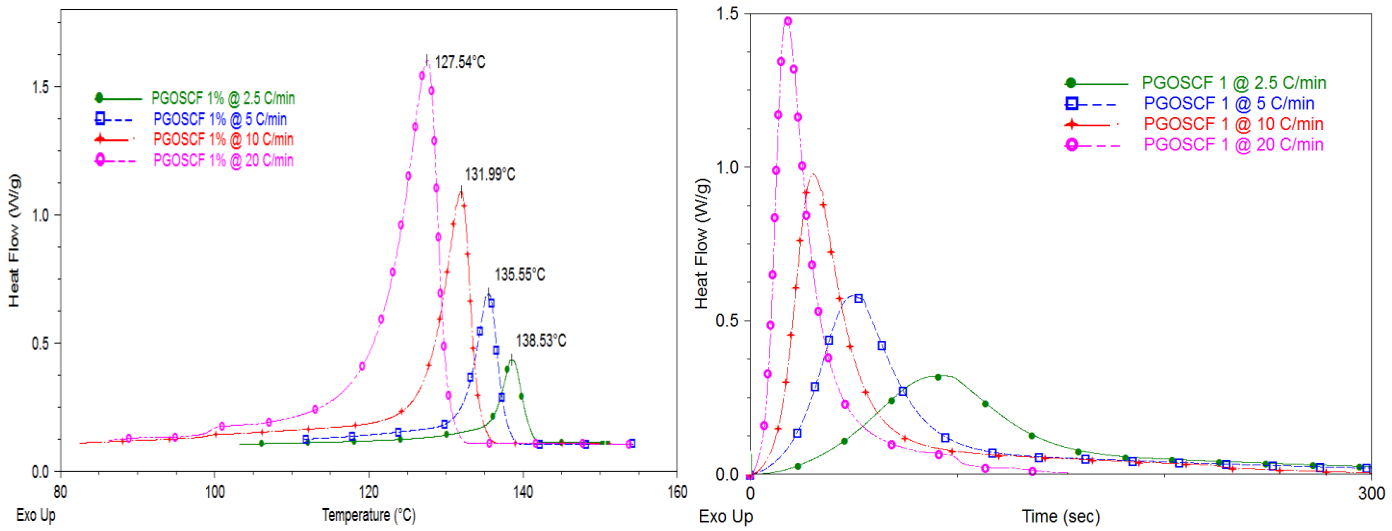

a. PGOSCF 1%

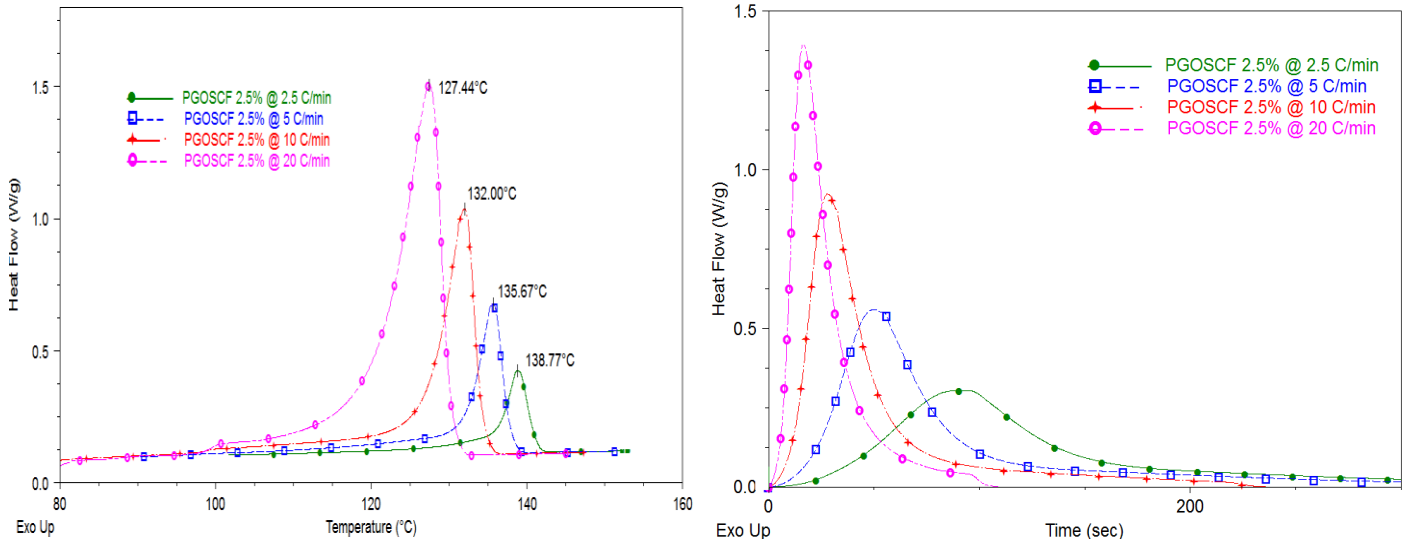

b. PGOSCF 2.5%

Figure 5.23 Heat flow curves with respect to time and temperature for porous Pebax GO composites

The crystallisation rate, k', increases with higher heating rates. However, this value gradually decreases with the addition of GO up to 2.5% compared to virgin Pebax. The increasing k' with higher cooling rate confirms a faster crystallisation process, however, these values decrease upon addition of GO particles which suggests that GO particles within the polymer matrix hinder the growth rate.

Table 5.12 Avrami parameters obtained from the Avrami plot for porous Pebax GO composites under non-isothermal conditions

Sample Type	ϕ (°C/min)	N	Average n	Log k'	k'	$t_{1/2}$ From Graph (min)	$t_{1/2}$ Calculated (min)	R^2
PebaxSCF	2.5	3.94	3.29	-0.21	0.62	0.99	1.03	0.999
	5	3.21		0.58	3.80	0.55	0.59	0.998
	10	3.04		1.19	15.49	0.34	0.36	0.997
	20	3.00		1.78	60.26	0.21	0.23	0.997
PGOSCF 0.5	2.5	3.38	3.46	-0.34	0.46	1.08	1.13	0.999
	5	3.23		0.48	3.02	0.58	0.63	0.996
	10	3.57		1.44	27.5	0.33	0.36	0.995
	20	3.69		2.48	302.0	0.18	0.19	0.996
PGOSCF 1	2.5	3.22	3.45	-0.36	0.44	1.10	1.15	0.999
	5	3.17		0.47	2.82	0.58	0.63	0.997
	10	3.69		1.37	23.44	0.36	0.39	0.995
	20	3.73		2.38	239.8	0.19	0.21	0.995
PGOSCF 2.5	2.5	3.33	3.36	-0.37	0.43	1.11	1.16	0.999
	5	3.38		0.47	2.95	0.60	0.65	0.997
	10	3.50		1.44	27.54	0.33	0.35	0.995
	20	3.25		2.13	134.90	0.18	0.20	0.995

The value of k' almost remains constant up to 10 °C/min cooling rates. However, at the higher cooling rate, the k' value decreases upon addition of GO to 2.5%. The values of k' for GO composites are higher than that of the graphene composite counterpart, indicating faster crystallisation in the case of GO composites (GO particles do not hinder the nucleation or growth rate when compared to G - this may be due to the interaction of polymer chain with the oxygen-rich GO). The same is observed in the $t_{1/2}$ values, where these values tend to increase up to the loading of 2.5% suggesting a slow crystallisation rate. Avrami analysis for non-isothermal conditions provides a good insight into the nature of the nucleation and growth process only. Therefore, a method devised by Ozawa was used, which has been specifically designed to model non-isothermal crystallisation kinetics. The Avrami equation was extended by Ozawa by modelling the change in the degree of crystallinity (X(T)) as a function of varying the cooling rate. The plot of ln(-ln(1-X(T)) vs. ln ϕ taken at different temperatures should give a linear fit, where the slope and intercept gives the kinetic parameters m and k*.The value m depends on the dimensions of the crystal growth and K(T) is a function of cooling rate φ which indicates how fast crystallisation occurs (Table 5.13).

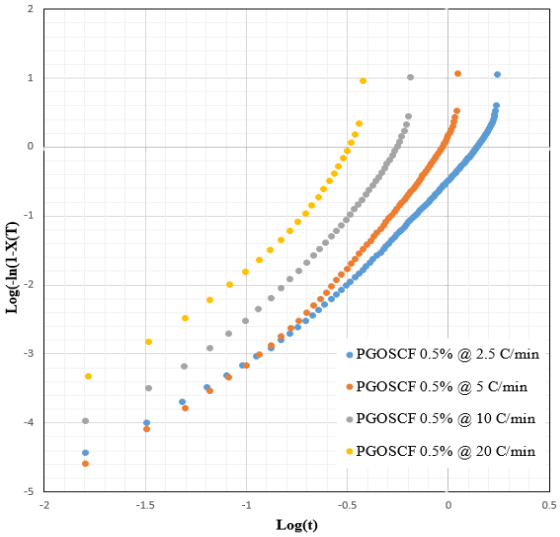

a. PGOSCF 0.5%

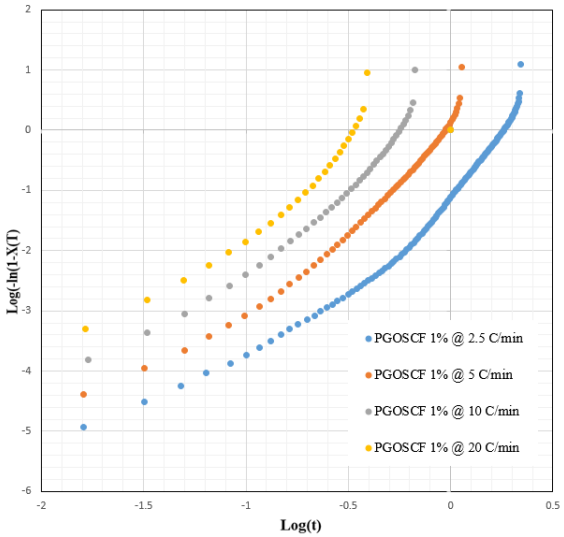

b. PGOSCF 1%

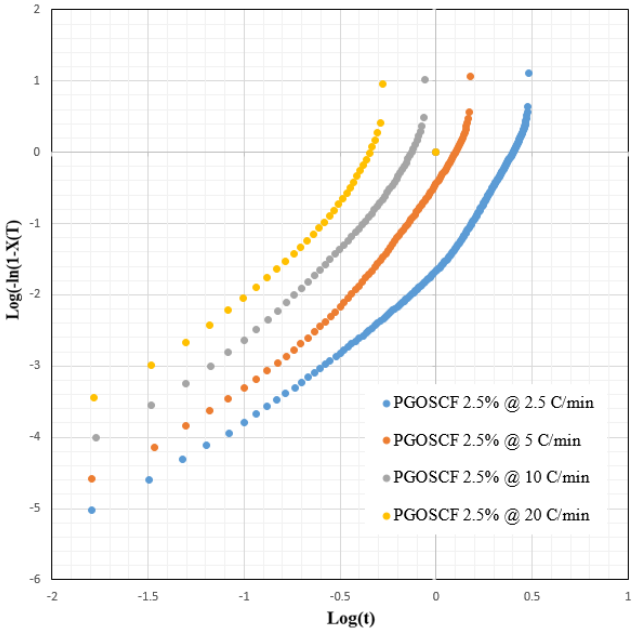

c. PGOSCF 2.5%

Figure 5.24 Avrami plot for porous Pebax GO composites under non-isothermal conditions

The heating reaction function Log k* tends to increase with temperature as the nucleation and growth rate is increased for all the sample type. In addition, the Ozawa exponent m decreases with increase in temperature. It is evident from the Ozawa plot that, a perfect linear fit cannot be achieved, due to the influence of secondary crystallisation (R^2 <<1). This suggests that mean m and k* values are difficult to achieve and thus the Ozawa method cannot be used to describe the crystallisation kinetics of Pebax GO composites under non-isothermal conditions. Therefore,

combining the Avrami and Ozawa model is used to in the next section to describe the kinetics of non-isothermal crystallisation.

Table 5.13 Ozawa parameters obtained from the Avrami plot for porous Pebax GO composites under non-isothermal conditions

Sample Type	T (°C)	M	Log k*	R^2
PebaxSCF	120	-0.90	2.14	0.898
	125	-2.83	4.44	0.764
	128	-2.06	2.91	0.891
	130	-3.98	4.90	0.853
	133	-3.78	3.77	1.000
PGOSCF 0.5	120	-0.42	1.65	0.843
	125	-0.54	1.55	0.941
	128	-1.04	2.04	0.859
	130	-2.14	3.38	0.767
	133	-2.12	2.75	0.890
	136	-7.39	8.03	0.879
PGOSCF 1	120	-0.38	1.62	0.728
	125	-0.55	1.58	0.889
	128	-1.05	2.06	0.828
	130	-2.07	3.30	0.759
	133	-5.85	7.96	0.759
	136	-5.88	6.35	0.872
PGOSCF 2.5	120	-0.58	2.12	0.928
	125	-0.68	1.90	0.979
	128	-1.16	2.34	0.880
	130	-2.19	3.56	0.788
	133	-1.97	2.68	0.889
	136	-6.61	7.29	0.871

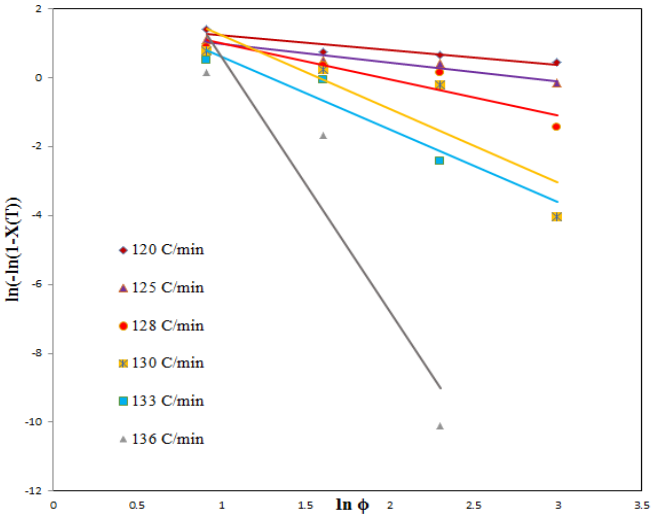

a. PGOSCF 0.5%

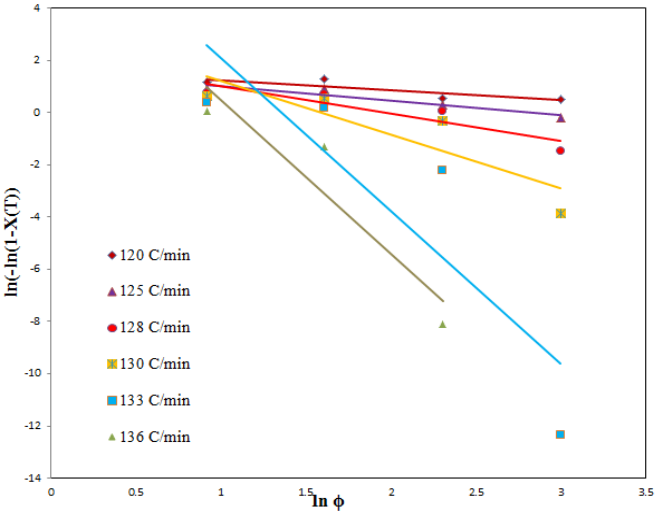

b PGOSCF 1%

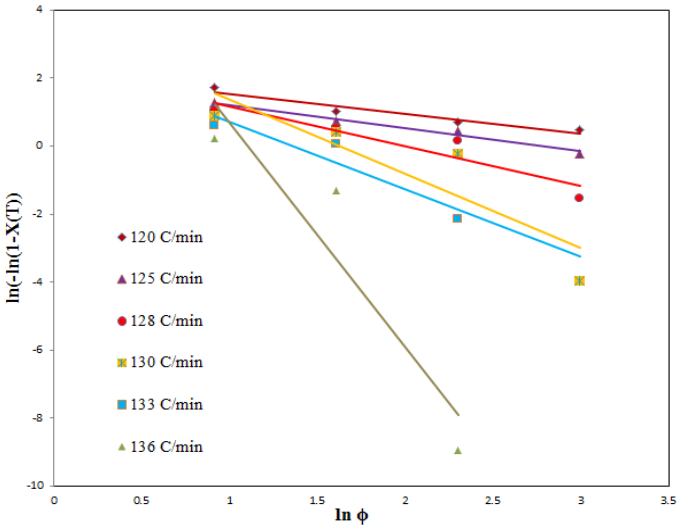

c. PGOSCF 2.5%

Figure 5.25 Ozawa plot for porous Pebax GO composites under non-isothermal conditions

Figure 5.26 demonstrates that lower cooling rates require a longer time (spreading of the ln t values) for crystallisation, while faster cooling rates require a shorter time for crystallisation (narrow ln t values). This spreading to narrowing of time for crystallisation with increasing cooling rate, indicates, that the value b is strongly dependent on the cooling rate. On the other hand, the value ln F(T) increases with the relative degree of crystallinity, indicating that larger crystallisation time is required at a higher cooling rate in order to reach unity degree of crystallinity. It is evident from the Table 5.14 that the F(T) values gradually increases with the addition of GO up to 2.5% indicating that the crystallisation rate decreases upon addition of GO (slower crystallisation). Unlike the huge increase in F(T) with graphene alone, the F(T) values do

not show a vast deviation from the virgin Pebax upon addition of GO. This suggests that GO particles might have better interaction with Pebax polymer chains than graphene particles.

Table 5.14 Mo parameters obtained from the combined Avrami and Ozawa plot for porous Pebax GO composites under non-isothermal conditions

Sample Type	X(T)	b	Mean 'n'	ln F(T)	F(T)	R^2
Pebax SCF	0.2	1.29	2.57	0.55	1.73	0.998
	0.4	1.35		0.78	2.18	0.997
	0.6	1.38		0.94	2.55	0.998
	0.8	1.41		1.07	2.91	0.997
PGO SCF 0.5	0.2	1.20	3.45	0.66	1.09	0.999
	0.4	1.17		0.91	2.48	0.999
	0.6	1.15		1.06	2.88	0.999
	0.8	1.13		1.17	3.22	0.999
PGO SCF 1	0.2	1.21	2.68	0.65	1.91	0.999
	0.4	1.20		0.92	2.50	0.998
	0.6	1.19		1.08	1.94	0.998
	0.8	1.18		1.20	3.32	0.999
PGO SCF 2.5	0.2	1.16	3.15	0.72	2.05	0.999
	0.4	1.10		0.97	2.63	0.999
	0.6	1.14		1.10	3.00	0.998
	0.8	1.10		1.21	3.35	1.000

This suggests that the addition of GO has lowered the rate of crystallisation compared to virgin Pebax (agreement with Avrami model); specifically due to hindrance at the crystal growth stage, however, has enhanced nucleating sites. It is found that the b value, which is the ratio of n/m, tends to increase upon the addition of GO PG 1%, suggesting that higher GO concentration induces a larger number of heterogeneous nucleation sites and limits crystal growth producing crystals of smaller size, therefore a clear decrease in the n value can be observed for 2.5 (the average Avrami n value also decreases).

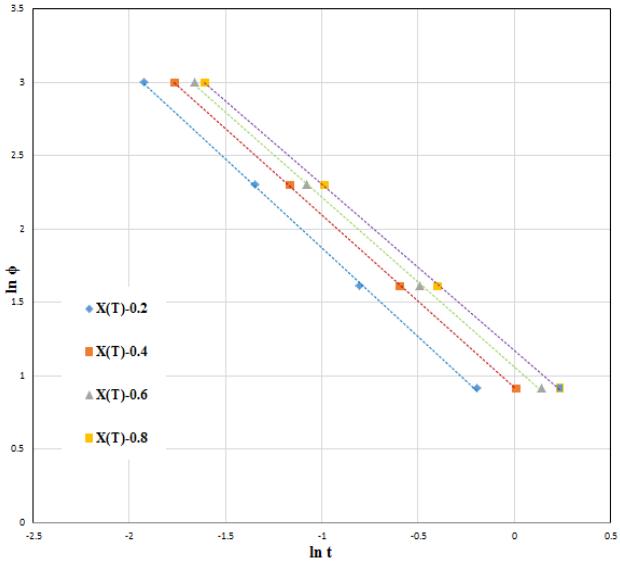

a. PGO SCF 0.5%

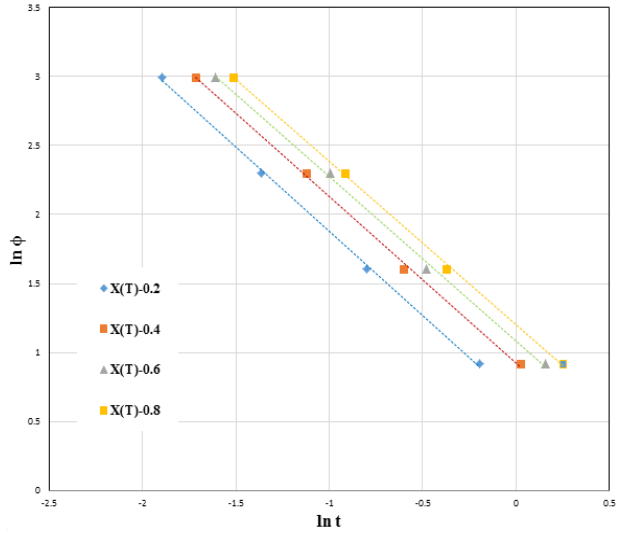

b. PGO SCF 1%

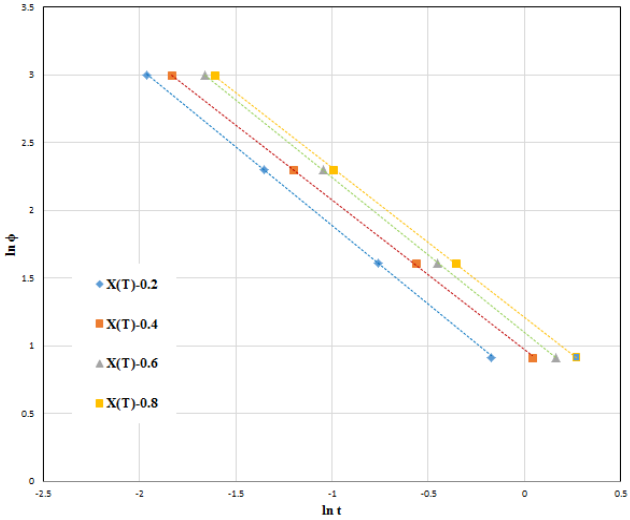

c. PGO SCF 2.5%

Figure 5.26 Combined Avrami – Ozawa (MO) plot for porous Pebax GO composites under non-isothermal conditions

The crystallisation activation energy under non-isothermal conditions was evaluated by using the Kissinger equation (Refer to Section 3.4.3.2). The crystallisation activation energy could be determined from the slope of the plot of ln (heating rate/Tc^2) versus 1/Tc. It can be observed from Table 5.15 and Figure 5.27 that the activation energy increases upon addition of graphene particles. The activation energy almost remains stable with the addition of GO up to 2.5% suggesting improved interaction of polymer to GO even at higher concentration. The increase in the activation energy upon the addition of GO can be attributed to the dominance of the hindrance

to movement of the polymer chains to initiate growth, which can be observed throughout the non-isothermal crystallisation analysis.

Table 5.15 Kissinger activation energy obtained from Kissinger plot for porous Pebax GO composites under non-isothermal conditions

Sample Type	Kissinger Activation Energy (KJ/mol)
Pebax SCF	190.48
PGOSCF 0.5%	282.14
PGOSCF 1%	278.32
PGOSCF 2.5%	275.32

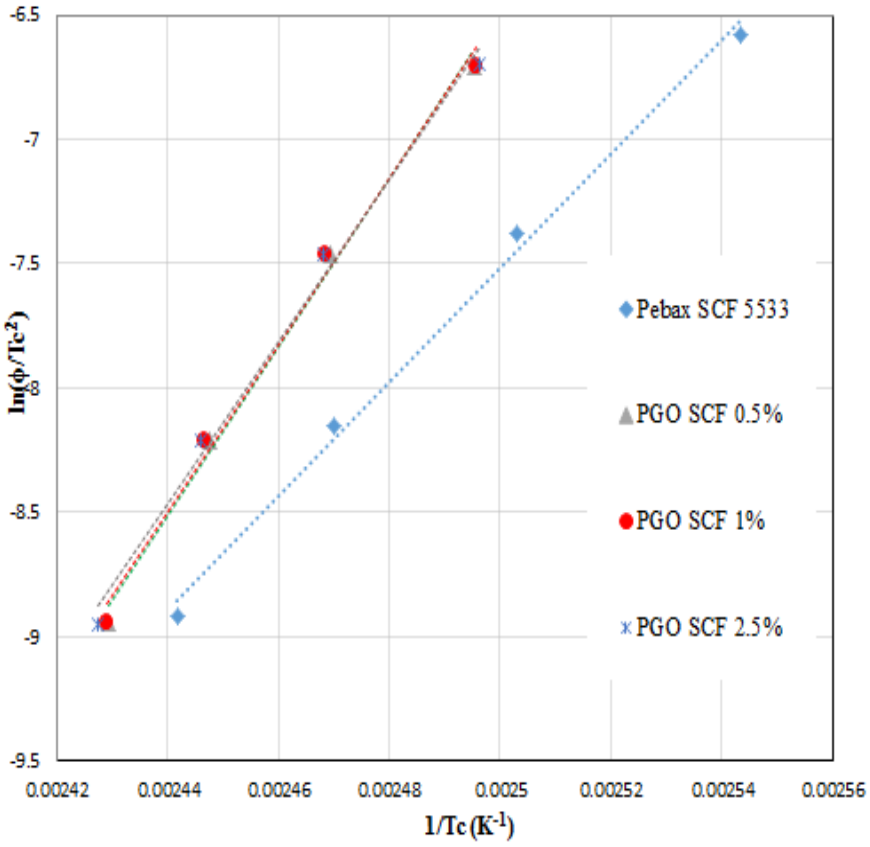

Figure 5.27 Kissinger's plot for porous Pebax GO composites under non-isothermal conditions

5.4.5 Dynamic Mechanical Analysis of Porous Pebax GO Composites

Figure 5.28 and the Table 5.16 represent the storage modulus in MPa at various temperatures and average storage modulus measured at 30 °C. It can be observed that the storage modulus

gradually increases from pure SCF Pebax (at around 78 MPa) upon the addition of GO to a loading of 1% (at around 129 MPa). Beyond 1% that is with 2.5% loading concentration the storage modulus decreases (93 MPa).

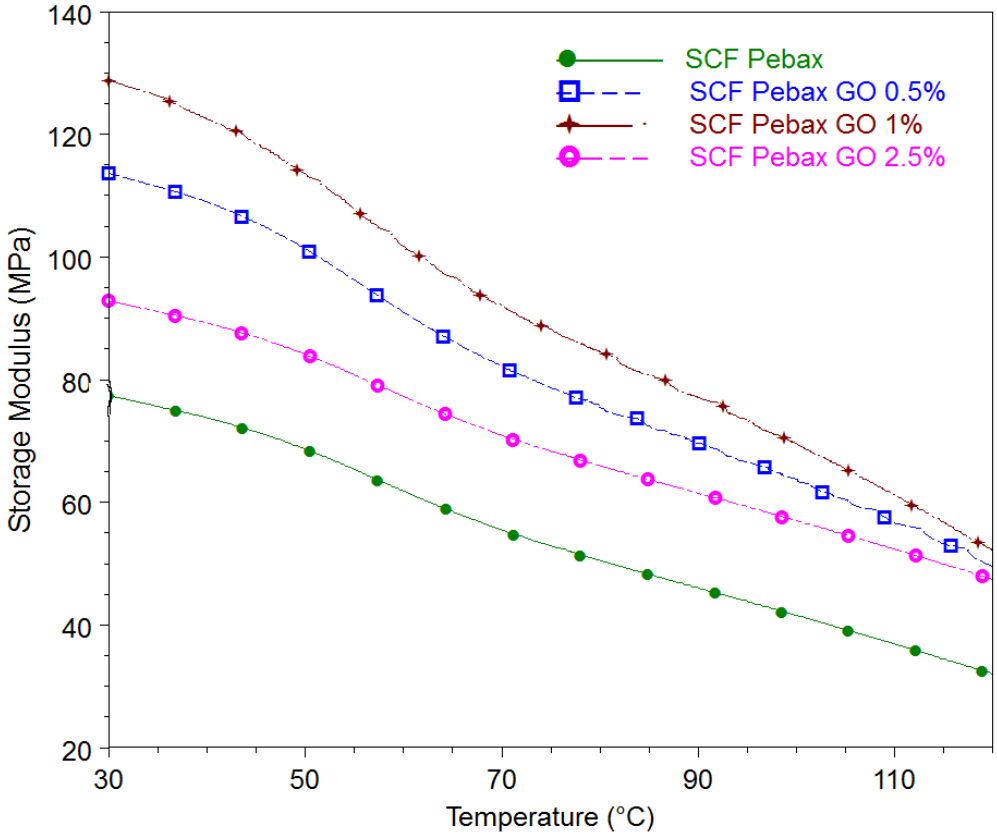

Figure 5.28 Storage modulus thermograms for porous Pebax GO composites

Such an increase in the storage modulus upon the addition of a filler suggests even dispersion and fairly good interaction between the polymer chain and the additive, which otherwise will tend to decrease due to agglomeration of additives (usually agglomeration occurs when the filler particles stack up one over the other at the polymer chain interaction site or in many cases in the availability of interactive polymer sites – poor interaction). Similar trends were observed with graphene loading, however, the storage modulus remains slightly higher for all the GO samples compared to graphene. The loss modulus is highest for 1% GO throughout the temperature range due to one to one polymer chain-graphene interaction which further restricts the free movement (acts as a more viscous material). With the increase in the loading concentration to 2.5%, the loss modulus decreases (less viscous), which can be attributed to free space that was created due to the agglomeration of GO, where polymer chains have free space to relax, resulting in easy movement.

Table 5.16 Storage, Loss and Tan delta measured at 30 °C for porous Pebax GO composites

Sample type	With SCF		
	Storage modulus	Loss Modulus	Tan Delta
	MPa	MPa	NA 10^{-3}
SCF Pebax	77.28±6.8	2.77	35.8
SCFPGO 0.5%	113.33±3.6	3.45	30.0
SCFPGO 1%	128.89±3.1	4.00	31.0
SCFPGO 2.5%	93.22±4.3	3.12	33.4

Figure 5.30, represents the tan delta or the loss factor curve over a temperature range. The tan delta is the lowest for 0.5% graphene GO oxide loading representing low loss due to friction or heat, however, increases upon increasing the loading to 1% and 2.5%. The appearance of a significant wide peak spread over the temperature range of 50 °C - 90 °C as seen from the tan delta of graphene studies (Chapter 5, Section 1), is not clearly visible with GO extrudates. However, a broad peak can be seen on the 1% GO curve on the thermograph. Similar peaks are also evident from the DSC section around the same range of temperatures due to the interaction between the nylon block and the graphene particles.

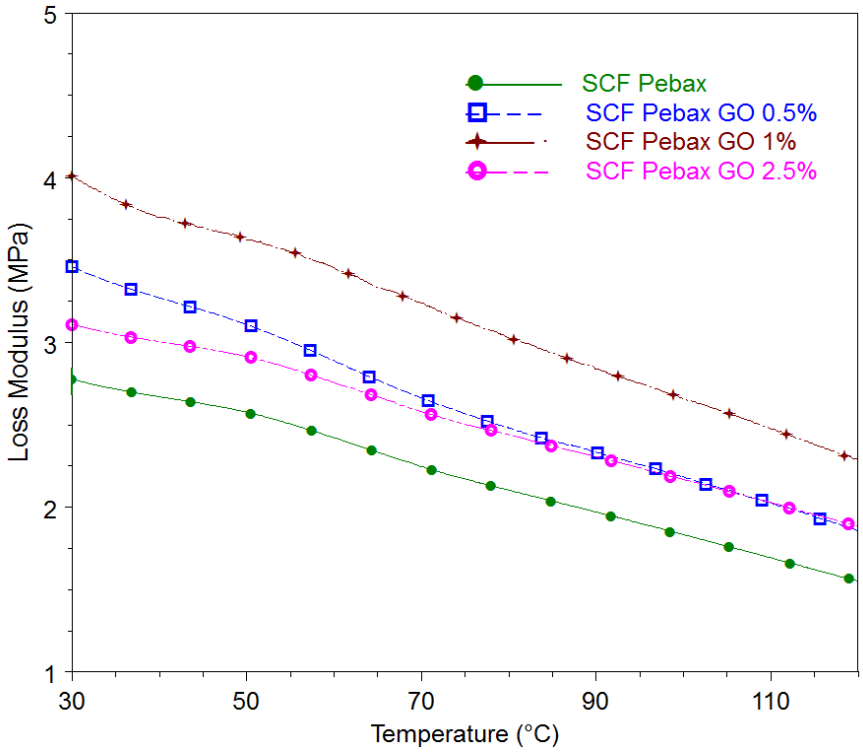

Figure 5.29 Loss modulus thermograms for porous Pebax GO composites

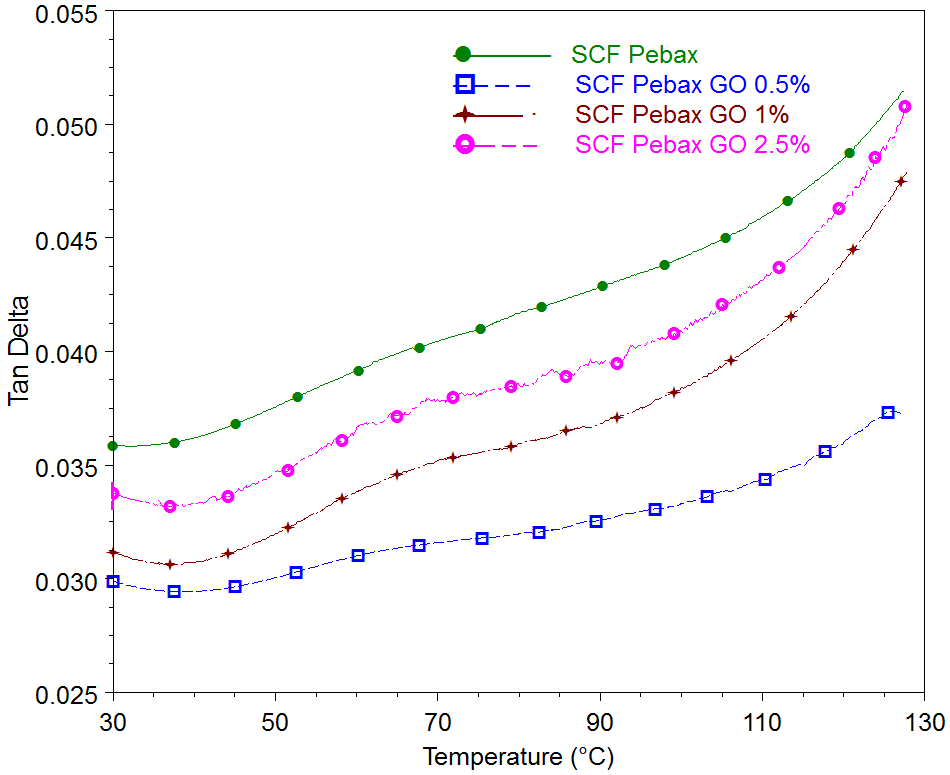

Figure 5.30 Tan delta thermograms for porous Pebax GO composites

5.4.6 Fourier Transform Infrared Spectroscopy of Porous Pebax GO Composites

Figure 5.31 presents the transmittance spectra of the porous Pebax GO composites. No significant changes or trends were observed for $scCO_2$ Pebax GO composites.

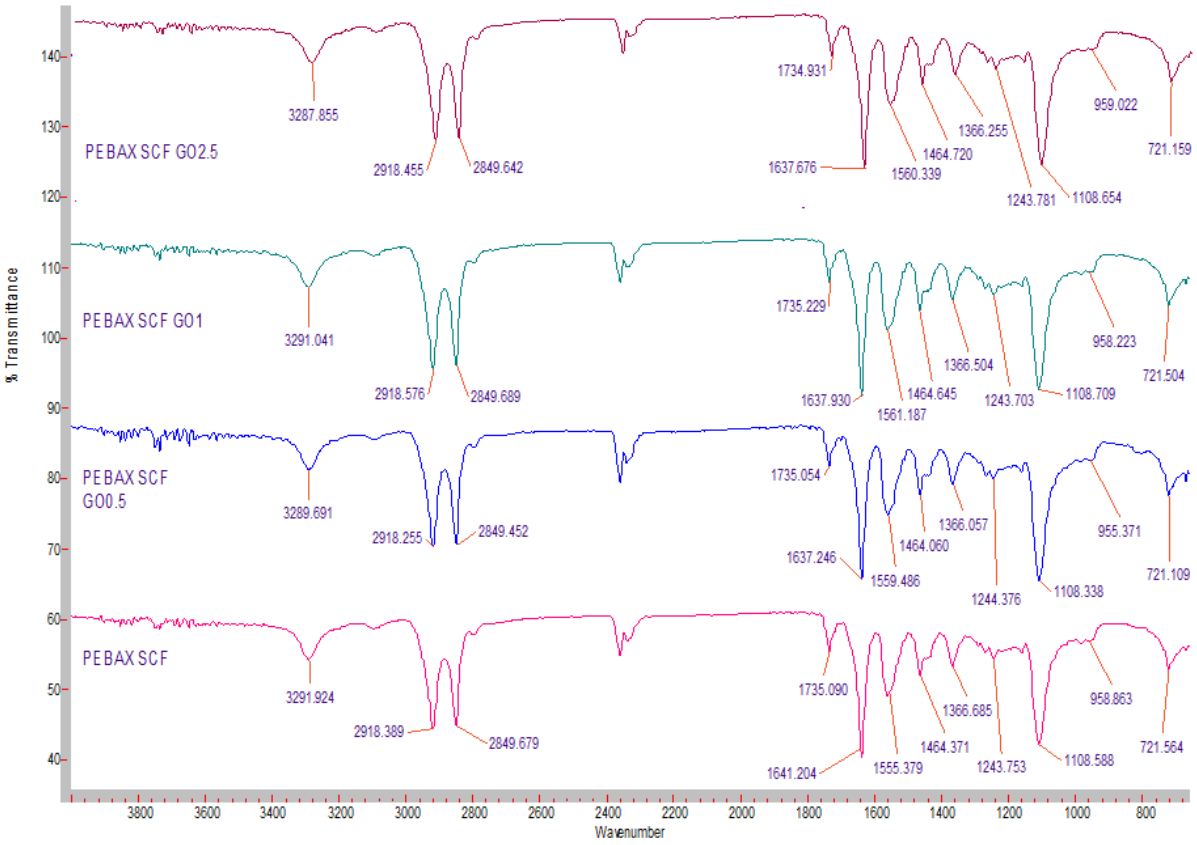

Figure 5.31 Transmittance IR spectra of porous Pebax GO composites

5.4.7 Tensile Testing of Porous Pebax GO Composites

Figure 5.32 shows the stress vs. strain curve for porous Pebax GO composites. The modulus of resilience and modulus of toughness enhancement can be observed throughout upon the addition of GO up to a maximum of 1%. However, as the loading was increased to 2.5%, the modulus of resilience and the toughness reduce. A similar effect has been observed throughout the section on the thermal and dynamic mechanical analysis. At very low strain % from 0.25% to 4%, the PGO SCF 0.5% loading has slightly higher stress, which may be due to the perfect interaction between the polymer chain and the GO particles. The results from the dynamic mechanical analysis and the tensile test are in agreement with the analysis/attribution made on the fact that the loading of 1% and above result in the agglomeration of particles.

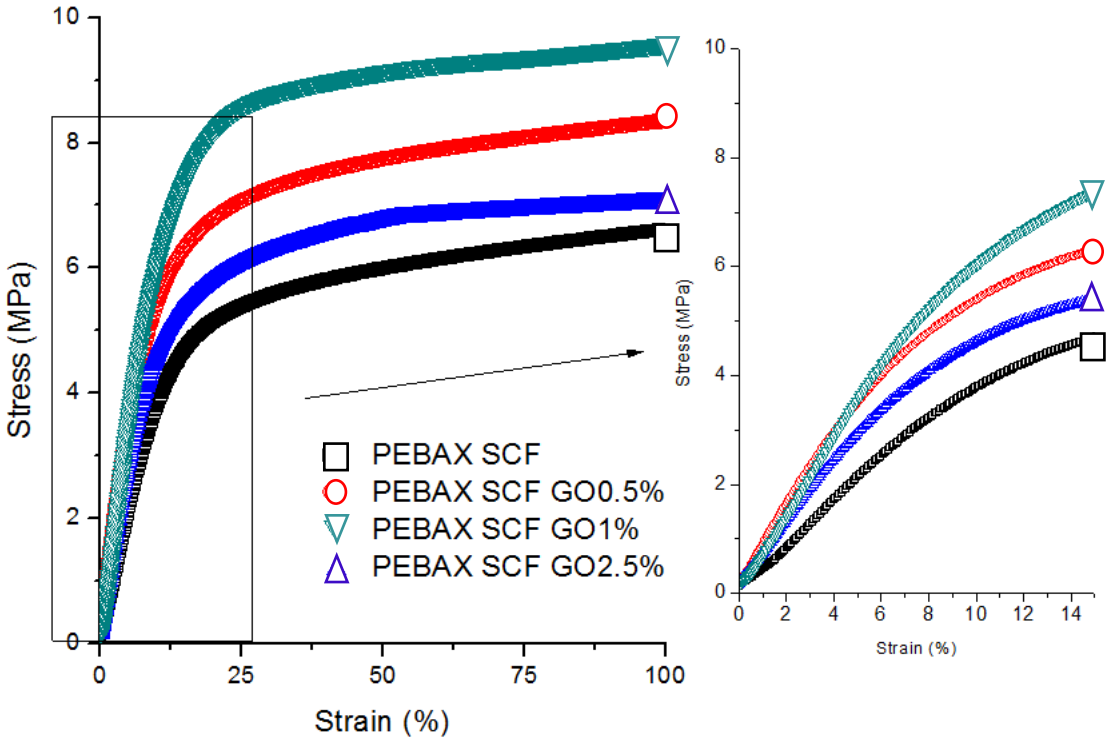

Figure 5.32 Stress vs. strain curves for porous Pebax GO composites

5.5 Keypoints Porous Pebax GO Composites with $scCO_2$

The aim of this section of Chapter 5 was to investigate the effects of incorporating GO filler materials when processed using $scCO_2$ extrusion. The following are the key observations:

- The crystallisation peak of virgin SCF Pebax can be observed at 136 °C. No shift or reduction in relative heat flow magnitude was observed with the addition of GO up to 2.5%.
- The Avrami exponent 'n' under isothermal crystallisation kinetics is in the range from 2 to 3, for all the samples indicating a complex two-dimensional growth phenomenon with branched fibrillar morphology. Under non-isothermal crystallisation kinetics, the average n values for all the samples lies between 3 and 4, indicate complex spherulite crystallites having three-dimensional growths.
- The parameter k tends to increase up to 1% GO loading (faster crystallisation) and remains constant for 2.5% loading. This suggests that the loading of 1% and above result in agglomeration of particles, thereby restricting the actual nucleation or growth of the crystal.
- The Arrhenius ΔE value increases upon GO loading. The activation energy is the highest at 2.5%. This shows that the GO particles in the Pebax matrix restrict the easy movement

of the polymer chain in order to progress through the crystallisation step of nucleation and crystal growth. Tc shifts to a higher value under non-isothermal crystalline kinetics indicate that heterogeneous nucleation dominates. The Tc almost remains constant (Tc-138 °C @ 2.5 °C/min for 0.5%, 1% and 2.5%) irrespective of GO loading concentration, which was not same in case of graphene composites (max Tc-140 @ 2.5 °C/min), suggesting that the addition of GO particles up to 2.5% does not add or act as additional nucleating sites.

- Although the increasing k' with higher cooling rate confirms a faster crystallisation process, however, these values decrease or remain constant upon addition of GO particles which suggests that GO particles within the polymer matrix hinder the growth rate. The value of k' almost remains constant up to 10 °C/min cooling rate, however, at the higher cooling rate the k' value decreases upon addition of 2.5% GO.
- The F(T) values gradually increase with the addition of GO up to 2.5% indicating that the crystallisation rate decreases upon the addition of graphene,(slower crystallisation). Unlike the huge increase in F(T) with graphene alone, the F(T) values do not show a vast deviation from the virgin Pebax upon the addition of GO. This suggests that GO particles might have better interaction with Pebax polymer chains than graphene particles. The increase in the activation energy upon the addition of GO can be attributed to the dominance of the hindrance to movement of the polymer chain to initiate growth, which can be observed throughout the non-isothermal crystallisation analysis
- The storage modulus gradually increases form pure SCF Pebax (at around 78 MPa) upon the addition of GO to a loading of 1% (at around 129 MPa). Beyond 1% filler concentration, that is with 2.5% loading, the storage modulus decreases (93 MPa). The tan delta is the lowest for 0.5% GO loading representing low loss due to friction or heat, however, the tan delta increases upon increasing the loading to 1% and 2.5%.
- A clear enhancement of the modulus of resilience and modulus of toughness can be observed throughout the addition of graphene up to 1%. However, as the loading was increased to 2.5%, the modulus of resilience and the toughness reduced.
- No significant changes or trends were observed in the IR spectroscopy for $scCO_2$ Pebax GO composites.

5.6 Conclusion for Pebax Graphene-based Composites with $scCO_2$

This chapter investigated Pebax graphene and GO composites using $scCO_2$ assisted polymer processing technique. In both the cases of graphene and GO, the maximum thermal degradation temperature remained unchanged at 460 °C. However, the loss in weight decreased in both the cases with an increase in the filler concentration suggesting that the filler interaction restricts the easy movement of the polymer chains. The endothermic peak seen at 80 °C for virgin SCF Pebax and is enhanced due to the restriction imposed by graphene particles upon polymer-additive interaction. However, in the case of graphene-oxide, the endothermic peak shifts to a lower temperature of around 50 °C. In both types of filler, the value of Avrami exponent 'n' is between 2 to 3 for isothermal conditions indicating a complex two-dimensional axialitic crystallisation process, while 'n' ranges from 3 to 4 for non-isothermal conditions indicating a spherulitic structure. The crystallisation rate 'k' increases up to 1% suggesting that the graphene particles loading up to 1% acts as nucleation sites; however 'k' decreases for 2.5% loading due to probable agglomeration of graphene particles. The value of k was much higher in the case of graphene composites compared to GO. One of the probable reasons for slower crystallisation rate in case of GO compared to graphene may be due to the oxygen-rich GO surface which readily initiates the interaction between the filler particle and Pebax resulting in slower nucleation and growth rate. The Arrhenius's activation energy (ΔE) decreased for 0.25%, further indicating graphene acted as nucleation sites, while ΔE increased from 0.5 till 2.5% in both graphene and GO loading suggesting a restriction induced by graphene polymer chain interaction due to agglomeration. Under non-isothermal conditions, the Tc peak shifted to higher temperatures suggesting the dominance of heterogeneous nucleation with graphene as filler particles while the Tc almost remained constant even at higher loading of GO. This suggests that the addition of GO particles up to 2.5% does not add in or act as additional nucleating sites. Unlike the huge increase in F(T) with graphene alone, the F(T) values do not show a vast deviation from the virgin Pebax upon addition of GO. This suggests that GO particles might have improved interaction with Pebax polymer chain than graphene particles. The increase in Kissinger's activation energy (ΔE) upon addition of graphene and GO can be attributed to the agglomeration of the graphene particles which hinder the transportation of the molecular segment to crystallite phase and formation of the nuclei size. The storage modulus and loss modulus increase while the tan delta decreases to 1% graphene/GO loading, similar to the results obtained from the crystallisation kinetics, suggesting good polymer graphene interaction. However, with 2.5%, the storage modulus and the loss modulus decrease due to agglomeration; a

similar decrease in crystallisation kinetic parameters was also noted for 2.5%. The modulus of resilience and modulus of toughness can be observed throughout upon addition of graphene/GO up to 1%. However, as the loading was increased to 2.5%, the modulus of resilience and the toughness reduce.

6 Supercritical Fluid Assisted Processing of SEBS Graphene Porous Polymer Composites

6.1 Introduction:

As an extension of the investigation carried out in Chapter 4, this chapter looks at the effects of $scCO_2$ assisted extrusion on the properties of graphene-based filler SEBS compounds. As seen in Chapter 5, graphene and GO-based filler material were used at supercritical conditions that were selected from Chapter 4 (processed at a pressure of 1200 psi). This chapter is divided into two sections, where the first section discusses the effects of using $scCO_2$ assisted processing of porous SEBS graphene-polymer composites, while the second section looks at the effects of using $scCO_2$ assisted processing of porous SEBS GO polymer matrix. This chapter bridges the existing gap on how to enhance the electroactive properties of the material using industrial manufacturing techniques. SEBS (Poly (styrene-ethylene-butylene-styrene)) was selected due to its intrinsic properties of being mechanically tough and its rubbery nature. Such elastomeric properties are most suitable for bending or elongation actuation in the case of artificial muscle applications. Many researchers have reported the capabilities of SEBS as bending or elongation actuators, however, a research gap still persists on an industrial scale and for the need for enhancement of electroactive properties [152-154]. The innovation of this chapter not only arises from the use of a supercritical extrusion polymer processing technique but also emerges from the use of graphene-based filler materials. This chapter provides a complete insight into how graphene and GO-based composites affect the thermal, mechanical and electrical properties. In both sections, the thermal mechanical and morphological properties are understood by using thermal gravimetric analysis (TGA) and differential scanning calorimetry (DSC), dynamic mechanical thermal analysis (DMA) and tensile testing and transmission electron microscopy (TEM). It is understood from this chapter that although the graphene-based polymer composites enhance the thermal, mechanical and electrical properties, GO-based composites favour the electroactive properties in the case of Ionic EAP. Therefore, the graphene-based polymer composites can be more suitable for electric field based applications (uses large activation energy to activate the material – works on polarisation ability) and GO composites can be suitable for ionic based applications (requires no activation voltage, works on low voltage transfer of charges).

6.2 Section 1: Supercritical Fluid Assisted Porous SEBS Graphene Composites

6.2.1 Thermal Gravimetric Analysis of Porous SEBS Graphene Composites

Thermogravimetric analysis (TGA) was performed to evaluate the effect on the thermal stability of all the $scCO_2$ assisted extrudates of SEBS graphene composites. It is evident from Figure 6.1 that the thermal stability increased with the use of $scCO_2$, and continued to shift to higher temperatures, even with the addition of graphene particles.

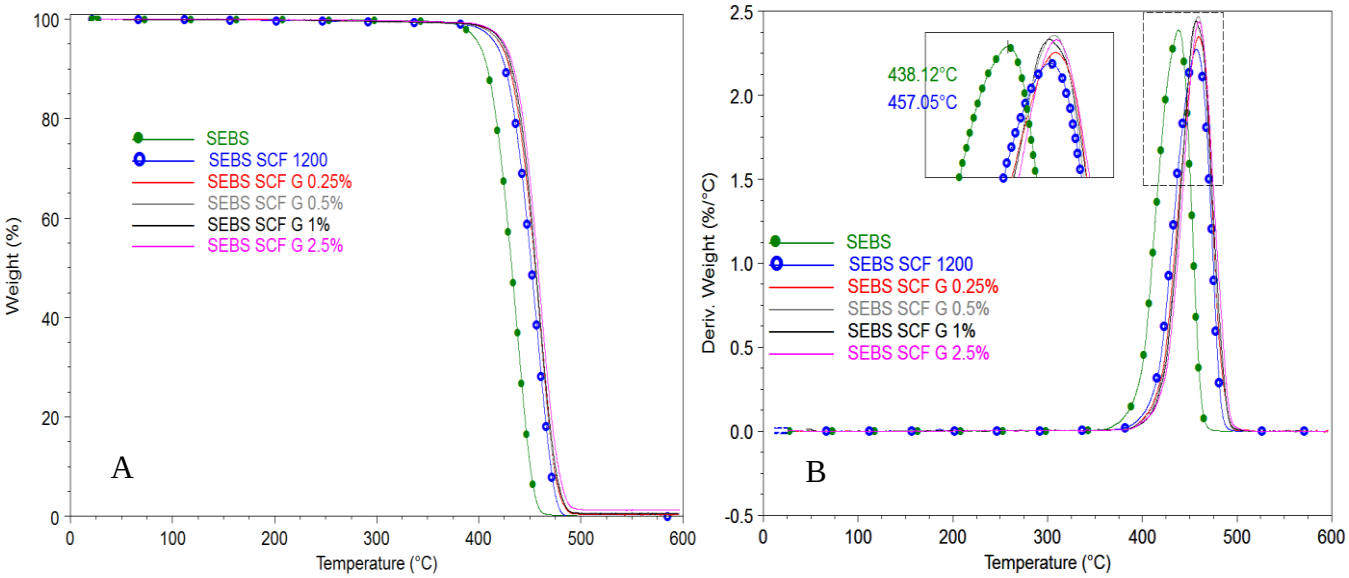

Figure 6.1 Degradation profiles of porous SEBS graphene composites (A: Weight change and B: Derivative weight change)

This increase in the degradation profile of porous SEBS graphene composites can be suggested to be due to high microphase formation extruded with $scCO_2$ (the creation of addition microphases is clearly described in Section 4.4.2), which in turn leads to the different structure of the materials and hence different degradation profiles of the thermoplastic elastomer as degradation temperature is related to the change in molecular structure and thermal kinetics [136]. The derivative weight change peak is maximum for SEBS SCFG 0.5% (maximum degradation temperature), suggesting even dispersion of graphene particles, while this peak remains almost constant at 459 °C. However, the area under the peak slightly decreases upon an increase in graphene particles due to agglomeration, which induces restriction on the molecular movement.

6.2.2 Differential Scanning Calorimetry of SEBS Graphene Porous Composites

Figure 6.2 shows the scanning calorimetry (DSC) thermograms for SEBS, SEBS 1200 and various ratios of SEBS graphene porous membranes. The relaxation due to entanglement can be observed in the heat flow thermogram at 8.54 °C, 12.43 °C and 10.28 °C for virgin SEBS, SEBS extruded at 1200 psi and SEBS extruded at 1200 psi with graphene at various loading concentrations (shifts to higher temperatures).

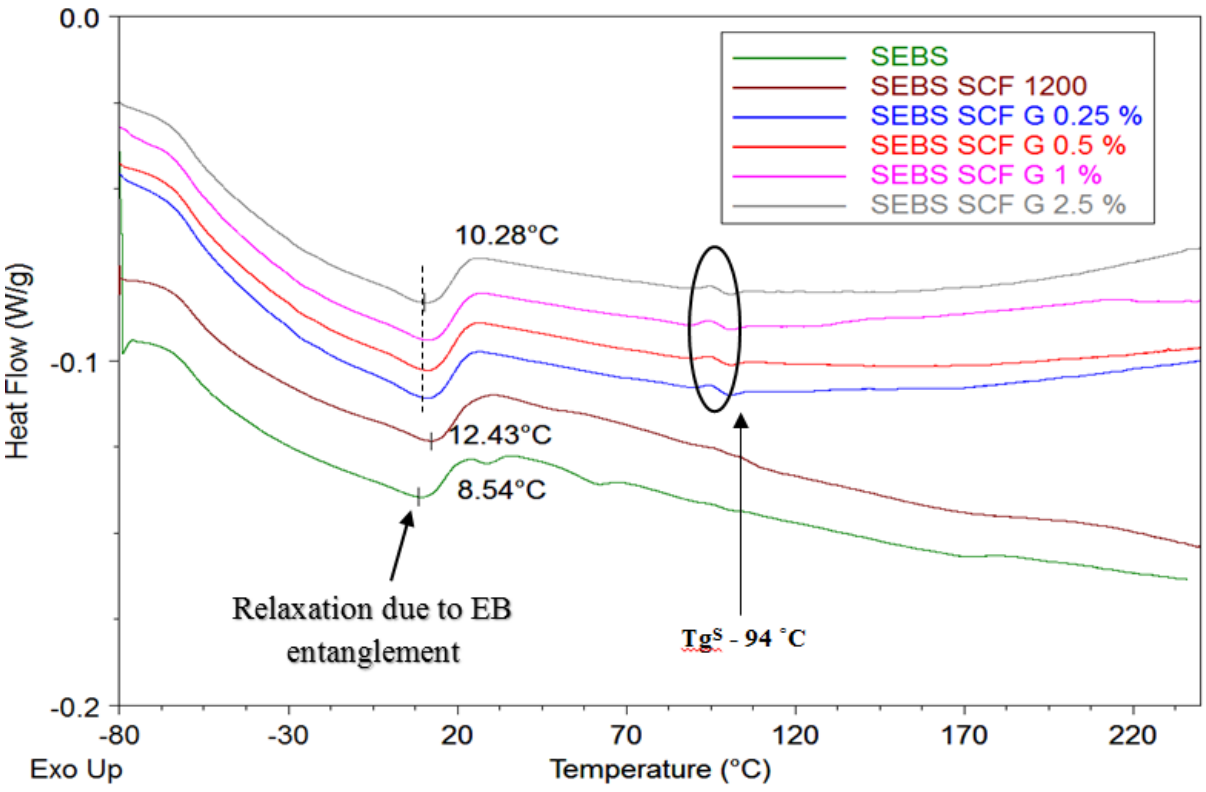

Figure 6.2 Heat flow thermographs of porous SEBS graphene composites

This increasing relaxation, when assisted with $scCO_2$, can be attributed to higher temperature requirements to completely resolve the entanglements/break down of physical crosslinks (between soft and hard block) and rearrangement of polymer graphene microstructures to behave like a viscous fluid. This suggests that the addition of graphene particles into the polymer increases the viscosity of the polymer melt. The Tg of pure styrene (S) rich phase (Tg^S) around 95 °C is not clearly visible in virgin SEBS and SEBS SCF 1200 psi thermograms. However, small exothermic peaks are evident at 94 °C for all the samples when graphene was added, showing the formation of microstructures or rearrangement/ interaction process of the pure S phase with graphene particles [139]. A single peak can be observed from the derivative reversing thermogram (Figure 6.3) at around -55 °C (attributed to Tg of the EB block for virgin SEBS), however, divided peaks can be observed at -58.68 °C and -52.59 °C for SEBS extruded at 1200

psi. The Tg of the EB block becomes wider and spreads with multiple evident peaks at -58 °C and -28 °C with graphene loading.

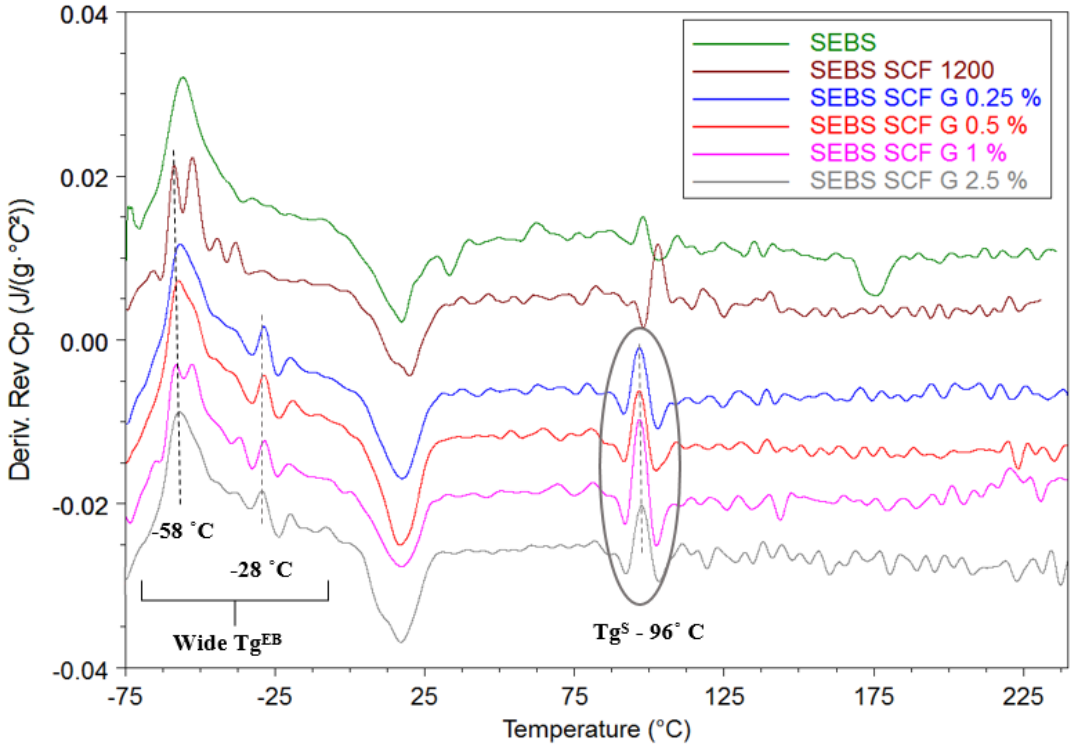

Figure 6.3 Derivative reversing heat capacity thermographs for porous SEBS graphene composites

Such spreading of Tg peaks suggests the formation of additional microstructures resulting in an increase in the microphase separation within the EB rich phase with the addition of graphene particles up to 2.5%. These multiple small peaks also suggest the creation of multiple microphases with specific Tg^I (Tg of interdomain microphases). The Tg of the S-rich microphase has a slight shift from 97 °C for virgin SEBS to 102 °C for $scCO_2$ treated SEBS, however, it remains constant at 96 °C, with the addition of graphene particles up to 2.5%.

The non-reversing kinetic or the time-dependent component is presented in Figure 6.4. The ordering of aromatic structures from intermixed phases and densification of styrene microphases between -10 to 35 °C increases upon the addition of graphene particles. This shows that the addition of graphene particles slows down the rearrangement process due to unavailability of free space within the polymer membrane. The in-depth analysis of thermal behaviour, non-reversing and reversing kinetics is well documented in initial studies as a part of this work [155]. The exotherm at 35 °C may arise due to twisting and alignment of the aromatic centre along with an ordered axis-styrene block, with an endotherm around 60 °C representing heat enthalpy

relaxation of the S block for virgin SEBS. This relaxation cannot be seen with $scCO_2$ or graphene addition, as $scCO_2$/graphene particles restrict the easy movement of styrene due to structural changes in the microdomain formation. In addition, the peak at Tg^S (96 °C) can be seen with the addition of graphene, suggesting styrene graphene interaction.

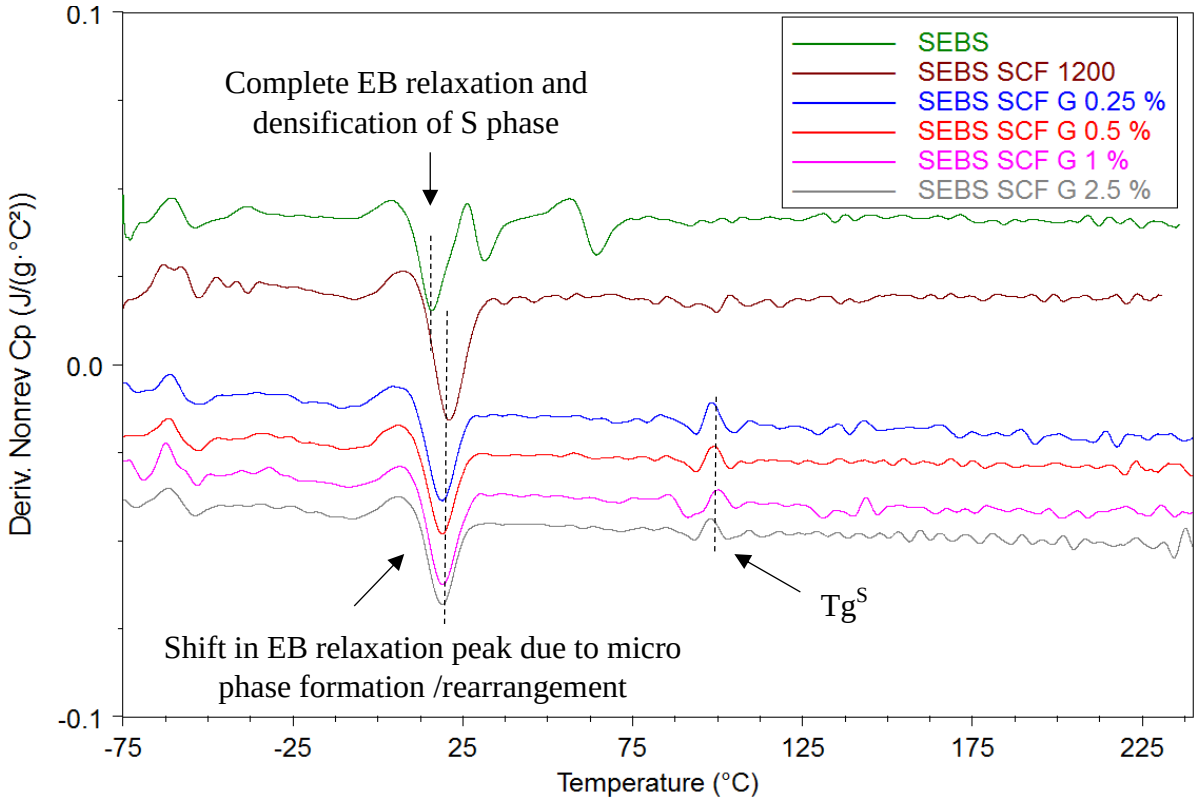

Figure 6.4 Derivative non-reversing heat capacity thermographs for porous SEBS graphene composites

6.2.3 Dynamic Mechanical Analysis of Porous SEBS Graphene Composites

Figure 6.5 presents the storage modulus curves for porous SEBS graphene composites. It can be observed that the storage modulus is lowest at 0.25% and highest for 0.5% graphene loading compared to virgin SEBS SCF. It is evident that the storage modulus of 1% and 2.5% remains higher than 0.25% but lower than virgin SEBS SCF. The storage modulus is highest for 0.5% suggesting that the graphene particles at 0.5% loading have good interaction/dispersion within the polymer matrix thereby enhancing the stiffness of the composites.

Figure 6.6 represents the loss modulus curves for porous SEBS graphene composite. It is evident that the loss modulus curves follow a similar trend to the storage modulus, however, the maximum peak of loss centred at 83°C on the loss modulus curve (related to physical property changes which are attributed to the molecular motion process, involving high frictional effects

and heating loss of S segment) shifts approximately to 94 °C for all the graphene added SEBS graphene composites. This peak solely represents the densification of the phase-separated styrene rich group.

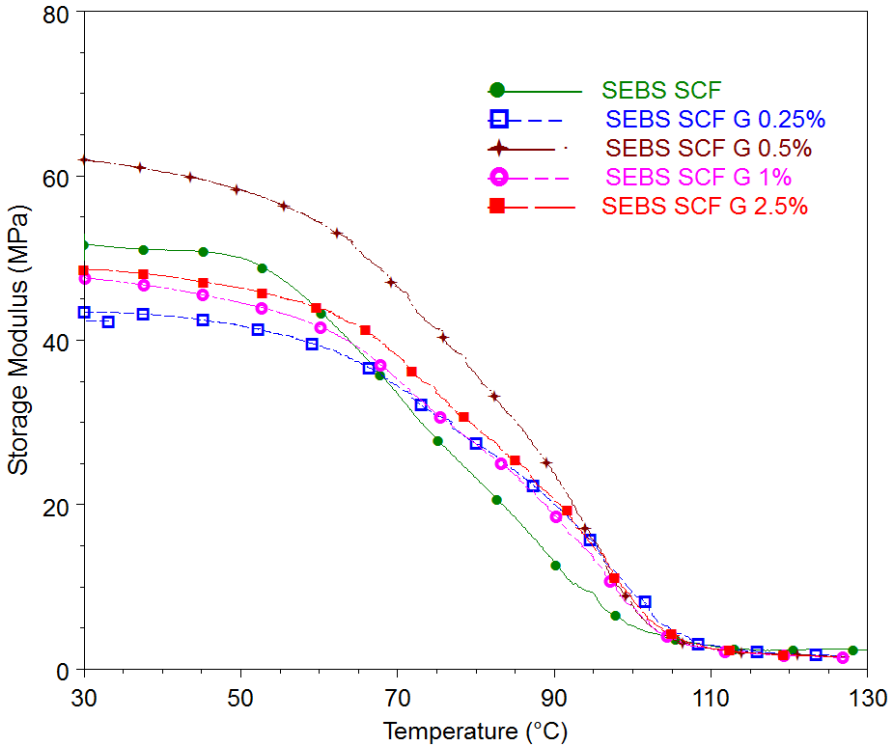

Figure 6.5 Storage modulus curves for porous SEBS graphene composites

Such shifts suggest that the graphene interacted styrene-rich phase and the peak is a maximum for 0.5% suggesting optimum dispersion and physical interaction between the polymer and the filler graphene. This peak tends to decrease for 0.25%, 1 and 2.5%, probably due to the lower graphene loading (at 0.25%), which might be very low to completely interact with all the available interactive sites and agglomeration of the particles at higher loading concentration (1% and 2.5%). Figure 6.7 shows the tan delta curves for the entire porous SEBS graphene composite, where the peak represents the Tg of the styrene-rich phase. The peak Tg of styrene rich phase shifts to 103 °C upon addition of graphene from 0.25% to 2.5%. This shift in peak is indicative of the fact that graphene particles are interacting with the styrene-rich phases where otherwise a shift in peak would not be clearly observed. Irrespective of the losses incurred, such as shifts and increase in the tan delta peak shows that $scCO_2$ enhances the graphene-polymer chain interaction. The tan delta peak undoubtedly shows enhancement in the peak for composites which is an indication of homogenisation which otherwise will broaden the tan delta peak.

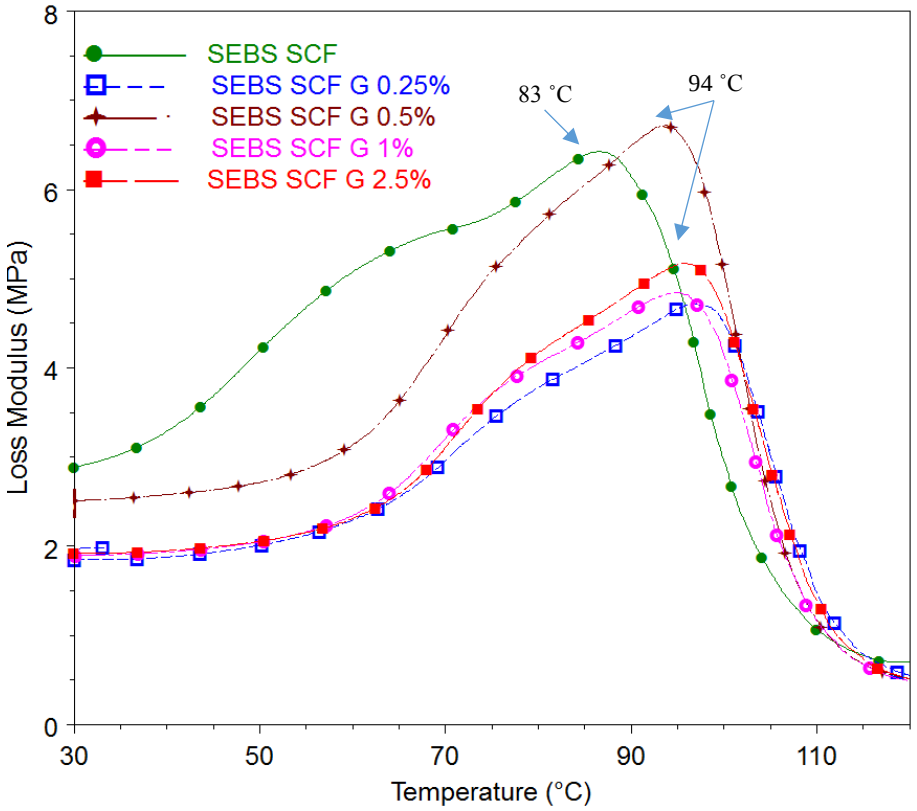

Figure 6.6 Loss modulus curves for porous SEBS graphene composites

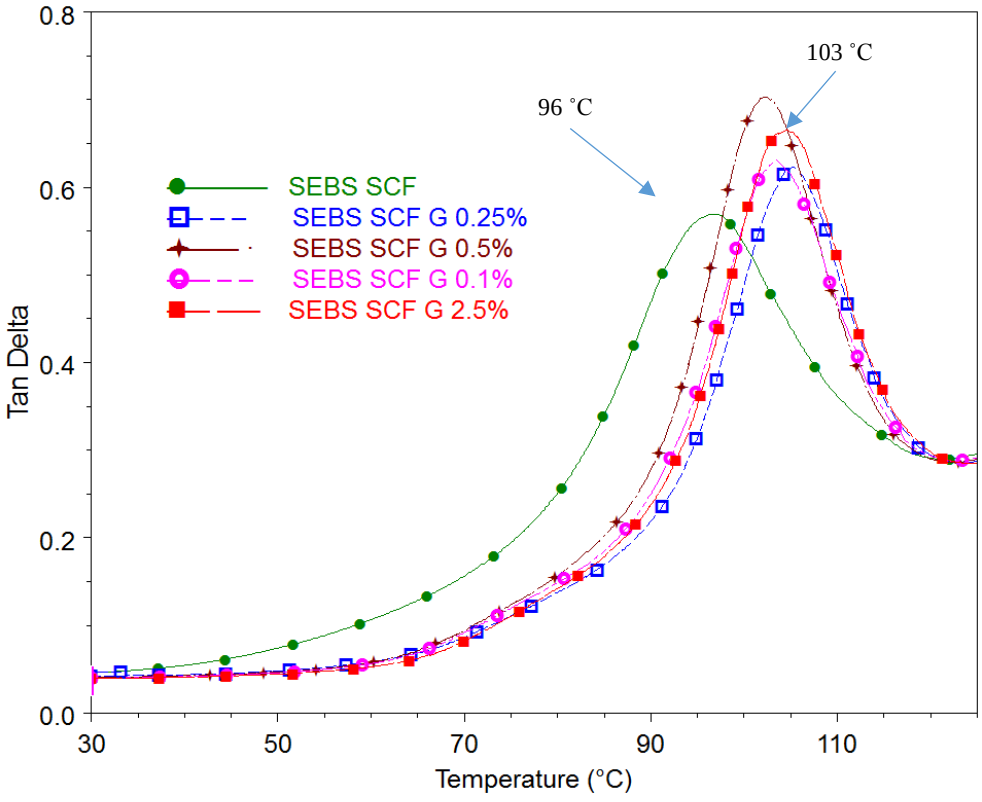

Figure 6.7 Tan delta curves for porous SEBS graphene composites

6.2.4 Fourier Transform Infrared Spectroscopy of Porous SEBS Graphene Nanocomposites

ATR-FTIR spectra, as shown in Figure 6.8 represent the effect of supercritical assisted extrusion on porous SEBS graphene. Peaks at 2920 cm^{-1} and 2851 cm^{-1} representing the asymmetrical stretching of $–CH_3$ and $–CH_2$ (the ethylene-butylene block) do not show any shift in the position with the addition of graphene up to 2.5% under critical pressures of 1200 psi. The aromatic C=C stretching of the aromatic system at peak 1600 cm^{-1} and 1492 cm^{-1} tend to broaden as graphene concentration is increased to 2.5% [156, 157]. This peak normally originates from the styrene group, however, with 2.5% graphene loading the concentration at the styrene graphene interface is higher as graphene particles overlap and agglomerate at the interaction sight. This shows that the pi electrons in graphene interact with C=C bonds of styrene groups of SEBS. The peak at 1377 cm^{-1} representing the bending of $-CH_3$, does not show any significant change upon addition of graphene.

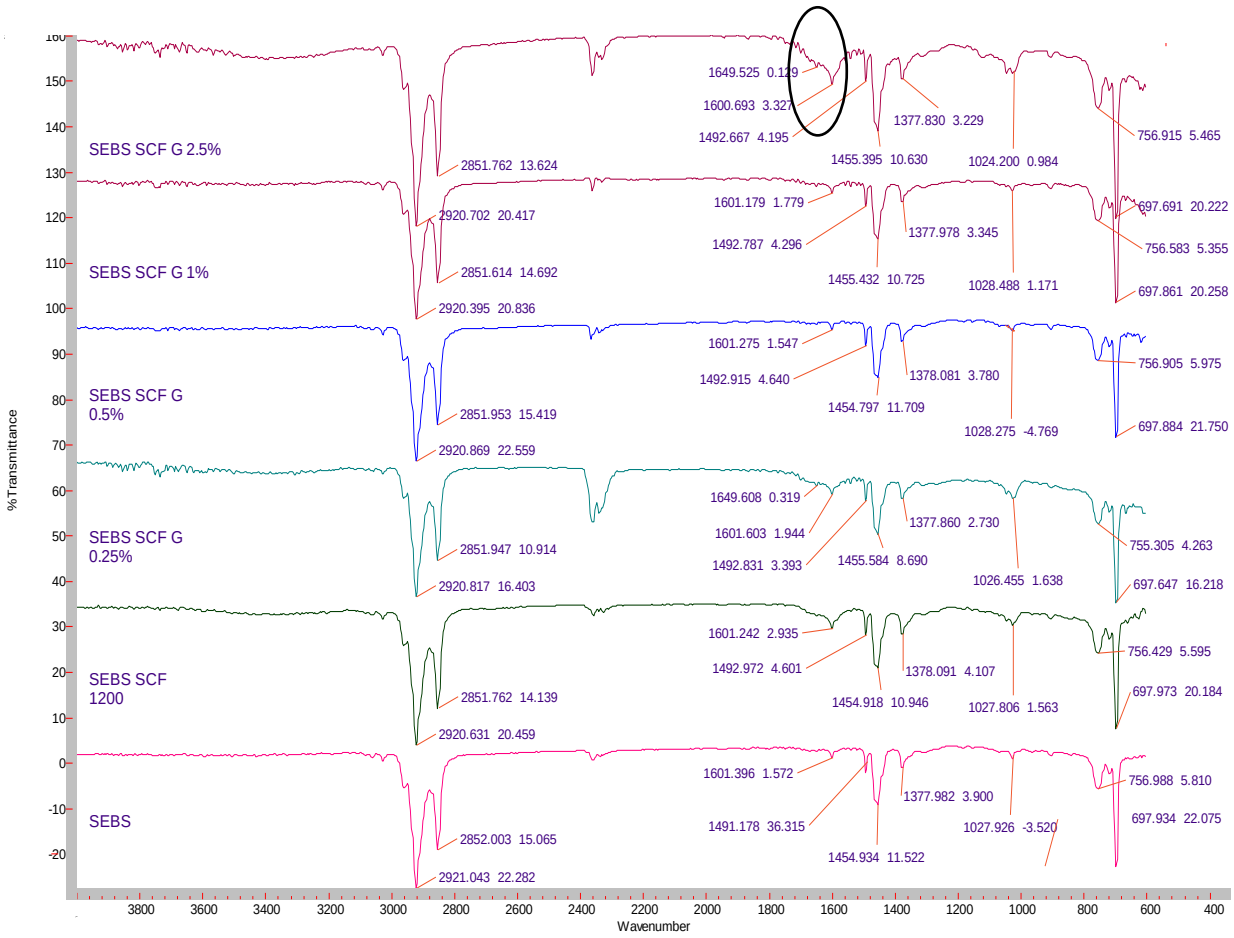

Figure 6.8 Transmittance spectra of porous SEBS graphene composites

The peak between 1250 cm^{-1} and 900 cm^{-1}, represents aromatic CH deformation vibrations within the styrene group. This peak tends to broaden with the addition of graphene, suggesting

graphene interaction with the styrene group of SEBS. The peaks 756 cm^{-1} and 697 cm^{-1} are attributed to a benzene group in the styrene moiety of SEBS.

6.2.5 Tensile Testing of Porous SEBS Graphene Nanocomposites

Figure 6.9 presents the tensile curves of SEBS composites with various graphene contents. The stress was measured up to an elongation of 200% for all samples and no breakage occurred. Both the resilience and toughness was reduced when extruded with $scCO_2$ (red curve) when compared with the virgin SEBS without $scCO_2$ (pink curve). It is evident from the stress-strain curves that no significant change in resilience was observed with the addition of graphene, except for porous SEBS SCF G 0.5% composite. It is suggested that graphene addition of 0.5% brings about an equilibrium between the available polymer sites to interact with graphene particles, which otherwise will agglomerate at the polymer interaction site, specifically as the graphene concentration is increased.

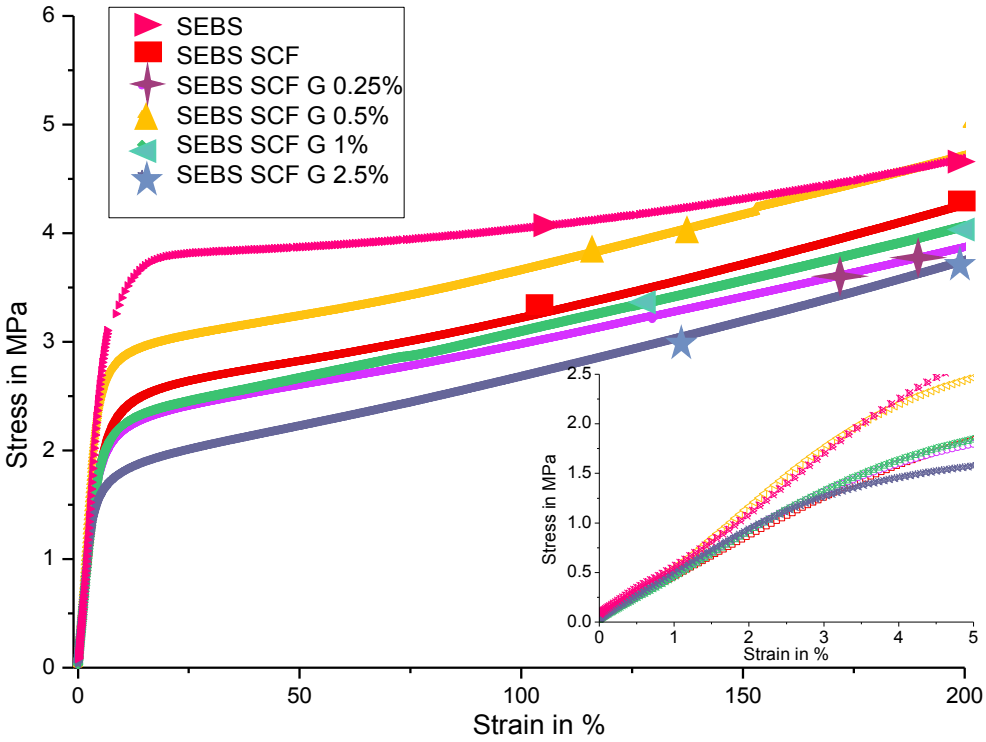

Figure 6.9 Stress vs. strain curves for porous SEBS graphene composites

The decrease in resilience can also be attributed to the formation of more microstructures when extruded with $scCO_2$, which has led to the heterogeneous composite network. This heterogeneity or formation of microstructures is mainly dependent on the dispersion of additives that may lead

to the formation of more microstructures. The modulus of toughness increases upon the addition of more than 0.5% graphene. This suggests that the addition of graphene allows for a perfect balance within the polymer matrix, which further blocks or restricts the easy dislocation motion, thereby increasing the toughness of the composites. A similar increase in the storage modulus on the dynamic mechanical analysis was observed.

Table 6.1 shows Young's modulus measured from the tangent slope obtained from 0.25 to 1% strain. The Young's modulus decreases upon introduction of $scCO_2$ (64 MPa for virgin SEBS and 48 MPa for SEBS SCF). The addition of graphene along with $scCO_2$ results in low Young's modulus at lower graphene concentrations and shows a gradual decrease in Young's modulus in an increase for graphene concentrations more than 0.5%. One reason for such a decrease in Young's modulus can be attributed to poor dispersion created between the polymer chains and graphene, making it inhomogeneous material, thereby, decreasing the modulus. However, at high graphene concentration, the interaction may be higher suggesting the stable formation of interphases, thereby gradually increasing the modulus

Table 6.1 Young's modulus from 0.5% to 1% strain for porous SEBS graphene composites

Sample type	**Young's modulus (tangent slope obtained from 0.5 to 1% strain)**
	MPa
SEBS	64.33±0.003
SEBS SCF	48.41±0.005
SEBS SCF G 0.25%	48.12±0.034
SEBS SCF G 0.5%	55.5±0.0557
SEBS SCF G 1%	47.32±0.119
SEBS SCF G 2.5%	51.65±0.073

6.2.5 Optical Polarised Microscopy of Porous SEBS Graphene Composite

Figure 6.10 shows the polarised optical microscope images at 20x magnification of SEBS SCF G 0.5% and SEBS SCF G 2.5%, representing the effects of graphene loading on the morphology of the extrudates using $scCO_2$. From Figure 6.10, the porous cell structure can be clearly seen at the lower graphene loading of 0.5%; however, at higher graphene loading of 2.5%, the porous cell structure seems to be distorted due to cell coalescence. Such increased cell coalescence can be ascribed to the increase in the viscosity of the polymer melt from graphene exfoliation.

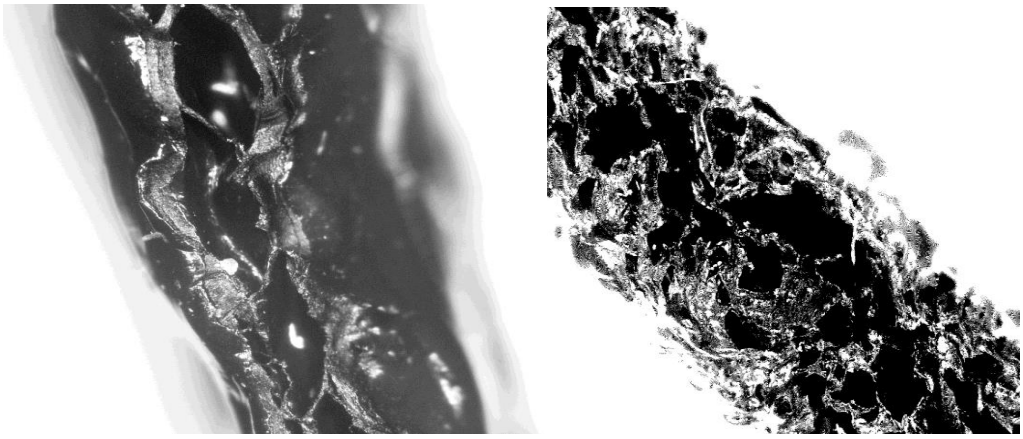

a. SEBS SCF G 0.5% b. SEBS SCF G 2.5%

Figure 6.10 Polarised optical microscope images of a. SEBS SCF G 0.5% and b SEBS SCF G 2.5%

6.3 Key Points for Porous SEBS Graphene Nanocomposites

The first section of this chapter investigated the effect of $scCO_2$ assisted processing of SEBS graphene composites. The following are the key observations made:

- It can be clearly seen from the derivative of the weight change thermogram that SEBSSCF 0.5% has the maximum peak due to a suggested graphene exfoliated phase, which otherwise decreases with higher graphene concentration.
- The results from DSC demonstrate that the relaxation due to entanglement shifts to higher temperatures is due to a suggested increase in the viscosity of the polymer with the introduction of graphene. In addition, the Tg of the S-rich phase is clearly evident with all the SEBS graphene composites due to ascribed graphene interaction with styrene phase leading to microstructure formation.
- The storage modulus is highest for 0.5% suggesting that the graphene particles at 0.5% loading have good interaction/dispersion with the polymer matrix thereby enhancing the stiffness of the composites. The tan delta peak at Tg of styrene rich phase (96 °C) shifts to 103 °C upon the addition of graphene from 0.25% to 2.5%. This shift in peak is indicative of the fact that graphene particles are interacting with styrene rich phases where otherwise a shift in peak would not be a clear observation.
- Addition of graphene along with $scCO_2$ results in low Young's modulus at lower graphene concentrations and demonstrates a gradual increase with graphene concentrations up to 0.5% and decreases for 1% and 2.5% graphene loading. One of the possible reasons for such a decrease in the modulus at 2.5% can be attributed to the actual

processing conditions. The viscosity of the composites increases with higher graphene content, this, in turn, helps the processing of $scCO_2$ assisted extrusion by forming a better plug within the system, thereby increasing the density of the foam. Additional morphology results are needed to support the above

- The aromatic C=C stretching of the aromatic system at peak 1600 cm^{-1} and 1492 cm^{-1} tend to broaden as graphene concentration is increased to 2.5%. This peak usually occurs with an increase in the styrene group, however, with 2.5% graphene loading the concentration at the styrene interaction is higher as graphene particles overlap and agglomerate at the interaction site. The results from FTIR compliment the increase in mechanical properties due to the graphene styrene interaction

6.4 Section 2: Supercritical Fluid Assisted Porous SEBS GO Composites

6.4.1 Thermal Gravimetric Analysis of Porous SEBS Graphene Oxide (GO) Composites

Figure 6.11 and Figure 6.12 show the thermal degradation profile of SEBS GO composites when extruded assisted with $scCO_2$. Paraffin oil was used to reduce the processing temperature (plasticiser) from 235 °C to 140 °C, in order to avoid degradation of GO during the extrusion process. Early degradation of SEBS starts with the addition of paraffin oil as paraffin oil absorbed in SEBS triblock starts to degrade at low temperature.

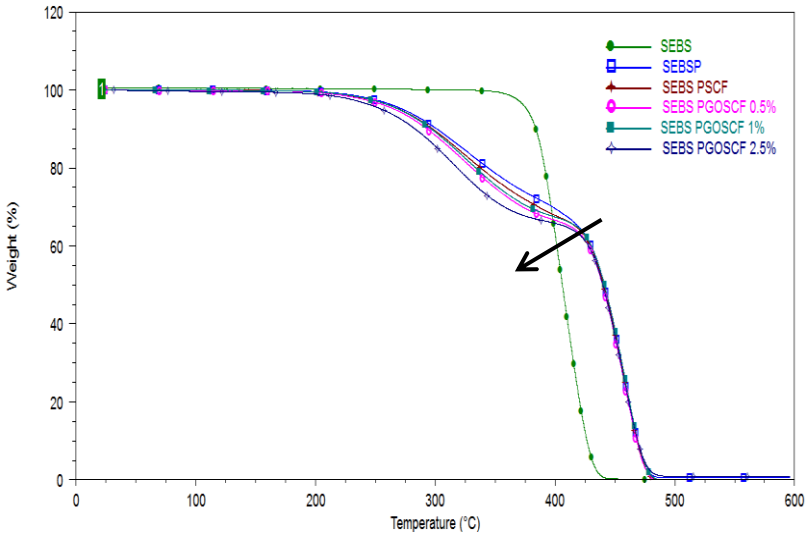

Figure 6.11 Weight percentage thermogram for porous SEBS GO composites

However, it is evident that the paraffin oil enhances the degradation temperature of SEBS triblock compared virgin SEBS as paraffin oil brings structural changes and enhances the microphase separation between the soft and hard block. A small peak is evident at 315 °C on the

virgin SEBSP extrudate which signifies the degradation of paraffin oil within the SEBS. This peak shifts to 324 °C (Figure 6.12)when GO is added into the SEBSP polymer. This suggests that GO interaction enhances the thermal stability of the composites throughout compared to the virgin SEBSP polymer matrix. However, no significant changes can be observed with respect to the maximum degradation temperature, which remains constant with all the GO loading ratios. With increasing the GO loading, the slope maximum degradation temperature decreases due to GO interaction. Usually, the incorporation of filler content tends to enhance the thermal stability of polymer composites. On the contrary, the incorporation of higher GO loading accelerated the decomposition process. This is likely to occur due to the effect of high temperature on the GO particles which tends to strip off the oxygen functional groups (refer to Figure 7.25- Thermal degradation profile of GO).

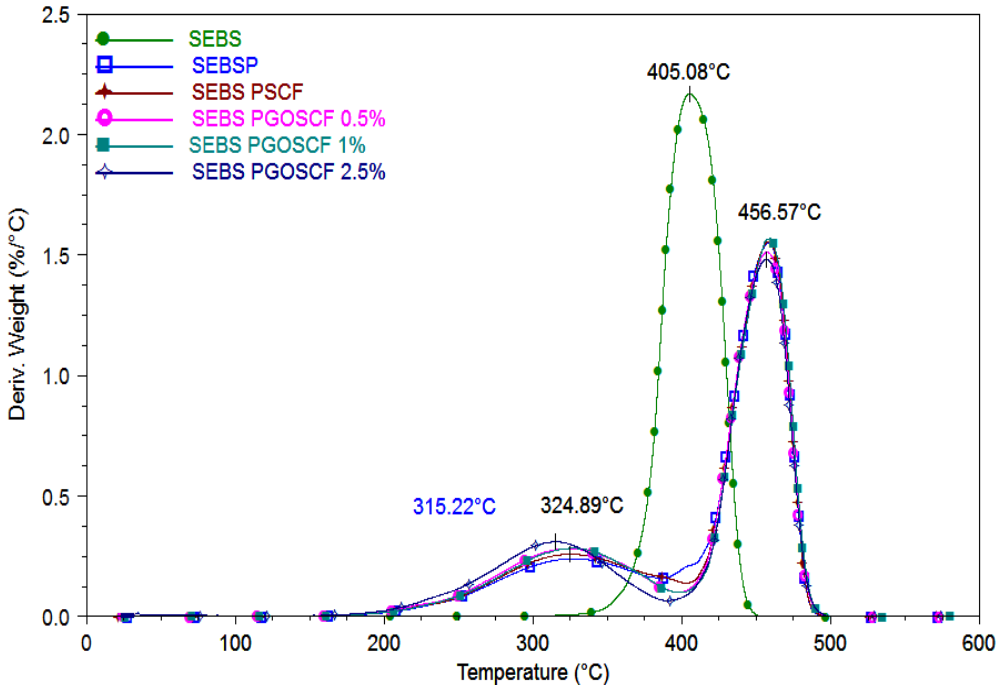

Figure 6.12 Derivative weight percentage thermogram for porous SEBS GO composites

6.4.2 Differential Scanning Calorimetry of Porous SEBS GO Composites

Figure 6.13 shows the heat flow thermogram of $scCO_2$ treated porous SEBS GO composites. The endothermic region found between -25 °C to 25 °C on the samples signifies the densification of the amorphous region (S-rich phase) as the EB block is in the rubbery state. The addition of paraffin oil along with $scCO_2$ shifts the maximum endothermic point towards lower temperatures. This point gradually shifts towards lower temperatures upon addition of GO, up to 2.5% loading. Such continuous shift suggests that there is a restriction imposed by GO particles

on EB block-ordering. One of the major reasons for such flattening of the thermogram is due to the effect of paraffin oil which acts as a plasticiser. For these reasons, a clear Tg of the S-rich phase is evident on all the SEBSP thermograms at around 95 °C, which otherwise is not evident on the virgin SEBS thermogram.

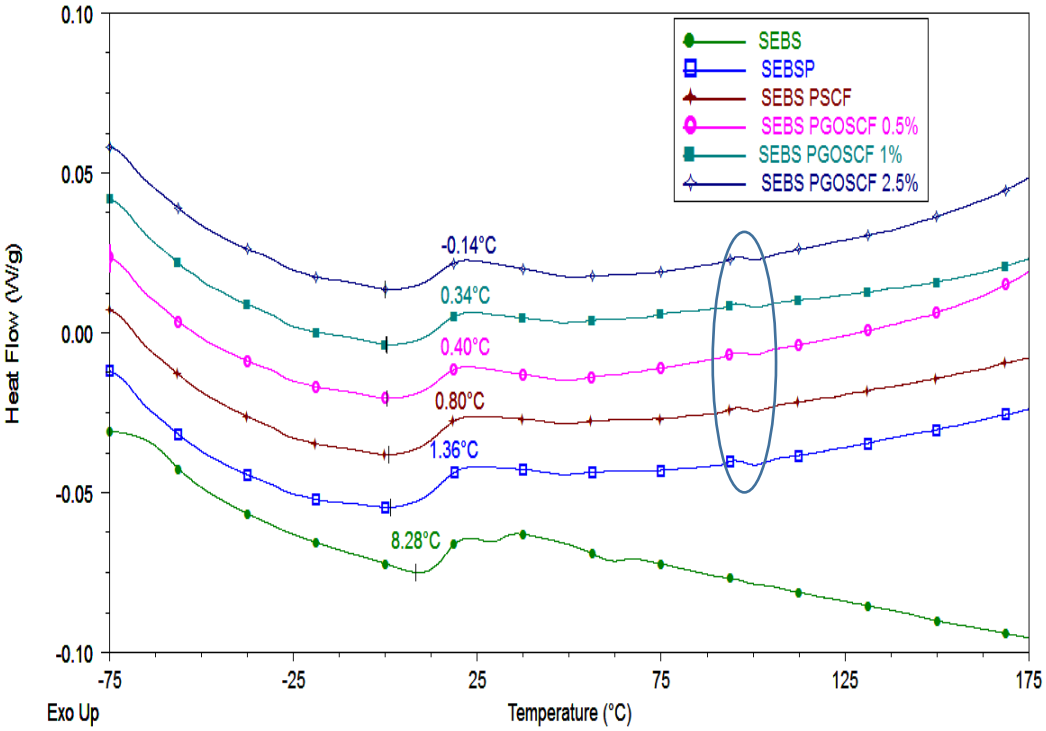

Figure 6.13 Heat flow thermogram of porous SEBS GO composites

The glass transition temperature of ethylene-butylene is –55 °C and the glass transition of S block around 96 °C can be observed from the derivatives of reversing heat capacity curves for virgin SEBS (Figure 6.14). The Tg^{EB} peak shifts to –65 °C with the use of paraffin oil (SEBSP), as paraffin oil acts as a plasticiser, thereby shifting the Tg to lower temperatures. The Tg of the styrene-rich phase remains at around 95 °C, however, this Tg peak seems to be enhanced suggesting the easy movement of the polymer chains. Throughout the thermogram, no significant changes can be observed with the addition of GO particles except for the appearance of additional peaks for loading concentration of 1% and 2.5%. Such peaks usually occur due to the formation of additional microphases or microphase separation as a result of GO interaction with SEBS. The endothermic peak between -10 to 25 °C is mainly due to the glass transition of the EB block, which induces ordering of aromatic structures from intermixed phases and results in the densification of the styrene microphases. This confirms that the addition of GO particles slows down the rearrangement process due to the unavailability of free volume within the polymer matrix.

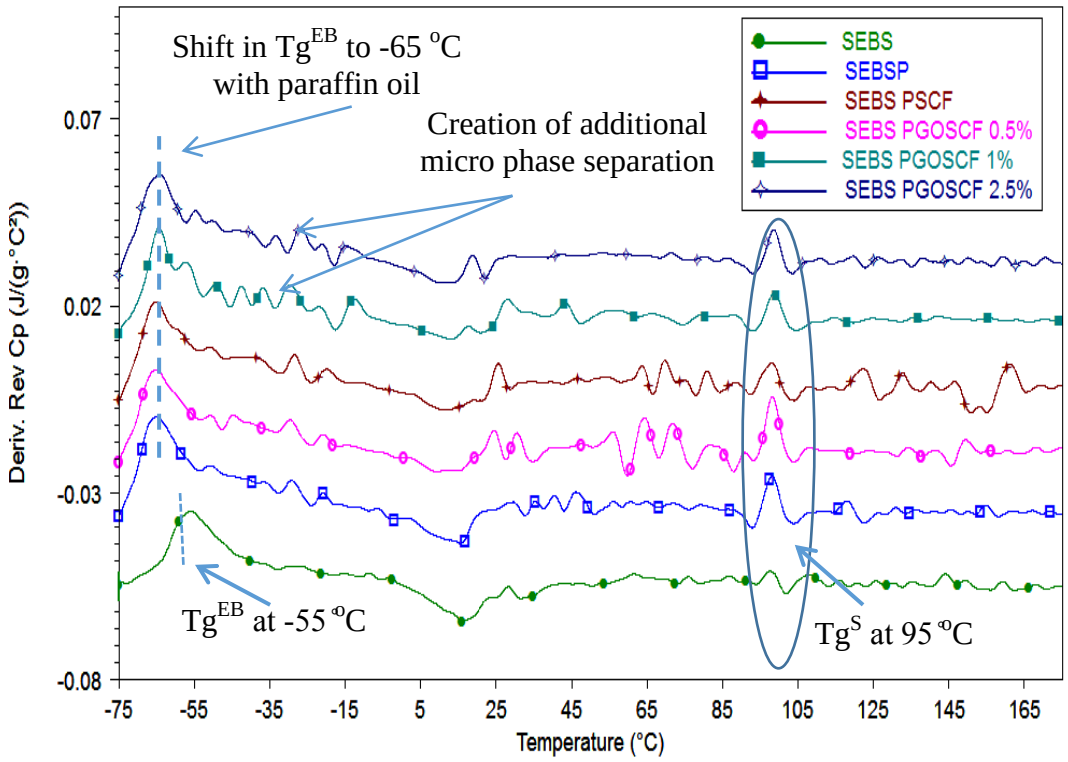

Figure 6.14 Derivative reversing heat capacity thermogram for porous SEBS GO composites

6.4.3 Dynamic Mechanical Analysis of Porous SEBS GO Composites

Figure 6.15 presents the storage modulus at various temperature ranges for porous SEBS GO composites. It is clearly seen that the storage modulus is the highest for 1% GO loading, and decreases to half value for 2.5% loading, with respect to virgin SEBSP. One of the main reasons for such a decrease in the modulus the can be suggested with an increase in the porous nature of the material as GO content is increased (increased viscosity of the material results in the formation of a plug within the extruder barrel resulting in increased coalescence or porosity (similar to results as seen with graphene composites).

Figure 6.16 shows the loss modulus curve for porous SEBS GO composites. The loss modulus representing the viscous nature of the composites is highest for 1% loading. The results obtained from tan delta conclude that; (a) at a sufficiently low temperature (below the onset glass transition temperature of the hard block), all the composite types have almost same tan delta values (Figure 6.17);

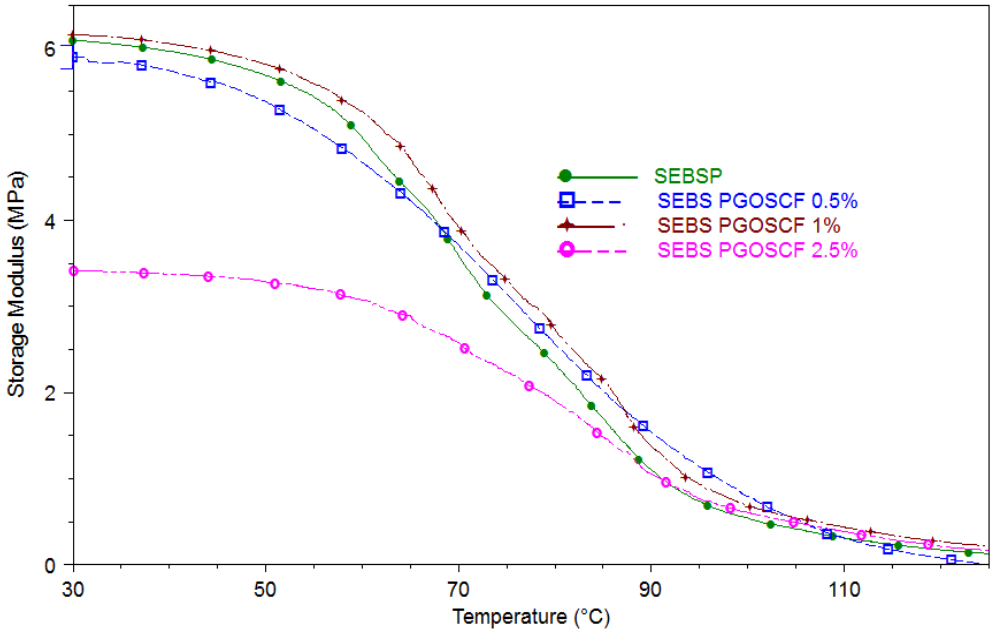

Figure 6.15 Storage modulus curves for porous SEBS GO composites

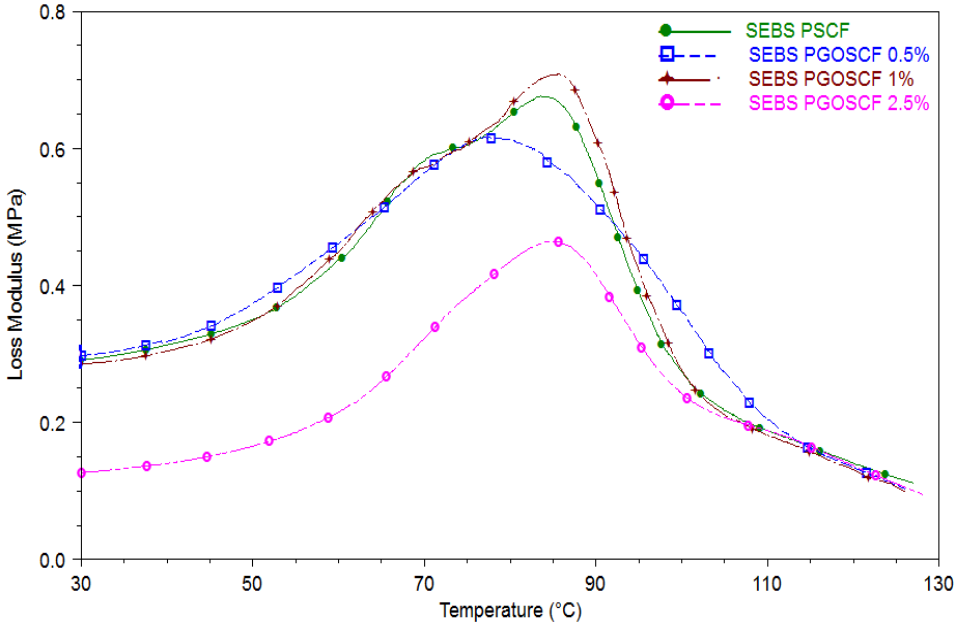

Figure 6.16 Loss modulus curves for porous SEBS GO composites

(b) above the onset glass transition temperature, composites with GO demonstrate slower relaxation of the hard block of a tri-block resulting in a higher reinforcement effect (this phenomenon is greater with an increased percentage of GO) and (c) the formation of a heterogeneous network between GO and S block leads to a decrease in the peak of the tan delta. Such reduced losses will be advantageous in terms of actuation performance (may reduce the back-straightening phenomenon).

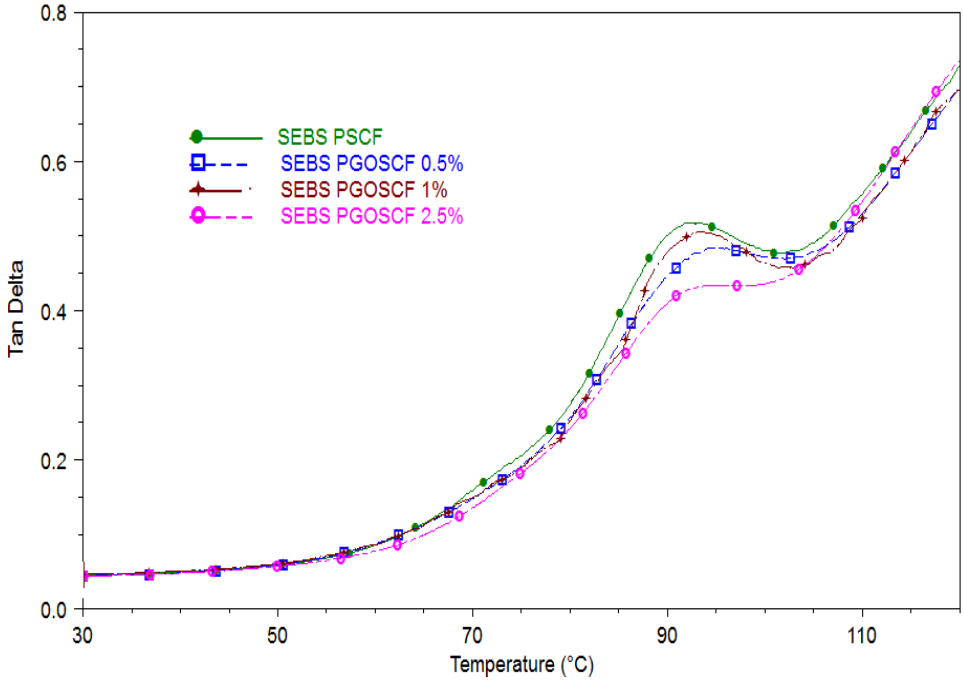

Figure 6.17 Tan delta curves for porous SEBS GO composites

6.4.4 Fourier Transform Infrared Spectroscopy of Porous SEBS GO Composites

ATR-FTIR spectra of transmittance for porous SEBS GO composites with $scCO_2$ are presented in Figure 6.18. Peaks at 2920 cm^{-1}, 2851 cm^{-1}, 698 cm^{-1} and 754 cm^{-1} represent the asymmetrical stretching of $–CH_3$ and $–CH_2$, out-of-plane bending of the CH groups in the styrene ring and vibrations of the CH groups in the aromatic ring. The samples do not show any shifts in these positions with the addition of GO. No significant changes can be observed in the transmittance spectra for porous SEBS GO composites due to the addition of concentrations of additive/filler within the polymer matrix.

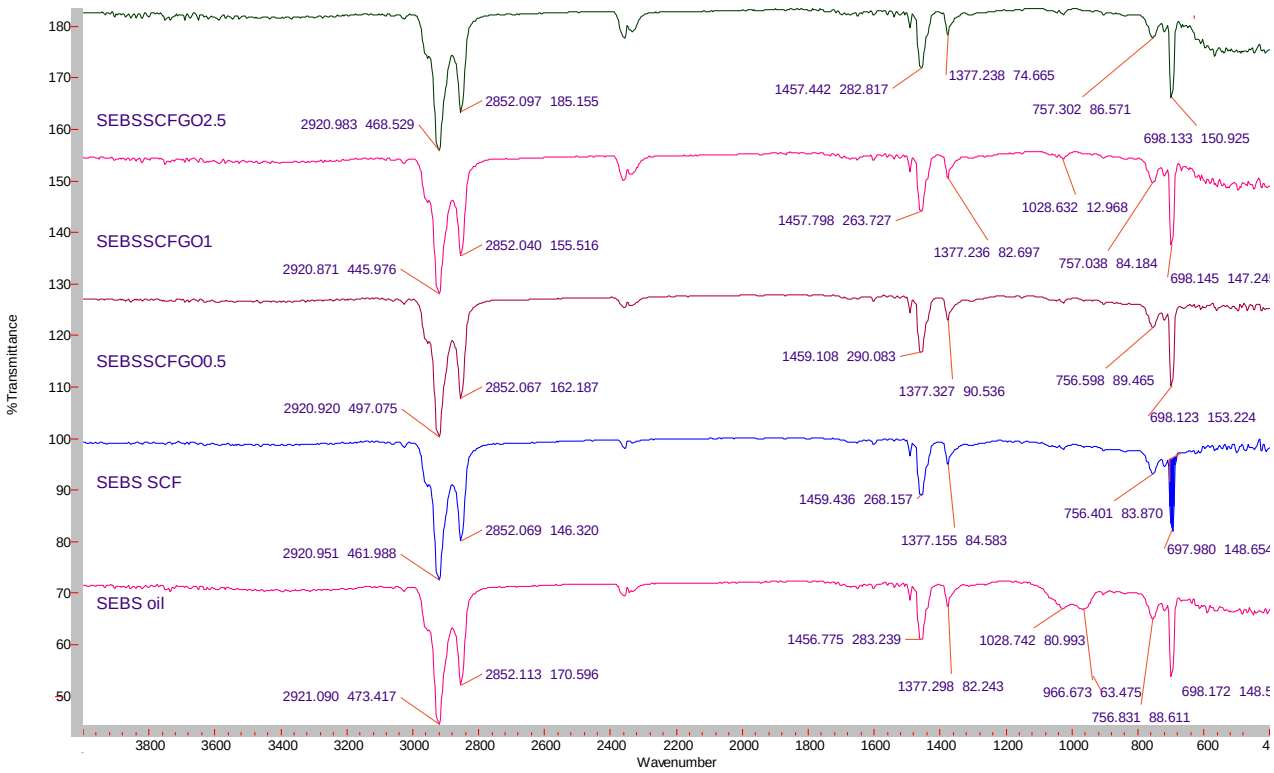

Figure 6.18 Transmittance spectra for porous SEBS GO composites

6.4.5 Tensile Testing of Porous SEBS GO Composites

The stress vs. strain curves for porous SEBS GO composites is presented in Figure 6.19. The zoomed part shows that the modulus of resilience is highest for SEBS with 1% GO loading and lowest for 2.5% loading. Similar results were also noted in the storage modulus curves on the DMA section. In all the cases the modulus of toughness remains higher than that of virgin SEBS PSCF sample.

Table 6.2 Tabulated Young's modulus of SEBSP GO composites

Sample type	**Young's modulus (tangent slope obtained from 0.5 to 1% strain)**
	MPa
SEBS	64.33±0.003
SEBS SCF	48.41±0.005
SEBS PSCF	6.68±0.054
SEBS PGOSCF 0.5%	7.01±0.0657
SEBS PGOSCF 1%	7.78±0.0109
SEBS PGOSCF 2.5%	6.03±0.0523

Addition of paraffin oil sufficiently reduces Young's Modulus as it is highly absorbed by ethylene-butylene block resulting two major effects (a) glass transition temperature of EB block as observed in DSC graphs and makes composites very soft at room temperature and (b) amount of hard block (polystyrene) in the triblock thereby decreasing overall Young's Modulus of triblock

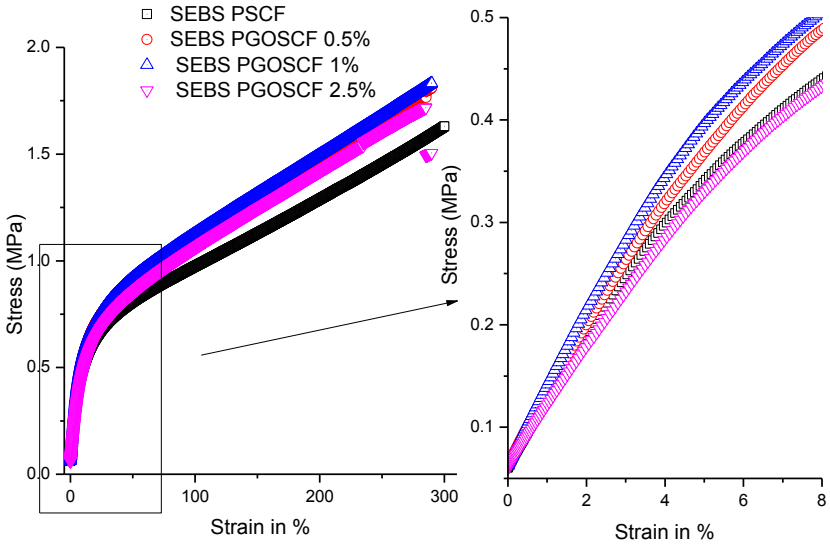

Figure 6.19 Stress vs. strain curves for porous SEBS GO composites

6.5 Key points for Porous SEBS GO Composites

The second section of the chapter investigated the effect of $scCO_2$ assisted processing of SEBS GO composites. The following are the observations made:

- The addition of paraffin oil shows the initial degradation at a very low temperature starting at degradation temperature of paraffin oil, but the degradation temperature of SEBS triblock is enhanced when compared to degradation temperature of virgin SEBS due to the higher microphase separation between the hard and the soft block. A small peak is evident at 315 °C on the virgin SEBSP extrudate shifts to 324 °C suggesting that GO interaction enhances the thermal stability of the composites. The maximum degradation temperature remains constant through all the GO loading ratios.
- The addition of paraffin oil along with $scCO_2$ shifts the maximum endothermic point shifts towards lower temperatures. This point gradually shifts towards lower temperatures upon addition of GO up to 2.5% loading, suggesting that there is a restriction imposed by GO particles on EB block-ordering. The Tg of EB block shifts from -55 °C to -65 °C due to the use of paraffin oil as a plasticiser, However, no change can be observed upon

incorporation of GO particles. The Tg of the S block remains constant throughout at 95 °C, showing the enhanced area under peak which is ascribed to the interaction between the styrene phase and GO particles.

- The storage modulus is the highest for 1% GO loading, and decreases to half value for 2.5% loading with respect to virgin SEBSP due to suggested increase in the porous nature of the material as GO content is increased. The area under Tg broadens upon increasing GO loading suggesting the formation of the heterogeneous network within styrene block.
- The IR spectroscopy spectra do not produce significant peak shifts upon addition of GO.

6.6 Conclusion for Porous SEBS Graphene Based Composites

One of the main factors that need to be considered when dealing with graphene-based composites is the effect of processing on the state of graphene itself, which is if the graphene is exfoliated or agglomerated. In both the cases of graphene and GO SEBS composites, the maximum thermal degradation temperatures do not change with the addition of filler particles. However, in the case of SEBS GO composites altered by paraffin oil, the degradation temperature of paraffin oil slightly shifts to a higher temperature due to suggested interaction with GO particles. The endothermic relaxation of the EB block shifts to higher temperatures upon addition of graphene and GO due to the restriction imposed by filler particles on the EB ordering. The Tg of EB and the S-rich phases do not show any changes upon the addition of the graphene or GO particles, however, the area under Tg of the S-rich phase is enhanced due to a suggested particle interaction with the S-rich phase. The storage modulus was highest for 0.5% graphene loading and 1% GO loading. Similar results can also be observed from the tensile test curves, where at 2.5% loading the mechanical property reduces. The area under the tan delta peak of the S-rich phase is enhanced with higher loading of graphene particles, which indicates good interaction resulting in homogenisation. The same tan delta peak broadens with GO, suggesting the formation of the heterogeneous network. On the polymer composite view, this shows that graphene particles interact better with styrene group, resulting in non-homogenised composites, while GO produces homogenous SEBS composites. The IR spectroscopy also shows similar results on the interaction of graphene particles with the S-rich phase, while no such evident interaction peak can be observed with respect to GO.

7 Investigation of the Effect of Supercritical Carbon Dioxide Assisted Reprocessing of Pebax Graphene-Based Composites

7.1 Introduction

Polymer composite processing techniques are of much interest to manufacturers and scientific research. This is mainly due to their ability to enhance intrinsic properties such as thermal, mechanical and electrical, which can be tuned for diverse applications. One of the main aims of this research was to use supercritical fluid carbon dioxide ($scCO_2$) in order to maintain the intrinsic properties of the filler/additive material and also to enhance the properties of the polymer matrix. Chapter 5 investigated the effect of $scCO_2$ assisted polymer processing of graphene-based (graphene and GO) Pebax porous composites. Although the use of $scCO_2$ assisted extrusion results in a porous matrix as seen in Chapter 4, a research gap, however, still remains in terms of what actually happens when such porous composites are reprocessed without $scCO_2$ in terms of dispersion of additives and the characteristic properties of the composites. Therefore in order to investigate this knowledge gap, the next two chapters concentrate on the investigation of the $scCO_2$ reprocessed polymer matrix of Pebax (Chapter 7) and SEBS (Chapter 8). Such processing of a polymer composite prepared using supercritical carbon dioxide has not been reported elsewhere.

Moreover, the effect of reprocessing such $scCO_2$ assisted polymer extrudates has not been investigated until now. This chapter mainly concentrates on the effects of reprocessing such evenly dispersed porous polymer-graphene composites using traditional extrusion and injection moulding techniques. Graphene was chosen as the filler/additive material with the polymer (Pebax) matrix in the first section of this chapter, mainly due to it excellent intrinsic mechanical and electrical properties. The second section of the chapter uses GO as the filler/additive material. As discussed in the literature review, graphene is relatively hard to produce and difficult to maintain the one atom thick physical property. In addition, the use of graphene particles as filler usually result in the electronic type of EAPs below the percolation threshold. Therefore, GO was also investigated in the second part of this section. GO is a single atomic layer oxidised form of graphene, which is laced with oxygen-containing groups on the surface and edges of the graphene layer. The novelty of this research arises from the fabrication of graphene-based polymer composites using supercritical assisted extrusion and investigating the effects of reprocessing on such a manufactured composite. The effects of processing such membranes are characterised based on the thermal, mechanical and electrical properties.

Differential Scanning Calorimetry (DSC) and Thermal Gravimetric Analysis (TGA) were used to study the thermal characteristics and thermal stability, respectively; Dynamic Thermal Mechanical Analysis (DMA) and tensile test were used to study the mechanical properties; Fourier transform infrared spectroscopy (FTIR) and Transmission Electron Microscope (TEM) were used to understand the chemical composition and possible interaction within the polymer composites; impedance spectroscopy was used to characterise the conductive properties of the manufactured composites.

7.2 Section 1: Pebax Graphene Composites

7.2.1 Throughput Test of Pebax Graphene Composites

To determine the throughput of the extruder with or without SCF, the total output in one-minute was measured for Pebax and Pebax-based nanocomposites 3 times and an average was taken (with all other conditions kept constant) (Table 7.1). It was evident that the total mean weight of Pebax-based composites extruded with SCF increased when compared to unassisted extrusion.

Table 7.1 Average weights of extruded Pebax for 1-minute

Sample type	**Average weight of Pebax based nanocomposite extruded for 1-minute**	
	Without SCF	With SCF Repro
	g	g
Pebax	27.73±3.2	38.76±5.2
PG0.25%	27.98±4.1	40.01±6.2
PG0.5%	27.55±5.3	41.22±4.7
PG1%	26.22±5.9	41.89±4.6
PG2.5%	24.90±4.4	40.56±5.1

This enhanced throughput is attributed to the change in the viscosity of the polymer melt when treated with SCF, which is often called the plasticisation effect. The sorption of $scCO_2$ into the polymer melt results in swelling, in turn causing an increase in the free volume and a reduction in the chain entanglements (reduces the glass transition temperature of the polymer) and thereby decreases the viscosity of the polymer melt. This reduced viscosity results in the easy flow of polymer along the extruder barrel (also reduced load pressure), hence resulting in increased throughput.

7.2.2 Thermal Gravimetric Analysis of Pebax Graphene Composites

The thermal degradation profile of Pebax graphene composites with and without $scCO_2$ is illustrated in Figure 7.1 and Figure 7.2. It is evident from Table 7.2 that the maximum

degradation temperature decreases by 12 °C upon addition of 2.5 wt.% graphene (without $scCO_2$). However, when Pebax graphene composite were extruded with assisted $scCO_2$, the degradation temperature does not show significant changes, while stabilising at 467 °C.

Table 7.2 Degradation temperature of Pebax graphene composites (with and without $scCO_2$)

Sample type	**Maximum degradation temperature**	
	Without SCF	With SCF Reprocessed
	°C	°C
Pebax	469.5	470.1
PG0.25%	467.4	469.4
PG0.5%	465.1	468.5
PG1%	464.8	466.8
PG2.5%	457.0	466.9

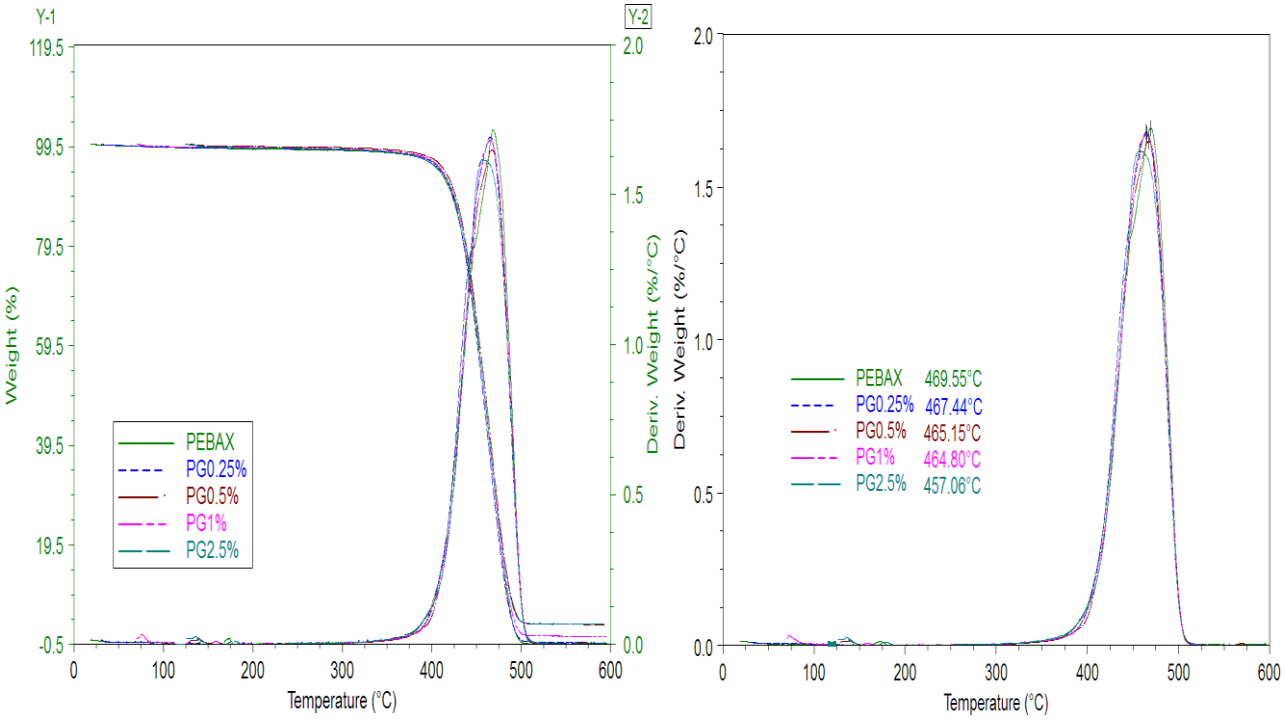

(a) (b)

Figure 7.1 Thermal degradation profiles of Pebax graphene composites without assisted $scCO_2$ (a. Weight Change and b. Derivative weight change)

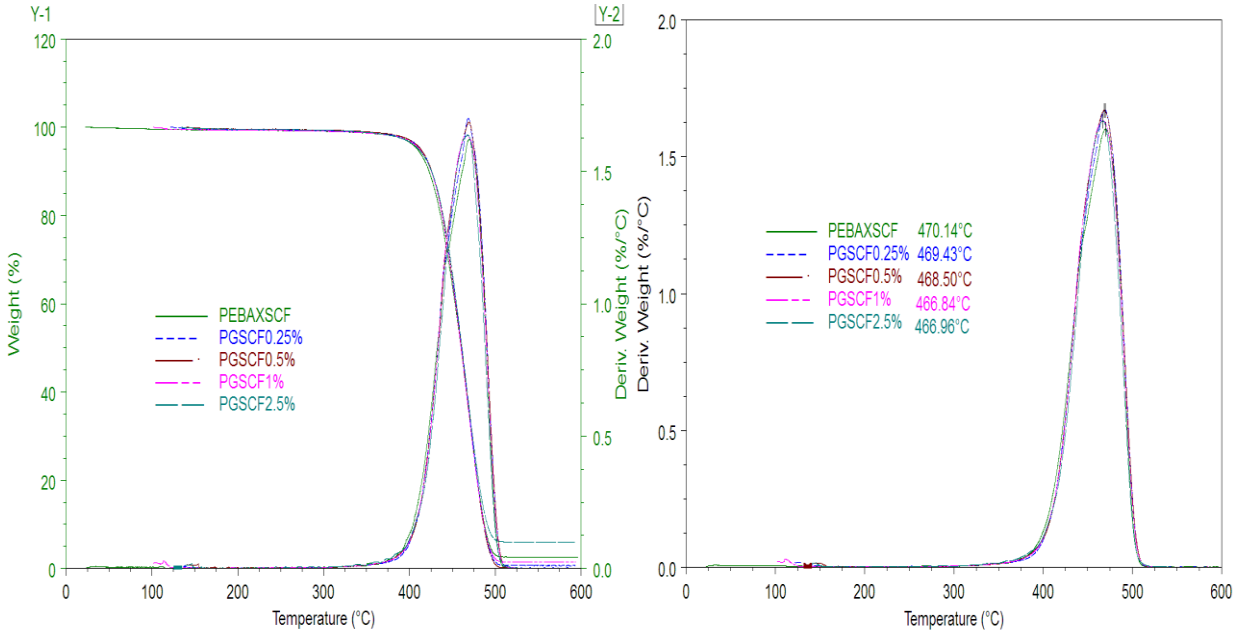

(a) (b)

Figure 7.2 Thermal degradation profile of Pebax graphene composites with assisted $scCO_2$ (a. Weight Change and b. Derivative weight change)

This decrease in degradation temperature by 12 °C upon addition of 2.5 wt. % of graphene (without $scCO_2$) can be attributed to agglomeration of graphene particles into graphite, which in turn results in reduced interaction with Pebax [158-161]. However, when Pebax graphene composite was extruded with $scCO_2$ (Figure 7.2), the degradation temperature does not drastically reduce to lower temperature, but gradually stabilises at 467 °C. This effect of $scCO_2$ on the stability of thermal degradation suggests the ability of $scCO_2$ to induce even dispersion of graphene (reduces agglomeration) within the polymer matrix. This suggested that strong interaction between the polymer matrix and the graphene might have decreased the polymer chain mobility near the graphene Pebax interface, thereby stabilising the thermal degradation temperature.

7.2.3 Differential Scanning Calorimetry of Pebax Graphene Composites

Figure 7.3 and Figure 7.4 show the heat flow thermograms of Pebax graphene composite which was extruded without $scCO_2$ and with $scCO_2$. It is evident from the heat flow curves (both first cycle and second cycle), that the melting temperature does not show much deviation from the virgin Pebax (162.90 °C), even with the addition of graphene (up to 2.5%- in both cases, without $scCO_2$ and with $scCO_2$).

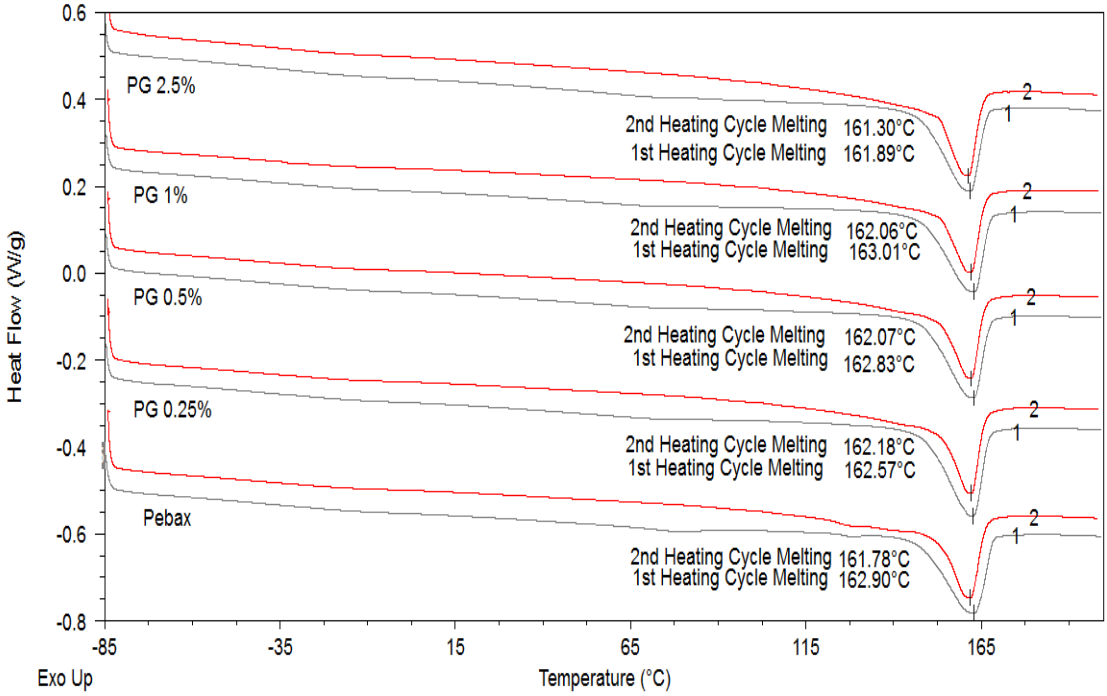

Figure 7.3 Heat flow thermogram of Pebax graphene composites (Step-1 Extrusion, Processed without $scCO_2$)

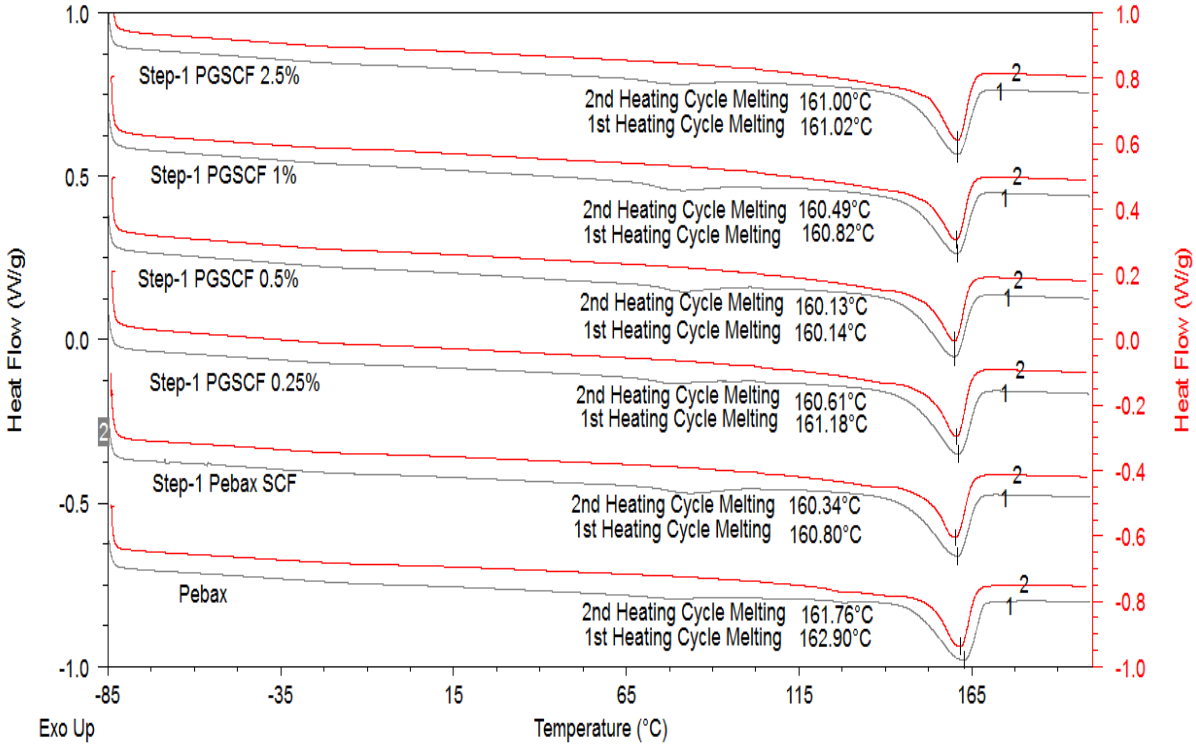

Figure 7.4 First and second heat flow thermogram of $scCO_2$ treated Pebax graphene composite (Step-1, $scCO_2$ assisted extrusion at 1200 psi)

It is evident from Figure 7.5 and Figure 7.6 that the crystallisation temperature gradually shifts towards higher temperatures with the introduction of graphene (even with a smaller percentage of graphene ratio) with $scCO_2$. It is also evident that the crystalline exotherms broaden as the

ratio of graphene filler is increased. During the cooling of the samples from its melt, the graphene fillers are most likely to interact with the polymer, thereby reducing the mobility, resulting in an initiation of density variation within the composites at higher temperatures. The surface of graphene particles act as nucleating sites and further induces crystalline growth. This shift in crystallisation temperature towards higher temperatures shows the effect of graphene acting as heterogeneous nucleating agents, thereby initiating the process of crystallisation at higher temperatures (faster crystallisation process) [162].

It is also evident that the crystalline exotherms broaden as the ratio of graphene filler is increased. This effect can be attributed to the slower radial growth rate of crystals; as higher graphene ratios will result in the formation of more interacting nuclei (more crystals with smaller crystallite size), thereby reducing the mobility of polymer to initiate full crystal growth, and therefore resulting in smaller crystallite size. This influence of crystalline temperature broadening is mainly due to the differentiated size of crystalline aggregates.

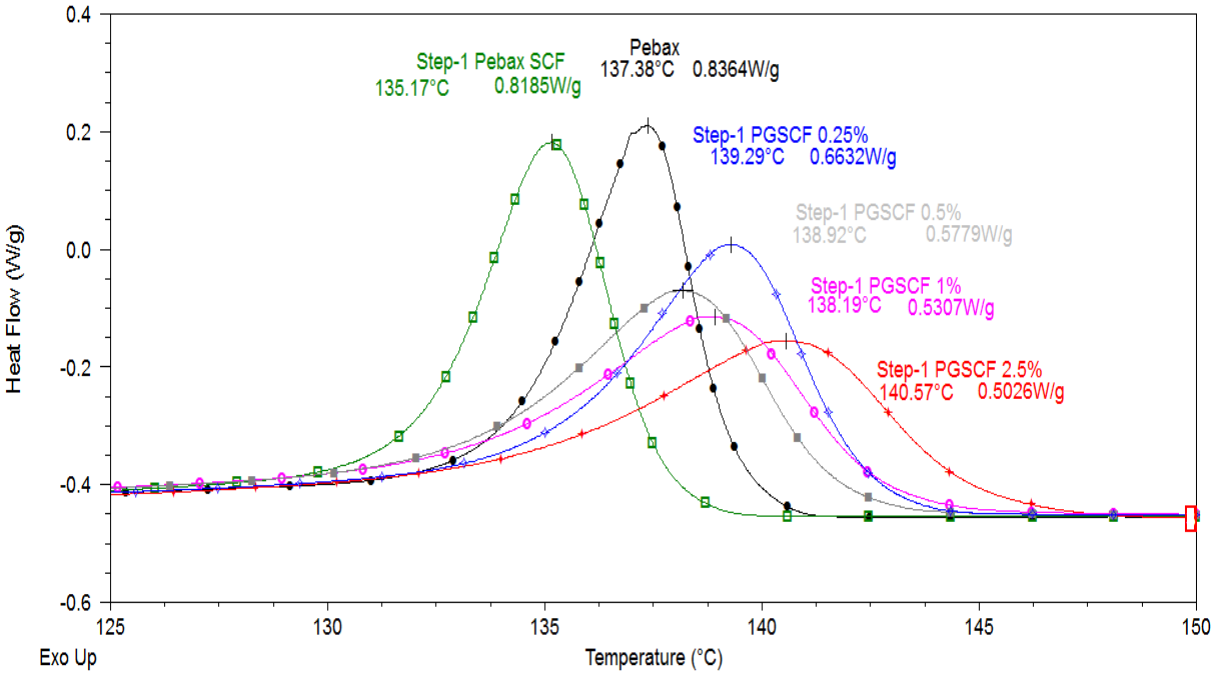

Figure 7.5 Cooling cycles of Pebax graphene composite extruded with $scCO_2$ (Step-1 Extrusion, processed with $scCO_2$)

Figure 7.6 exhibits the comparative crystallisation peaks of Pebax graphene composites, $scCO_2$ assisted extrusion Pebax graphene composites (Step-1) and Step-1 reprocessed Pebax graphene composites (Step-2). It is evident, that the first step composite extrusion without $scCO_2$ produces a heterogeneous polymer composite (higher crystallisation temperature), while $scCO_2$ assisted extrudates (Step-1) and reprocessed extrudates (Step -2) resulted in lowering of crystallisation

temperature, thereby manufacturing a homogeneous polymer matrix (evenly dispersed polymer matrix). However, as the graphene percentage within the polymer matrix is increased to 2.5%, the effect of $scCO_2$ (i.e. reduction in the crystallisation temperature) does not change the crystallisation temperature. The crystallisation temperature almost remains the same but a reduced/broadening of the peak can be observed. This suggests that supercritical fluid treatment does not affect the homogeneity of higher graphene percentage. This can be attributed to saturation/unavailability of polymer interactive sites to interact with the graphene surface, where each graphene particle act as nuclei for further crystal growth.

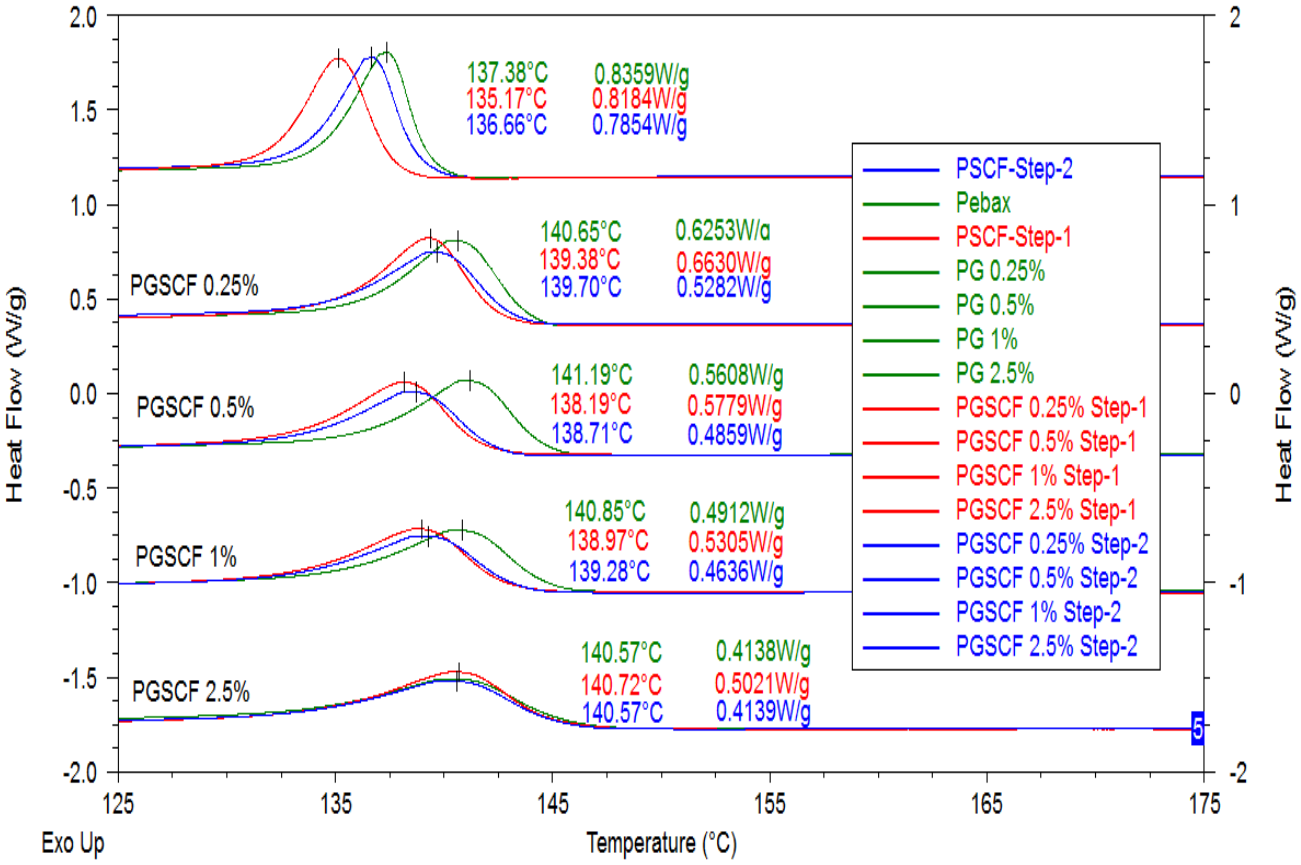

Figure 7.6 Cooling cycles of Step-1 and Step-2 Pebax graphene composite

7.2.3.1 Isothermal Crystallisation Kinetics of Pebax Graphene Reprocessed Polymer Composites

The Avrami model was used to understand the isothermal crystallisation kinetics of reprocessed Pebax graphene-polymer composites at various percentages of graphene loading levels. The Avrami model is clearly described in the methodology section of Chapter 3 (3.4.3.1). The parameters n and k can be obtained from the slope and the intercept of the Avrami plot of log [-ln (1-X(t))] vs. log t. Table 7.3 shows the parameter n and k along with $t_{1/2}$ values, which were obtained from the heat flow thermograms and the theoretically calculated value. The value of n

is found between 2 and 3 for all the samples, indicating complex fibrillar two-dimensional crystallite structure.

The k value tends to decrease with increasing isothermal temperatures for all the samples. The value of k for samples that are processed without $scCO_2$ increases up to 0.5% loading, highest being 0.5% (9.12) and then slowly decreases and settles for 1% and 2.5% graphene loading (6.02). The value of k for samples treated with $scCO_2$ was much lower than the untreated virgin counterpart.

Table 7.3 Avrami parameters of Pebax graphene composites (with and without $scCO_2$) under isothermal conditions

Sample type	Tm (°C)	n	Log k	k	$t_{1/2}$* (min)	$t_{1/2}$ (min)	G (min^{-1})	R^2
Pebax	141	2.55	0.50	2.97	0.52	0.54	1.8	0.999
	142	2.65	0.23	1.71	0.69	0.71	1.4	0.999
	143	**2.69**	**-0.07**	**0.85**	**0.88**	**0.92**	**1.0**	**0.999**
	144	**2.85**	**-0.38**	**0.41**	**1.16**	**1.19**	**0.8**	**1.000**
PebaxSCF	141	2.56	0.40	2.51	0.56	0.60	1.6	0.999
	142	2.84	0.19	1.54	0.72	0.75	1.3	0.999
	143	**2.70**	**-0.07**	**0.83**	**0.91**	**0.93**	**1.0**	**0.999**
	144	**2.89**	**-0.37**	**0.42**	**1.16**	**1.18**	**0.8**	**1.000**
	145	2.94	-0.71	0.19	1.53	1.54	0.6	1.000
	146	3.20	-1.17	0.067	2.06	2.06	0.4	1.000
PG 0.25	**143**	**2.00**	**0.80**	**6.30**	**0.31**	**0.33**	**3.0**	**0.999**
	144	**2.26**	**0.65**	**4.46**	**0.41**	**0.43**	**2.3**	**0.999**
	145	2.30	0.43	2.69	0.53	0.55	1.8	0.999
	146	2.54	0.21	1.62	0.70	0.71	1.4	1.000
	147	2.71	-0.10	0.79	0.95	0.95	1.0	1.000
	148	2.81	-0.40	0.39	1.25	1.22	0.8	0.999
PGSCF 0.25	**143**	**2.24**	**0.61**	**4.07**	**0.42**	**0.45**	**2.2**	**0.999**
	144	**2.36**	**0.45**	**2.81**	**0.52**	**0.55**	**1.8**	**0.999**
	145	2.61	0.23	1.69	0.69	0.70	1.4	1.000
	146	2.51	-0.007	0.98	0.86	0.86	1.1	1.000
	147	2.57	-0.29	0.50	1.13	1.13	0.8	1.000
	148	2.63	-0.62	0.23	1.51	1.50	0.6	0.999
PG 0.5	**143**	**2.14**	**0.95**	**9.12**	**0.30**	**0.29**	**3.4**	**0.999**
	144	**2.26**	**0.80**	**6.30**	**0.36**	**0.37**	**2.7**	**0.999**
	145	**2.41**	**0.58**	**3.80**	**0.49**	**0.49**	**2.0**	**0.999**
	146	2.53	0.33	2.13	0.63	0.64	1.5	1.000
	147	2.60	0.095	1.24	0.79	0.79	1.2	1.000
	148	2.56	-0.191	0.64	1.01	1.02	0.9	0.999
PGSCF 0.5	**143**	**2.47**	**0.53**	**3.38**	**0.51**	**0.52**	**1.9**	**1.000**
	144	**2.67**	**0.30**	**1.99**	**0.66**	**0.67**	**1.4**	**1.000**
	145	**2.55**	**0.03**	**1.07**	**0.83**	**0.84**	**1.1**	**1.000**
	146	2.97	-0.35	0.44	1.17	1.15	0.8	0.999

	147	2.80	-0.65	0.22	1.53	1.49	0.6	0.999
	148	2.81	-1.14	0.07	2.18	2.23	0.4	0.999
PG 1	**144**	**2.05**	**0.78**	**6.02**	**0.31**	**0.34**	**2.9**	**0.999**
	145	**2.41**	**0.72**	**5.24**	**0.41**	**0.43**	**2.3**	**0.999**
	146	2.39	0.38	2.39	0.56	0.59	1.6	1.000
	147	2.73	0.12	1.31	0.79	0.79	1.2	0.999
	148	2.90	-0.23	0.58	1.08	1.05	0.9	0.999
	149	2.79	-0.56	0.27	1.39	1.39	0.7	0.999
PG SCF 1	**144**	**2.20**	**0.46**	**2.88**	**0.51**	**0.52**	**1.9**	**1.000**
	145	**2.54**	**0.22**	**1.65**	**0.70**	**0.70**	**1.4**	**1.000**
	146	2.71	-0.06	0.87	0.93	0.91	1.0	0.999
	147	2.77	-0.39	0.40	1.22	1.21	0.8	1.000
	148	2.78	-0.77	0.16	1.68	1.65	0.6	0.999
	149	2.85	-1.18	0.06	2.23	2.28	0.4	0.999
PG 2.5	**145**	**2.60**	**0.78**	**6.02**	**0.42**	**0.43**	**2.3**	**1.000**
	147	**2.91**	**0.01**	**1.02**	**0.89**	**0.87**	**1.1**	**0.999**
	148	2.43	-0.25	0.56	1.09	1.09	0.9	1.000
	149	2.63	-0.64	0.22	1.49	1.52	0.6	0.999
	150	2.72	-0.96	0.10	1.91	1.97	0.5	0.999
PGSCF 2.5	**147**	**2.71**	**0.13**	**1.34**	**0.78**	**0.78**	**1.2**	**0.999**
	148	2.68	-0.19	0.64	1.04	1.02	0.9	0.999
	149	2.42	-0.49	0.32	1.35	1.37	0.7	1.000
	150	2.63	-0.88	0.13	1.81	1.87	0.5	0.999
	151	2.82	-1.29	0.05	2.46	2.69	0.3	0.999

For example, Pebax @ 141 °C has a k value of 2.97 while PebaxSCF @ 141 °C has a k value of 2.51 and PG 0.5 @ 143 °C has a k value of 9.12 while PGSCF 0.5 @ 143 °C has a k value of 3.38. The lower k value, when treated with $scCO_2$ suggests a better interaction between the polymer chains and the graphene particles which further reduces the availability of nucleation sites and imposes a restriction on the free movement of the polymer chains, hence reducing the rate of crystallisation. The $t_{1/2}$ value decreases upon addition of graphene particles up to 1% and increases for 2.5% suggesting that graphene particles are acting as nucleating agents up to 1% and agglomerates at 2.5%. The lowering crystallisation rate can also be understood by increasing $t_{1/2}$ value (lower crystallisation rate – longer time required to reach 50% crystallisation) for samples that are treated with $scCO_2$. Clearly, the $t_{1/2}$ value of $scCO_2$ treated is much higher than that of the untreated virgin samples, in addition, this value is highest for 0.5% and gradually tends to decrease till 2.5% loading. This suggests that $scCO_2$ initiates exfoliation and improved interaction of graphene particles which further restricts the nucleation and the growth process, however, as the loading concentration is increased, agglomeration of graphene particles results in free space, therefore lesser time to crystallise.

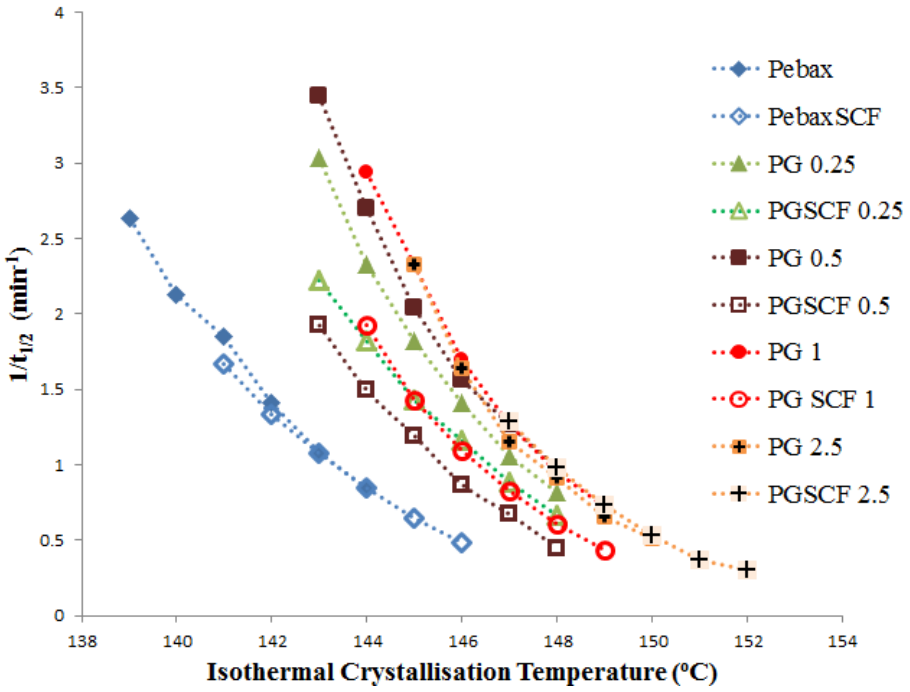

Figure 7.7 Crystallisation rate at various temperatures for Pebax graphene composite (with and without $scCO_2$) under isothermal conditions

Figure 7.7 presents $G=1/t_{1/2}$, (which can also be referred to as the crystallisation rate) plotted vs. various isothermal temperatures. It can be clearly seen that the crystallisation rate increases upon addition of graphene particles, however, the crystallisation rate decreases when the composites were treated with $scCO_2$ (suggesting exfoliation and improved interaction of graphene particles with the polymer chain). The rate of crystallisation stabilises for 2.5% with or without $scCO_2$ and remains the same at varying temperatures.

Table 7.4 Arrhenius Activation Energy of Pebax graphene composites (with and without $scCO_2$) under isothermal conditions

Samples	Arrhenius Activation Energy (KJ/mol)	Isothermal Crystallisation Range (°C)
Pebax	-356.488	141 - 144
PebaxSCF	-315.982	141 - 144
PG 0.25	-351.308	143 - 146
PGSCF 0.25	-310.436	143 - 146
PG 0.5	-357.111	143 - 146
PGSCF 0.5	-368.252	143 - 146
PG 1	-386.518	144 - 147
PGSCF 1	-391.007	144 - 147
PG 2.5	-428.213	147 - 150
PGSCF 2.5	-436.843	147 - 150

The Arrhenius equation was used to determine the activation energy under isothermal conditions. The slope of the plot ln (K)*1/n vs. 1/Tc determines the ΔE/R as shown in Figure 7.8 and the calculated activation energy tabulated in Table 7.4. It is obvious that the activation energy decreases for 0.25% and gradually starts to increase to 2.5% graphene loading. When the samples are treated with $scCO_2$, the activation energy is lower than their counterpart at low loading (up to 0.25%), however, the $scCO_2$ graphene composites have higher activation energy for 0.5, 1 and 2.5% compared to the untreated composites.

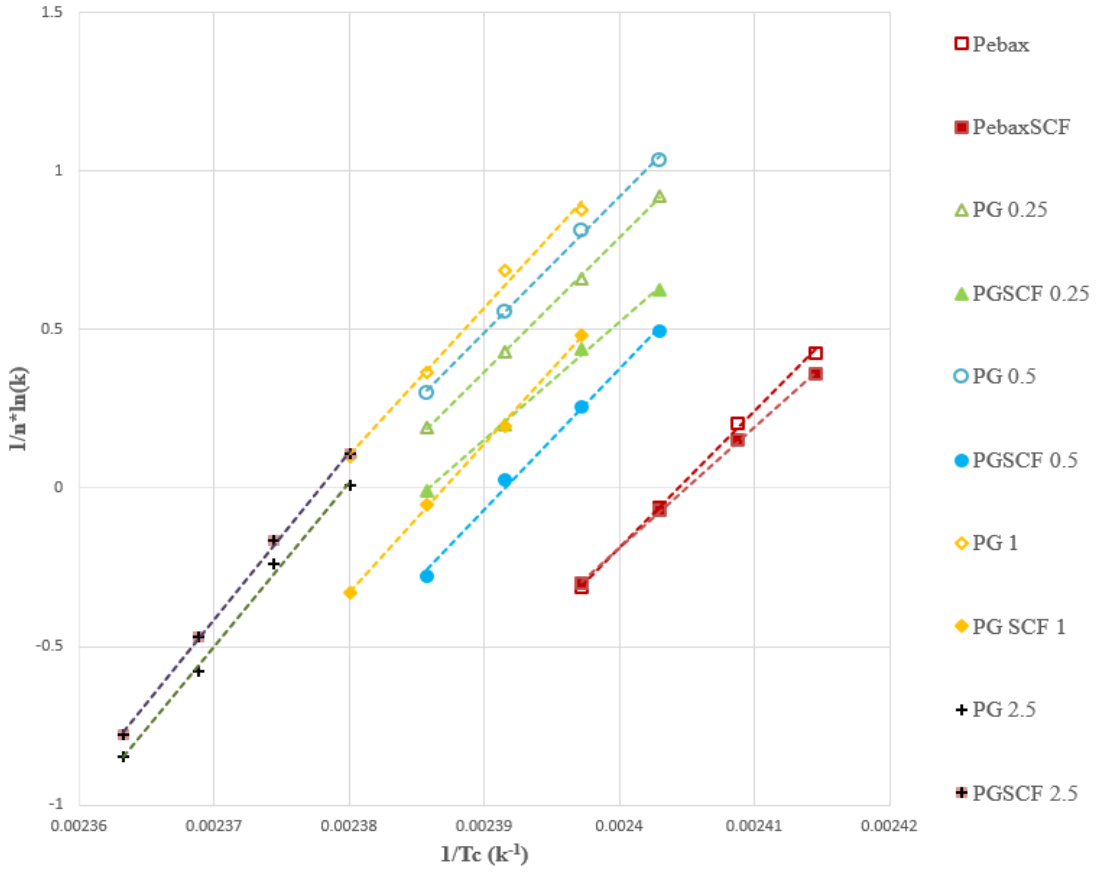

Figure 7.8 Arrhenius Activation Energy plot of Pebax graphene composites (with and without $scCO_2$) under isothermal conditions

These results indicate that at low graphene loadings, graphene acts as nucleating sites, however as the loading is increased the interfacial interactions restrict the easy movement to crystal growth, thus increasing the activation energy. One of the major observations that can be noted is that the PebaxSCF (315 KJ/mol) activation energy is far less than that of the virgin Pebax (356 KJ/mol). The k, $t_{1/2}$ and G values of $scCO_2$ treated Pebax are much lower than the virgin Pebax, suggesting a slow crystallisation rate, due to homogenisation between the hard block and the soft block. However, the activation energy tends to decrease, which otherwise should have increased depending on the Avrami hypothesis. This suggests that the reduction of activation energy may

be due to faster growth rate and not due to the nucleation rate, where $scCO_2$ allows slower re-crystallisation in a more favourable manner.

7.2.3.2 Non-Isothermal Crystallisation Kinetics of Reprocessed Pebax Graphene Composites

The non-isothermal crystallisation kinetics of Pebax-graphene nanocomposites with (reprocessed) and without $scCO_2$ was studied under various cooling rates. The thermogram for virgin Pebax at various non-isothermal conditions is shown in Figure 7.9. It can be clearly observed that the crystallisation onset temperature (Tc_{on}), peak crystallisation temperature (Tc) and crystallisation offset temperature (Tc_{off}) shifts to lower temperature and become broader with an increase in the cooling rate from 2.5 °C/min to 20 °C/min, suggesting heterogeneous nucleation with the addition of graphene (Tc shifts to higher temperature-samples without $scCO_2$ - Table 7.5). The DSC thermograms also demonstrate that the crystallisation process occurs much faster at the higher cooling rates when compared to lower cooling rates. The crystallisation enthalpy (ΔHc) also decreases with increasing cooling rates for all samples, which is attributed to changing nucleation densities with the different cooling rates.

Table 7.5 Tabulated Tc_{on},Tc,Tc_{off} of Pebax graphene composites (with and without $scCO_2$) under non-isothermal conditions

Sample Type	Cooling Rate (°C/min)	Tc_{on} (°C)	Tc_{off} (°C)	Tc (°C)	ΔHc (J/g)	Xc (%)
Pebax	2.5	144.11	113.14	140.91	40.36	38.40
	5	140.54	108.24	137.05	39.07	35.09
	10	136.74	105.15	132.70	36.88	51.11
	20	131.84	80.02	127.54	37.32	26.97
PebaxSCF	2.5	146.49	100.02	141.40	39.36	37.39
	5	142.88	100.03	137.32	38.21	37.26
	10	138.35	88.91	132.92	38.19	35.34
	20	133.97	83.31	127.75	35.93	34.48
PG 0.25	2.5	148.36	119.30	144.04	36.58	36.55
	5	145.39	106.02	140.39	36.15	37.55
	10	141.29	99.01	136.36	37.02	36.32
	20	138.22	94.99	131.82	35.65	40.60
PGSCF 0.25	2.5	147.44	125.33	143.09	34.27	36.38
	5	144.21	102.23	139.35	40.41	29.57
	10	140.87	95.98	135.35	38.99	27.18
	20	136.80	95.80	130.77	36.85	31.28
PG 0.5	2.5	148.65	122.22	144.34	34.72	39.50
	5	145.05	112.10	140.04	34.68	37.39
	10	141.59	103.06	136.03	33.41	33.34
	20	137.86	100.01	131.21	32.05	31.99
	2.5	146.88	113.14	142.00	35.42	31.62

PGSCF 0.5	5	143.42	108.01	138.07	35.54	31.90
	10	139.84	98.85	133.77	34.16	31.26
	20	136.65	95.87	128.75	34.34	31.39
PG 1	2.5	148.62	116.33	144.29	36.84	35.10
	5	146.25	105.32	140.86	36.96	39.70
	10	143.81	98.30	136.97	36.43	30.14
	20	139.39	98.00	131.56	34.64	17.33
PG SCF 1	2.5	147.67	107.72	142.62	39.16	29.59
	5	144.50	104.27	138.86	37.28	31.35
	10	141.65	95.60	134.79	36.75	29.65
	20	137.96	97.62	129.96	34.31	29.40
PG 2.5	2.5	149.51	105.11	143.47	39.62	30.40
	5	147.44	97.30	140.3	39.11	23.02
	10	145.21	97.00	136.55	36.26	30.12
	20	142.07	96.02	132.31	34.69	33.20
PG SCF 2.5	2.5	149.29	118.52	143.76	33.29	32.89
	5	147.24	113.03	140.44	31.65	33.74
	10	145.13	100.76	136.82	32.05	31.32
	20	142.24	99.35	132.20	31.76	34.00

The Avrami equation was used to understand the non-isothermal crystallisation kinetics. The degree of phase conversion is given by the equation, $X(t) = 1 - e^{-kt^n}$, Where, k is the Avrami constant describing the nucleation rate and the growth rate. 'n' is the Avrami exponent which is dependent on the process dimensionalities (refer to Chapter 3). Plots of log (-ln (1 – X(t))) versus log t are shown in Figure 7.10 for Pebax graphene composites with and without $scCO_2$. The corresponding Avrami parameters n and k were obtained from the slope and intercept of the plots and are listed in Table 7.6. In addition, $t_{1/2}$ (calculated from Equation. 4) and corresponding R^2 values are tabulated in Table 7.6 for all the Pebax graphene composites with and without $scCO_2$. The value of k' increases with increasing cooling rate and the $t_{1/2}$ decreases with increasing cooling rate. As observed in the isothermal crystallisation kinetics, the k' value decreases upon addition of graphene from 0.80 for virgin Pebax to 0.29 for PebaxSCF, suggesting slow crystallisation kinetics (time taken to reach 50% crystallisation also increases).

Kazarian [23] reported that $scCO_2$ plasticisation of the semi-crystalline polymer may induce the formation of crystallites, where $scCO_2$ induces mobility of polymer chain which then allows them to rearrange into the kinetically more favourable configuration. Therefore, a lower k' value for $scCO_2$ assisted samples (specifically PebaxSCF) suggests $scCO_2$ reduces the crystallisation and growth rate in order to initiate formation of perfect crystallite (note that the n values for $scCO_2$ are greater than 3). This $scCO_2$ initiated the process of rearrangement into kinetically favourable manner has resulted in a slow crystallisation rate with larger $t_{1/2}$. With the introduction

of graphene particles (processed without $scCO_2$), the k' value decreases from 0.80 for Pebax to 0.29 PG 0.25% and continues to decrease until PG 2.5% (0.09), suggesting slow crystallisation rate due to a hindrance to free chain movement upon addition of graphene particles.

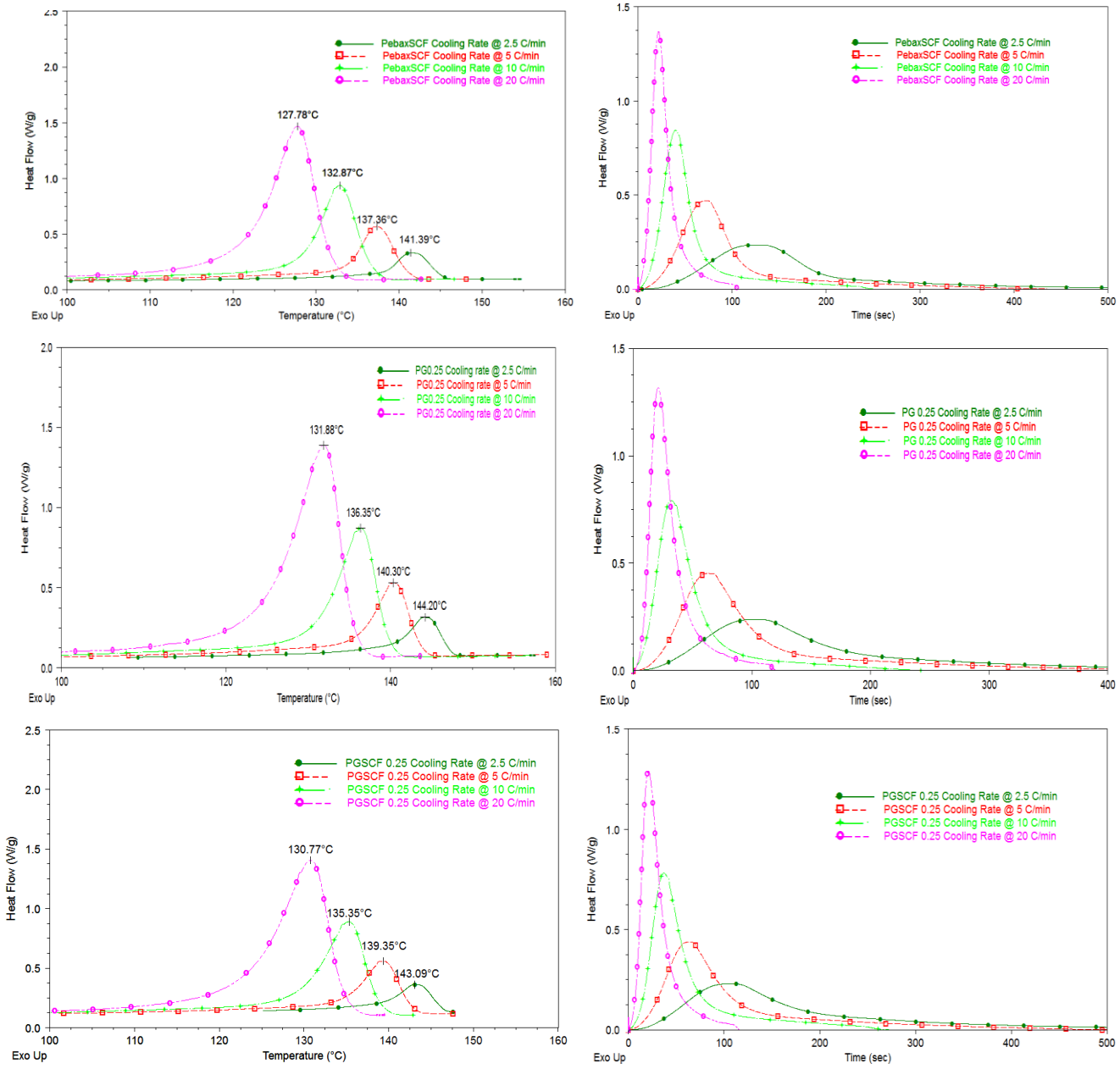

Figure 7.9 Heat flow plots vs. temperature and time plot of Pebax graphene composites (with and without $scCO_2$) under non-isothermal conditions

The k' value tends to decrease when processed with $scCO_2$, suggesting that $scCO_2$ processing may have resulted in exfoliation which in turn enhances the polymer graphene interaction, thereby imposing restrictions on the crystal growth. A similar decrease in the value of k' was also reported by Zhang et al [145] for nylon6/graphene composites, where such decreasing k' upon addition of graphene was attributed to a negative effect on crystallisation mainly as

graphene particles restrict migration and diffusion of the polymer chains to the surface of the nucleus (slow crystallisation process – longer time).

Another important observation is the shift of the n values from 2 to 3 specifically when the samples were processed with $scCO_2$. The average n values for samples extruded without $scCO_2$ are 2.57 for virgin Pebax, 2.99 for PG 0.25%, 2.76 for PG 0.5%, 2.72 for PG 1% and 2.68 for PG2.5 %. The average n values for samples extruded with $scCO_2$ are 3.06 for virgin PebaxSCF, 3.16 for PGSCF 0.25%, 3.43 for PGSCF 0.5%, 3.45 for PGSCF 1% and 3.15 for PGSCF 2.5%. The value for virgin Pebax lie between 2.42 to 2.70, indicating complex plate-like lamellar–spherulite aggregates nearing three-dimensional growth. Similar experimental data were reported by Wunderlich and McFerran et al for Nylon 12 [163-165].

Table 7.6 Avrami parameters of Pebax graphene composites (with and without $scCO_2$) under non-isothermal conditions

Sample Type	ϕ (°C/min)	n	Log k'	k'	$t_{1/2}$ From Graph (min)	$t_{1/2}$ Calculated (min)	R^2
Pebax	2.5	2.72	-0.09	0.80	0.95	1.01	0.993
	5	2.66	0.24	1.73	0.56	0.70	0.990
	10	2.70	0.86	7.24	0.32	0.41	0.982
	20	2.53	1.48	30.19	0.17	0.22	0.985
PebaxSCF	2.5	3.25	-0.77	0.16	1.50	1.54	0.998
	5	3.20	-0.02	0.95	0.86	0.90	0.997
	10	2.84	0.84	6.91	0.42	0.44	0.988
	20	2.99	1.58	38.01	0.25	0.26	0.989
PG 0.25	2.5	3.08	-0.53	0.29	1.75	1.51	0.998
	5	3.25	0.14	1.38	1.09	0.85	0.998
	10	2.74	0.19	1.54	0.60	0.49	0.990
	20	2.89	1.41	25.70	0.31	0.26	0.983
PGSCF 0.25	2.5	3.18	-0.51	0.30	1.27	1.57	0.998
	5	3.01	0.17	1.47	0.73	0.85	0.994
	10	3.38	0.99	9.77	0.43	0.47	0.993
	20	3.09	1.70	50.11	0.23	0.22	0.986
PG 0.5	2.5	2.92	-0.48	0.33	1.22	1.48	0.997
	5	2.62	0.12	1.31	0.76	0.86	0.995
	10	2.64	0.70	5.01	0.44	0.49	0.990
	20	2.87	1.39	24.54	0.25	0.27	0.989
PGSCF 0.5	2.5	3.51	-0.73	0.18	1.44	1.57	0.999
	5	3.16	0.08	1.20	0.81	0.86	0.997
	10	3.29	0.85	7.07	0.47	0.50	0.995
	20	3.78	1.71	51.28	0.31	0.23	0.992
PG 1	2.5	2.60	-0.47	0.33	1.22	1.41	0.995
	5	2.80	-0.03	0.93	0.82	1.00	0.996
	10	2.96	0.48	3.01	0.54	0.58	0.990

	20	2.54	0.98	9.54	0.28	0.34	0.986
PG SCF 1	2.5	3.35	-0.74	0.18	1.46	1.49	0.998
	5	3.13	0.04	1.09	0.83	0.88	0.997
	10	3.32	0.68	4.78	0.52	0.54	0.994
	20	4.01	1.82	66.06	0.31	0.32	0.998
PG 2.5	2.5	2.78	-1.04	0.09	1.78	1.01	0.982
	5	2.86	-0.36	0.43	1.10	0.70	0.992
	10	2.60	0.17	1.47	0.63	0.41	0.990
	20	2.50	0.69	4.89	0.38	0.22	0.987
PGSCF 2.5	2.5	3.20	-0.85	0.14	1.60	1.54	0.996
	5	3.10	-0.28	0.52	1.05	0.90	0.994
	10	3.28	0.39	2.45	0.70	0.44	0.990
	20	3.05	0.99	9.77	0.39	0.26	0.986

This indicates a clear shift from complex two-dimensional crystallite to complex three-dimensional crystallite, for samples with $scCO_2$. This suggests that the inclusion of graphene particles along with $scCO_2$ processing might have favoured heterogeneous nucleation through exfoliation of graphene particles and this exfoliation/interaction may have initiated a complex crystallisation process (where the adhesion of graphene might act as nuclei). This increasing n value suggests that graphene particles at a lower concentration may have aligned/well dispersed, where these particles act as nucleation sites, thereby increasing the rate of crystallisation. However, higher graphene ratio increases the nucleation sites but hinders the diffusion of polymer chains to the growing crystallite which results in decreasing the rate of crystallisation. Therefore, higher graphene concentrations induce a larger number of heterogeneous nucleation sites and limits crystal growth producing crystals of smaller size, therefore a clear decrease in the n value can be observed for 1% and 2.5% graphene ratio. The Avrami extended model by Ozawa is used, where the change in the degree of crystallinity (X(T)) as a function of varying cooling rate is considered.

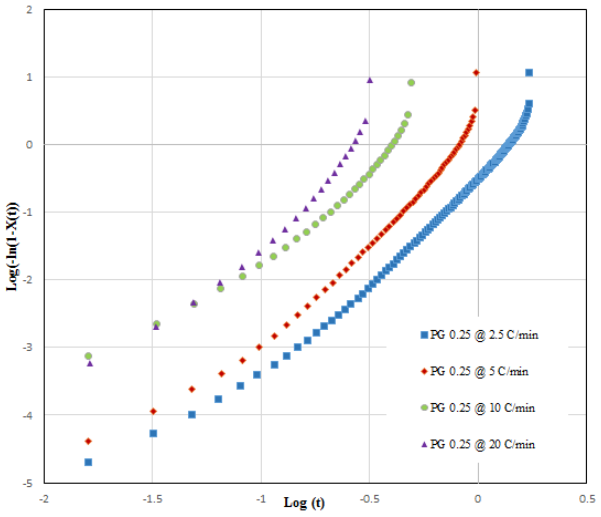

a. PG 0.25%

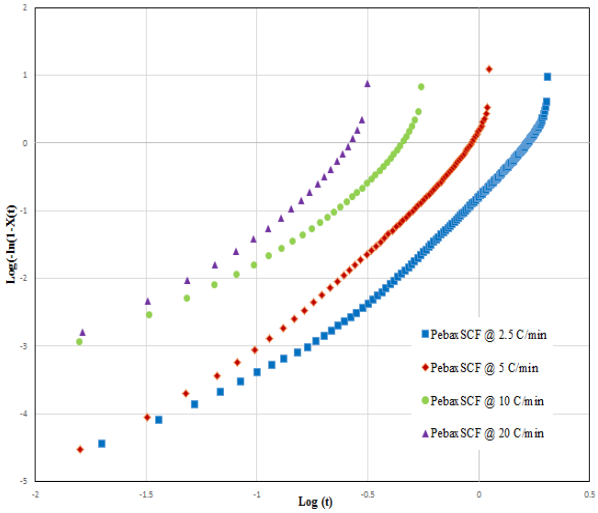

b. PG SCF

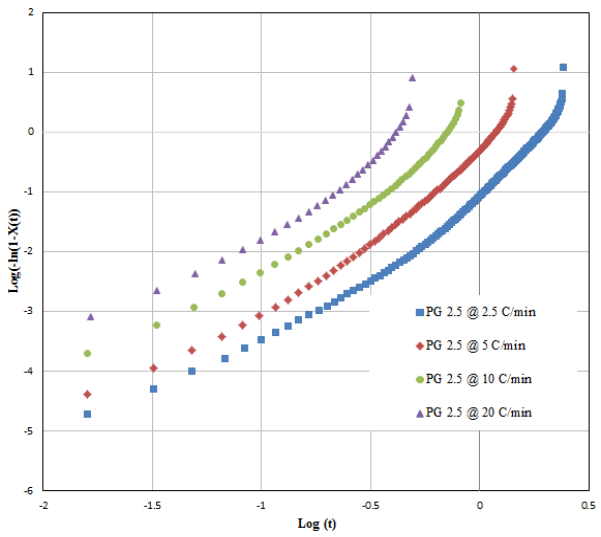

a. PG 2.5%

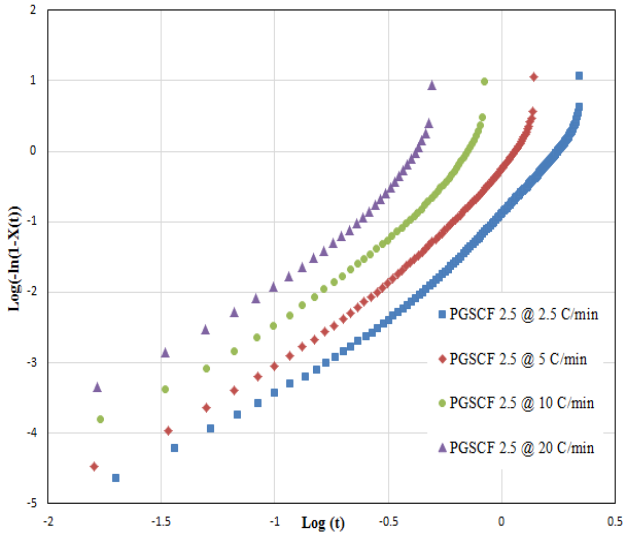

b. PG SCF 2.5%

Figure 7.10 Avrami plot of Pebax graphene composites (with and without $scCO_2$) under non-isothermal conditions

Figure 7.11 and Table 7.7 show the parameters obtained from the Ozawa model. The plot of ln (-ln (1-X(T)) vs. ln ϕ taken at different temperatures ranging from 125 °C to 144 °C. gives a linear fit, where the slope and intercept gives the kinetic parameters m and k*. Both Log k* and m values do not show any significant changes when graphene particles are introduced (m and k* independent of graphene filler ratio). However, the m values of samples extruded with $scCO_2$ are slightly higher, while the Log k* values tend to decrease, suggesting a lower crystallisation rate with $scCO_2$. It is evident from the Ozawa plot that, a perfect linear fit cannot be achieved, due to the influence of secondary crystallisation (R^2 <<1). This suggests that a mean m and k* values are difficult to achieve and thus Ozawa method cannot be used to describe the crystallisation kinetics of Pebax graphene composites under non-isothermal conditions.

Table 7.7 Ozawa parameters of Pebax graphene composites (with and without $scCO_2$) under non-isothermal conditions

Sample Type	T (°C)	M	Log k*	R^2
Pebax	125	-0.52	1.73	0.842
	128	-1.13	2.39	0.744
	133	-1.27	2.06	0.843
	138	-3.82	3.88	0.993
	140	-4.18	3.40	0.981
PebaxSCF	125	-0.46	1.42	0.953
	128	-0.81	1.76	0.845
	133	-2.80	4.07	0.786
	138	-4.63	5.02	0.894
	141	-3.36	2.52	1.000
PG 0.25	125	-0.52	1.90	0.940
	128	-0.57	1.78	0.974
	133	-1.20	2.29	0.874
	138	-3.43	4.58	0.876
	141	-4.83	5.19	0.903
PGSCF 0.25	125	-0.34	1.30	0.991
	127	-0.82	2.34	0.877
	130	-0.94	2.19	0.961
	135	-2.46	3.71	0.861
	140	-4.49	4.81	0.929
	143	-6.02	4.77	1.000
PG 0.5	125	-0.58	2.10	0.954
	128	-0.64	1.96	0.972
	133	-1.37	2.56	0.863
	138	-3.62	4.83	0.875
	141	-4.70	5.04	0.906
PG SCF 0.5	125	-0.57	1.75	0.970
	127	-0.69	1.79	0.939
	130	-1.11	2.14	0.875
	135	-3.13	4.26	0.846
	141	-2.95	2.46	1.000
PG 1	125	-0.43	1.62	0.959
	128	-0.49	1.52	0.996
	133	-0.88	1.72	0.927
	138	-2.33	3.07	0.886
	141	-4.41	5.04	0.907
PGSCF 1	125	-0.43	1.43	0.992
	128	-0.59	1.48	0.949
	130	-0.80	1.63	0.909
	145	-2.11	2.91	0.858
	140	-3.52	3.34	0.937
	142	-3.67	2.60	1.000
	125	-0.30	1.16	0.960
	128	-0.38	1.12	0.961

PG 2.5	133	-0.75	1.29	0.918
	138	-1.69	1.93	0.924
	141	-2.56	2.34	0.961
PGSCF 2.5	125	-0.52	1.89	0.999
	130	-0.64	1.69	0.968
	132	-0.79	1.73	0.942
	136	-1.44	2.17	0.899
	140	-2.50	2.78	0.944
	144	-3.73	2.56	0.986

The values b and F(T) can be obtained from the slope and intercept of the plot (Figure 7.11). It is evident from the plots and the Table 7.8 that there is a good match between the Mo analysis [111] and the experimental data for all the sample types. The value F(T) increases with the relative degree of crystallinity, indicating that higher crystallisation time is required at a higher cooling rate in order to reach unity degree of crystallinity. It is clearly evident from Table 7.8 that the ln F(T) values gradually increases with the addition of graphene up to 1% (consider samples without $scCO_2$). This increase indicates that at unity crystallisation time, a higher cooling rate should be used in order to obtain a higher degree of crystallinity. All the Pebax graphene composites had a larger ln F(T) when compared to the virgin Pebax for all the relative degree of crystallinity values. It suggests that the addition of graphene has lowered the rate of crystallisation compared to virgin Pebax (agreement with the Avrami model); thereby hindering the nucleation or growth rate. The addition of $scCO_2$ further increases the F(T) value, indicating much slower crystallisation rate when compared to its untreated counterpart.

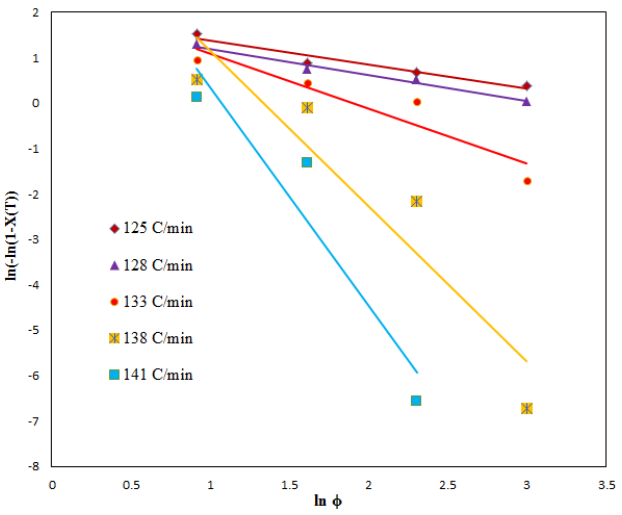

c. PG 0.25%

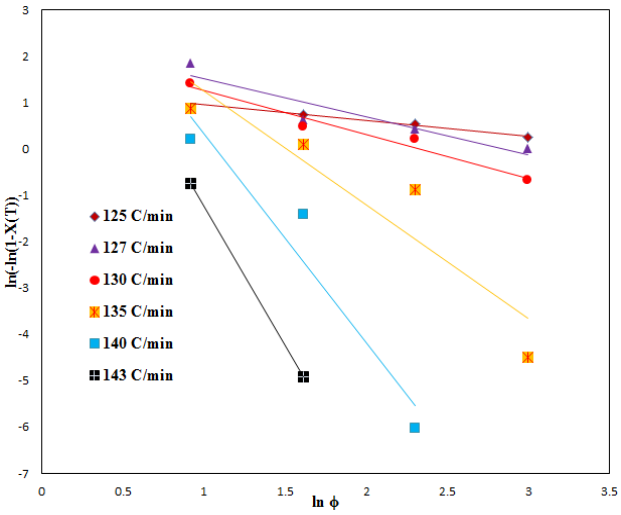

d. PGSCF 0.25%

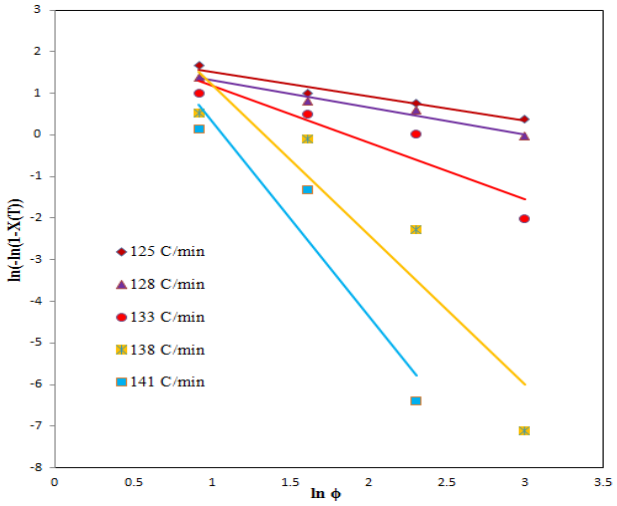

e. PG 0.5%

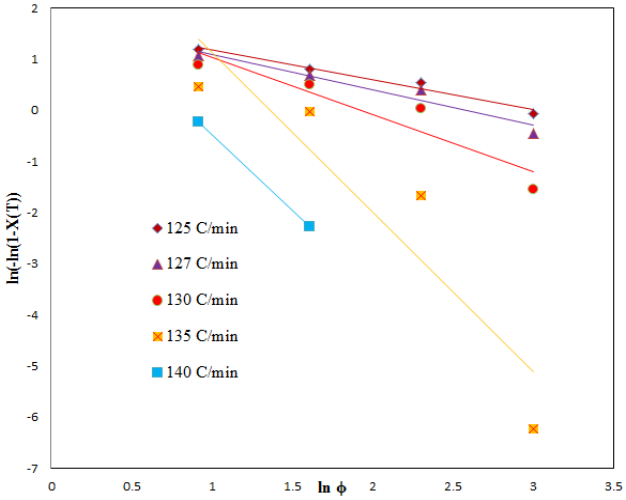

f. PGSCF 0.5%

Figure 7.11 Ozawa plot of Pebax graphene composites (with and without $scCO_2$) under non-isothermal conditions

As discussed in the Avrami Section 3.4.3.2 (Non-Isothermal Crystallisation Kinetics of Pebax Graphene-based Composites), $scCO_2$ lowers the crystallisation rate which is likely due to two possible reasons. First, due to induced rearrangement of the polymer chain to kinetically more favourable configuration and second, due to graphene exfoliation which hinders the transformation during the growth phase.

Table 7.8 Avrami-Ozawa (Mo) parameters of Pebax graphene composites (with and without $scCO_2$) under non-isothermal conditions

Sample Type	X(T)	b	Mean 'n'	ln F(T)	F(T)	R^2
Pebax	0.2	1.31	2.57	0.429	1.53	0.981
	0.4	1.27		0.716	2.04	0.988
	0.6	1.26		0.882	2.41	0.991
	0.8	1.25		1.00	2.71	0.993
PebaxSCF	0.2	1.15	3.06	1.053	2.86	0.997
	0.4	1.14		1.315	3.72	0.998
	0.6	1.13		1.463	4.31	0.999
	0.8	1.11		1.597	4.93	0.999
PG 0.25	0.2	1.28	2.99	0.825	2.28	0.991
	0.4	1.27		1.134	3.10	0.999
	0.6	1.21		1.300	3.66	0.991
	0.8	1.20		1.439	4.21	0.992
PSCFG 0.25	0.2	1.27	3.16	0.829	2.29	0.999
	0.4	1.21		1.129	3.09	0.998
	0.6	1.23		1.309	3.70	0.999
	0.8	1.25		1.425	4.15	0.999
PG 0.5	0.2	1.40	2.76	0.701	2.01	0.998
	0.4	1.35		1.052	2.86	0.998
	0.6	1.32		1.261	3.52	0.999
	0.8	1.29		1.422	4.14	0.999
PG SCF 0.5	0.2	1.37	3.43	0.938	2.55	0.997
	0.4	1.35		1.237	3.44	0.996
	0.6	1.32		1.435	4.19	0.996
	0.8	1.29		1.591	4.90	0.997
PG 1	0.2	1.45	2.72	0.777	2.17	0.992
	0.4	1.40		1.141	3.12	0.994
	0.6	1.40		1.382	3.98	0.990
	0.8	1.36		1.557	4.74	0.991
PG SCF 1	0.2	1.40	3.45	1.016	2.76	0.999
	0.4	1.35		1.335	3.79	0.999
	0.6	1.35		1.520	4.57	0.999
	0.8	1.31		1.695	5.44	0.999
PG 2.5	0.2	1.38	2.68	1.304	3.68	0.999
	0.4	1.38		1.601	4.95	0.999
	0.6	1.33		1.798	6.03	0.999
	0.8	1.33		1.933	6.91	0.999
PGSCF 2.5	0.2	1.60	3.15	1.180	3.25	0.999
	0.4	1.46		1.515	4.54	0.999
	0.6	1.44		1.720	5.58	0.999
	0.8	1.43		1.905	6.71	0.999

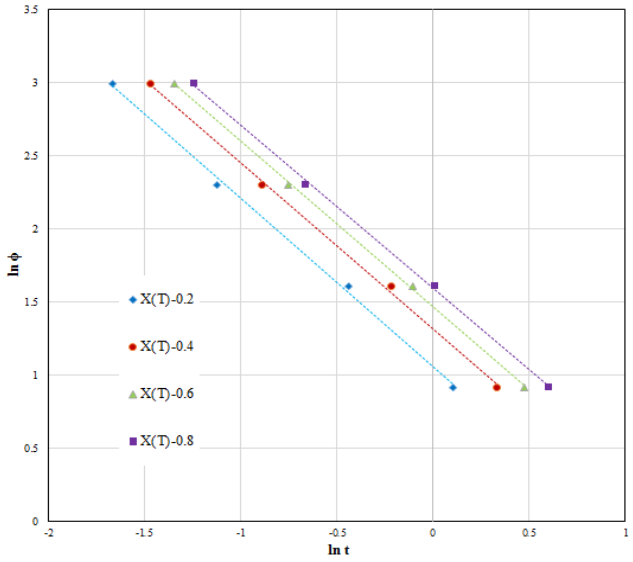

a. PebaxSCF

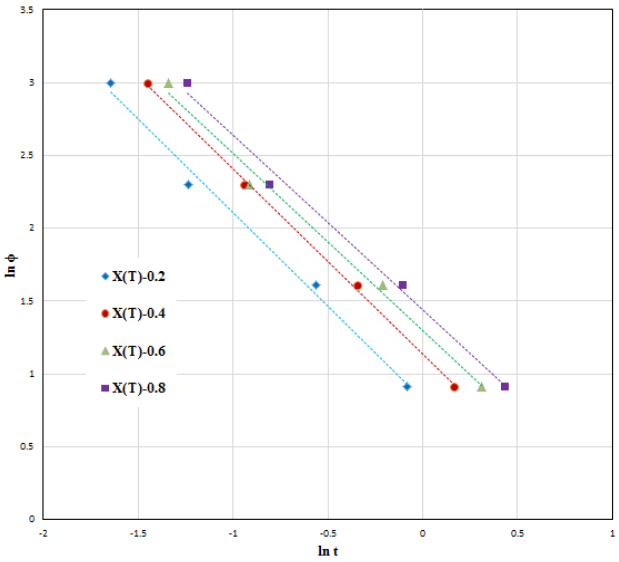

b. PG 0.25%

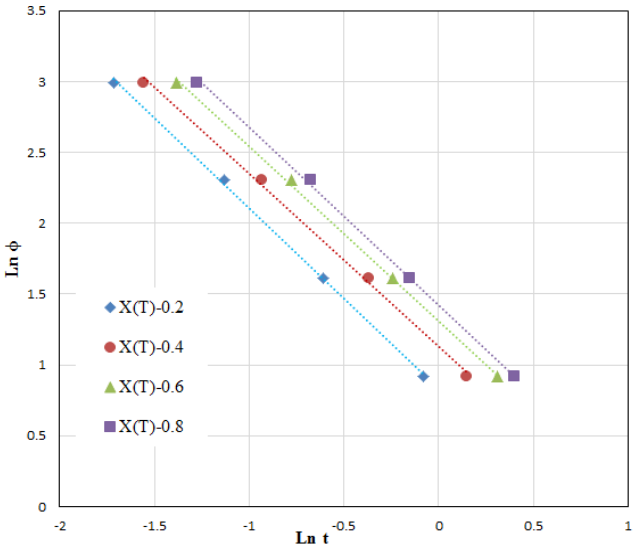

c. PGSCF 0.25%

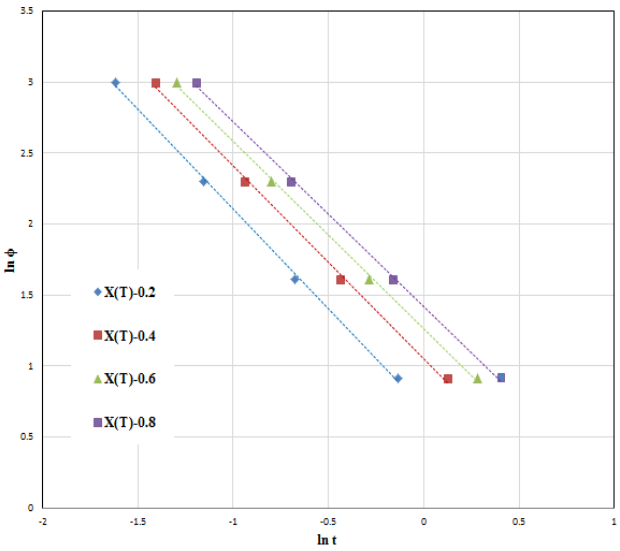

d. PG 0.5%

Figure 7.11 Avrami - Ozawa (Mo) plot of Pebax graphene composites (with and without $scCO_2$) under non-isothermal conditions

At a graphene content of 2.5%, the crystallisation rate slightly increases as more sites are available to nucleate with slower growth rates, where, crystals would grow to a much smaller crystal grain size (F(T) increases - faster crystallisation rate but slower growth) and ceases to grow further, leading to a shorter overall crystallisation time.

It is found that the b value, which is the ratio of n/m tends to increase upon addition of graphene particles except for PG 0.25%. This is because the entire graphene composites had higher mean n values. As the filler content is increased to 2.5 %, the b value decreases due to complexity in the crystallisation geometry. The b value is maximum for PG 1%, suggesting that higher graphene

concentration induces a larger number of heterogeneous nucleation sites and limits crystal growth producing crystals of smaller size, therefore a clear decrease in the n value can be observed for 1% and 2.5% graphene ratio. The influence of various cooling rates under non-isothermal crystallisation conditions on the activation energy can be described using the Kissinger equation (3.4.3.2). The plot of $\ln(\phi/Tc^2)$ vs. 1/Tc gives the linear slope determining the ΔE (Figure 7.13) and is given in Table 7.9 The activation energy increases with the addition of graphene particles suggesting the actual hindrance that progresses during the transformation phase. However, the activation energy for samples with $scCO_2$ tends to reduce when compared to its counterpart samples without $scCO_2$.

Table 7.9 Kissinger's activation energy of Pebax graphene composites (with and without $scCO_2$) under non-isothermal conditions

Sample Type	Kissinger Activation Energy (KJ/mol)
Pebax	-233.39
PebaxSCF	-230.81
PG 0.25	-258.93
PGSCF 0.25	-256.18
PG 0.5	-244.01
PGSCF 0.5	-237.80
PG 1	-248.58
PGSCF 1	-243.75
PG 2.5	-280.43
PGSCF 2.5	-272.71

As described by Fan Zhang et al [145], the activation energy (ΔE) consists of two components, first the free transport activation energy (ΔE*) for transporting the molecular segment to a crystalline phase and second, the nucleation activation energy (ΔF*) for the formation of critical size nuclei. It is suggested that the graphene interaction with the hydrogen bond of the amide group weakens the bond thereby restricting the process of crystallisation and the transport activation energy [111, 145]. In addition, graphene particles also act as nuclei, which decrease the nucleation activation energy.

For this reason, the activation energy under non-isothermal conditions has an increasing trend upon addition of graphene up to 2.5 wt. %. It can be observed that ΔE value PG 0.25% is higher than PG 0.5% and PG 1%; this reduction in activation energy can be attributed to even dispersion and interaction of graphene particles with the hydrogen bond which in turn reduces the activation energy for transporting molecular segments across the phase boundary to crystallisation phase. As the graphene percentage is increased, the nucleation activation energy dominates as graphene particles tend to agglomerate acting as crystallisation nuclei. In all the cases the activation energy of $scCO_2$ treated samples remains less than the untreated counterpart.

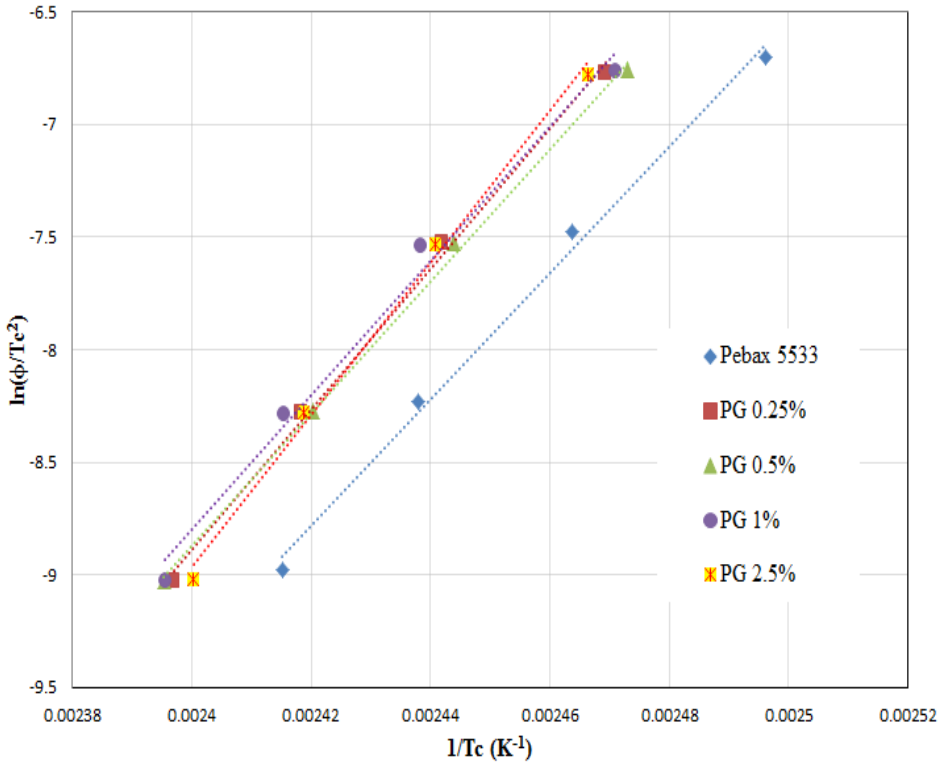

Figure 7.12 Kissinger plot of Pebax graphene composites (without $scCO_2$) under non-isothermal conditions

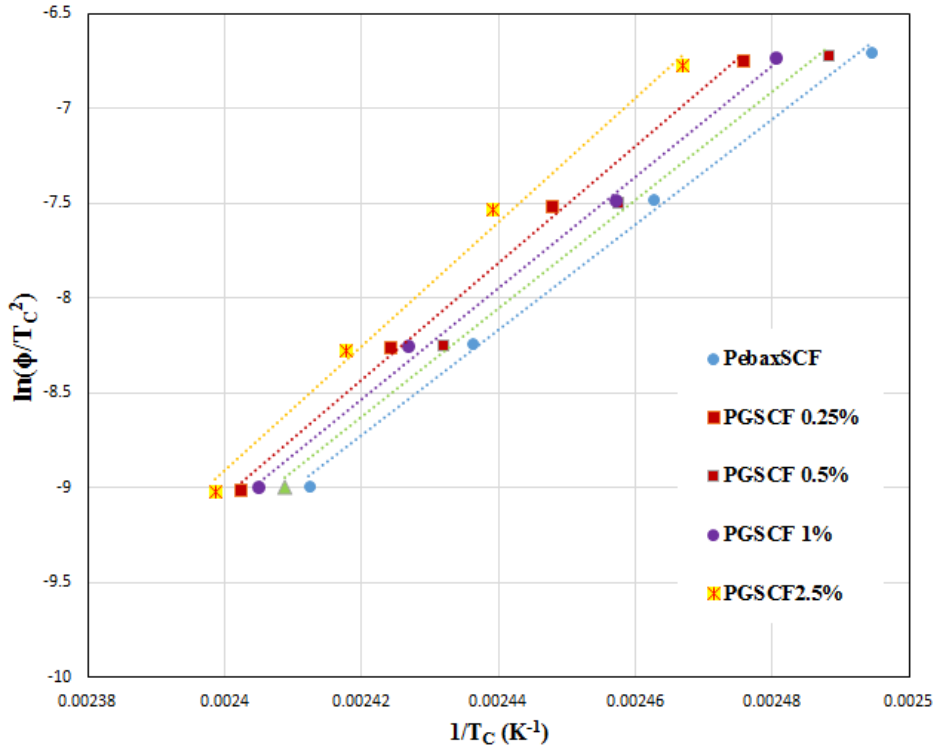

Figure 7.13 Kissinger plot of Pebax graphene composites (with $scCO_2$) under non-isothermal conditions

7.2.4 X-ray Diffraction of Pebax Graphene Composites

XRD analysis was used to understand the effects of increasing graphene concentration and the influence of $scCO_2$ assisted processing of Pebax graphene composite. Pebax is a semi-crystalline copolymer consisting of a crystalline PA-12 block and an amorphous PE block. Therefore, a relatively broad peak is expected due to the semi-crystalline nature of Pebax rather than a sharp peak on the XRD pattern which would indicate a highly crystalline structure for a given material. The XRD pattern of virgin Pebax (Figure 7.14) shows a peak approximately at $2\theta=22°$, occurring mainly from the inter-chain hydrogen bonding of crystalline PA-12. The d-spacing of the $scCO_2$ treated Pebax shows a slight decrease from 4.18 for untreated Pebax to 4.03 for $scCO_2$ treated Pebax (PebaxSCF), suggesting that the $scCO_2$ treatment reduces the spacing between planer lattice (i.e. tightens up the lattice within the crystal) of the Pebax polymer matrix. In addition, the full width at half maximum (FWHM) increases from 1.88 for neat Pebax to 2.43 for $scCO_2$ treated Pebax, indicating peak broadening, suggesting decreased crystallite size. In order to quantify the effects such as peak broadening on the crystallite size, Scherrer's equation was used. Table 7.10 shows the recorded d-spacing, 2θ peak, FWHM and calculated crystallite size. In all the cases the $scCO_2$ treated polymer composites result in broadening of the peak. It can be seen from Table 7.10 (consider samples without $scCO_2$) that the crystallite size tends to reduce

except for PG 1% and PGSCF 1%. Such reduction in the crystallite size can be expected as graphene particles act as nucleating sites which in turn reduce the overall individual crystal size due to higher crystal density.

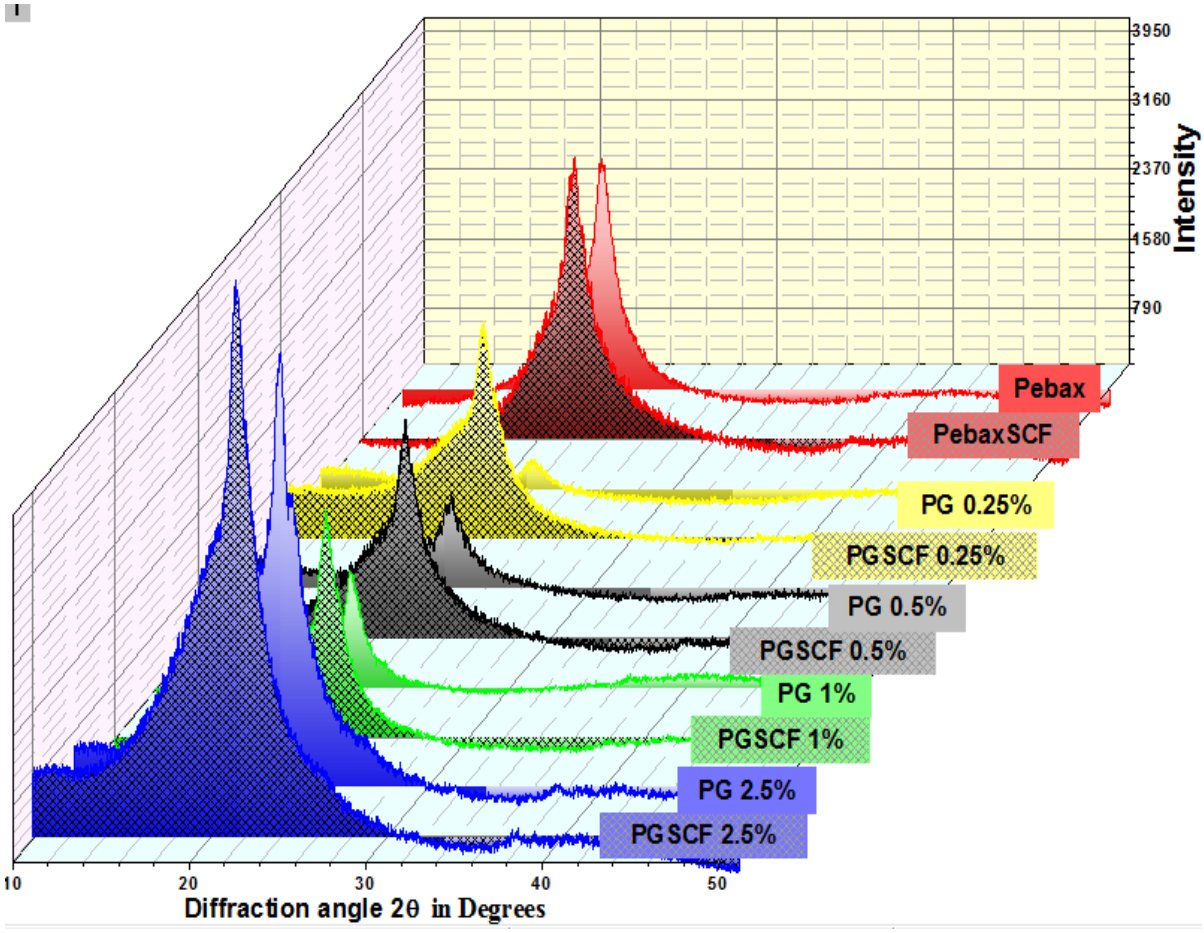

Figure 7.14 XRD pattern for Pebax-graphene composites with and without $scCO_2$

Such increased nucleation sites leading to reduced crystallite size can be validated from the crystallisation kinetics parameters obtained from both isothermal and non-isothermal crystallisation kinetics; where the value of crystallisation rate (k) increases and Tc shifts to higher temperatures. However, when the samples are processed with $scCO_2$, the crystallite size tends to reduce compared to its untreated counterpart (except for 1% loading), as $scCO_2$ induces crystallisation process in a kinetically favourable manner and also due to probable exfoliation of graphene particles. In addition, it is evident that the crystallite size is lowest for PGSCF 0.25% at 2.48 nm and slowly increases till 1% (PGSCF 1% with crystallite size of 3.98 nm) graphene loading which is indicative of the percolation threshold beyond which the graphene particle tends to agglomerate and become graphite [166, 167].

Table 7.10 List of parameters and calculated crystallite size using Scherrer's equation for Pebax-graphene composites with and without $scCO_2$

Sample Size	d-spacing in Å	Peak Position (2θ) in Degree	FWHM in Degree	Calculated Crystallite Size in nm
Pebax	4.18	21.26	1.88	4.49
PebaxSCF	4.03	22.03	2.43	3.48
PG 0.25	4.05	21.88	2.54	3.32
PGSCF 0.25	4.07	21.54	3.40	2.48
PG 0.5	4.03	22.06	2.89	2.92
PGSCF 0.5	4.14	21.60	2.74	3.08
PG 1	4.06	21.05	1.73	4.87
PGSCF 1	4.11	21.95	2.12	3.98
PG 2.5	4.09	21.68	3.01	2.80
PGSCF 2.5	4.16	21.50	3.11	2.71

7.2.5 Dynamic Mechanical Analysis (DMA) of Pebax Graphene Composites

Figure 7.15 and Figure 7.16 presents the storage modulus (G'), and the loss modulus (G'') (Figure 7.16 – without $scCO_2$ and Figure 7.17 – with $scCO_2$) and tan delta of Pebax graphene composite with and without SCF-assisted extrusion. These were measured at a test frequency of 1 Hz and 25 °C temperature in a parallel direction to the axis of extruder screw rotation. It is clearly seen that the addition of graphene has resulted in an increase in the storage modulus; however, tan delta remains almost constant when samples are not treated with SCF. This increase in storage moduli (Figure 7.15) for untreated (processed without SCF) polymer matrix was directly proportional to the ratio of graphene present in the polymer. The % Δ gives the percentage change in stiffness of the polymer matrix with respect to pure Pebax (Table 7.11). Upon addition of 2.5 wt. % of graphene, the storage modulus at room temperature improved by 58% compared to pure Pebax (Table 7.11: processed without SCF).

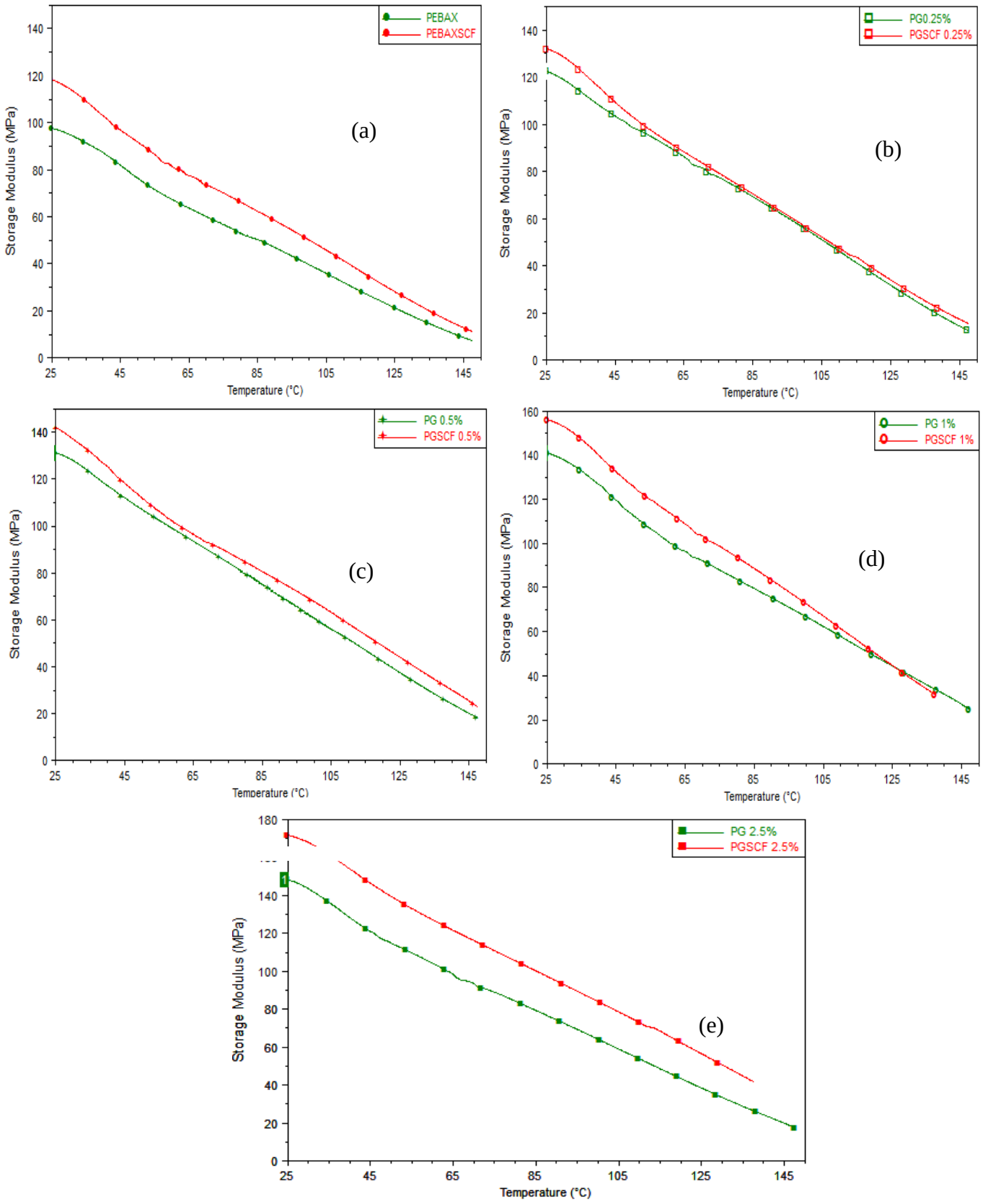

Figure 7.15 Storage modulus curves of Pebax graphene composite with and without $scCO_2$ (a:Pebax, b:PG 0.25%,c:PG0.5%,d:PG1% and e:PG2.5%)

This increase in the storage modulus and loss modulus suggests that graphene particles restrict further movement of polymer chains due to superior mechanical properties of graphene particles. The $scCO_2$ assisted polymer matrix for virgin Pebax showed an increase in storage modulus by 21.5% with respect to unassisted virgin Pebax (also equivalent to PG 0.25% without SCF nanocomposite). This increase in storage modulus, when treated with $scCO_2$, suggests that supercritical treatment further enhances/strengthens the polymer-filler interaction. Tan delta represents the damping factor due to energy dissipation of material occurring from interfacial friction and heat. The damping factor is higher in samples without $scCO_2$ than with a $scCO_2$ counterpart. This is mainly because the graphene particles are loosely bound (less interaction between the graphene and polymer chain) to the polymer chain thereby increasing the friction at the graphene-polymer interface.

Kazarian [95] and many other researchers [25-27, 168-170] have reported that $scCO_2$ induced plasticisation may induce crystallisation in certain semi-crystalline polymers, allowing the polymer chain to rearrange into kinetically favourable configurations, thereby increasing crystallisation and increasing the stiffness of the polymer matrix. In addition, the results from the crystallisation kinetics indicating the slower crystallisation rate and higher dimension 'n' value can be the reason to enhance the stiffness of the composite when treated with $scCO_2$.

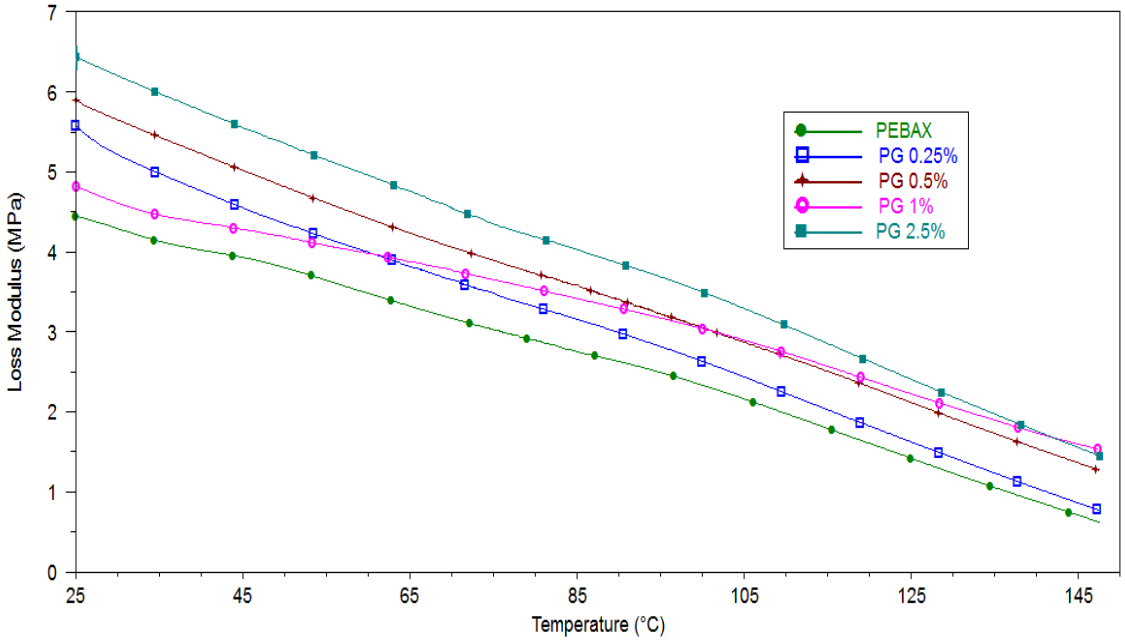

Figure 7.16 Loss modulus curves of Step-1 Pebax graphene composite

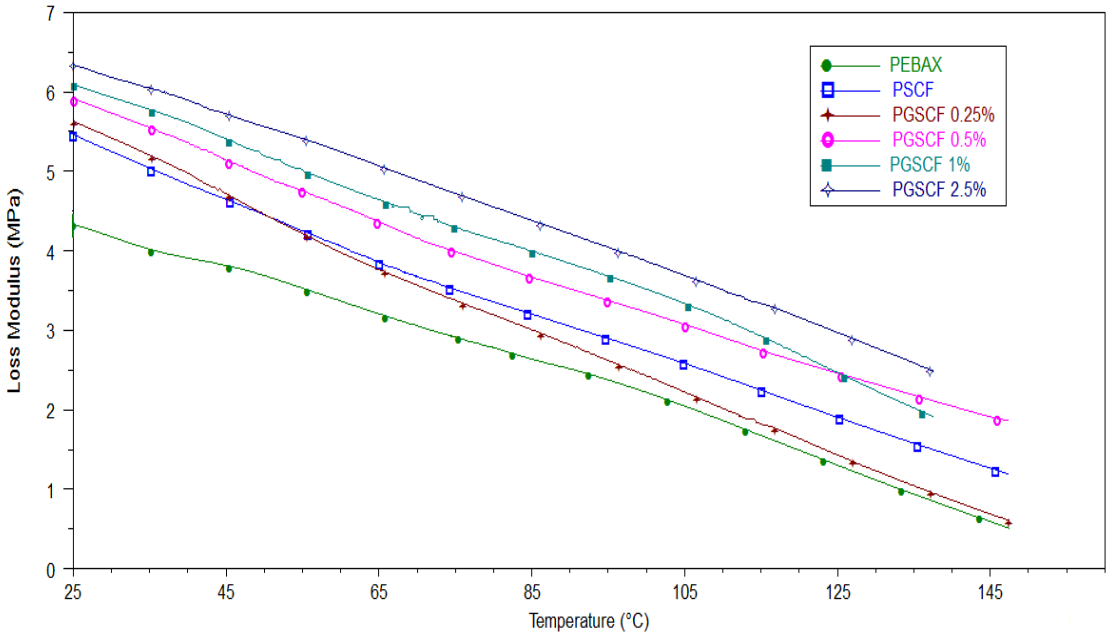

Figure 7.17 Loss modulus of Step-2 (reprocessed Step-1) Pebax graphene composite

The % Δ of storage modulus gives the percentage change in stiffness of the polymer matrix with respect to pure Pebax. Upon addition of 2.5 wt. % of graphene, the storage modulus at room temperature improved by 58% compared to pure Pebax. The $scCO_2$ treated PG0.25% and PG0.5% exhibit an increase in storage modulus by 11% for its equivalent untreated polymer composites. As the graphene content increased to 1% and 2.5%, the storage modulus increased over 18% when compared to its equivalent untreated polymer composites (Figure 7.18). Also, a gradual decrease in the tan delta was observed when compared to the untreated polymer composites. The $scCO_2$ treated PG0.25% and PG0.5% demonstrated an increase in storage modulus and loss modulus by 11% for its equivalent untreated polymer composites. As the graphene content increased to 1% and 2.5%, the storage modulus increased over 18% when compared to its equivalent untreated polymer composites. A gradual decrease in tan delta (Table 7.11) with $scCO_2$ treatment was observed when compared to the untreated polymer composites. Tan delta also represents the measure of friction or adhesion at the polymer chain and the filler interface. Improved graphene interaction with the polymer chain offers greater load-bearing capacity at the graphene-polymer interface. This allows a small part of the polymer chain to be strained, thereby restricting easy chain movement and reducing the friction and damping factor.

Table 7.11 Storage modulus (G'), loss modulus (G'') and tan delta of Pebax graphene composite with and without SCF-assisted extrusion

Sample type	**Without SCF**			**With SCF**		
	Storage modulus	Loss Modulus	Tan Delta	Storage Modulus	Loss Modulus	Tan Delta
	MPa (% Δ)	MPa	NA 10^{-3}	MPa (% Δ)	MPa	NA 10^{-3}
Pebax	98.56 ±5.3	4.39	44	119.8 ± 3.5	5.45	45
PG 0.25%	122.4 ±3.8 (24.2)	5.24	42	132.9 ±6.9 (11.0)	5.66	43
PG 0.5%	131.9 ±5.2 (33.9)	5.87	44	141.3 ±4.1 (18.0)	5.96	42
PG 1%	140.1 ±3.3 (42.0)	4.84	34	158.45 ±3.9 (32.3)	6.19	39
PG 2.5%	156.6 ±3.8 (58.9)	6.45	41	173.9 ±3.7 (44.3)	6.34	36

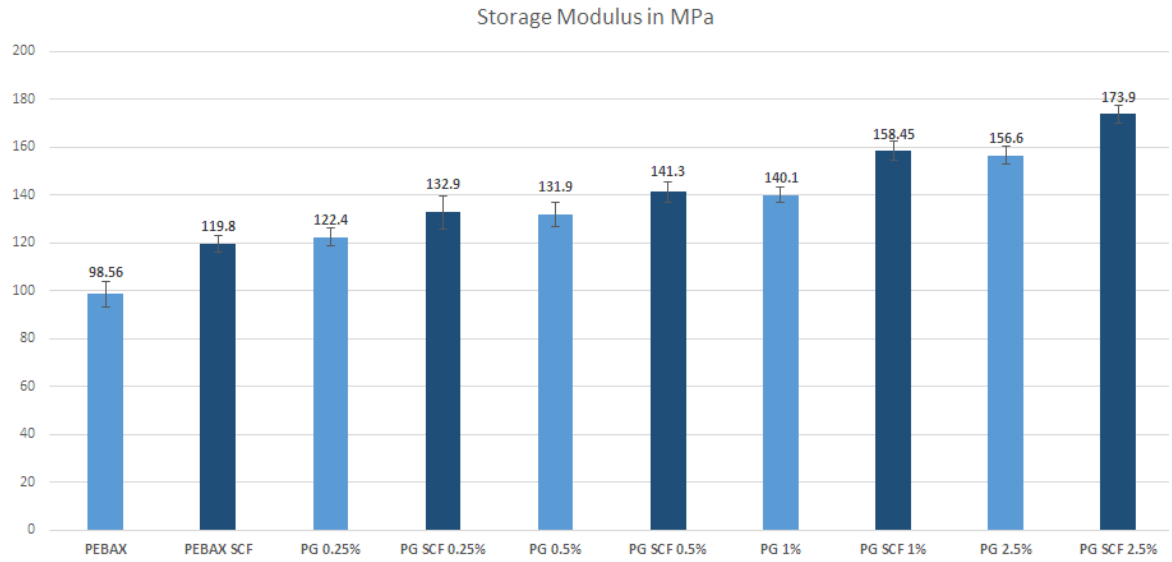

Figure 7.18 Storage modulus of Step-2 (reprocessed Step-1) Pebax graphene composite

7.2.6 Tensile Test of Pebax Graphene Composites

Figure 7.19 and Figure 7.20; show the tensile profile of Pebax graphene-based nanocomposite with and without SCF-assisted processing technique respectively. The strain was measured up to 500% and no breakage was observed for all the samples in all composites. Significant enhancement in the modulus of resilience was observed for composites without $scCO_2$; however,

this reinforcement was improved when treated with $scCO_2$. A noticeable increase in Young's modulus (Figure 7.21) was observed on SCF-treated Pebax when compared with the virgin material (specifically PebaxSCF, PGSCF0.25%, PGSCF0.5% and PGSCF1%). Although the major increase in the stress was not observed mainly due to the anisotropic nature of the composite samples produced from the injection moulding machine, a gradual reinforcement was evident depending upon the weight percentage of graphene. This may be due to low melting temperature and reciprocating screw speed within the injection moulding machine which might have resulted in lower molecular orientation, causing agglomerations of nanoparticles, therefore, resulting in no significant reinforcement [171, 172].

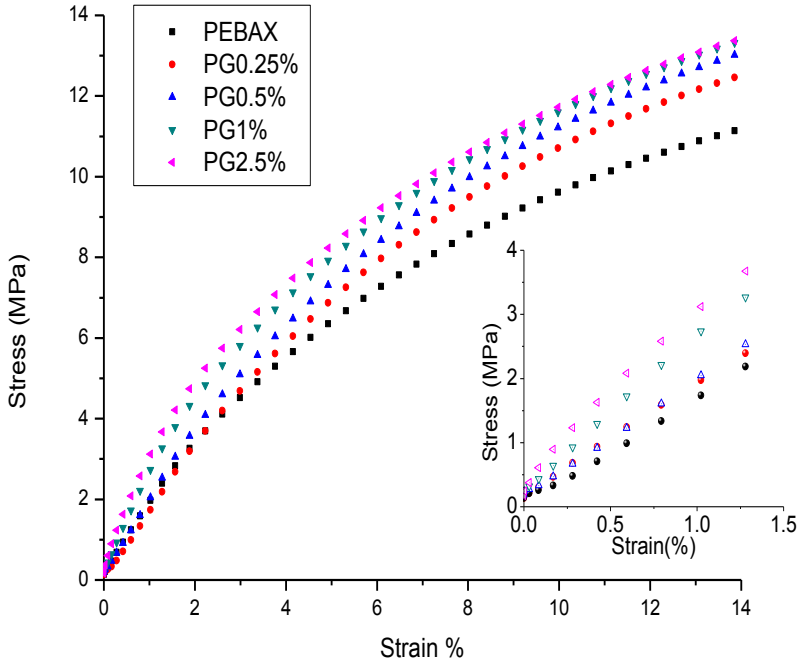

Figure 7.19 Stress vs. strain curve for various ratios of Pebax graphene composite using injection moulding without $scCO_2$ assisted composite granules

This increase in the modulus of resilience is due to increases in the graphene nanoparticle ratio within the polymer composite. The increased modulus shows the ability of $scCO_2$ to enhance the mechanical properties of semi-crystalline materials such as Pebax. A similar reinforcing trend (both with and without SCF/ $scCO_2$) was observed in the storage modulus of the DMA results, which means that the ability of a material to absorb energy is increased with higher stress, without suffering damage and thereby increasing the material's stiffness. Moreover, gradual

reinforcement resulting in an increase in Young's modulus was observed, which was directly proportional to the loading of graphene nanoparticles.

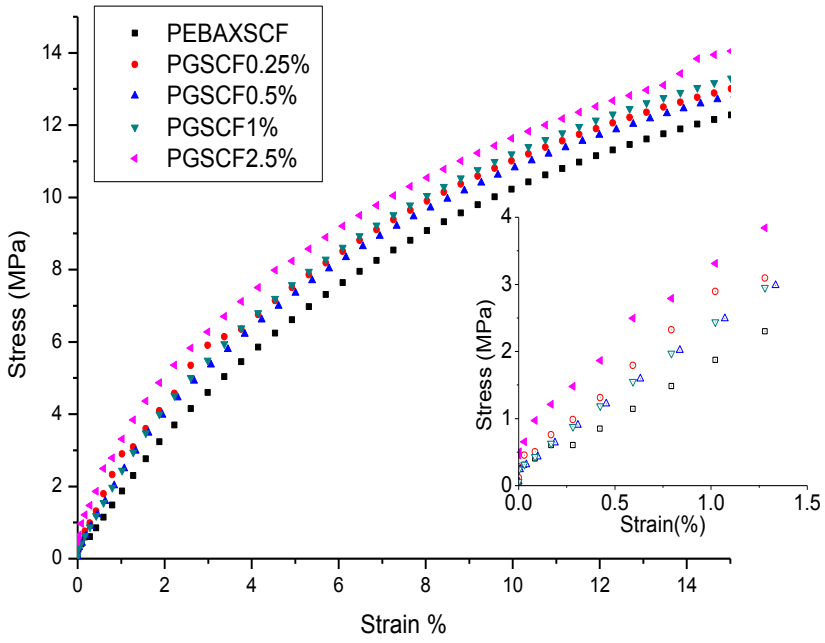

Figure 7.20 Stress vs. strain curve for various loading of Pebax graphene composite using injection moulding with $scCO_2$ assisted composite granules

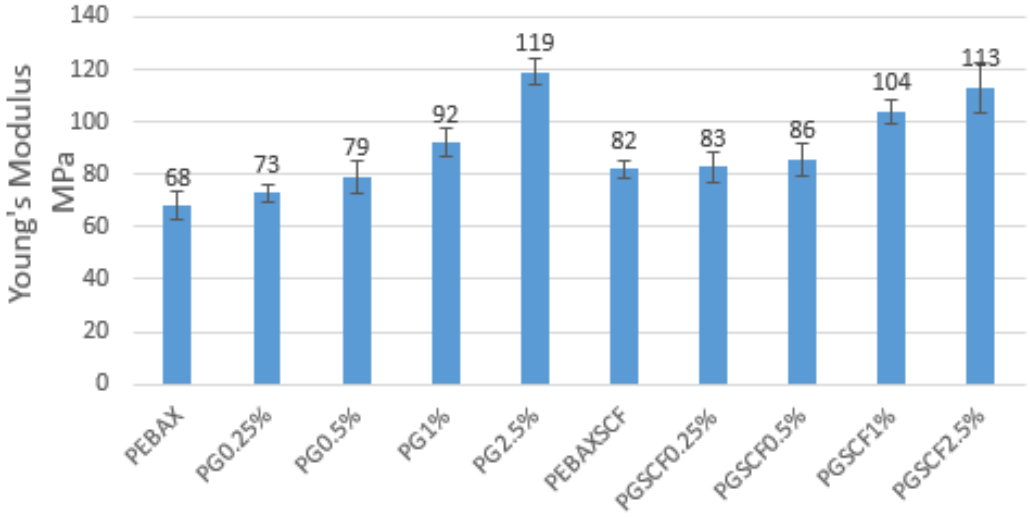

Figure 7.21 Mean Young's Modulus of Pebax graphene composite for injection moulded samples

This suggests that $scCO_2$ enhances the heterogeneous network of the soft block and hard block present in Pebax leading to a sufficient increase in stiffness, which leads to a minimum increase in a heterogeneous network of Pebax with graphene, at a low concentration level. However, this

effect of reinforcement has been predicted to escalate at high concentrations of graphene nanoparticles [171, 172].

7.2.7 Fourier Transform Infrared Spectroscopy Analysis of Pebax Graphene Composites

Figure 7.22 presents the transmittance spectra of Pebax graphene composites with and with $scCO_2$. The peaks at 1465 cm^{-1} and 1365 cm^{-1} represent CH_2 vibration and C-N stretching of the amide group, respectively. The soft PTMO blocks exhibit stretching vibration of the C-O ether peak at 1100 cm^{-1}. No significant changes were observed for untreated (without $scCO_2$) Pebax graphene nanocomposite. However, when the polymer matrix was treated with $scCO_2$, the peak at 1555 cm^{-1} (PebaxSCF) showed a gradual increase to 1562 cm^{-1} (for PG1% and PG2.5%) depending on the graphene nanoparticle content. In addition, gradual increase in peak wave number from 1366 cm^{-1} for PebaxSCF to 1366 cm^{-1} for PG0.25% and PG0.5%, 1369 cm^{-1} for PG1% and 1372 cm^{-1} for PG2.5% was observed. It is evident from the literature, that the characteristic peaks at 1735 cm^{-1} and 1638 cm^{-1} represent the presence of O-C=O stretching of the carbonyl group of ester linkage and N-C=O carbonyl vibration of the PA-12 group [126, 127]. The amide carbonyl band at 1638 cm^{-1} is sensitive to hydrogen-bonding distance between the segments. Usually, amorphous amide has a larger distance while the crystalline state has a sharper peak. The peak at 1555 cm^{-1} is ascribed to CNH vibration with NH bending and CN stretching. In both cases, the gradual shift in peaks is mainly because of the amphoteric nature of NH and the carboxylic group present in Pebax. Specifically, electropositive graphene interacts through NH and CN vibrations present in the amide group of the polymer. The presence of such evident shifts in SCF-treated composites also indicated that $scCO_2$ has resulted in exfoliation of graphene nanoparticles, thereby reducing the number of layers and increasing the availability of pi electrons for further polymer-graphene interactions [173, 174].

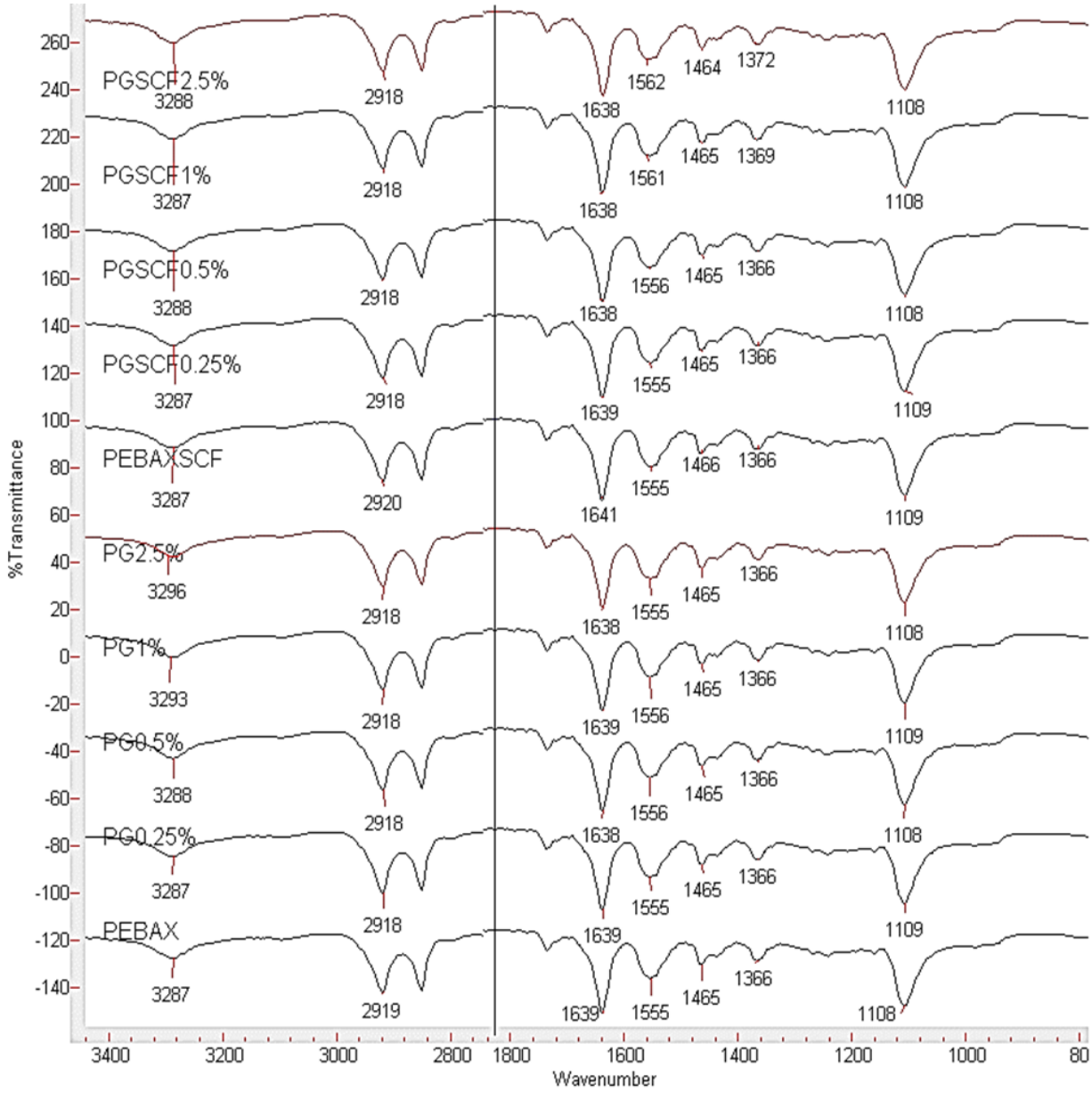

Figure 7.22 ATR-FTIR spectra of Pebax graphene composites

7.2.8 Electrical Conductivity Test of Pebax Graphene Composites

Figure 7.23 shows the conductivity calculated at a various range of frequency for Pebax graphene composites. It is evident that the conductivity gradually increases with the addition of graphene nanoparticles from 0.25 wt. % to 2.5 wt. % at lower frequencies (specifically between 1 Hz to 10 Hz). A significant increase in the conductivity can be observed with an increase in the graphene wt. % ratios; however, this increase in conductivity is much enhanced for the same wt. % when extruded with $scCO_2$.

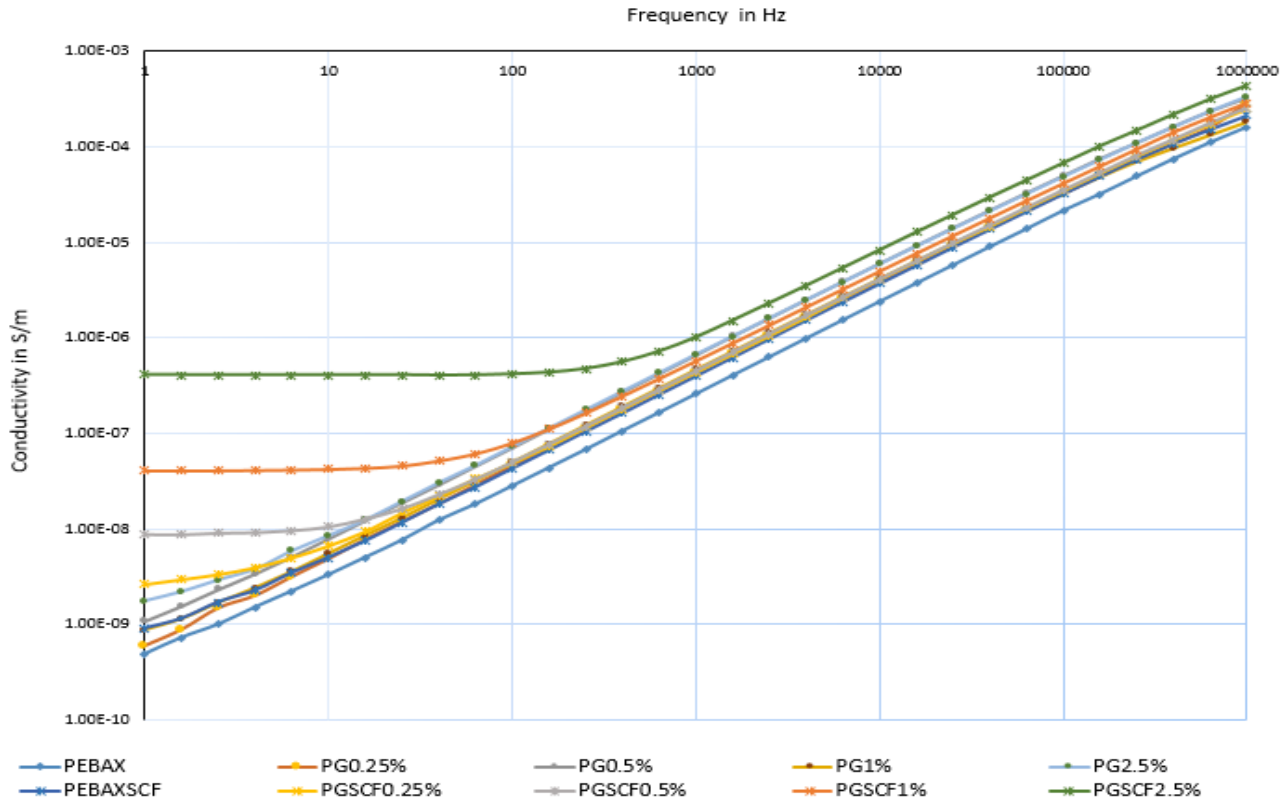

Figure 7.23 AC conductivity of with and without $scCO_2$ of Pebax graphene composite

A clear increase in conductivity can be observed in both with and without SCF Pebax graphene composites. Use of $scCO_2$ during extrusion further avoids the stacking of graphene layers due to weak Van der Waals forces (effect of exfoliation) and provides improved dispersion of graphene within the polymer matrix, where the physical properties of graphene are maintained (confined to few layers). Therefore, the $scCO_2$-treated Peabx graphene samples demonstrated increased conductivity (with same graphene wt. %) when compared to polymer composites without SCF-assisted extrusion. The process of electrical conductivity within a polymer takes place in three stages, namely: a. lower conductivity due to low filler fraction, b. gradual formation of the interconnecting network leading to tunnelling of electrons through neighbouring graphene particles followed by c. formation of the conductive path at the percolation threshold. Further increase in the filler concentration will result in enhancement of the conducting network thereby increases conductivity until the threshold is reached. Although electrical conductivity and percolation threshold is dependent on filler concentration, additional parameters such as filler aggregation, processing method, aspect ratio, functionalization, polymer-graphene interaction and distribution (wrinkles or folds) also influence the conductivity [34, 88, 90, 159, 175].

AC Conduction mechanism in nanocomposites can be divided into two parts (i) conduction due to the transfer of charge from one point to the other and (ii) conduction due to a high polarisation effect. With the addition of carbon-based nanoparticles such as graphene, the conduction due to the transfer of charge is prominent only after the percolation threshold, beyond which materials become highly conductive. Whereas the AC conductivity due to the polarisation effect is highly prominent just below the percolation threshold. In addition, frequency dependent conductivity can be divided into two regions depending on lower and higher frequency. Low-frequency region is described as a flat region representing DC conductivity and gives the resistance value (Z=R, at low frequency). The region at higher frequencies is frequency dependent and represents AC conductivity (Capacitive nature as Z=-1/wC). The AC conductivity of composites increased exponentially with increase in frequency due to lower mobility in induced dipoles at a higher frequency (acts like a capacitor). When the electric field is applied to the samples at lower frequencies, the charge from the electrode tends to move and accumulate between the polymer and the graphene particles. This movement and accumulation of charges at the interface cause large polarisation, producing flat regions on the conductivity graph.

7.2.9 Transmission Electron Microscope Morphology of Pebax Graphene Composites

Figure 7.24 shows the TEM morphology of Pebax graphene composites at 1% graphene loading without (Image A and B) and with (Image C and D) $scCO_2$. As the samples were prepared by manual slicing of the extrudates, the images depict a very thick sample or overlapped samples. Large graphene platelets can be clearly seen from image A and B, while graphene particles appear to be well dispersed and broken down into smaller particles in image C and D. Another important observation is the clear appearance of nylon lamellar crystalline structure forming a Pebax lattice where graphene concentration is neighbouring to such lattice. The images suggest that $scCO_2$ assisted processing of polymer composites results in exfoliation and even dispersion of graphene particles within the polymer. Similar analysis using thermal, mechanical, electrical, FTIR and XRD have been discussed throughout in relation to the probable interaction/graphene exfoliation with the nylon (PA-12) group of Pebax polymer.

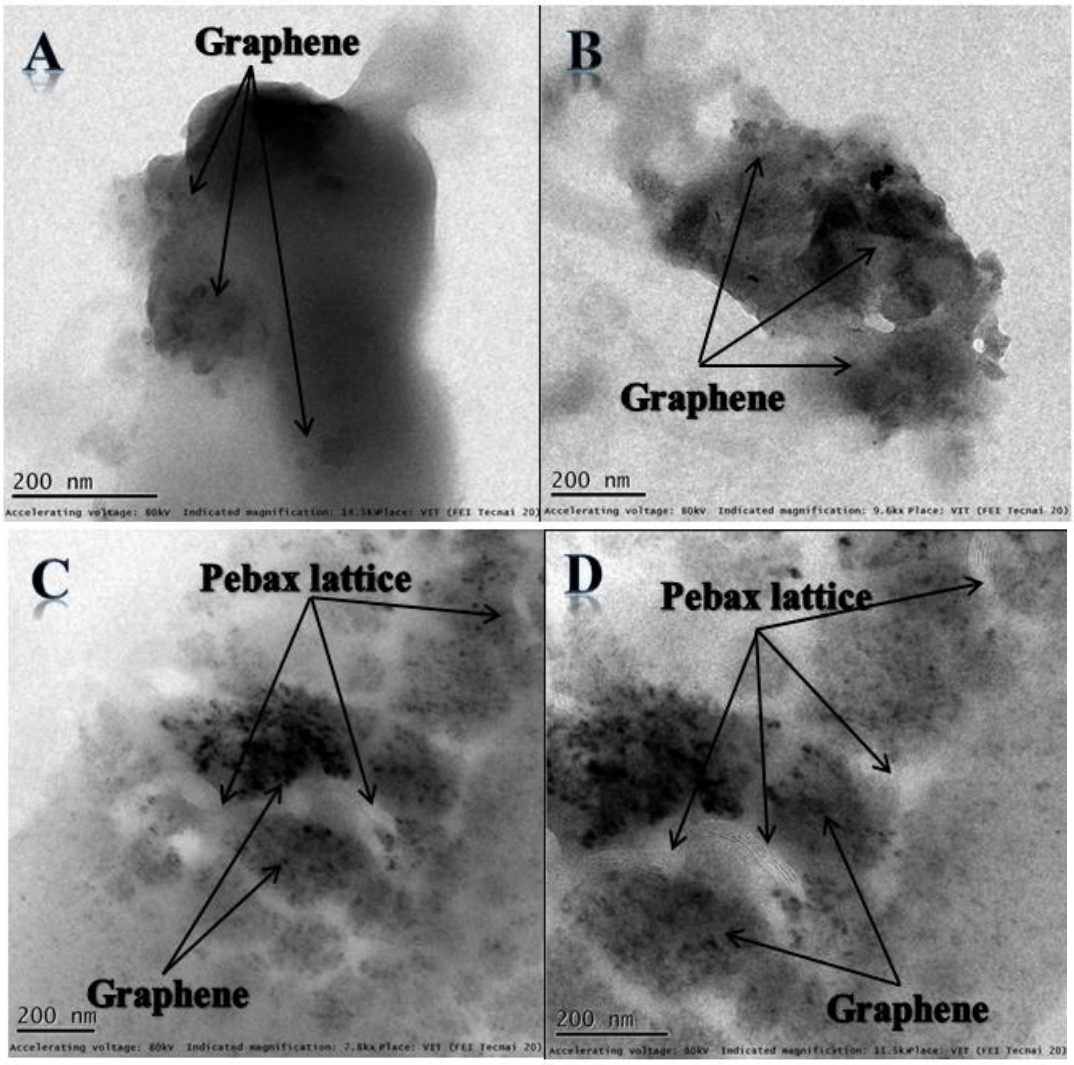

Figure 7.24 TEM Images of Pebax graphene composites: A and B – PG1% and; C and D – PGSCF1%

7.3 Key Points for Reprocessed Pebax Graphene Composites

This study evaluated the thermal, mechanical and electrical performance and interactions of Pebax nanocomposites at various graphene concentration with and without $scCO_2$.The following are the key observation made:

- A 1-minute melt flow test on the Pebax based composite showed that the use of $scCO_2$ during the extrusion process has reduced the viscosity of the polymer melt and thereby increased the throughput of the extruder.
- The thermal stability of Pebax graphene composites at higher loading is improved due to the strong interaction between the polymer and graphene. This, in turn, decreases polymer chain mobility near the graphene Pebax interface, thereby stabilising the thermal degradation temperature at higher loading.

- The Avrami exponent ‘n’ under isothermal and non-isothermal conditions is in the range from 2 to 4 for all the samples, indicating a complex two or three-dimensional growth phenomenon with branched fibrillar morphology. The value of k for samples that are processed without $scCO_2$ increases up to 0.5% loading, highest being 0.5% (9.12) and then slowly decreases and settles for 1% and 2.5% graphene loading (6.02).
- The rate of crystallisation value ‘k’, decreased with $scCO_2$ compared to without $scCO_2$ composites, suggests a better interaction between the polymer chain and the graphene particles. This suggests that $scCO_2$ initiates exfoliation and improved interaction of graphene particles which further restricts the nucleation and the growth process. The $scCO_2$ graphene composites have higher activation energy for 0.5,1 and 2.5% compared to their untreated composites. These results indicate that at low graphene loading, graphene acts as nucleating sites and as the loading is increased the interfacial interactions restrict the easy movement to crystal growth, thus increasing the activation energy.
- DMA results showed a significant increase in stiffness (storage modulus) for untreated polymer composites with respect to pure Pebax (58%) result, while $scCO_2$ treated composites gave a lower increasing stiffness with respect to untreated composites (10 to 18% when treated with $scCO_2$).
- Tensile test results show a similar behaviour to DMA results, where a significant and gradual increase in Young’s modulus is observed for untreated polymer matrices. However, an additional 8 to 10% increases in Young’s modulus was observed when treated with $scCO_2$.
- ATR-FTIR spectra showed an increase in the interaction between the amphoteric NH in the amide group and the electropositive graphene surface when treated with $scCO_2$. The presence of such evident shifts in SCF-treated composites also suggests that $scCO_2$ has resulted in the exfoliation of graphene nanoparticles, thereby reducing the number of layers and increasing the availability of pi electrons.
- The frequency dependence of AC conductivity shows that the conductivity increases depending on the graphene loading. However, when the composites were reprocessed with $scCO_2$, the conductivity increased from 10^{-9} S/m to 10^{-6} S/m, while untreated composites showed lower conductivity when compared to $scCO_2$ assisted extrusion.

7.4 Section 2: Pebax Graphene Oxide Composites

7.4.1 Throughput Test of Pebax GO Composites

Pebax GO-based nanocomposites throughput for one-minute was repeated 3 times and the average was taken (with all other conditions kept constant) (Table 7.12). The total mean weight of the SCF-assisted extruded composites had a higher average weight when compared to samples extruded without SCF. The total weight extruded with SCF is due to the plasticisation effect, where $scCO_2$ changes the viscosity of the polymer melt and thereby increases the throughput.

Table 7.12 Average weights of extruded Pebax GO composite for 1-minute

Sample type	Average weight of Pebax GO-based nanocomposite extruded for 1-minute	
	Without SCF	With SCF
	G	g
Pebax	14.55±4.3	26.92±3.4
PGO 0.5%	13.11±6.3	22.89±6.8
PGO 1%	10.70±3.5	19.06±3.3
PGO 2.5%	10.91±2.1	20.66±5.8

7.4.2 Thermal Gravimetric Analysis of Pebax GO Composites

It was observed (Table 7.13) that GO eliminates the loosely bound water and gas molecules below 100 °C and GO completely degrades at 218 °C, which is due to degradation of oxygen-containing functional groups. Figure 7.26 and Table 7.13, showed no significant difference in the degradation temperature for GO Pebax composites with and without $scCO_2$.

Table 7.13 Degradation temperature profile of Pebax GO composites (with and without $scCO_2$)

Sample type	Maximum degradation temperature	
	Without SCF	With SCF
	° C	° C
Pebax	468.1	465.5
PGO 0.5%	467.9	467.6
PGO 1%	466.1	467.1
PGO 2.5%	470.8	471.7

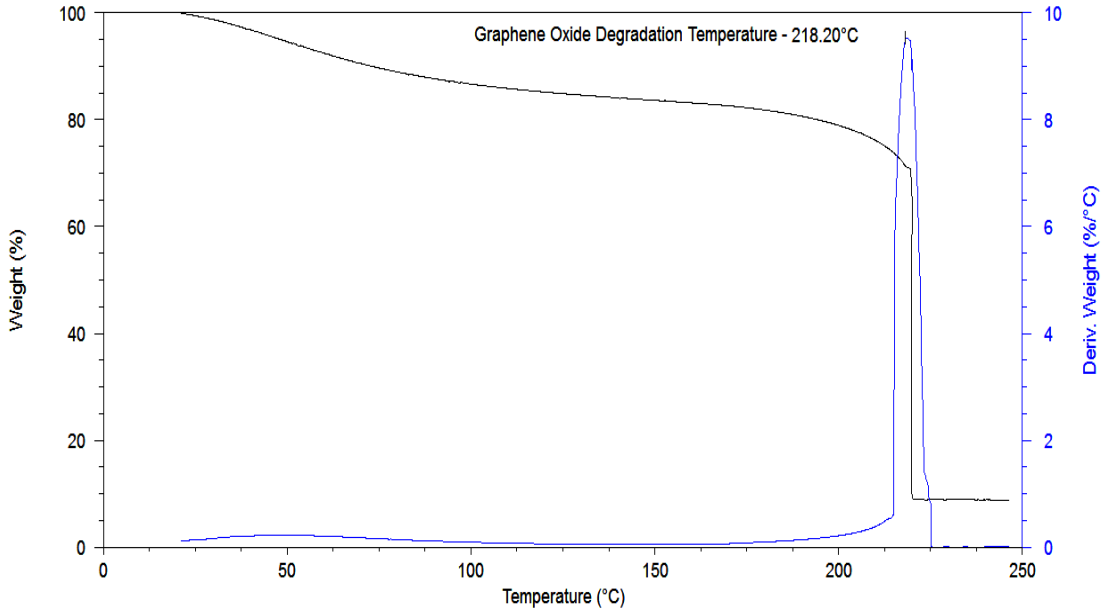

Figure 7.25 Thermal degradation profile of GO

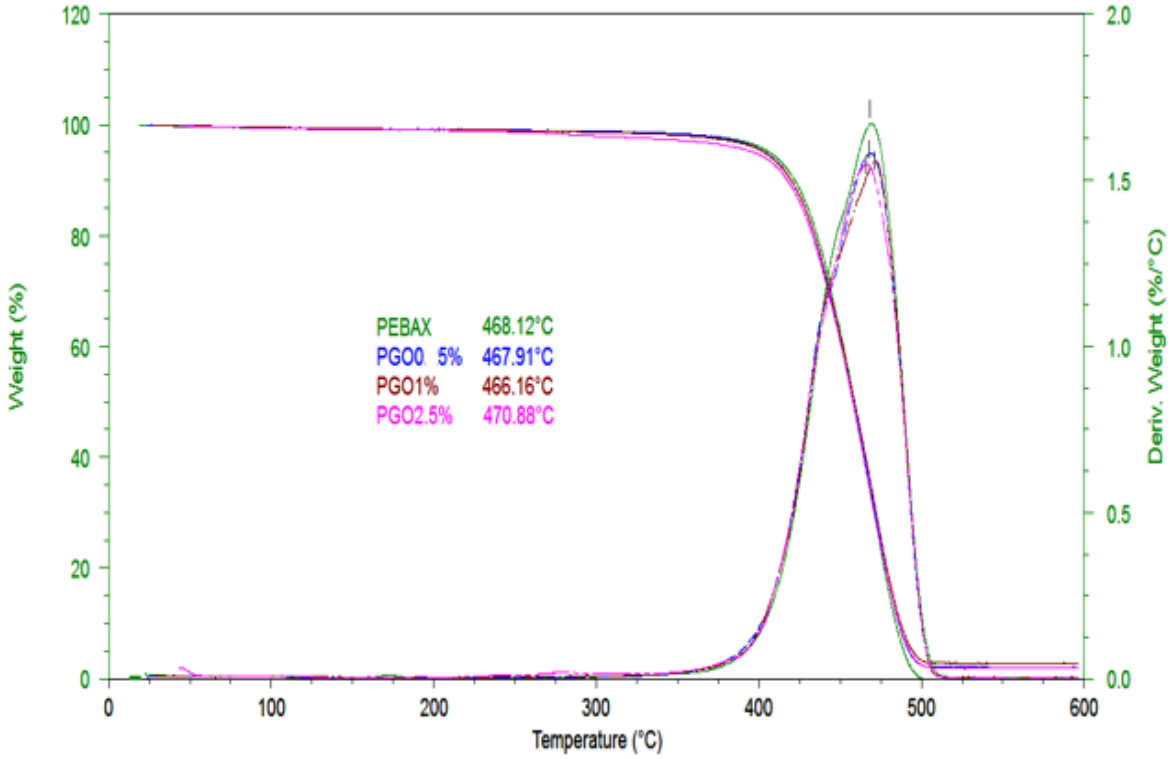

Figure 7.26 Thermal degradation profiles of Pebax GO composites without $scCO_2$

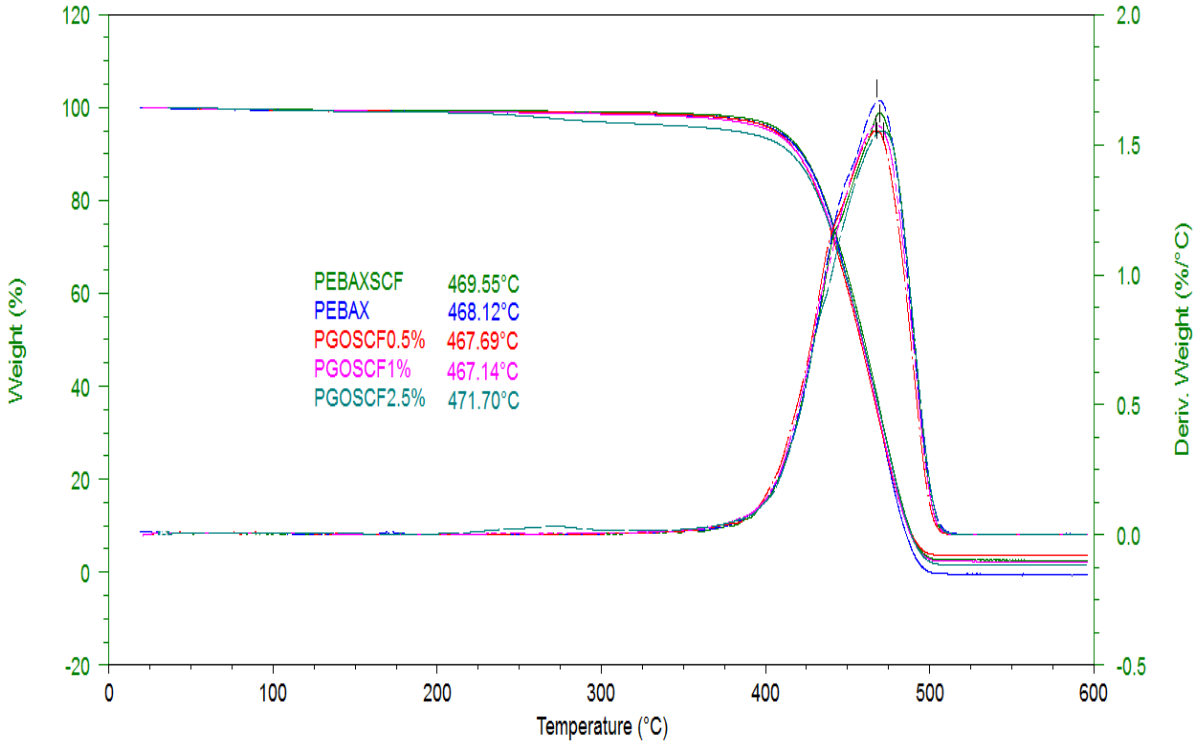

Figure 7.27 Thermal degradation profiles of Pebax GO composites with $scCO_2$

7.4.3 Differential Scanning Calorimetry of Pebax GO Composites

Figure 7.28 and Figure 7.29, present the heat flow thermogram of Pebax GO composites which were extruded with and without assisted $scCO_2$. It is evident from the heat flow curves (both first cycle and second cycle – in both the cases of with and without assisted $scCO_2$), that the melting temperature does not show significant deviation from the virgin Pebax (162.90 °C), even with the addition of GO up to 2.5%. Figure 7.30 presents the crystallisation thermograms of various Pebax graphene composites during the cooling cycle (extruded with and without assisted $scCO_2$). The GO fillers interact well with the Pebax polymer chains and result in the lowering of crystallisation temperature with respect to virgin Pebax. Although the crystallisation temperature is lowered, the peak broadens with the addition of GO for 0.5% and 2.5% loading suggesting differences in crystallite size.

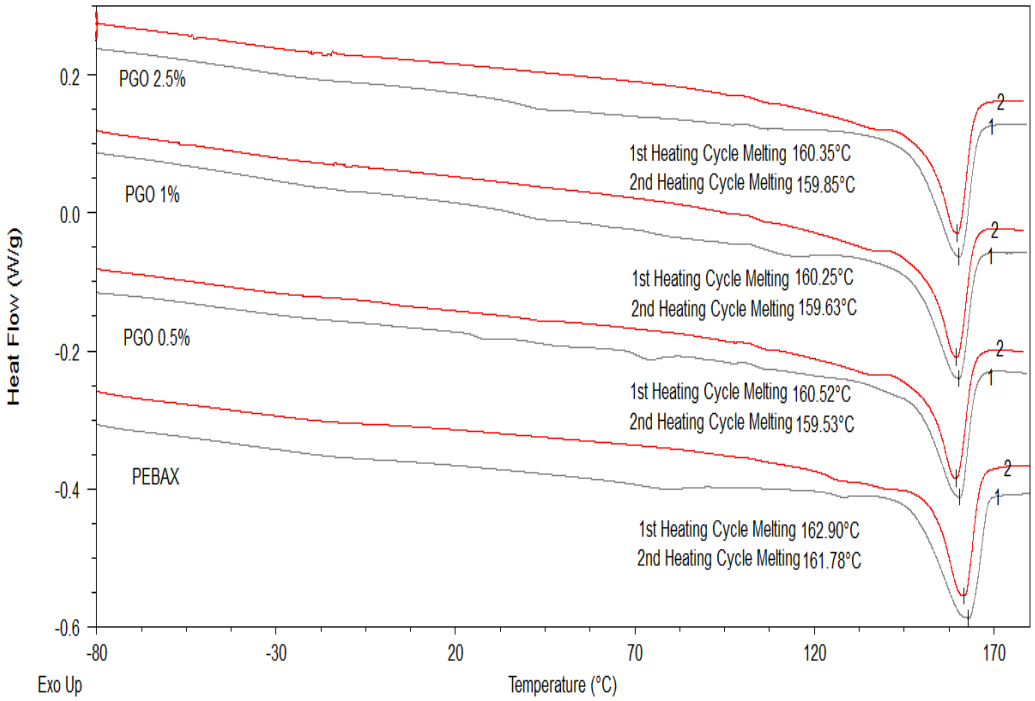

Figure 7.28 Heat flow thermogram of Pebax GO composite without $scCO_2$

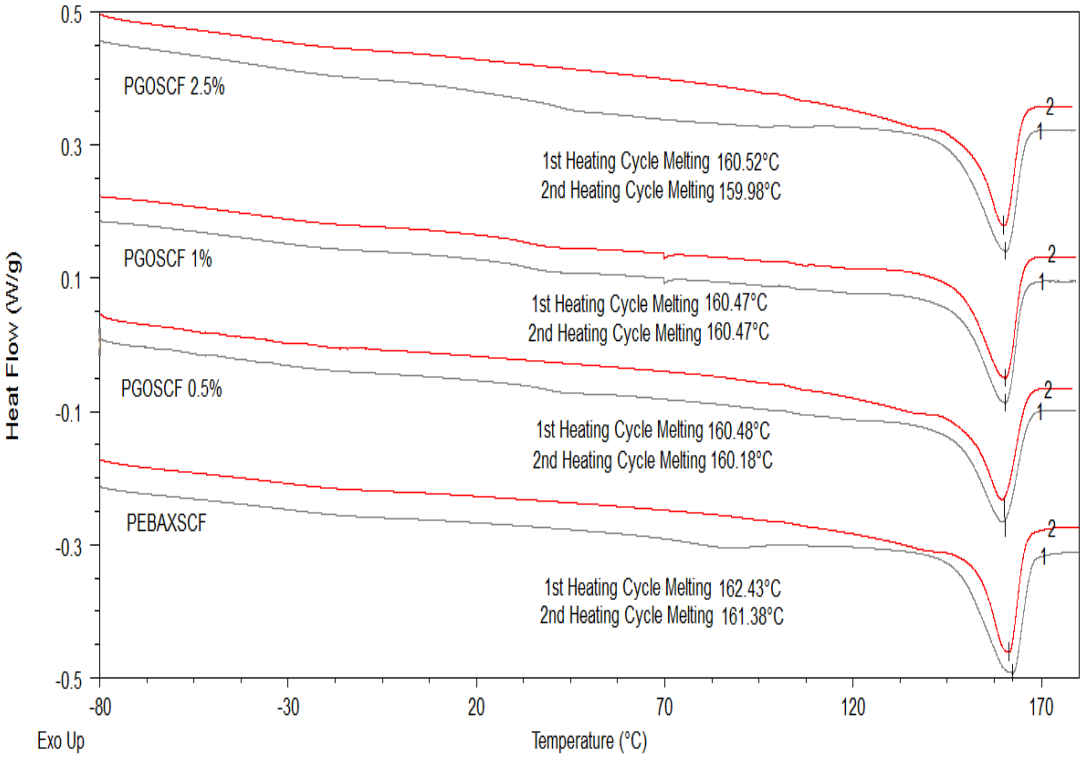

Figure 7.29 Heat flow thermogram of Pebax GO composite (output of scCO2 reprocessed without $scCO_2$)

The shift in crystallisation temperatures towards lower temperatures suggests that the GO has interacted well with the Pebax polymer chain thereby improving the homogeneity of the composites. In the case of heterogeneous polymer composites, where there was less interaction between the polymer and the filler particles, the crystallisation temperature shifts towards higher temperatures. In the case of $scCO_2$ treated composites, the GO fillers interact well with Pebax polymer chain and result in lowering the crystallisation temperature with respect to virgin Pebax. Although the crystallisation temperature was lowered, the peak broadens with the addition of GO for 0.5% and 2.5% loading showing differences in crystallite size. This shows that the $scCO_2$ assisted extrusion and reprocessing results in a broadening of crystallisation temperature, thereby affecting the crystallite size.

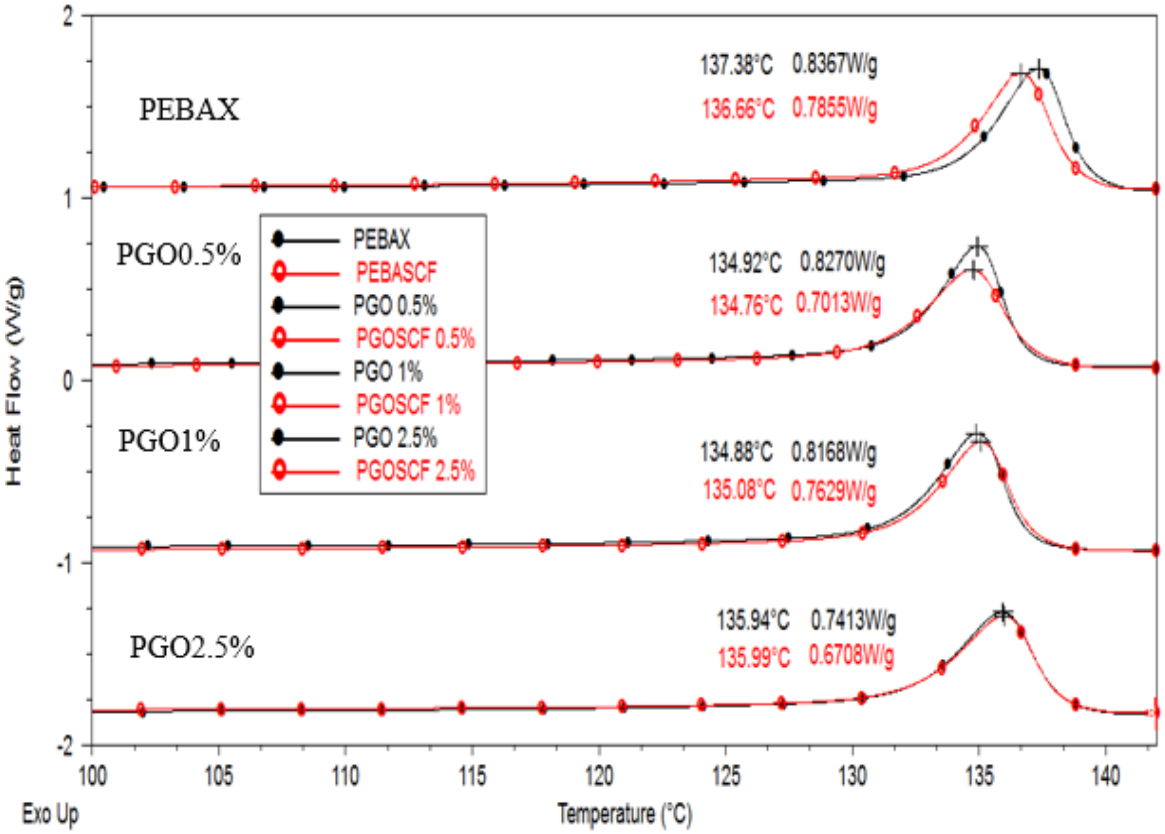

Figure 7.30 Comparison of crystallisation peak of Pebax GO composites with and without $scCO_2$

The crystallisation temperature of Pebax graphene composites tends to shift to higher temperatures making it a heterogeneous network, while Pebax GO crystallisation temperature shifts to lower temperatures making it a homogenous network. The crystallisation temperature shifts to lower temperatures and results in a broadening effect when the polymer composites (both graphene and GO) were processed with $scCO_2$. This demonstrates that $scCO_2$ not only

helps to provide exfoliation or improved dispersion of additives but also induces a certain amount of crystallinity to the polymer itself by arranging the polymer chain in a more favourable manner.

7.4.3.1 Isothermal Crystallisation Kinetics of Reprocessed Pebax GO Composites

The Avrami model was used to understand the isothermal crystallisation kinetics of reprocessed Pebax GO (with and without $scCO_2$) polymer composites at various percentages of graphene loading levels. The Avrami model is clearly described in the methodology section of Chapter 3 (3.4.3.1). The parameters n and k can be obtained from the slope and the intercept of the Avrami plot of log [-ln (1-Xt)] vs. log t. Table 7.14 shows the parameter n and k along with $t_{1/2}$ values which were obtained from the heat flow thermograms and the theoretically calculated value. It is evident that the value of n remains between 2 and 3 for all the samples, indicating complex fibrillar two-dimensional crystallite structure.

The k value tends to decrease with increasing isothermal temperatures for all the samples. The value of k decreases upon addition of GO 0.5%, refer to highlighted Tc on Table 7.14 (Tc @ 144 °C has k= 0.093) and 1% (Tc @ 144 °C has k= 0.15) while increases for 2.5% (Tc @ 144 °C has k= 5.75) compared to virgin Pebax (Tc @ 144 °C has k= 0.41). The $t_{1/2}$ value also follows the same trend where, the time taken to reach 50% crystallisation increases for 0.5% and 1%, indicating slow crystallisation rate and a significant decrease for 2.5% loading, indicating faster crystallisation rate with respect to virgin Pebax. These values indicate that the addition of GO particles reduces the crystallisation rate at a lower loading of 0.5% and gradually increases for 1% and 2.5%. The use of $scCO_2$ does not have a significant effect on the crystallisation parameter k up to 1%, however, the k value is much higher for 2.5% compared to its untreated counterpart indicating faster crystallisation rate with $scCO_2$.

Table 7.14 Avrami parameters of Pebax GO composites with and without $scCO_2$ under isothermal conditions

Sample Type	Tm (°C)	n	Log k	k	$t_{1/2}$* (min)	$t_{1/2}$ (min)	G (min^{-1})	R^2
Pebax	139	2.64	0.95	8.91	0.36	0.38	2.6	0.999
	140	2.72	0.72	5.75	0.45	0.47	2.1	0.999
	141	2.55	0.50	2.97	0.52	0.54	1.8	0.999
	142	2.65	0.23	1.71	0.69	0.71	1.4	0.999
	143	2.69	-0.07	0.85	0.88	0.92	1.0	0.999
	144	**2.85**	**-0.38**	**0.41**	**1.16**	**1.19**	**0.8**	**1.000**
	141	2.56	0.40	2.51	0.56	0.60	1.6	0.999
	142	2.84	0.19	1.54	0.72	0.75	1.3	0.999

PebaxSCF	143	2.70	-0.07	0.83	0.91	0.93	1.0	0.999
	144	2.89	-0.37	0.42	1.16	1.18	0.8	1.000
	145	2.94	-0.71	0.19	1.53	1.54	0.6	1.000
	146	3.20	-1.17	0.067	2.06	2.06	0.4	1.000
PGO 0.5	141	2.57	-0.07	0.83	0.90	0.93	1.0	0.999
	142	2.74	-0.32	0.47	1.11	1.14	0.8	1.000
	143	2.92	-0.65	0.22	1.47	1.47	0.6	0.999
	144	**3.09**	**-1.03**	**0.093**	**1.95**	**1.91**	**0.5**	**1.000**
	146	2.70	-1.54	0.028	3.06	3.24	0.3	0.999
PGOSCF 0.5	141	2.76	-0.10	0.79	0.92	0.95	1.0	0.999
	142	2.71	-0.31	0.48	0.52	1.11	0.8	0.999
	143	2.74	-0.58	0.26	1.41	1.42	0.7	1.000
	144	2.79	-0.89	0.12	1.81	1.82	0.5	1.000
	146	2.72	-1.52	0.03	3.16	3.16	0.3	0.999
PGO 1	141	2.48	0.09	1.23	0.75	0.79	1.2	0.999
	142	2.43	-0.14	0.72	0.93	0.98	1.0	0.999
	143	2.75	-0.47	0.33	1.28	1.29	0.7	1.000
	144	**2.91**	**-0.81**	**0.15**	**1.68**	**1.67**	**0.5**	**1.000**
	146	2.76	-1.41	0.03	2.73	2.83	0.3	1.000
PGOSCF 1	141	2.54	0.004	1.00	0.81	0.86	1.1	0.999
	142	2.47	-0.20	0.63	0.98	1.03	0.9	1.000
	143	2.76	-0.52	0.30	1.33	1.35	0.7	1.000
	144	2.69	-0.79	0.16	1.70	1.71	0.5	1.000
	146	2.80	-1.56	0.02	3.01	3.16	0.3	0.999
PGO 2.5	**144**	**2.05**	**0.76**	**5.75**	**0.32**	**0.34**	**2.80**	**0.999**
	146	2.42	0.36	2.29	0.60	0.61	1.63	1.000
	147	2.42	0.18	1.51	0.70	0.72	1.38	1.000
	148	2.58	-0.06	0.87	0.91	0.91	1.09	1.000
	149	2.44	-0.26	0.54	1.10	1.10	0.90	1.000
	150	2.82	-0.59	0.25	1.46	1.42	0.70	0.999
PGOSCF 2.5	144	2.29	0.87	7.41	0.78	0.35	2.8	0.999
	146	2.28	0.41	2.57	1.04	0.56	1.7	0.999
	147	2.31	0.26	1.81	1.35	0.65	1.5	1.000
	148	2.37	0.02	1.04	1.81	0.84	1.1	0.999
	149	2.54	-0.19	0.64	2.46	1.02	0.9	1.000
	150	2.64	-0.43	0.37	3.16	1.26	0.7	1.000

The value of $1/t_{1/2}$ can be used to describe the crystallisation rate and is plotted in Figure 7.31 as a function of isothermal crystallisation temperature. It can be clearly seen that the crystallisation rate G ($1/t_{1/2}$) decreases upon addition of GO at lower concentration levels (@0.5% and 1%), however, the crystallisation rate significantly increases for 2.5% loading. Such phenomena of increased G and k value upon addition of graphene up to 1% is usually attributed to heterogeneous nucleation rates as described by Kirkorian et al [176].

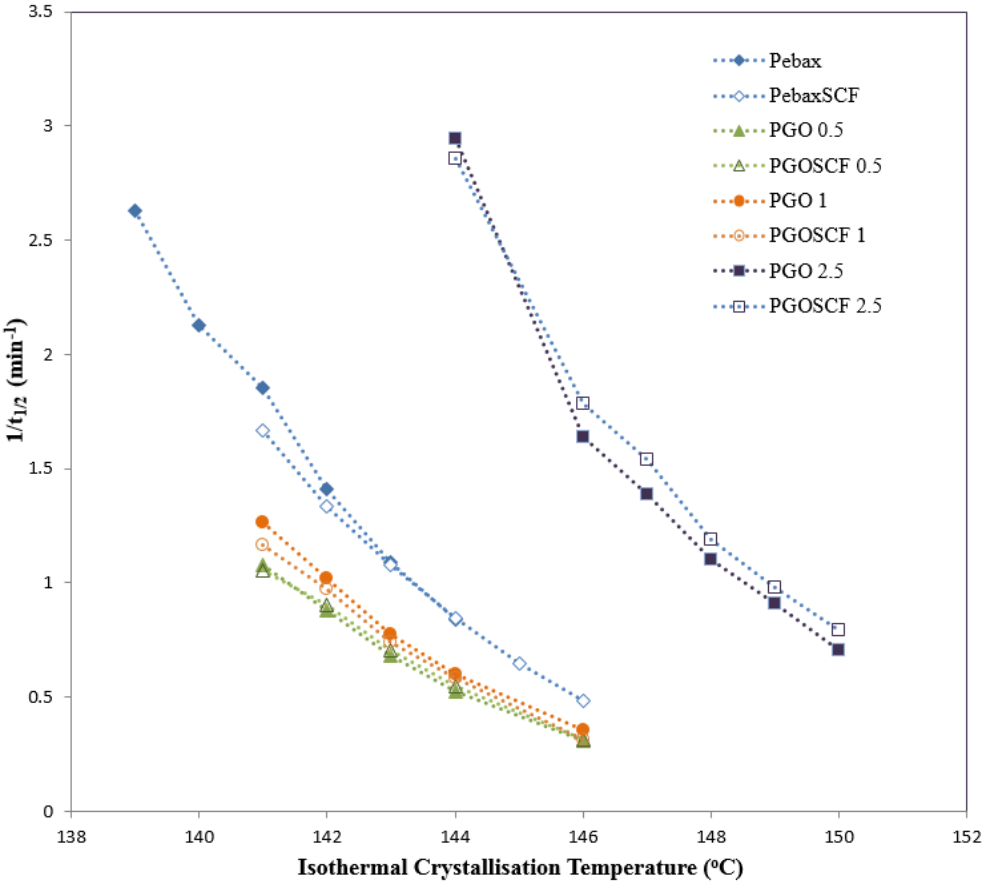

Figure 7.31 Crystallisation rate plotted at various isothermal crystallisation temperatures peak of Pebax GO composites with and without $scCO_2$

The crystallisation rate parameter was described by an Arrhenius type equation (refer to Section 3.4.3.1). The slope of the plot ln (K)*1/n vs. 1/Tc as shown in Figure 7.32 determines the ΔE/R. where the activation energy is calculated and is tabulated in Table 7.15. The ΔE value decreases for 0.5% loading, increases for 1% and decreases for 2.5 % loading virgin Pebax. However, the activation energy is the lowest for 2.5%. This demonstrates that the GO particles in the Pebax for 2.5% acted as nuclei, suggesting heterogeneous nucleation, which decreased the crystallisation free energy barrier, thereby decreasing or maintaining the crystallisation activation energy. However, at lower concentrations of 0.5% and 1%, the interaction between the Pebax and GO may act as restricting agents for the phase transformation, thus resulting in increasing the crystallisation free energy barrier and thus the activation energy. In all cases, the $scCO_2$ treated samples show lower activation energy required for phase transformation compared to their untreated counterparts. The activation energy increases for PGOSCF 0.5% and PGOSCF 1%, while decreases for PGOSCF 2.5%, clearly indicating heterogeneous nucleation at higher GO loading.

Table 7.15 Arrhenius activation energy for Pebax GO composites with and without $scCO_2$ under isothermal conditions

Samples	Arrhenius Activation Energy (KJ/mol)
Pebax	-356.488
PebaxSCF	-315.982
PGO 0.5	-334.846
PGOSCF 0.5	-322.317
PGO 1	-355.357
PGOSCF 1	-329.301
PGO 2.5	-329.151
PGOSCF 2.5	-308.682

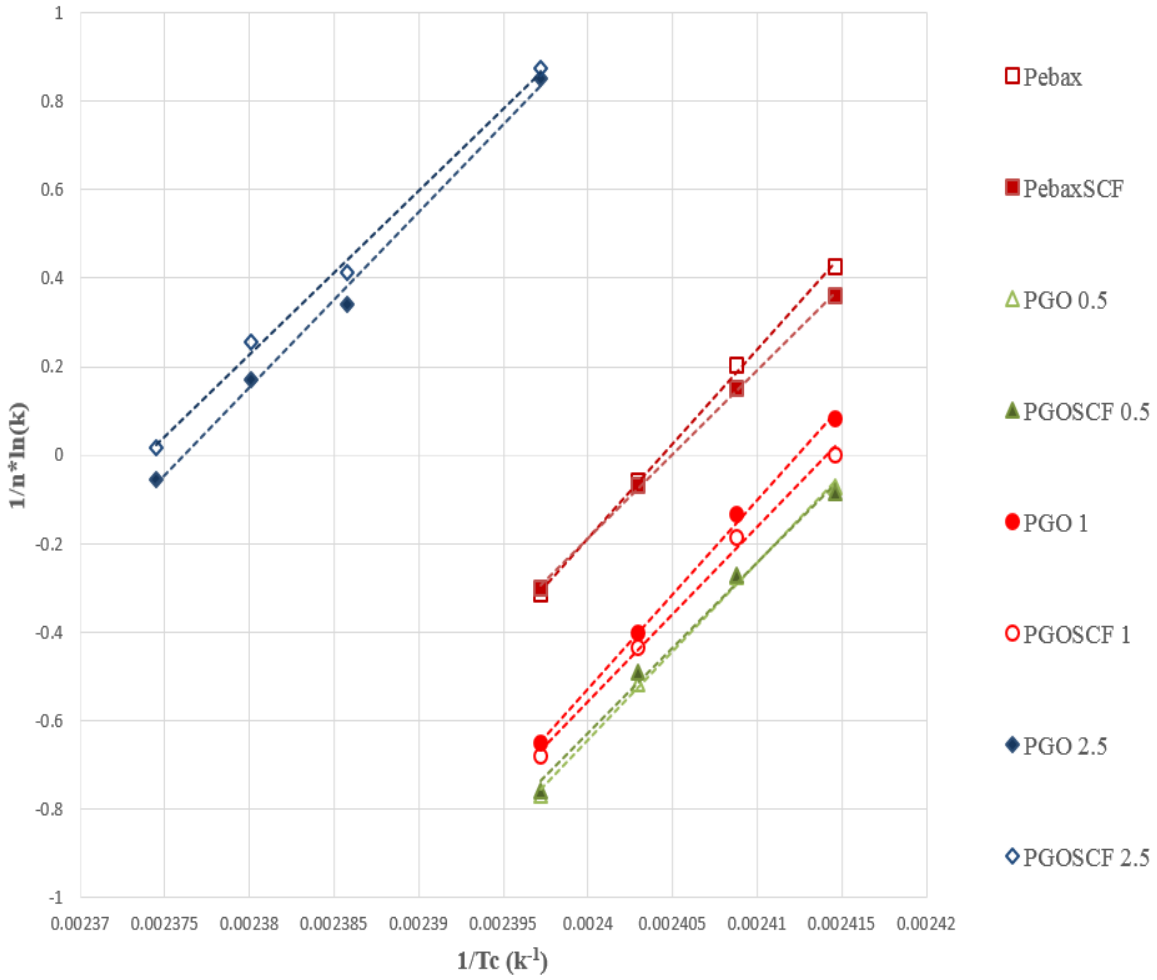

Figure 7.32 Arrhenius activation energy plot for Pebax GO composites with and without $scCO_2$ under isothermal conditions

7.4.3.2 Non-Isothermal Crystallisation Kinetics of Reprocessed Pebax GO Composites

The non-isothermal crystallisation kinetics of Pebax graphene composites with $scCO_2$ was studied under various cooling rates. Figure 7.33 shows the Tc and appropriate time in seconds to reach Tc at various cooling rates. Table 7.16 shows that the crystallisation onset temperature (Tc_{on}), peak crystallisation temperature (Tc) and crystallisation offset temperature (Tc_{off}) shifts to lower temperature and become broader with an increase in the cooling rate from 2.5 °C/min to 20 ˚C/min.

Table 7.16 Heat flow parameters for Pebax GO composites with and without $scCO_2$ under non-isothermal conditions

Sample Type	Cooling Rate (°C/min)	Tc_{on} (° C)	Tc_{off} (°C)	Tc (°C)	ΔHc (J/g)	Xc (%)
Pebax	2.5	144.11	113.14	140.91	40.36	38.40
	5	140.54	108.24	137.05	39.07	35.09
	10	136.74	105.15	132.70	36.88	51.11
	20	131.84	80.02	127.54	37.32	26.97
PebaxSCF	2.5	146.49	100.02	141.40	39.36	37.39
	5	142.88	100.03	137.32	38.21	37.26
	10	138.35	88.91	132.92	38.19	35.34
	20	133.97	83.31	127.75	35.93	34.48
PGO 0.5	2.5	143.99	111.48	139.19	38.09	35.96
	5	138.72	104.11	135.95	38.19	36.76
	10	134.92	97.70	132.20	38.50	31.63
	20	130.28	89.55	126.98	38.14	28.15
PGO SCF 0.5	2.5	144.09	113.14	139.10	35.63	40.92
	5	140.86	108.01	135.85	36.19	38.68
	10	137.20	98.85	131.76	35.34	33.22
	20	133.09	95.87	127.70	35.97	28.38
PGO 1	2.5	143.97	108.11	139.34	35.91	40.51
	5	141.22	105.32	136.15	36.02	36.45
	10	138.54	98.30	132.45	34.97	33.94
	20	133.64	95.22	127.48	34.38	31.61
PGO SCF 1	2.5	144.20	114.13	139.38	35.88	43.47
	5	141.40	106.34	136.20	36.61	36.62
	10	137.85	93.45	132.64	38.78	31.87
	20	134.42	92.62	128.60	37.65	29.05
PGO 2.5	2.5	151.99	120.12	145.75	36.66	37.37
	5	148.42	110.18	142.17	38.98	35.60
	10	145.66	99.54	138.46	40.09	34.33
	20	142.99	96.02	134.72	40.49	32.21
PGO SCF 2.5	2.5	151.69	117.77	146.01	39.00	37.46
	5	148.72	114.70	142.91	40.07	36.96
	10	145.33	96.66	138.99	41.53	34.60
	20	143.06	96.87	135.07	40.56	32.61

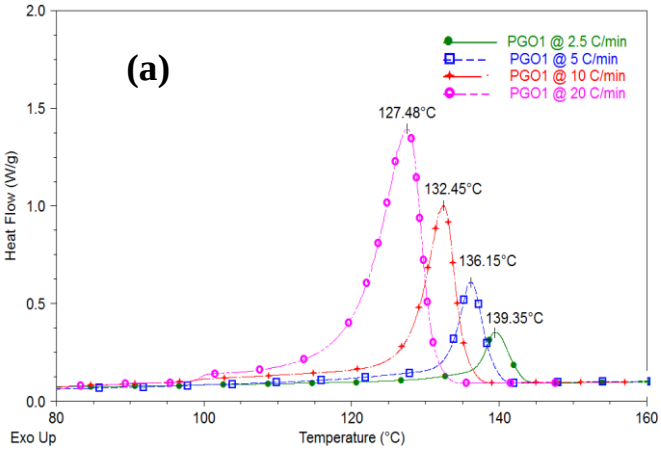
(a)
PGO1 @ 2.5 C/min
PGO1 @ 5 C/min
PGO1 @ 10 C/min
PGO1 @ 20 C/min
127.48°C
132.45°C
136.15°C
139.35°C
Heat Flow (W/g)
Exo Up
Temperature (°C)

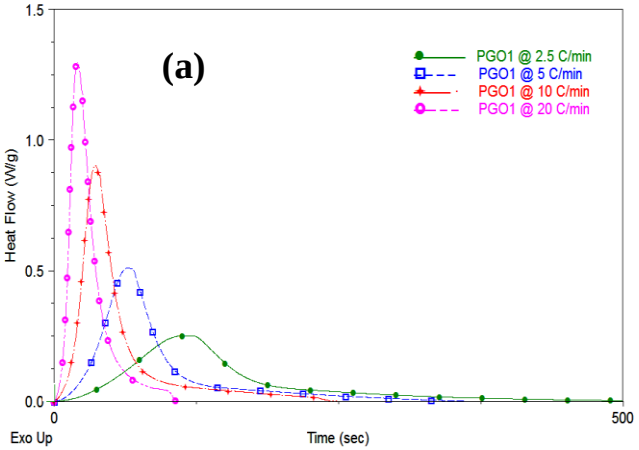
(a)
PGO1 @ 2.5 C/min
PGO1 @ 5 C/min
PGO1 @ 10 C/min
PGO1 @ 20 C/min
Heat Flow (W/g)
Exo Up
Time (sec)

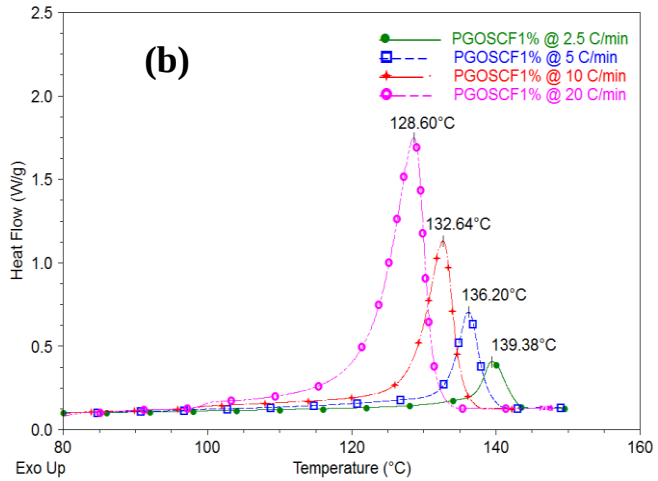
(b)
PGOSCF1% @ 2.5 C/min
PGOSCF1% @ 5 C/min
PGOSCF1% @ 10 C/min
PGOSCF1% @ 20 C/min
128.60°C
132.64°C
136.20°C
139.38°C
Heat Flow (W/g)
Exo Up
Temperature (°C)

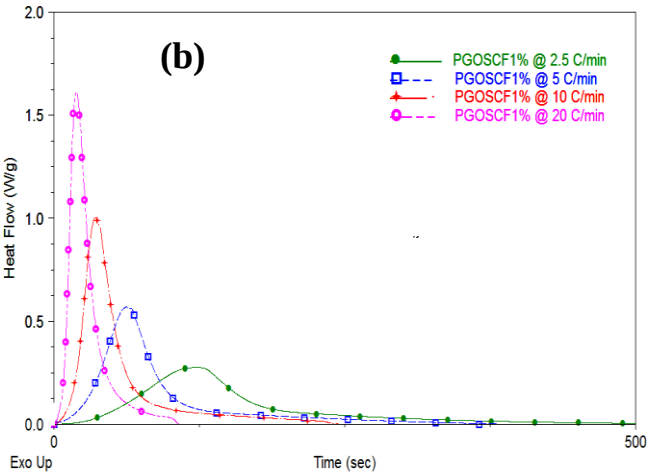
(b)
PGOSCF1% @ 2.5 C/min
PGOSCF1% @ 5 C/min
PGOSCF1% @ 10 C/min
PGOSCF1% @ 20 C/min
Heat Flow (W/g)
Exo Up
Time (sec)

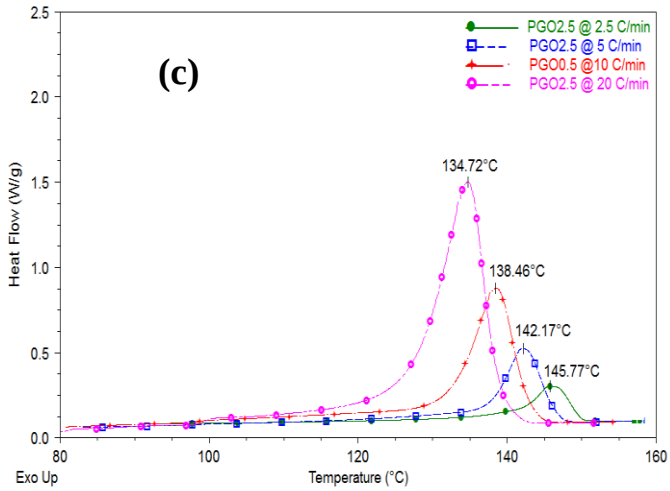
(c)
PGO2.5 @ 2.5 C/min
PGO2.5 @ 5 C/min
PGO0.5 @10 C/min
PGO2.5 @ 20 C/min
134.72°C
138.46°C
142.17°C
145.77°C
Heat Flow (W/g)
Exo Up
Temperature (°C)

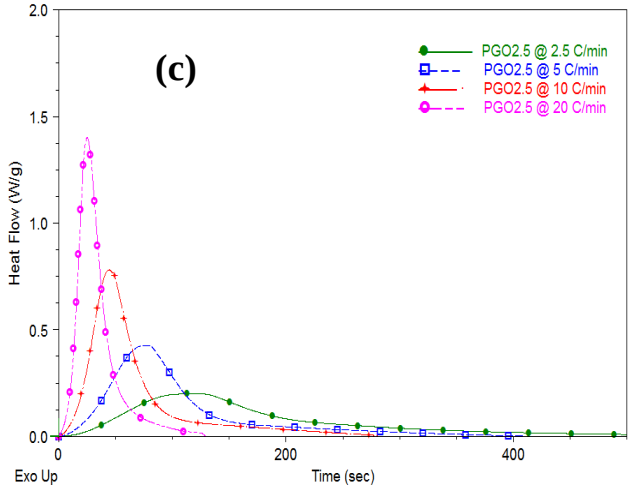
(c)
PGO2.5 @ 2.5 C/min
PGO2.5 @ 5 C/min
PGO2.5 @ 10 C/min
PGO2.5 @ 20 C/min
Heat Flow (W/g)
Exo Up
Time (sec)

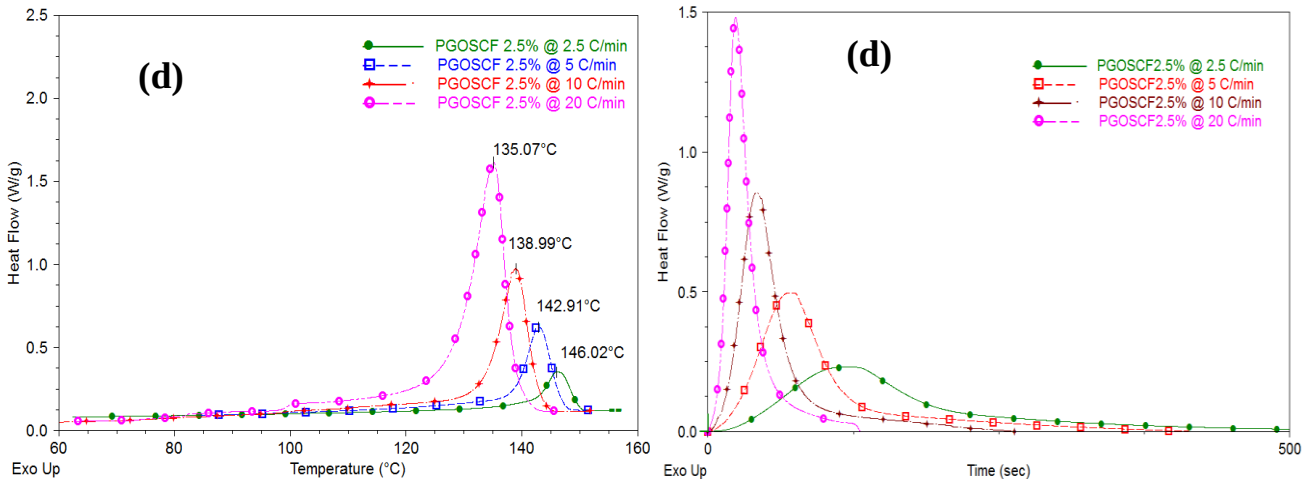

Figure 7.33 Heat flow curves at various temperatures and time for Pebax GO composites with and without $scCO_2$ under non-isothermal conditions (a. PGO 1%, b. PGOSCF 1%, c. PGO2.5%, d. PGOSCF 2.5%)

It can be clearly observed that the Tc values have a decreasing trend for all the samples (with and without $scCO_2$) except for 2.5% loading concentration (where the Tc value increases to 145 ˚C). This shifting of Tc peak to higher temperatures with the addition of graphene suggests the dominance of the heterogeneous nucleation process at higher GO content.

Avrami plot is presented in Figure 7.34 for Pebax GO composites with and without $scCO_2$. The corresponding Avrami parameters n and k were obtained from the slope and intercept of the plots, $t_{1/2}$ (calculated from the Equation. 4) and corresponding R^2 and are listed in Table 7.17. The value of k' increases with increasing cooling rate and the $t_{1/2}$ decreases with increasing cooling rate. As observed in the isothermal crystallisation kinetics, the k' value decreases upon addition of GO from 0.80 for virgin Pebax to 0.18 for 0.5%, 0.21 for 1% and 0.24 for 2.5%. An increase in k' can be observed for 2.5% GO loading suggesting slightly faster crystallisation compared to 0.5%. The k' value further reduces the treatment of $scCO_2$ assisted extrusion. This indicates slow crystallisation rate which might have occurred due to improved Pebax GO interaction which in turn limits the free chain movement during the crystal formation phase.

Another important observation is the shift of the n values from 2 to 3 specifically when the Pebax GO samples were processed with $scCO_2$. The average n values for samples extruded without $scCO_2$ are 2.57 for virgin Pebax, 3.08 for PGO 0.5%, 3.10 for PGO 1% and 2.91 for PG2.5%. The average n values for samples extruded with $scCO_2$ are 3.06 for virgin PebaxSCF, 3.22 for PGOSCF 0.5%, 3.26 for PGOSCF 1% and 3.10 for PGOSCF 2.5%. This indicates a clear shift from complex two-dimensional crystallite to complex three-dimensional crystallite, for samples with $scCO_2$. This suggests that the inclusion of GO particles along with $scCO_2$

assisted processing might have favoured exfoliation of graphene particles and this exfoliation/interaction may have initiated a complex crystallisation process (where the adhesion of GO particles on to polymer chain may act as nuclei).

Table 7.17 Avrami parameters for Pebax GO composites with and without $scCO_2$ under non-isothermal conditions

Sample Type	ϕ (°C/min)	n	Average n	Log k'	k'	$t_{1/2}$ From Graph (min)	$t_{1/2}$ Calculated (min)	R^2
Pebax	2.5	2.42	2.57	-0.09	0.80	0.95	1.01	0.993
	5	2.66		0.24	1.73	0.56	0.70	0.990
	10	2.70		0.86	7.24	0.32	0.41	0.982
	20	2.53		1.48	30.19	0.17	0.22	0.985
PebaxSCF	2.5	3.25	3.06	-0.77	0.16	1.50	1.54	0.998
	5	3.19		-0.02	0.95	0.86	0.90	0.997
	10	2.84		0.84	6.91	0.42	0.44	0.988
	20	2.99		1.58	38.01	0.25	0.26	0.989
PGO 0.5	2.5	3.14	3.08	-0.73	0.18	1.46	1.51	0.999
	5	2.99		0.04	1.09	0.78	0.85	0.997
	10	2.96		0.75	5.62	0.44	0.45	0.996
	20	3.23		1.72	52.48	0.23	0.26	0.997
PGOSCF 0.5	2.5	3.53	3.22	-0.86	0.13	1.54	1.57	0.999
	5	3.01		0.04	1.09	0.78	0.85	0.998
	10	3.13		0.85	7.07	0.43	0.47	0.997
	20	3.21		1.92	83.17	0.20	0.22	0.995
PGO 1	2.5	2.98	3.10	-0.67	0.21	1.42	1.48	0.999
	5	3.14		0.04	1.09	0.80	0.86	0.998
	10	3.09		0.79	4.78	0.43	0.53	0.996
	20	3.19		1.64	66.06	0.22	0.23	0.996
PGO SCF 1	2.5	3.42	3.26	-0.83	0.14	1.53	1.57	0.999
	5	2.85		0.017	1.03	0.76	0.86	0.997
	10	3.19		0.79	6.16	0.45	0.50	0.994
	20	3.58		2.06	114.8	0.22	0.23	0.995
PGO 2.5	2.5	2.98	2.91	-0.61	0.24	1.40	1.41	0.999
	5	2.75		-0.16	0.69	0.91	1.00	0.998
	10	3.01		0.54	3.46	0.54	0.58	0.997
	20	2.92		1.20	15.84	0.29	0.34	0.995
PGOSCF 2.5	2.5	3.20	3.10	-0.72	0.19	1.46	1.49	0.999
	5	3.05		-0.003	0.99	0.84	0.88	0.998
	10	3.18		0.67	4.67	0.50	0.54	0.997
	20	2.97		1.28	19.05	0.29	0.32	0.993

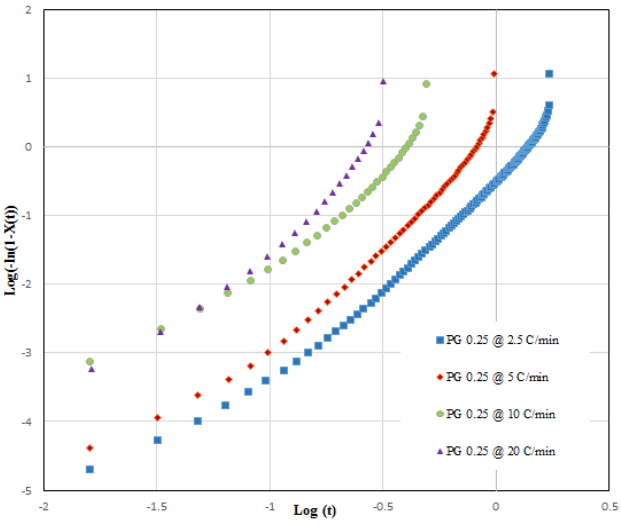

a. PGO 0.25%

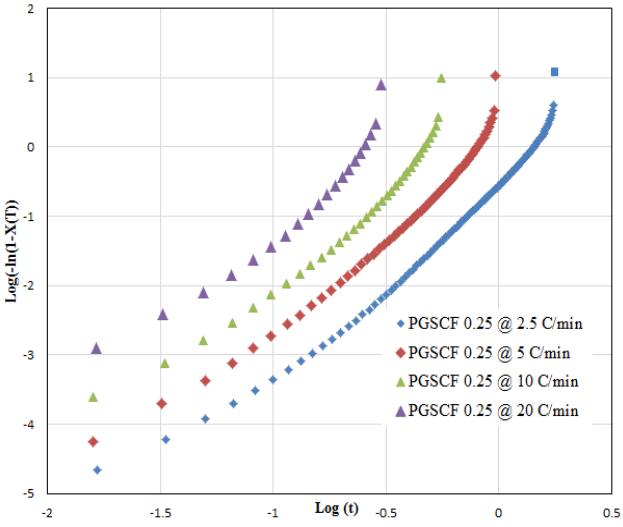

b. PGOSCF 0.25%

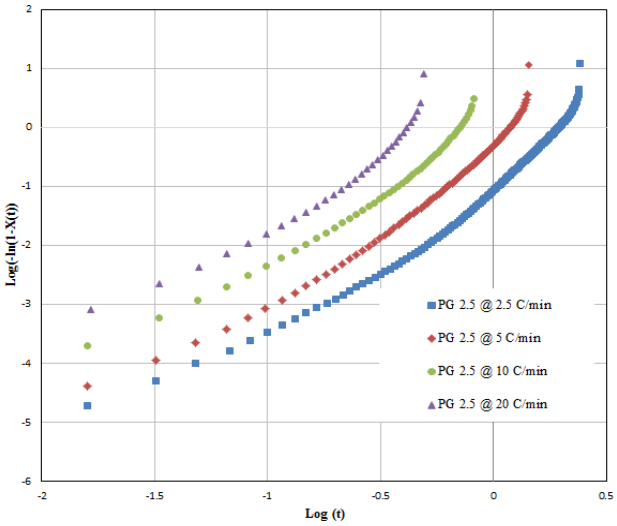

c. PGO 2.5%

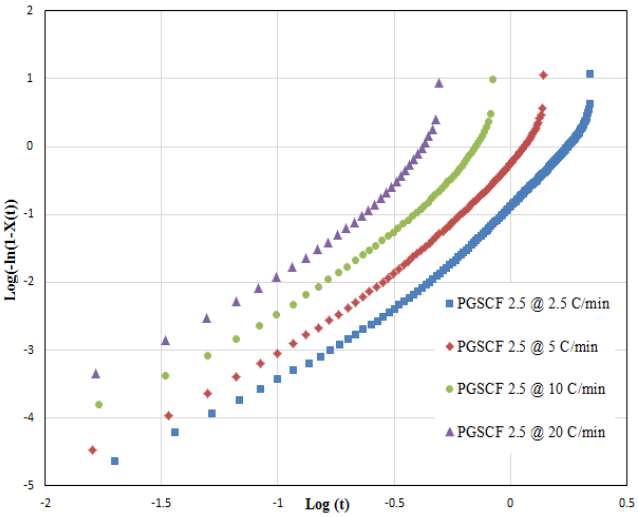

d. PGOSCF 2.5%

Figure 7.34 Avrami plot for Pebax GO composites with and without $scCO_2$ under non-isothermal conditions

Another important observation is the shift of the n values from 2 to 3 specifically when the Pebax GO samples were processed with $scCO_2$. The average n values for samples extruded without $scCO_2$ are 2.57 for virgin Pebax, 3.08 for PGO 0.5%, 3.10 for PGO 1% and 2.91 for PG2.5%. The average n values for samples extruded with $scCO_2$ are 3.06 for virgin PebaxSCF, 3.22 for PGOSCF 0.5%, 3.26 for PGOSCF 1% and 3.10 for PGOSCF 2.5%. This indicates a clear shift from complex two-dimensional crystallite to complex three-dimensional crystallite, for samples with $scCO_2$. This suggests that the inclusion of GO particles along with $scCO_2$ assisted processing might have favoured exfoliation of graphene particles and this exfoliation/interaction may have initiated a complex crystallisation process (where the adhesion of GO particles on to the polymer chain may act as nuclei).

Table 7.18 Ozawa parameters for Pebax GO composites with and without $scCO_2$ under non-isothermal conditions

Sample Type	T (°C)	m	Log k*	R^2
Pebax	125	-0.52	1.73	0.842
	128	-1.13	2.39	0.744
	133	-1.27	2.06	0.843
	138	-3.82	3.88	0.993
	140	-4.18	3.40	0.981
PebaxSCF	125	-0.46	1.42	0.953
	128	-0.81	1.76	0.845
	133	-2.80	4.07	0.786
	138	-4.63	5.02	0.894
	141	-3.36	2.52	1.000
PGO 0.5	124	-0.56	1.63	0.902
	126	-0.74	1.76	0.847
	130	-1.99	3.21	0.743
	133	-4.61	6.38	0.759
	136	-3.57	3.93	0.900
PGOSCF 0.5	125	-0.61	1.82	0.975
	127	-0.82	1.96	0.923
	130	-1.84	3.11	0.811
	132	-3.01	4.44	0.816
	135	-3.31	3.97	0.863
	138	-3.73	3.30	1.000
PG 1	125	-0.55	1.60	0.939
	128	-0.97	1.99	0.834
	130	-1.66	2.80	0.777
	134	-2.64	3.92	0.779
	136	-3.36	3.70	0.892
PGSCF 1	125	-0.53	1.69	0.996
	128	-0.89	1.86	0.933
	130	-1.45	2.60	0.827
	135	-2.45	3.75	0.798
	138	-3.51	3.19	1.000
PG 2.5	130	-0.48	1.64	0.991
	134	-0.73	1.72	0.940
	138	-1.69	1.26	0.867
	140	-2.40	3.25	0.897
	142	-3.63	4.37	0.915
PGSCF 2.5	130	-0.46	1.61	0.983
	132	-0.82	1.79	0.899
	136	-1.66	2.67	0.838
	140	-2.40	3.35	0.874
	144	-2.37	2.78	0.875

As described in the earlier sections of non-isothermal analysis (5.2.2.2), an Avrami extended model by Ozawa is used, where the change in the degree of crystallinity (X(T)) as a function of

varying cooling rate is considered. The Figure 7.35 and the Table 7.18 show the parameters obtained from the Ozawa model.

The plot of ln (-ln (1-X(T)) vs. ln ϕ taken at different temperatures ranging from 125˚C to 144˚C, where the slope and intercept gives the kinetic parameters m and k*. Both Log k* and m values do not show any significant changes when graphene particles are introduced (m and k* independent of graphene filler concentration). It is evident from the Ozawa plot that, a perfect linear fit cannot be achieved, due to inflthe uence of secondary crystallisation (R^2 <<1). This suggests that mean m and k* values are difficult to achieve and thus the Ozawa method cannot be used to describe the crystallisation kinetics of Pebax GO composites under non-isothermal conditions.

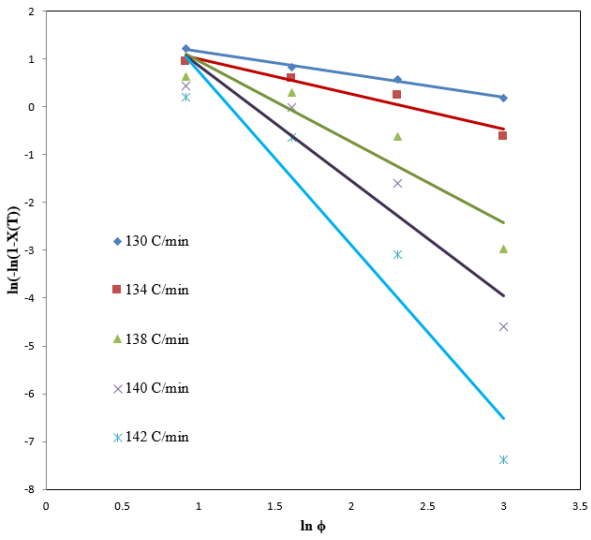

e. PGO 2.5%

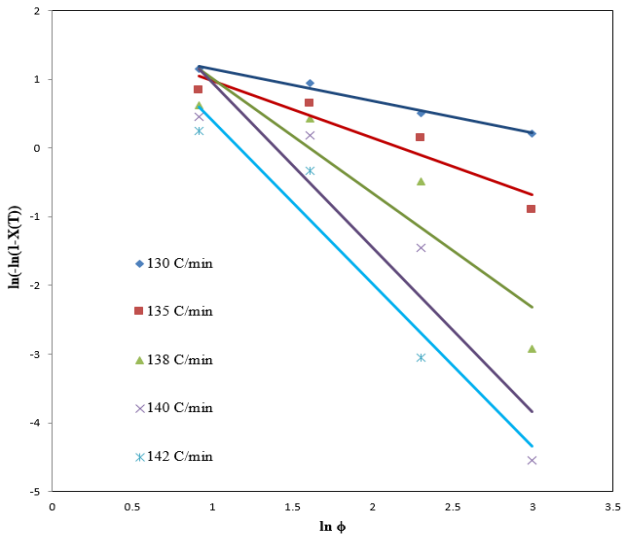

f. PGOSCF 2.5%

Figure 7.35 Ozawa plot for Pebax GO composites with and without $scCO_2$ under non-isothermal conditions

The combined Avrami and Ozawa equation as reported by Mo et al [111] was used to describe the kinetics of non-isothermal crystallisation by plotting the log ϕ vs. log t at a specific value of X(t). The values b and F(T) can be obtained from the slope and intercept of the plot (Table 7.19). It is clearly evident from the table that the ln F(T) values gradually increases with the addition of GO (consider samples without $scCO_2$). A trend can be observed where the F(T) values are the highest for 0.5% (without scCO2) and lowest for 2.5% GO loading. This suggests that the rate of crystallisation is faster for 2.5% loading concentration compared to other lower loading concentrations. This increase indicates that at unity crystallisation time, a higher cooling rate should be used in order to obtain a higher degree of crystallinity.

Table 7.19 Combined Avrami and Ozawa parameters for Pebax GO composites with and without $scCO_2$ under non-isothermal conditions

Sample Type	X(T)	b	Mean 'n'	ln F(T)	F(T)	R^2
Pebax	0.2	1.31	2.57	0.42	1.52	0.981
	0.4	1.27		0.71	2.03	0.988
	0.6	1.26		0.88	2.41	0.991
	0.8	1.25		1.00	2.71	0.993
PebaxSCF	0.2	1.15	3.06	1.05	2.85	0.997
	0.4	1.14		1.35	3.85	0.998
	0.6	1.13		1.46	4.30	0.999
	0.8	1.11		1.59	4.90	0.999
PGO 0.5	0.2	1.16	2.76	1.00	2.71	0.999
	0.4	1.12		1.24	3.45	0.999
	0.6	1.11		1.40	4.05	0.999
	0.8	1.11		1.51	4.52	0.999
PGO SCF 0.5	0.2	1.01	3.43	1.09	2.97	0.999
	0.4	1.03		1.29	3.63	0.999
	0.6	1.04		1.42	4.13	0.999
	0.8	1.03		1.52	4.57	1.000
PGO 1	0.2	1.22	2.72	0.97	2.63	0.999
	0.4	1.18		1.24	3.45	0.999
	0.6	1.17		1.41	4.09	0.999
	0.8	1.14		1.53	4.61	0.999
PGO SCF 1	0.2	1.14	3.45	1.05	2.85	0.999
	0.4	1.09		1.28	3.59	0.999
	0.6	1.07		1.42	4.13	0.999
	0.8	1.06		1.52	4.57	0.999
PGO 2.5	0.2	1.40	2.68	0.95	2.58	0.999
	0.4	1.33		1.30	3.66	0.999
	0.6	1.33		1.52	4.57	0.999
	0.8	1.29		1.67	5.31	0.999
PGOSCF 2.5	0.2	1.34	3.15	0.98	2.66	0.999
	0.4	1.27		1.28	3.59	0.999
	0.6	1.24		1.48	4.39	0.998
	0.8	1.23		1.62	5.05	0.999

All the Pebax GO composites had a larger ln F(T) when compared to the virgin Pebax for all the relative degree of crystallinity values. It suggests that the addition of GO has lowered the rate of crystallisation compared to virgin Pebax (agreement with the Avrami model); thereby hindering the nucleation or the growth rate. The addition of $scCO_2$ further increases the F(T) value, indicating much slower crystallisation rate when compared to its untreated counterpart. As discussed in Avrami section 5.2.2.2, $scCO_2$ lowers the crystallisation rate likely due to two possible reasons, first, due to induced rearrangement of the polymer chain to kinetically more favourable configuration and second, due to GO exfoliation which hinders the transformation during the growth phase.

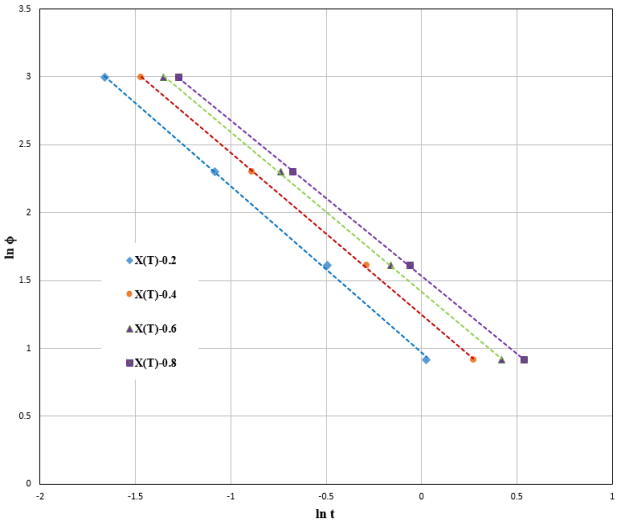

a. PGO 1%

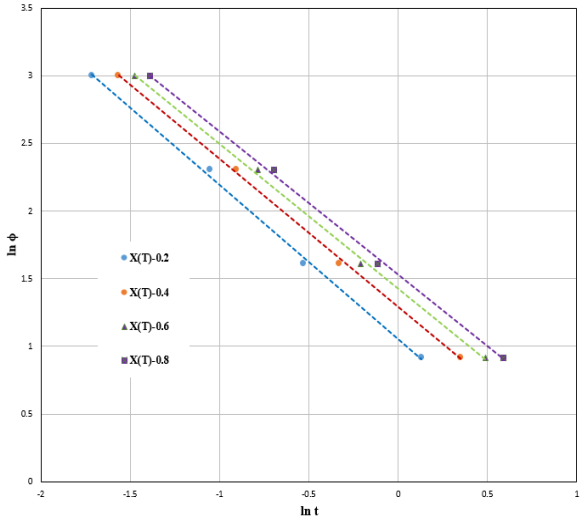

b. PGOSCF 1%

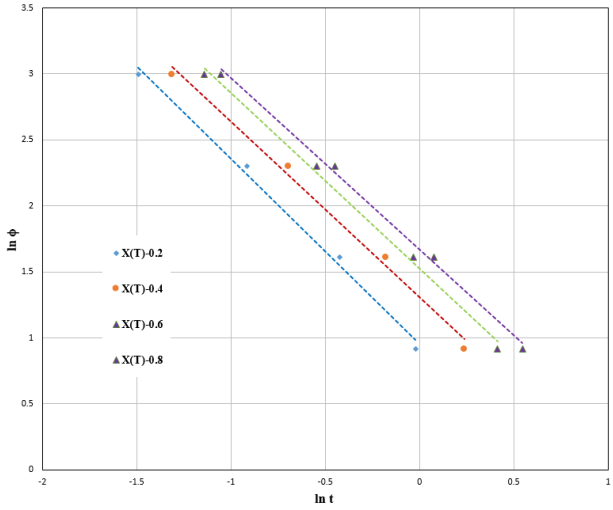

c. PGO 2.5%

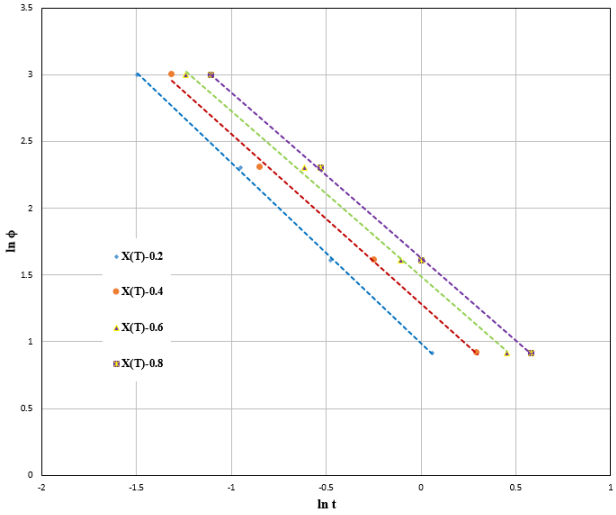

d. PGOSCF 2.5%

Figure 7.36 Combined Avrami and Ozawa plot for Pebax GO composites with and without $scCO_2$ under non-isothermal conditions

The influence of various cooling rates under non-isothermal crystallisation process on the activation energy can be described using the Kissinger equation. The plot of $\ln(\phi/Tc^2)$ vs. 1/Tc (Figure 7.37 and Figure 7.38) gives the linear slope determining the ΔE and is given in Table 7.20. The activation energy increases upon addition of graphene particles suggesting the actual hindrance that progress during the transformation phase. The activation energy for samples with $scCO_2$ tends to increase when compared to its counterpart samples without $scCO_2$. Although the shifting of Tc to higher values from 2.5% loading suggesting heterogeneous nucleation, the activation energy has increased recommending the dominance of restriction that is imposed by Pebax GO interaction. This increase in activation energy upon addition of GO suggests that $scCO_2$ might have enhanced the interaction between the polymer chain and the filler particle.

Table 7.20 Kissinger's activation energy for Pebax GO composites with and without $scCO_2$ under non-isothermal conditions

Sample Type	Kissinger Activation Energy (KJ/mol)	R^2
Pebax	233.39	0.994
PebaxSCF	230.81	0.996
PGO 0.5	252.62	0.999
PGOSCF 0.5	268.37	0.997
PGO 1	260.04	0.988
PGOSCF 1	285.54	0.996
PGO 2.5	287.61	0.999
PGOSCF 2.5	287.55	0.996

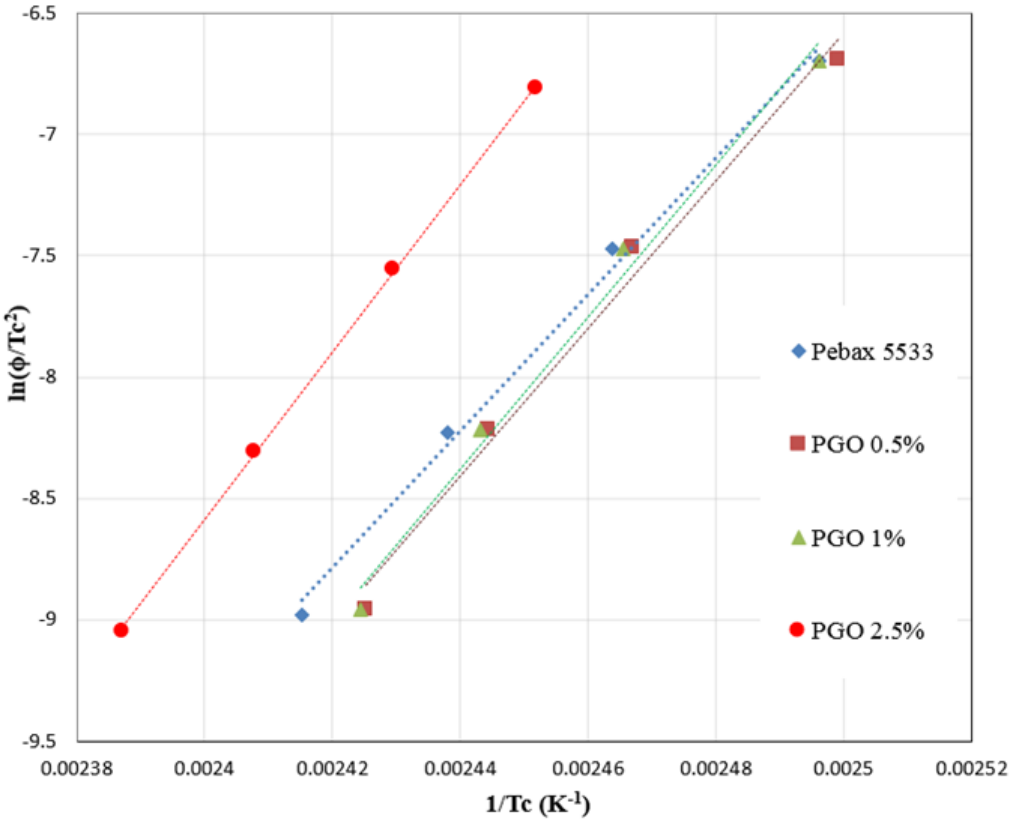

Figure 7.37 Kissinger's plot for Pebax GO composites without $scCO_2$ under non-isothermal conditions

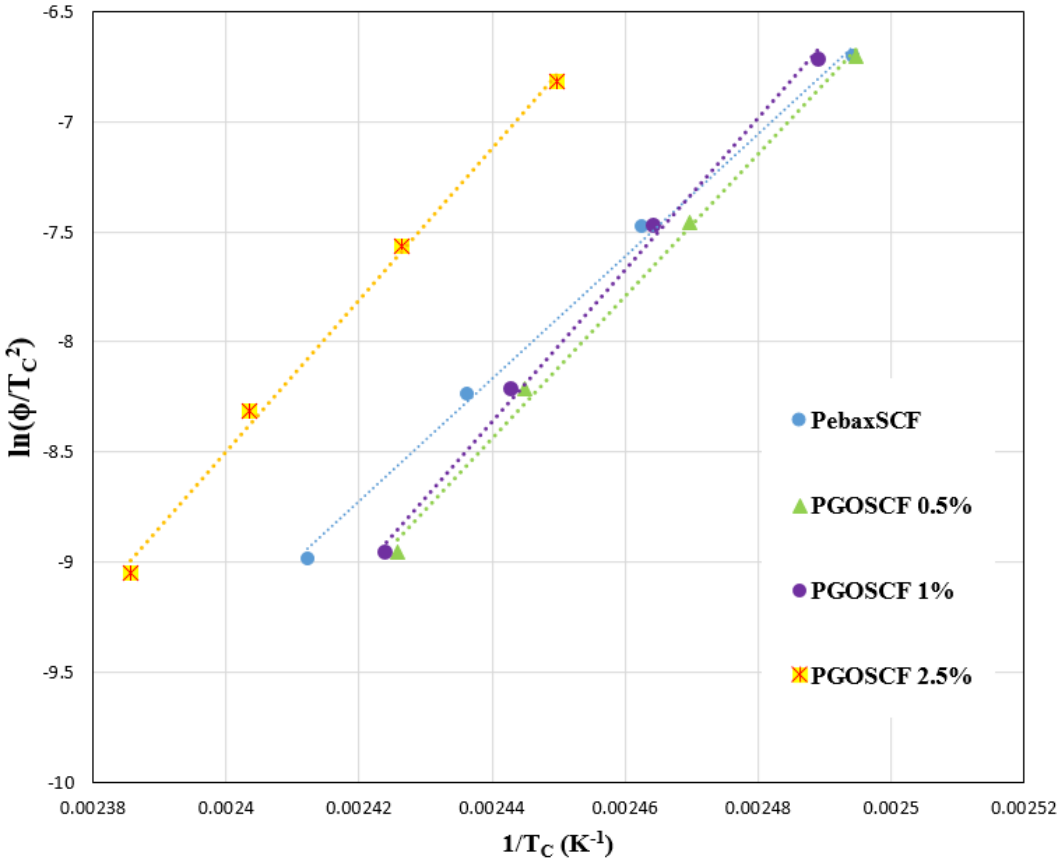

Figure 7.38 Kissinger's plot for Pebax GO composites with $scCO_2$ under non-isothermal conditions

7.4.4 X-Ray Diffraction of Pebax GO Composites

Figure 7.39, the XRD pattern of virgin Pebax shows a peak at approximately 2θ=22°, occurring mainly from the inter-chain hydrogen bonding (refer to FTIR analysis of Section 4.2.5) of the crystalline PA-12. It can be clearly seen that the addition of GO reduces the peak height and results in broadening of the peak at 2θ=22°, suggesting an increase in the amorphous content. As discussed in Section 7.2.4, the full width at half maximum (FWHM) increases from 1.88 for neat Pebax to 2.43 for $scCO_2$ treated Pebax, indicating peak broadening, suggesting decreased crystallite size. Table 7.21 shows the recorded d-spacing, 2θ peak, FWHM and calculated crystallite size using Scherrer's equation. The $scCO_2$ treated polymer matrix results in broadening of the peak due to proposed polymer-GO interaction and exfoliation. Similar results can also be observed from the crystallisation kinetics parameters obtained from both isothermal and non-isothermal crystallisation kinetics, where the value of crystallisation rate (k) decreases and Tc peak broaden; indicating restriction imposed to easy crystal growth and an increase in the number of the nuclei.

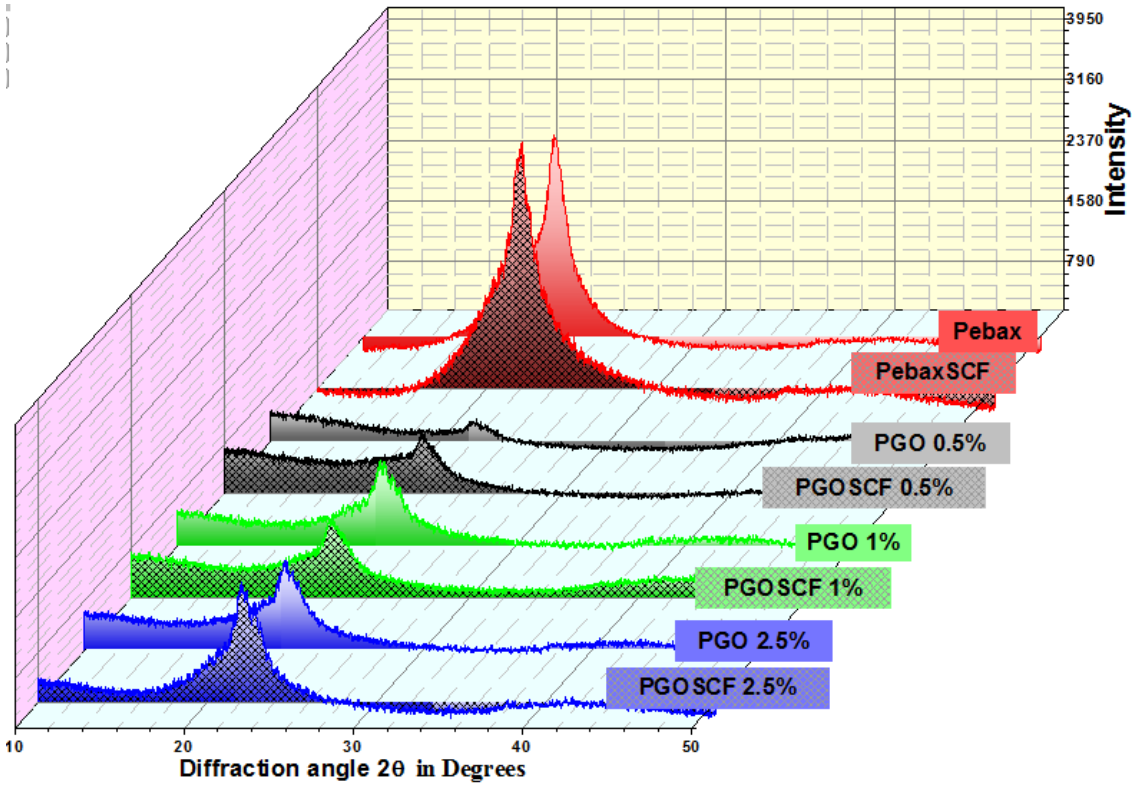

Figure 7.39 XRD spectra of Pebax GO composites at various loading concentrations with and without $scCO_2$

When the samples are processed with $scCO_2$, the crystallite size tends to reduce compared to its untreated counterpart (lowest for 0.5% loading), as $scCO_2$ induces the crystallisation process in a kinetically favourable manner and also due to suggested exfoliation of GO particles. In addition, the value of PGOSCF 0.5 is indicative of the percolation threshold beyond which the graphene particles tend to agglomerate, hence an increase in crystal size [166, 167].

Table 7.21 List of d-spacing, peak position at 2θ, obtained full wave half maximum from the plot and calculated crystal size from Scherrer equation

Sample Size	d-spacing in Å	Peak Position (2θ) in Degree	FWHM in Degree	Calculated Crystallite Size in nm
Pebax	4.18	21.26	1.88	4.49
PebaxSCF	4.03	22.03	2.43	3.48
PGO 0.5	4.05	21.91	4.15	2.11
PGOSCF 0.5	4.08	21.73	5.06	1.67
PGO 1	4.06	21.88	3.10	2.73
PGOSCF 1	4.10	21.64	3.90	2.16
PGO 2.5	4.07	21.79	3.27	2.59
PGOSCF 2.5	4.06	21.88	3.24	2.60

7.4.5 Mechanical Analysis of Pebax GO Composites

It can be clearly seen from Figure 7.40, Figure 7.41 and Figure 7.42, that addition of GO increases the storage modulus (extruded and compressed to obtain flat samples) and the increase in storage modulus is directly proportional to the concentration of GO fillers. A similar effect of reinforcement was also observed at higher temperatures with or without $scCO_2$. This increase in storage modulus is associated with the strong interaction between the GO and the polymer chains [133]. However, when the same polymer composite is treated with $scCO_2$, the storage modulus gradually increases to higher values. This shows that $scCO_2$ assisted extrusion enhances the stiffness of the composite (Table 7.22). A similar effect of reinforcement was also observed even at higher temperatures (in both the cases of with or without $scCO_2$). This is attributed to the $scCO_2$ ability to initiate the Van der Waals interaction between the Pebax polymer chain and the oxygen-rich GO. In addition, the specific increase in the storage modulus can also be attributed to the ability of the polymer chain to arrange into a kinetically more favourable manner when treated with $scCO_2$, which in turn affects the crystalline structure of the polymer.

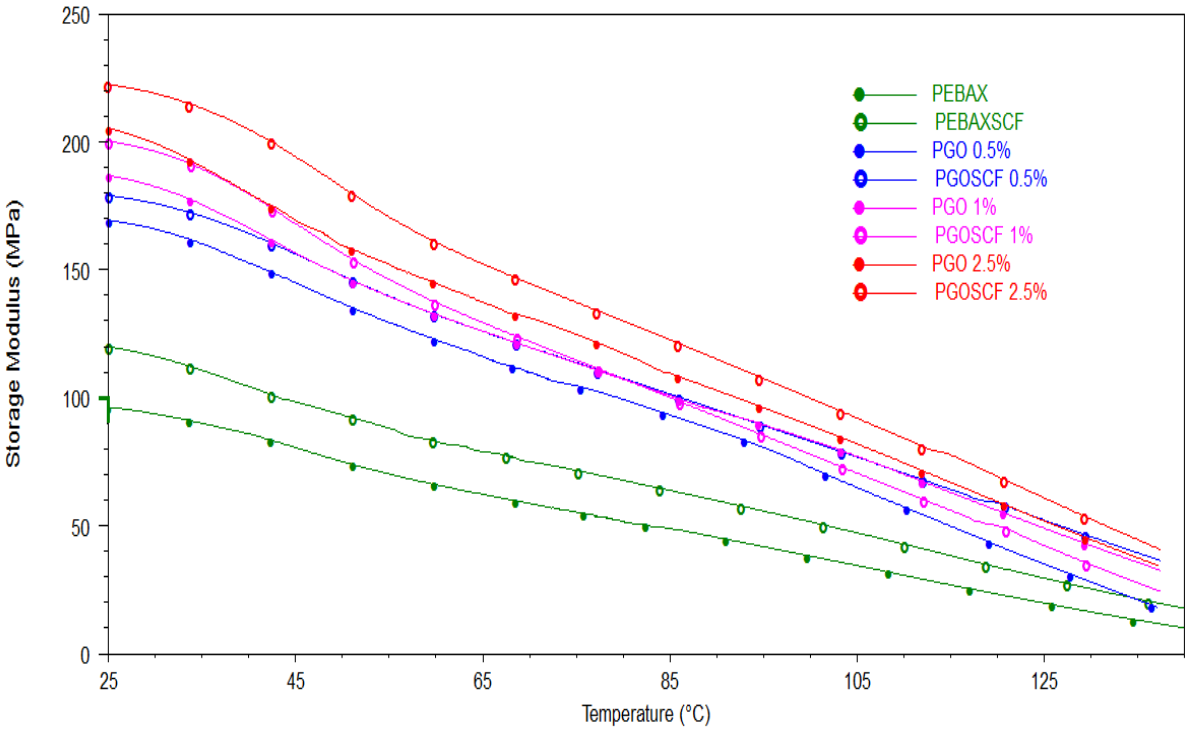

Figure 7.40 Storage modulus measured at 1 Hz for Pebax GO composites with and without $scCO_2$

A similar difference in crystallite size (broadening of crystalline temperature peak) was observed during the cooling cycle of the DSC thermogram. The value of Δ gives the percentage change in stiffness of the polymer matrix with respect to pure Pebax.

Table 7.22 Storage modulus (G'), loss modulus (G'') and tan delta of Pebax graphene composite with and without SCF-assisted extrusion

Sample type	Without SCF			With SCF		
	Storage modulus	Loss Modulus	Tan Delta	Storage Modulus	Loss Modulus	Tan Delta
	MPa (Δ)	MPa	NA 10^{-3}	MPa (% Δ)	MPa	NA 10^{-3}
PEBAX	98.56 ±5.3	4.39	44	119.8 ± 3.5	5.45	45
PGO 0.5%	170.2 ±6.1 (71.6)	6.31	37	179.9 ±5.5 (60.1)	6.29	34
PGO 1%	186.7 ±7.9 (88.1)	6.82	36	200.2 ±4.2 (80.4)	7.54	36
PGO 2.5%	199.8 ±5.4 (101.2)	8.19	40	222.4 ±6.6 (102.6)	7.84	35

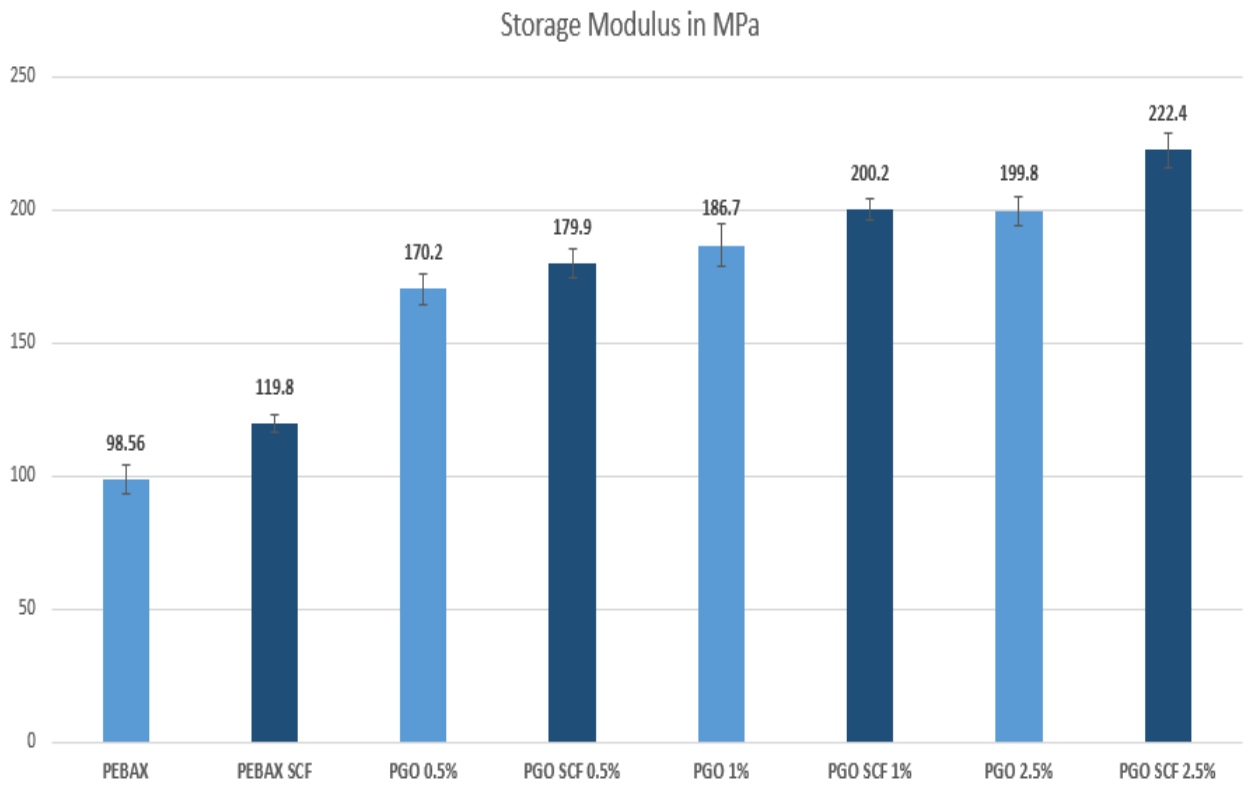

Figure 7.41 Storage modulus measured at 1Hz of all the Pebax GO composites with and without SCF

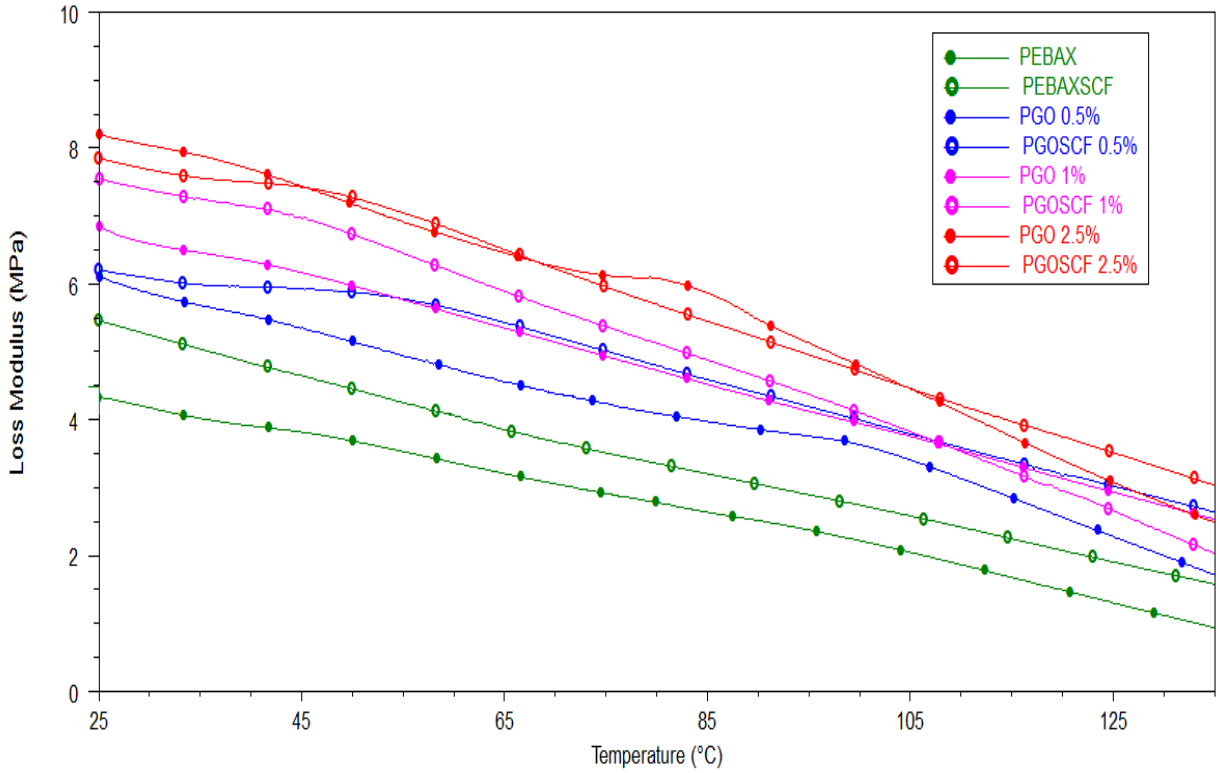

Figure 7.42 Loss modulus for Pebax GO composites with and without $scCO_2$

It was observed that the loss modulus increased in accordance with the addition of GO (Figure 7.42). It was seen from the tan delta curves from Figure 7.43, that the damping of composites was less than the virgin Pebax. The tan delta values shift to higher values with increase in the GO content within the matrix, however, when the composites (2.5%) was treated with an SCF, the damping factor reduces. It was observed from Figure 7.42 that the loss modulus increases with the addition of GO (Table 7.22). The addition of GO reduces the chain mobility, thus increasing the rigidity of the chain segment making the material more viscous in nature. The loss factor is considerably reduced between the interface because the weak Van der Waals interaction between the polymer and GO restricts the mobility due to inherent properties of GO. It was observed that the tan delta values shift to higher values with an increase in the GO content within the matrix. This suggests the existence of a poor interaction at the polymer chain GO interface which is also referred to as the softening of the interface [177].

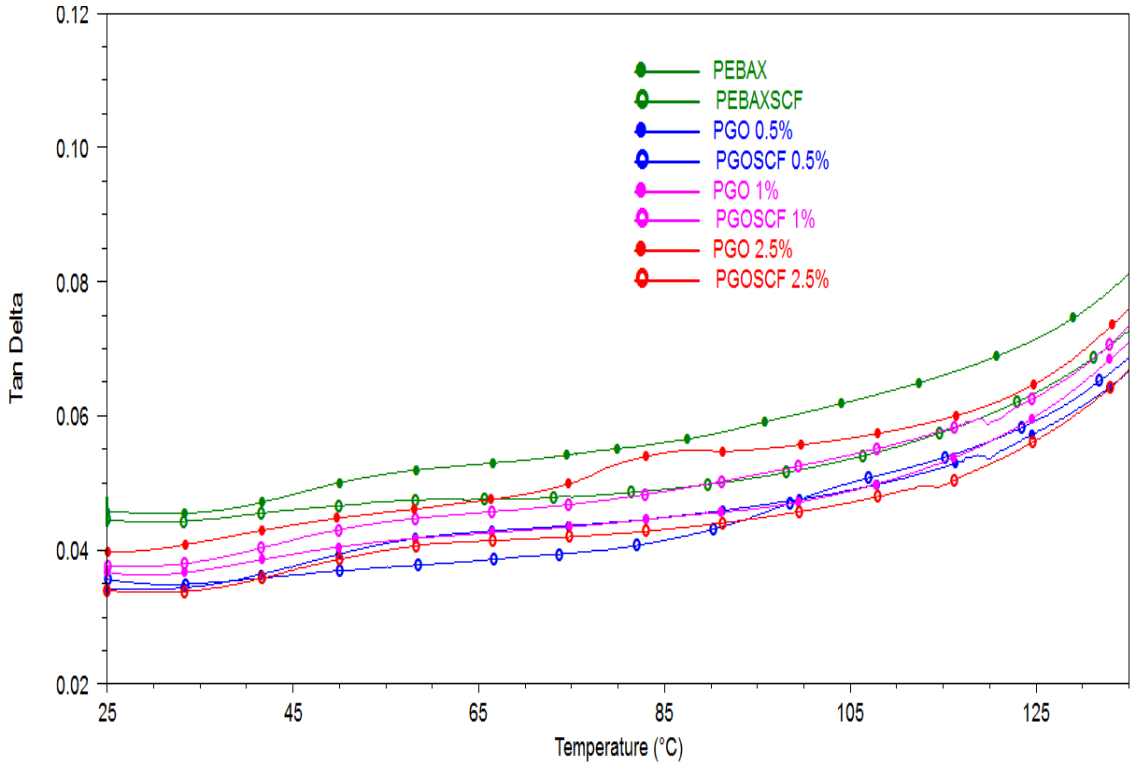

Figure 7.43 Tan delta measured at 1Hz for Pebax GO composites with and without $scCO_2$

This usually occurs when GO content crosses the availability of polymer chain for interaction and often results in higher energy at the interface due to an increase in the interfacial area. Therefore, more energy is dissipated as the GO loading is increased. However, when the composite (2.5%, refer to Table 7.22) was treated with SCF, the damping factor reduces. This shows that $scCO_2$ induces swelling of the polymer, which in turn increases the GO Pebax interaction due to an increase in free volume that opens all the polymer chain, in turn reducing the loss factor.

7.4.6 Tensile Test of Pebax GO Composites

Figure 7.44 and Figure 7.45 shows the stress vs. strain curves of Pebax GO-based nanocomposite up to 50% strain with and without SCF-assisted processing extrusion technique. However, no breakage was observed for all the samples up to strain extension of 500%. A noticeable increase in Young's modulus was observed on SCF-treated Pebax GO as tabulated in Table 7.23 (Figure 7.46).

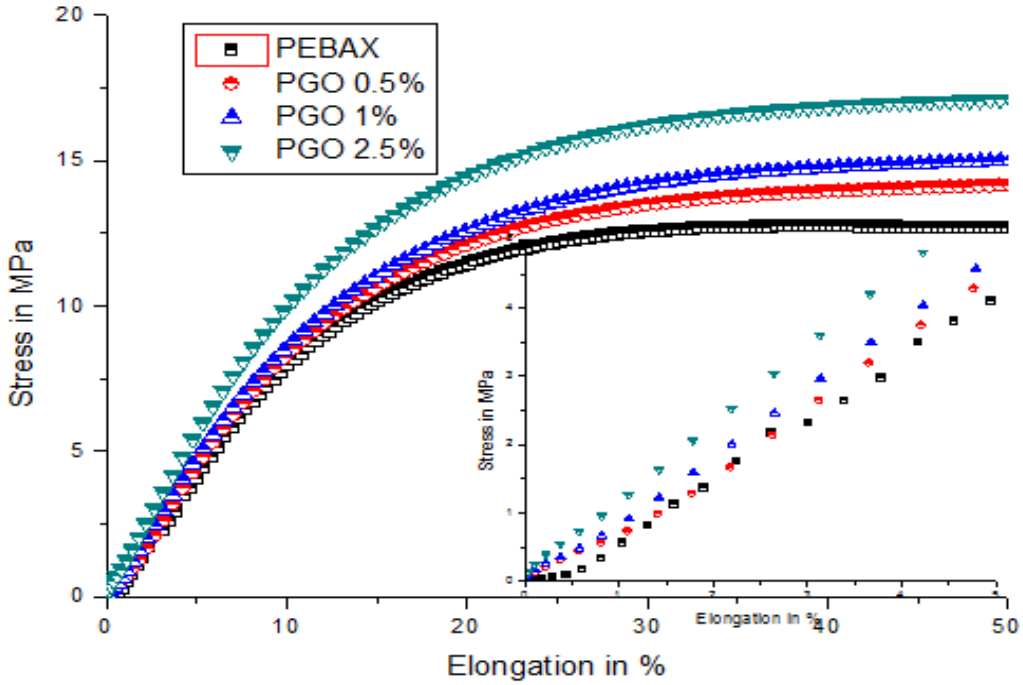

Figure 7.44 Stress vs. strain curve for Pebax GO composite without $scCO_2$ assisted extrusion

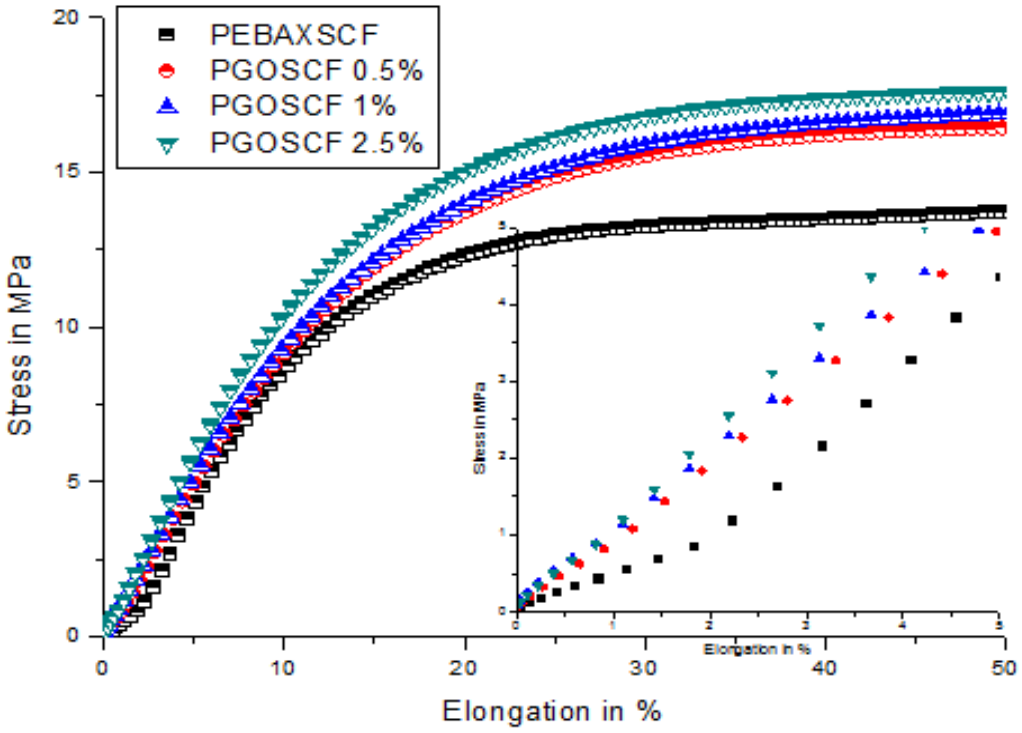

Figure 7.45 Stress vs. strain curve for Pebax GO composite with $scCO_2$ assisted extrusion

Table 7.23 Young's modulus of Pebax GO composites measured with and without $scCO_2$

Sample Type	Young's Modulus in MPa
Pebax	66.2±8.3
PebaxSCF	73.8±5.9
PGO 0.5%	77.4±7.1
PGOSCF 0.5%	86.1±5.6
PGO 1%	83.3±8.4
PGOSCF 1%	96.8±7.3
PGO 2.5%	98.9±6.3
PGOSCF 2.5%	109.3±8.9

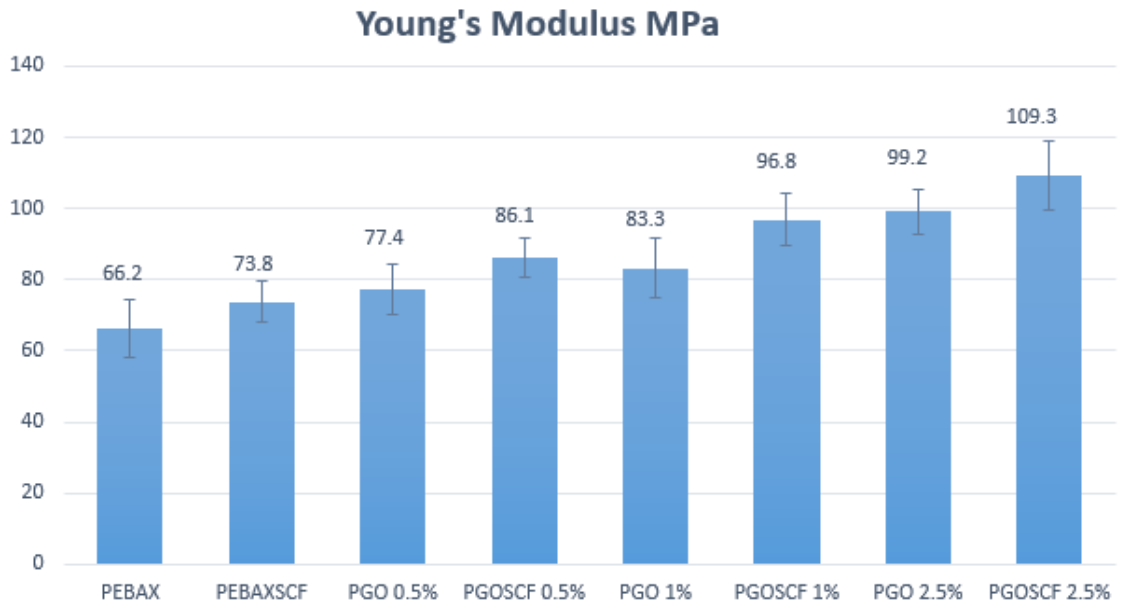

Figure 7.46 Young's modulus of Pebax GO composites with and without $scCO_2$

The increase in the modulus of resilience is proportional to GO loading within the polymer matrix. However, when treated with $scCO_2$, the composite loading of 0.5% shows almost equal Young's modulus value with respect to 1% loading. This can be attributed to the rearrangement of the polymer chain GO interface, due to compression moulding, however, a gradual reinforcement was evident depending on the weight percentage of GO. A noticeable increase in Young's modulus was observed on SCF-treated Pebax GO (Figure 7.46) when compared with virgin material. This shows the ability of $scCO_2$ to enhance the mechanical properties of semi-crystalline materials like Pebax. This indicates that $scCO_2$ enhances the GO particle interaction

with the polymer chain, making it a more homogeneous network in turn leading to a sufficient increase in stiffness.

7.4.7 Fourier Transform Infrared Spectroscopy Analysis of Pebax GO Composites

In the GO spectra (Figure 7.47), the peak at 1050 cm^{-1} corresponds to stretching vibration of C-O-C bonds of epoxy or carboxylic group. The peak at 1225 cm^{-1} corresponds to C-OH bonds (mainly due to the epoxide C-O stretch). The characteristic peak at 1622 cm^{-1} was attributed to skeletal vibration of un-oxidised C=C bonds (un-oxidised - sp^2 hybridized bonds).

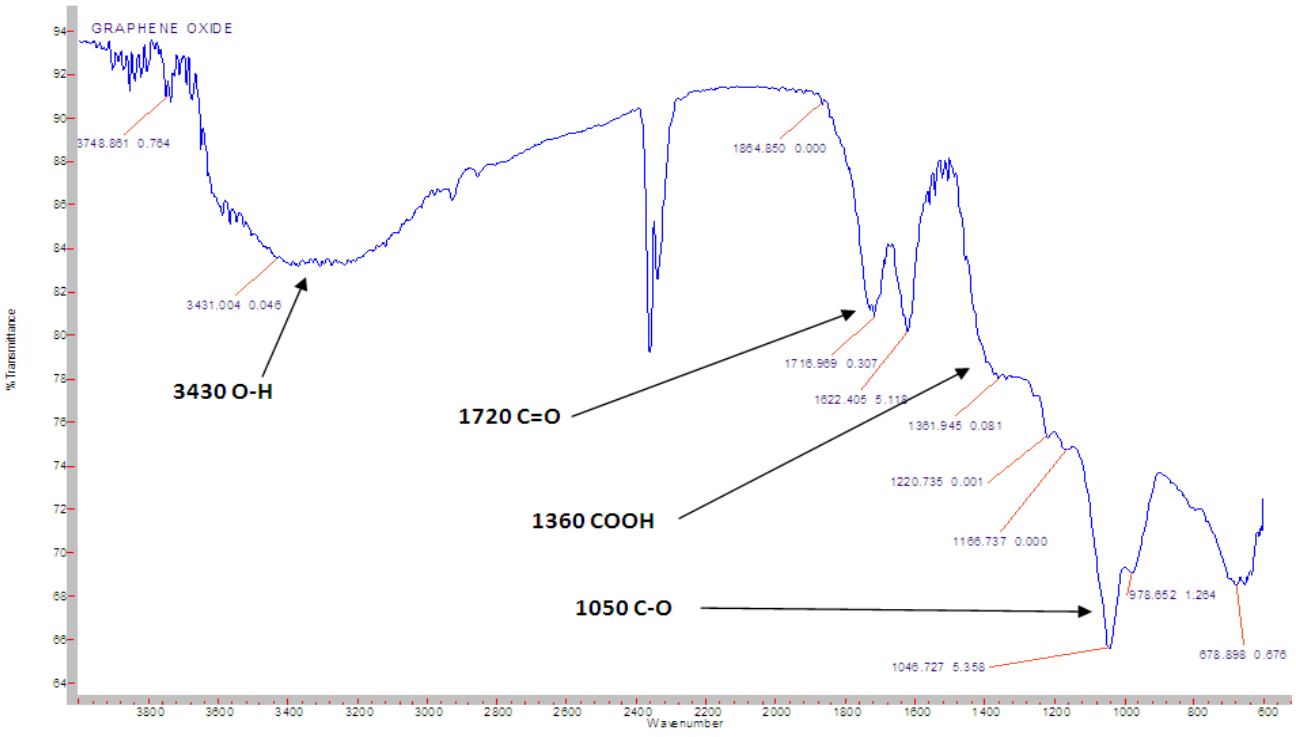

Figure 7.47 FTIR transmittance spectra for synthesised GO

The peak located at 1720 cm^{-1} is based on the stretching vibration of C=O in carboxylic acid and carbonyl moieties. The peak at 1360 cm^{-1} is attributed to the COOH symmetric and asymmetric stretching (mainly due to O-H deformation). The peak at 3430 cm^{-1} is aligned to OH stretching vibrations. The peak at 1220 cm^{-1} represents the C-OH stretching [97, 99, 178]. No significant changes were observed from the FTIR spectra (Figure 7.48) for various concentrations of Pebax GO nanocomposite extruded without $scCO_2$. The spectra from 1500-1800 cm^{-1} provide information on the hard segment (PA-12) and extenders in the block copolymer. Specifically, the characteristic peaks at 1735 cm^{-1} and 1638 cm^{-1} represent the presence of O-C=O stretching of the carbonyl group of ester linkage and N-C=O carbonyl vibration of the PA-12 group, respectively. When the Pebax GO composites at various concentrations were extruded with

assisted $scCO_2$, several shifts can be observed from the FTIR transmittance spectra as shown in Figure 7.49.

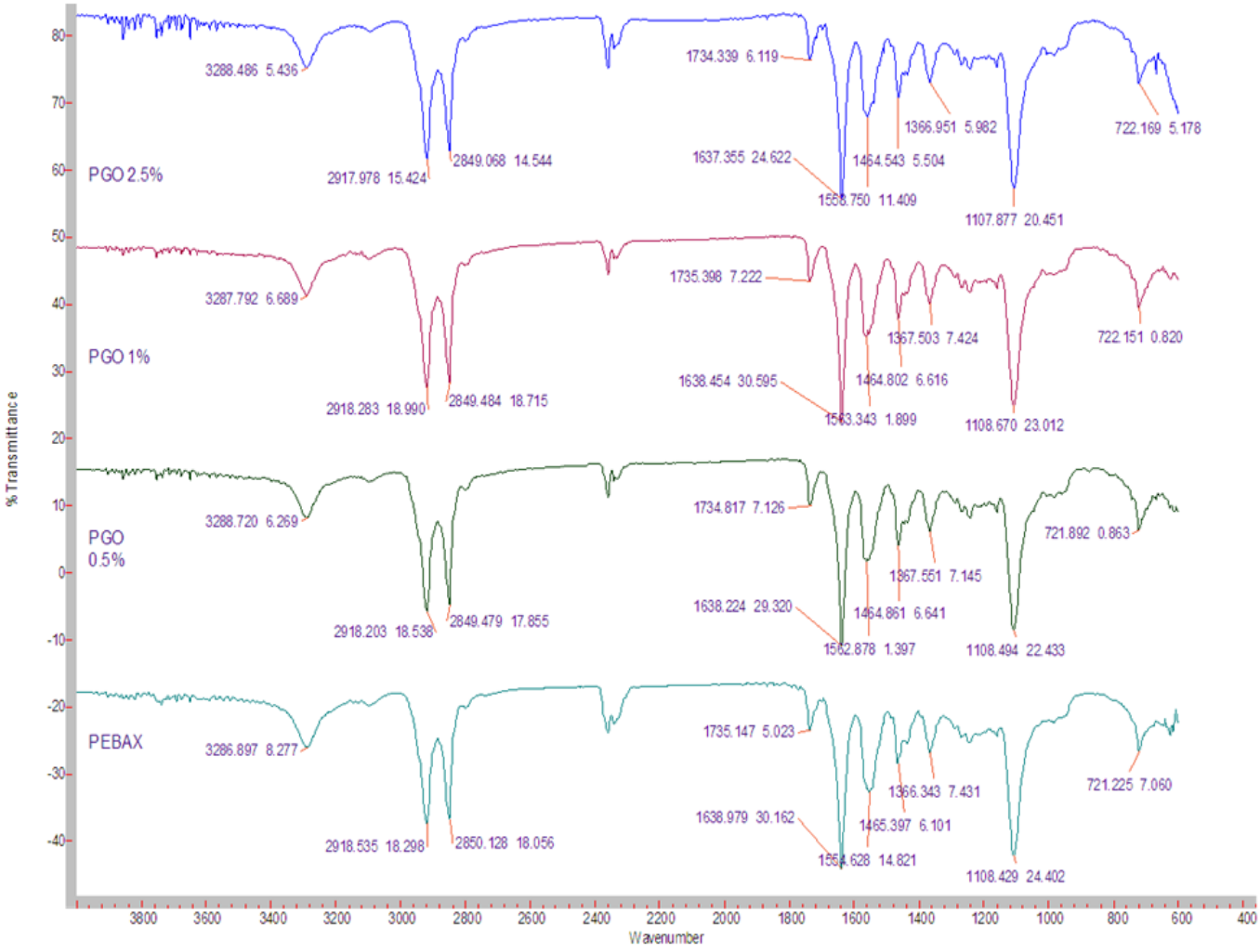

Figure 7.48 FTIR transmittance spectra for Pebax GO composite without $scCO_2$

The characteristic peak at 1641 cm^{-1} represents the N-C=O carbonyl vibration of PA-12 and shifts towards lower wavenumbers (1637 cm^{-1}). The peak at 1554 cm^{-1}, which corresponds to the CNH vibration with NH bending and CN stretching, shifts to the higher wavenumber of 1564 cm^{-1}, showing enhanced hydrogen-bonding between the amide group and epoxide group (or carboxylate amino stretch) of GO [179].

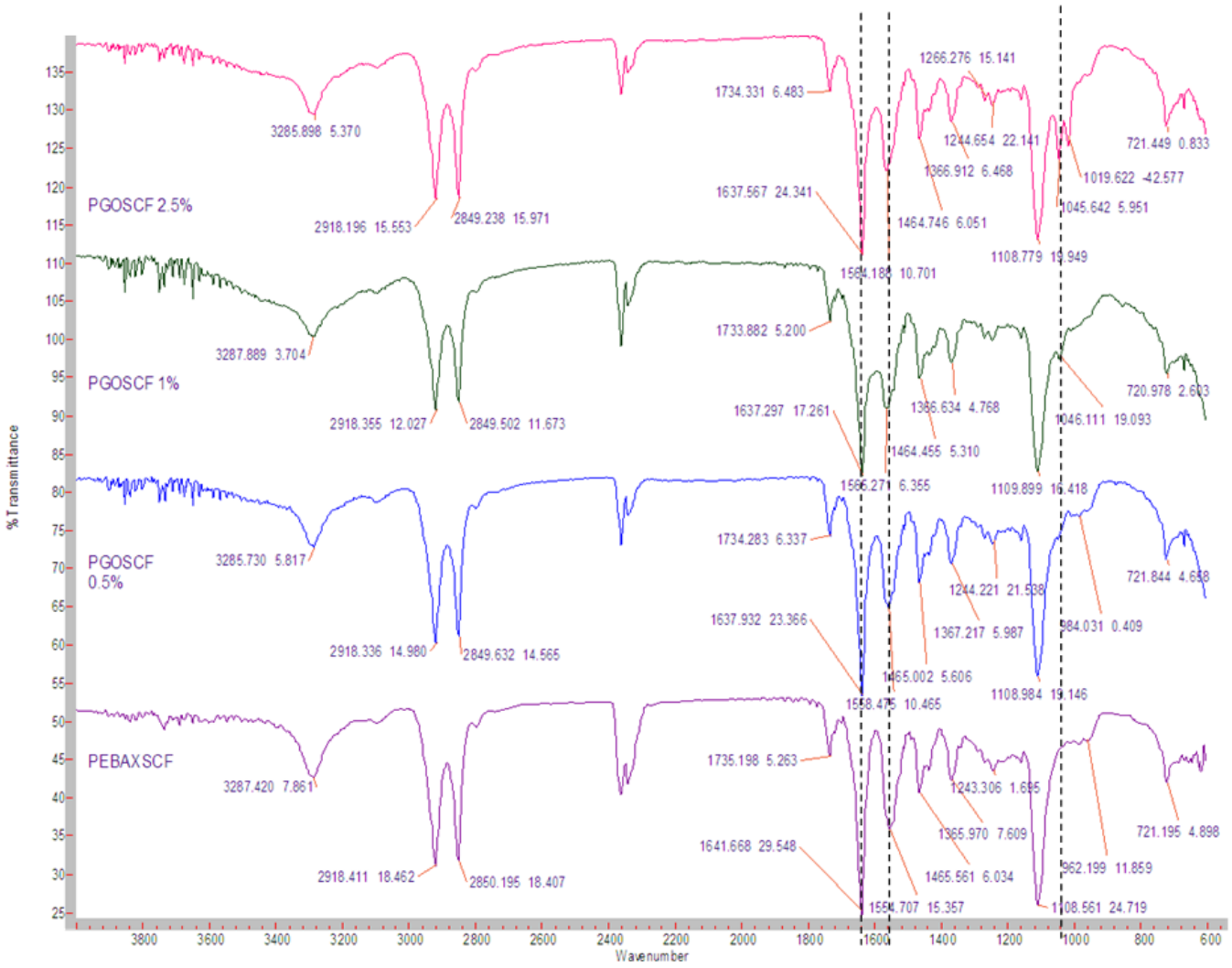

Figure 7.49 FTIR transmittance spectra for Pebax GO composite with $scCO_2$

The peak at 962 cm^{-1} is attributed to CH_2 wagging of the nylon group [180]). However, a new peak appears at 1046 cm^{-1} (on the addition of 1%) representing the alkoxy C-O stretching vibration of GO [181] thereby decreasing the relative intensity of CH_2 wagging at 962 cm^{-1}. At higher GO percentage peaks at 1045 cm^{-1} and 1019 cm^{-1} appear, which correspond to the C-O stretching of the carboxylic acid group [182].

One of the main reasons for such behaviour may be due to the reduction of GO to graphene resulting in a reduction in the oxidation state mainly due to multiple exposures of GO to high temperatures and a long residence times inside the extruder. When the Pebax GO composites were extruded with assisted $scCO_2$, a number of shifts can be observed from the FTIR transmittance spectra as shown in Figure 7.49. The characteristic peak at 1641 cm^{-1} represents the N-C=O carbonyl vibration of the PA-12 group and shifted towards lower wavenumbers (1637 cm^{-1}). The peak at 1554 cm^{-1}, which corresponds to CNH vibration with NH bending and

CN stretching, shifted to a higher wavenumber of 1564 cm^{-1}, showing enhanced hydrogen-bonding between the amide group and epoxide group (or carboxylate amino stretch) of GO [179]. A similar interaction was reported by Kumar et al [183]. This also showed that the oxidation was still retained when processed with $scCO_2$ and suggests a possible interaction between Pebax and GO. This suggests that supercritical fluid not only provides even dispersion and exfoliation effects but also retains the oxidation levels when processed at a high temperature such as would be in the case for injection moulding, compression moulding and hot melt extrusion.

7.4.8 Conductivity Test of Pebax GO Composites

Figure 7.50 present the conductivity plotted for Pebax GO composites without $scCO_2$ over a range of frequencies. It is evident that the conductivity increases as the GO loading increases within the polymer.

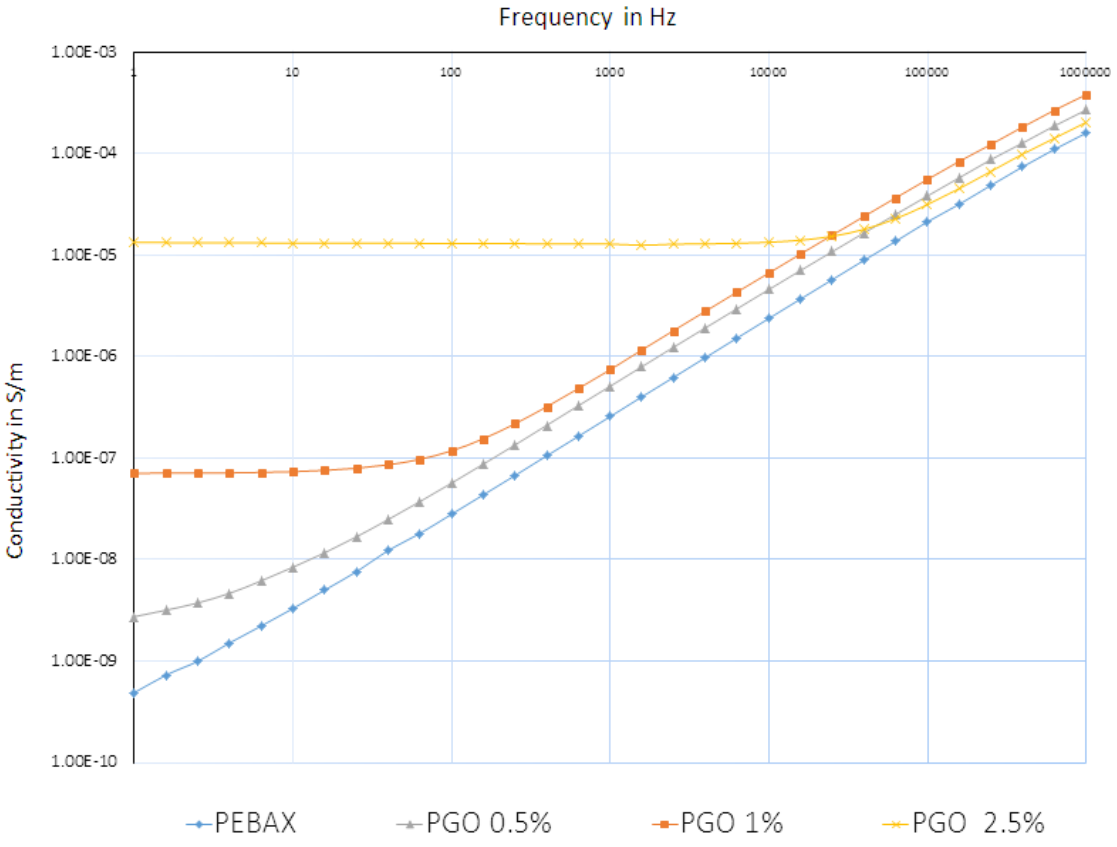

Figure 7.50 Conductivity of Pebax GO composite without $scCO_2$

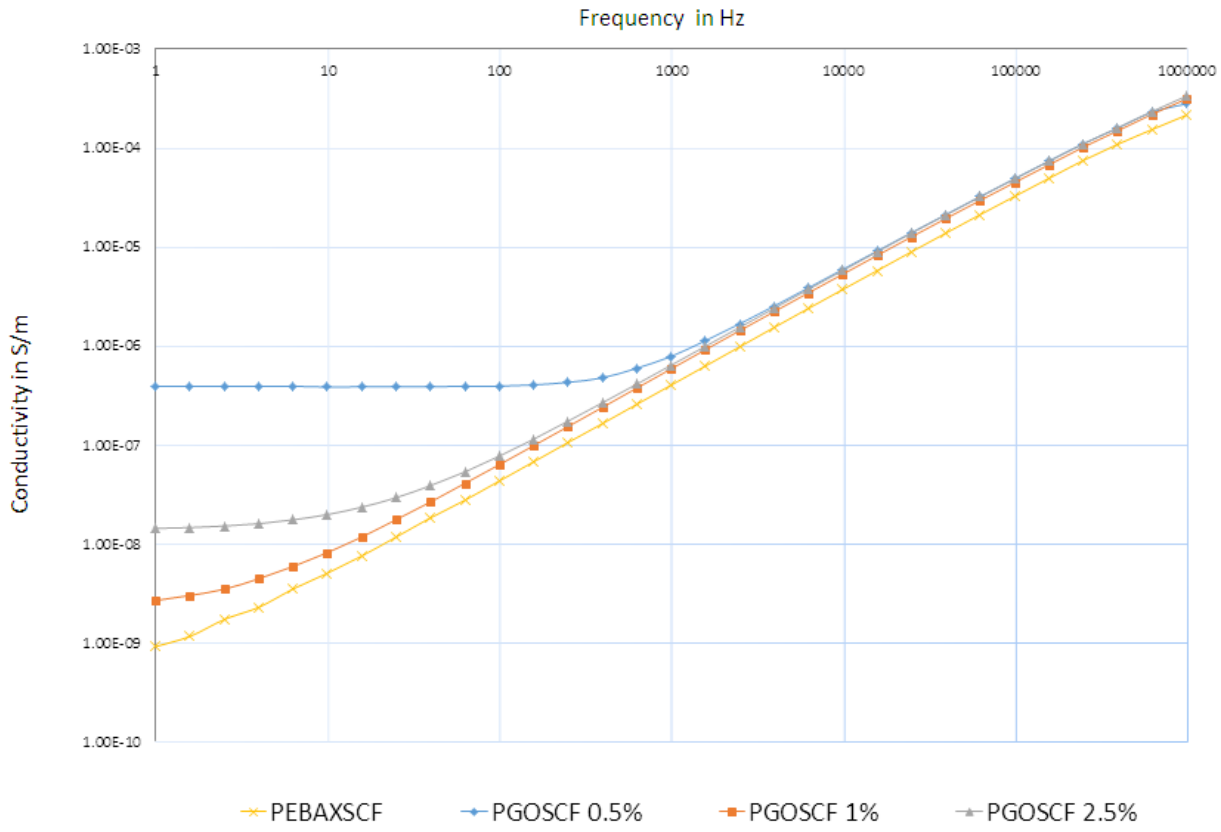

Figure 7.51 Conductivity of Pebax GO composite with $scCO_2$

When the composite samples were extruded with $scCO_2$ and reprocessed without $scCO_2$, PGOSCF 0.5% showed an increase in conductivity, while the conductivity of PGOSCF 1% and PGOSCF 2.5% reduces which behaves as an insulator against higher conductive Pebax GO samples prepared without $scCO_2$.

It was evident that the conductivity increased as the GO loading increased within the polymer matrix. Although GO is considered to be an insulator due to its highly oxygenated groups on the surface, thus having limited or unavailability of free electrons on the surface, the conductivity increases in a linear fashion depending on the GO content. This demonstrated that the conductivity of GO was directly dependent on the degree of oxidation. Sreeprasad et al [184] and many other researchers have [30, 31, 99, 185] reported that the oxidation process continuously removes the sp2 electrons and replaces with sp3 carbons having oxygen groups. Because GO reduces upon thermal treatment, the oxidation levels decrease, thereby increasing the conductivity; therefore, the conductivity of samples may have been increased as multiple thermal treatments might have resulted in depletion of oxidation levels and producing reduced GO (rGO).

When the composite samples were extruded with $scCO_2$ and reprocessed without $scCO_2$, PGOSCF 0.5% exhibited an increase in conductivity; while the conductivity of PGOSCF 1% and PGOSCF 2.5% reduce behaving as an insulator against higher conductive Pebax GO samples without $scCO_2$. This would suggest that processing GO composites with $scCO_2$ did not result in a reduction of GO to rGO, and maintained the oxidation level. This effect is mainly attributed to the $scCO_2$ ability to reduce the viscosity of the polymer and increase the throughput. This, in turn, reduces the exposure of GO Pebax composites to high temperature within the extruder (decrease residence time within the extruder) thereby retaining the oxidative properties of the GO composite. This may also occur due to unavailability of interactive polymer sites for higher GO loading within the composites.

7.4.9 Transmission Electron Microscope of Pebax GO Composites

Figure 7.52 presents the TEM image of Pebax GO composite without (A and B) and with (C and D) $scCO_2$ at 1% GO loading. The faded region in image A shows a thin layer of Pebax graphene composite, while the darker region shows the uneven or multilayer composite when processed without assisted $scCO_2$. The faded region throughout show multiple platelet-like structures, which are indicative of the agglomerated GO particles (can be easily seen from image B). When the composite is processed with assisted $scCO_2$, such platelet structures are missing and graphene particles seem to have exfoliated and evenly dispersed throughout the polymer matrix in image C (2 µm). Image D at a scale of 200 nm shows the actual nylon crystalline matrix and the dispersion of GO particles around the Pebax lattice. When compared to Pebax graphene images, the $scCO_2$ Pebax graphene samples still show agglomeration, while both image C and D show even dispersion with less agglomeration in case of Pebax GO composites. The result of such exfoliation and even dispersion results in enhancement of thermal, mechanical and electrical properties as described from the analysis above. The TEM results are in agreement with the hypothesis that $scCO_2$ assisted processing of GO composites results in exfoliation and even dispersion within a polymer matrix.

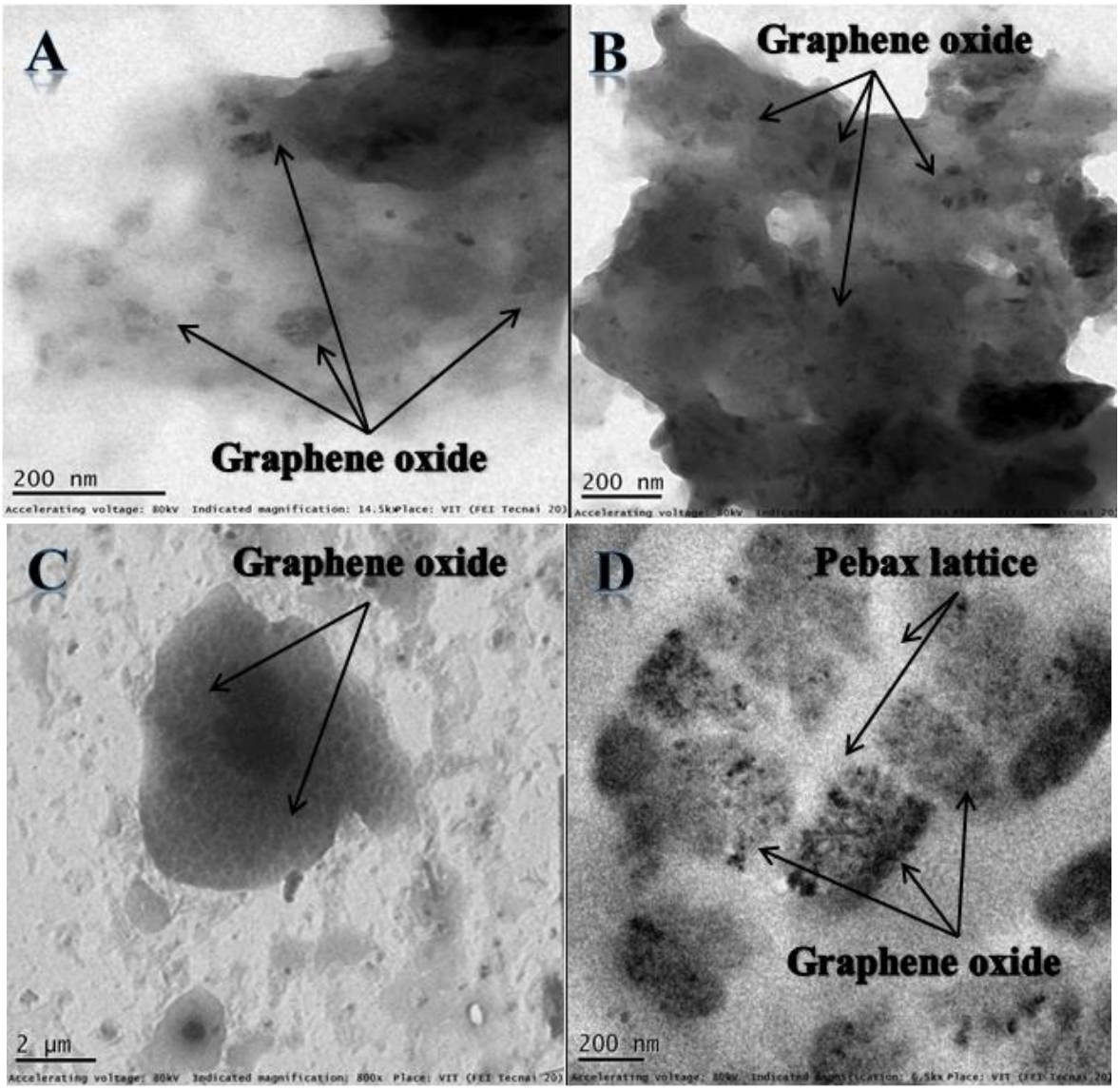

Figure 7.52 TEM Images of Pebax graphene composites: A and B – PGO1% and; C and D – PGOSCF1%

7.5 Key Points for Reprocessed Pebax GO Composites

Pebax GO (GO) composites were prepared with varying GO loading of 0.5%, 1% and 2.5%. Supercritical (SCF) assisted polymer processing was used to investigate the effect on thermal, mechanical and electrical properties against the virgin Pebax GO composites.

- The throughput of the $scCO_2$ treated composite increased when compared to untreated composites. The thermal degradation temperature of synthesised GO was 218 °C, where more than 60% of oxidation diminishes. No significant change in thermal degradation was observed for both with and without $scCO_2$.

- The DSC heat flow thermogram did not show a significant difference for both the cycles with and without $scCO_2$, with respect to melting temperatures. However, the crystallisation temperature on the cooling cycle shifts towards lower temperatures upon addition of GO. Upon use of $scCO_2$, the composites with 0.5% the crystallisation temperatures shifts to lower temperature when compared to $scCO_2$ 1% GO, which shifts to a higher temperature. This demonstrates that the $scCO_2$ assisted processing technique further enhances the interaction between the polymer and additive, and reduces the crystallite size.
- The crystallisation rate k decreases upon addition of GO from 0.80 for virgin Pebax to 0.18 for 0.5%, 0.21 for 1% and 0.24 for 2.5%. An increase in k can be observed for 2.5% GO loading suggesting slightly faster crystallisation compared to 0.5%. The k value further reduces with $scCO_2$ assisted extrusion. This indicates slow crystallisation rate which might have occurred due to improved Pebax GO interaction which in turn limits the free chain movement during the crystal formation phase.
- The DMA results exhibit an increase in storage modulus in accordance with the GO loading. However, when processed with $scCO_2$ the storage modulus further increases from 15 to 20%, when compared to the virgin Pebax composites. The loss tangent curves gradually increased with the addition of GO due to the reduced availability of interactive polymer sites at higher concentrations. The $scCO_2$ processed composites show a reduced loss tangent, indicating enhanced interaction due to swelling of the polymer matrix.
- The FTIR spectra of $scCO_2$ assisted Pebax GO composites to show enhanced hydrogen-bonding between the amide group and epoxide group on the GO surface. Upon the addition of 1% and 2.5% GO, alkoxy and carboxylic acid groups C-O stretching vibration of GO are evident in the transmittance spectra. This shows that SCF not only provides even dispersion and an exfoliation effect but also retains the oxidation levels, which otherwise were not observed for virgin Pebax GO composites.
- In addition, this action of reduced or absence of oxidation can be observed from the conductivity test. Virgin Pebax GO composites demonstrated enhanced conductivity upon addition of GO, while the $scCO_2$ processed composites decreased in conductivity (i.e. it acts as an insulator).
- The calculated crystallite size using XRD peaks shows that the crystallite size tends to reduce when the samples are processed with $scCO_2$, compared to its untreated counterpart. Such reduction in crystallite size is lowest at lower loading concentration,

however, both untreated and treated crystallite size becomes equal at 2.5% due to agglomeration.

7.6 Conclusions for Reprocessed Pebax Graphene Based Composites

This Chapter investigated the effect of $scCO_2$ processing on Pebax composites using graphene and GO. To validate the reduction in viscosity when processed with supercritical carbon dioxide, throughput tests were carried out on both graphene and GO-based Pebax composites. In both cases, the throughput increased when treated with supercritical carbon dioxide showing a reduction in viscosity with SCF processing. The DSC studies identified the shifting of the crystallinity peak to higher temperatures and reduced the heat of enthalpy on increasing graphene percentage. These showed the formation of heterogeneous crystallites with varying crystallite size. However, the crystallinity peak shifted towards lower temperatures with GO Pebax composites. The interaction between the polymer chain and oxides on the GO surface made the material behave in a more homogenous manner. The results from crystallisation kinetics study showed that the crystallisation rate increased upon addition of graphene while decreased with GO up to 1%, suggesting that GO particles have improved interaction with the polymer where the process of aggravated nucleation and chain growth is reduced (GO particles produce homogenous matrix). With the use of $scCO_2$, the crystallisation rate increased in case of graphene with respect to virgin Pebax but remained less than the untreated composite counterpart suggesting improved interaction with the polymer matrix due to exfoliation. However, in the case of GO, the crystallisation rates were almost equal compared to the untreated counterpart but were less than the virgin Pebax which is indicative of GO uniform distribution. The calculated crystallite size in both cases of graphene and GO was found to be less than the untreated counterpart at loading concentration less than 1% in $scCO_2$. This shows that $scCO_2$ induces crystallisation process in a kinetically favourable manner with probable exfoliation of graphene-based particles. Similar effects can be seen from TEM images. The FTIR analysis validates that $scCO_2$ helps to retain the property of additives, specifically GO which was not reduced to graphene even after reprocessing 3 times. This suggests that $scCO_2$ processing of GO-based composite retain the oxygenated GO particles and do not induce the reduction process of GO even after several heat treatments (reprocessed multiple times). The conductivity of $scCO_2$ processed Pebax graphene composites enhanced with respect to virgin Pebax graphene composites. This shows that $scCO_2$ has further exfoliated graphene particles resulting in more sp^2 delocalised electrons thereby increasing conductivity, thus graphene remains exfoliated.

While in the case of GO composites, the oxygen-rich surface diminished on reprocessing unassisted GO Pebax composites. However, when the composites were processed using SCF, the oxygen-rich surface remained, thereby retaining the insulator property of the GO composites. The results from $scCO_2$ treated composites thereby show that industrial processing conditions can still be used for processing sensitive oxygen-rich materials such as GO, without diminishing their inherent properties.

8 Investigation of the Effect of Supercritical Carbon Dioxide Assisted Reprocessing of SEBS Graphene-Based Composites

8.1 Introduction

Poly(styrene-b-ethylene-butylene-b-styrene) (SEBS) is a microphase-separated block copolymer which consists of polystyrene as hard end blocks and ethylene-butylene as soft mid-block [186, 187]. Conventionally available actuators such as pneumatic actuators, motors, hydraulic cylinders or piezoelectric actuators, suffer from high power consumption, heavyweight, restrictive shapes, limited size and low strain [188]. These properties are of major concerns specifically when applied to mechanical pumps, valves, micro-robots and biomedical devices. Therefore, electroactive dielectric elastomers have garnered much attention, mainly due to their attractive properties such as large electromechanical strain, fast response, high power to mass ratio, soft elastic nature, ease of processability into any shape or size and low cost [14, 188, 189]. SEBS is considered as a relatively new material option in the case of using it as IPMC bending actuators. The ability to enhance the mechanical and polarisation properties of SEBS by using additional fillers such as carbon black is well documented in review books and research papers (specific to dielectric elongation actuators) [190-192]. However, the ability to tailor mechanical and ionic properties using SEBS composites is under consideration by researchers for further investigations. Nevertheless, one of the major concerns in the composite industry is to evenly disperse the fillers within the polymer matrix that in turn leads to better mechanical and electrical properties [187, 190, 191, 193, 194].

As a continuation of Chapter 6, this chapter of the thesis investigates the mechanical, thermal and electrical properties of reprocessed SEBS graphene-based composites extrusion technique. As seen in Chapter 6, graphene and GO were used as filler/additive particles. In addition, the manufactured membranes were sulfonated in order to enhance the ion exchange and tested for its bending capabilities. GO-based SEBS composites demonstrated bending capabilities and the bending performance was enhanced with SEBS GO membranes processed with $scCO_2$.

8.2 Section 2: SEBS Graphene Composites

8.2.1 Throughput Test of SEBS Graphene Composites

Table 8.1 shows the average of 3 throughput rates with all the other processing parameters maintained constant. The total mean weight of SEBS based composites extruded with $scCO_2$

decreases as graphene loading increases. The $scCO_2$ processing results in a plasticisation effect, in turn, reducing the melt viscosity and increase in the throughput of SEBS composites.

Table 8.1 Average weight of SEBS based nanocomposite extruded for 1-minute

Sample type	**Average weight of SEBS based nanocomposite extruded for 1-minute**	
	Without SCF	With SCF
	g	g
SEBS	39.40±5.6	52.18±3.3
SG0.25%	37.55±7.8	53.01±3.7
SG0.5%	38.96±4.9	52.77±2.9
SG1%	34.34±5.3	49.89±3.6
SG2.5%	32.92±4.2	49.96±3.1

8.2.2 Thermal Gravimetric Analysis of SEBS Graphene Composites

The thermal degradation profile of SEBS graphene composites with and without $scCO_2$ was investigated. The results of measurements are shown in Table 8.2, Figure 8.1and Figure 8.2. The results identify an enhanced thermal stability with respect to graphene content without $scCO_2$. This result can be attributed to the increased interfacial interaction between SEBS and graphene. This interaction leads to heterogeneous dispersion of graphene which ceases the oxygen supply by forming a charged layer on the surface of the composites. This might be one of the reasons to increase the onset degradation temperature thereby enhancing thermal stability [195, 196].

Table 8.2 Maximum degradation temperature profile of SEBS graphene composites

Sample type	**Maximum degradation temperature of SEBS graphene composites**	
	Without SCF	With SCF
	°C	°C
SEBS	423.9	455.4
SEBSG0.25%	464.8	457.6
SEBSG0.5%	464.7	456.9
SEBSG1%	469.8	458.2
SEBSG2.5%	468.9	458.8

The use of $scCO_2$ enhances the thermal stability of virgin SEBS, however, no significant enhancement in thermal stability can be observed upon addition of graphene up to 2.5%. However, the degradation temperature slightly decreases when the graphene composite polymer matrix is extruded with $scCO_2$ compared to samples without $scCO_2$. This decrease suggests the

exfoliation of graphene particles, which in turn results in improved intermolecular interactions where otherwise the graphene particles would have agglomerated. Most of the research work published using graphene nanocomposites report enhanced thermal stability, that is, increase in the thermal degradation temperature upon graphene filler loading greater than 2 to 3% [158-161].

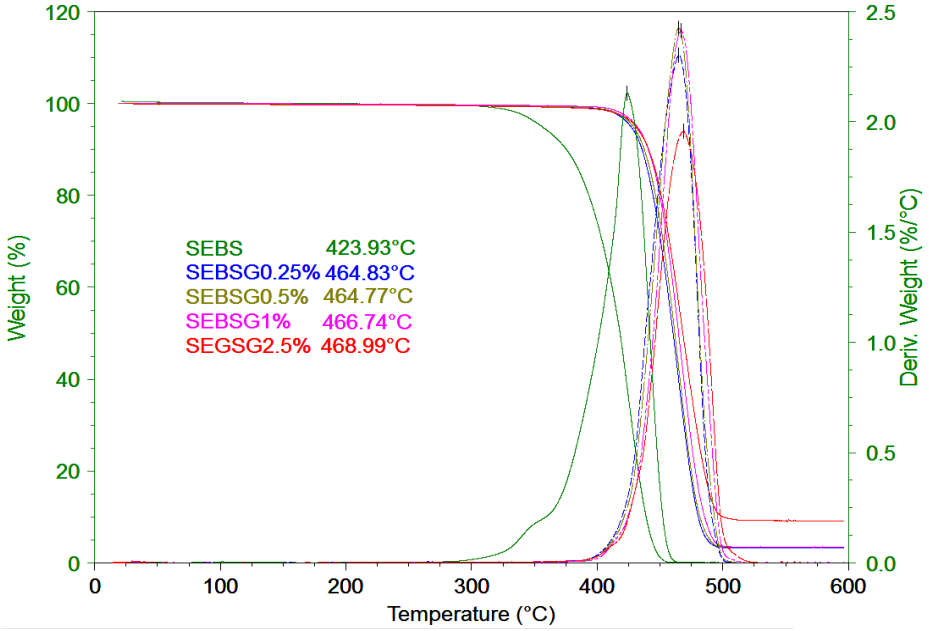

Figure 8.1 Thermal degradation profile of virgin SEBS and SEBS graphene composites

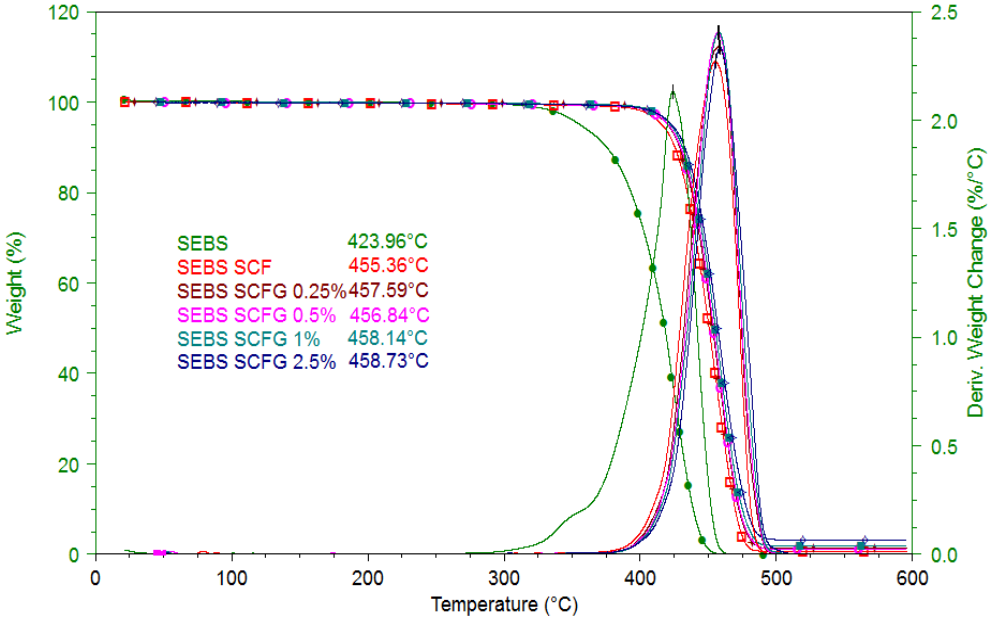

Figure 8.2 Thermal degradation profile of SEBS graphene composites with $scCO_2$

8.2.3 Differential Scanning Calorimetry of SEBS Graphene Composites

Figure 8.3 and Figure 8.4 show the heat flow thermogram of SEBS graphene composites with and without $scCO_2$ assisted extrusion. The weak crystalline nature of ethylene-butylene (EB) block ($–(CH_2\text{-}CH_2)–_n$) melting is around 20-30 °C. Phase separated microstructures are certain physical and morphological characteristics of SEBS as polystyrene and poly(ethylene-butylene) are thermodynamically immiscible. Therefore, the glass transition temperature of ethylene-butylene is at (Tg) –55 °C and the glass transition of S block around 96 °C along with heat enthalpic relaxation of styrene block at 60 °C (Figure 8.3) [155]. The endothermic region found between -25 °C to 25 °C on the SEBS thermogram (green) is mainly due to the effect of the glass transition temperature of EB block-ordering of aromatic structure from intermixed phase, following exotherm at 22 °C could signify densification of the amorphous region (S-rich phase) as the EB block is in the rubbery state.

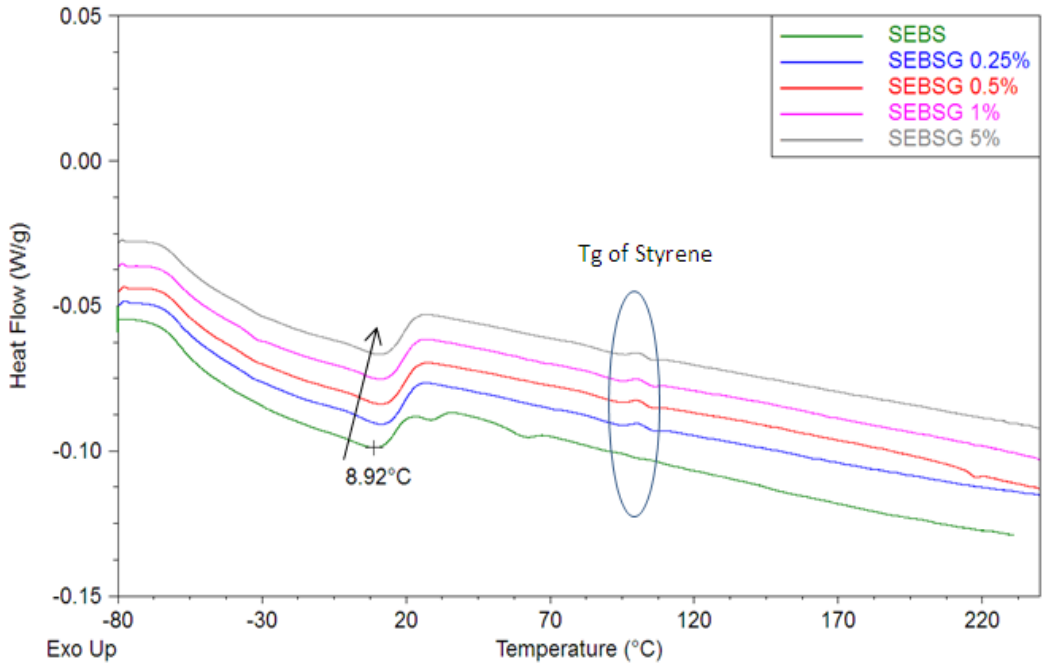

Figure 8.3 DSC heat flow thermogram of SEBS graphene composites without $scCO_2$

However, when the samples are treated with $scCO_2$ (Figure 8.4), no significant shifts can be observed due to EB block-ordering and the maximum endotherm remains constant at 10 °C. It is evident from the heat flow thermogram, that this endothermic region (or densification of the S-rich phase) slightly shifts higher to a temperature in accordance with the graphene percentage ratio. This shows that the addition of graphene reduced the free flow or rearrangement of the EB block which also indicative of graphene dispersion in the EB and the S domain. Although, the Tg

of styrene is not clearly visible from the virgin SEBS thermogram, a Tg at around 95 °C is clearly evident upon graphene addition. This clearly suggests that the interaction of graphene particles and the styrene-rich phase of SEBS restricts the easy movement of styrene at its Tg which led to the exothermic peak. A similar S rich Tg can be observed when extruded with $scCO_2$, which is indicative of supercritical fluid ability to induce rearrangement of the polymer chain in a more favourable manner.

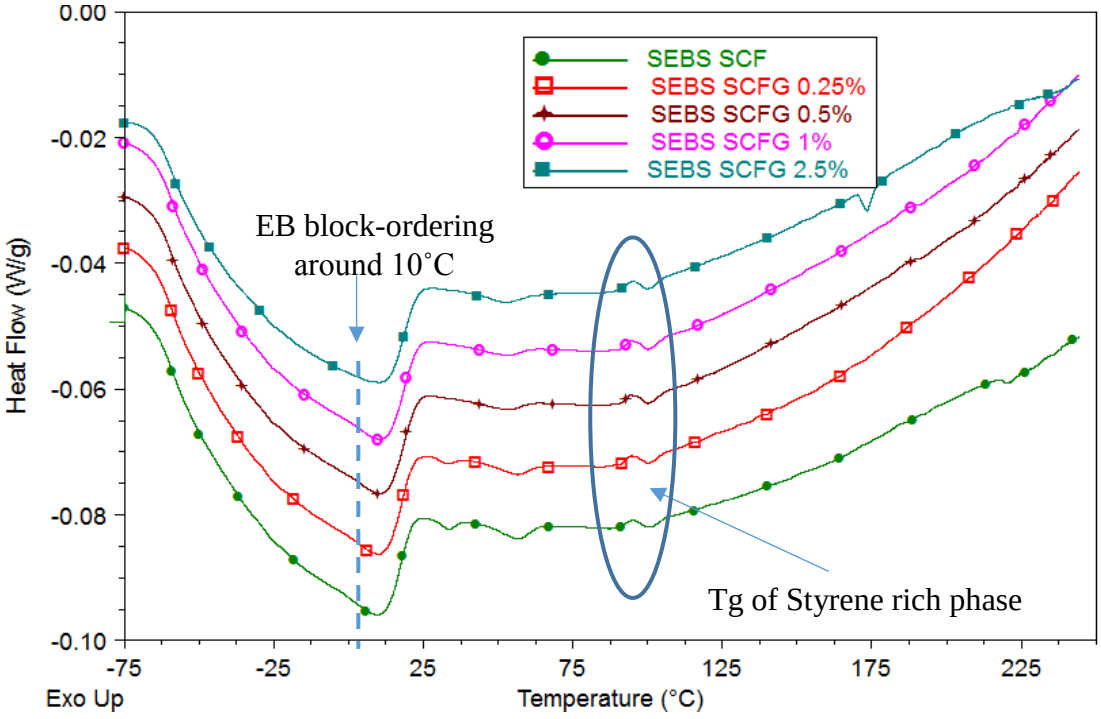

Figure 8.4 DSC heat flow thermogram of SEBS graphene composites with $scCO_2$

The derivative reversing heat capacity thermogram from Figure 8.5 presents similar effects as seen on the heat flow thermogram. After glass transition (Tg^{EB} at -55 °C), the long polymer chains are oriented randomly and have more freedom to move which results in a change in the microstructure of the material, resulting in higher specific heat capacity [121, 197]. No significant changes can be observed when the samples were extruded with assisted $scCO_2$. The specific heat capacity, which is also called the measure of molecular motion, reduces between -30 to 25 °C (almost becomes flat at 2.5%). This shows that the addition of graphene hinders the molecular movement or rearrangement of interphase domains. This creation of multiple interphase domains is more evident with $scCO_2$, due to microphase separation. The Tg of the styrene-rich phase is also clearly seen in the reversing heat capacity curve (Figure 8.6).

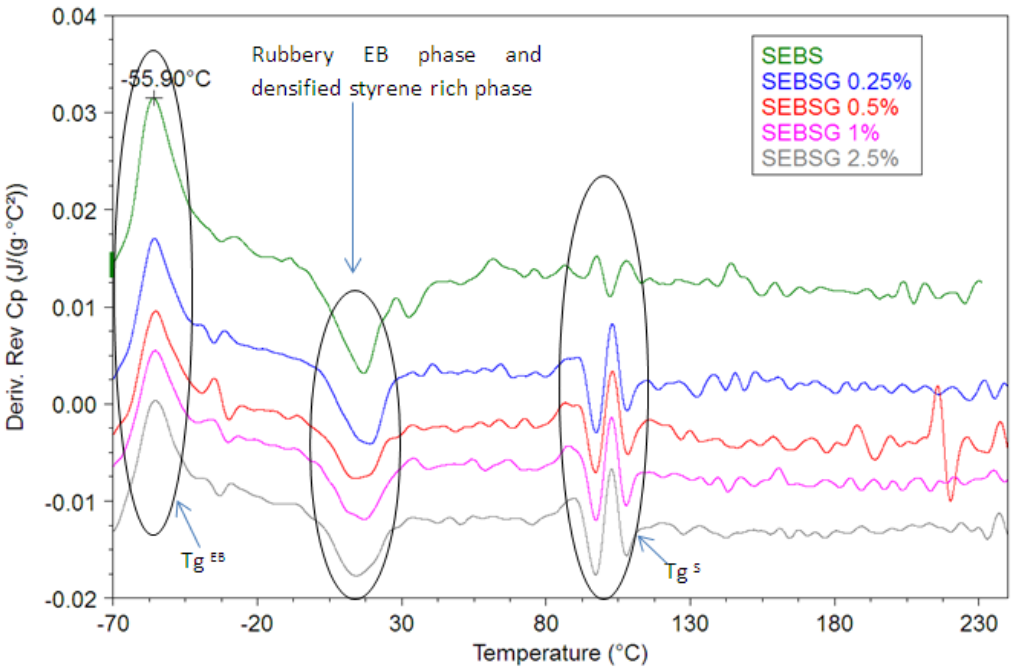

Figure 8.5 Derivative of reversing heat capacity thermogram for SEBS graphene composites

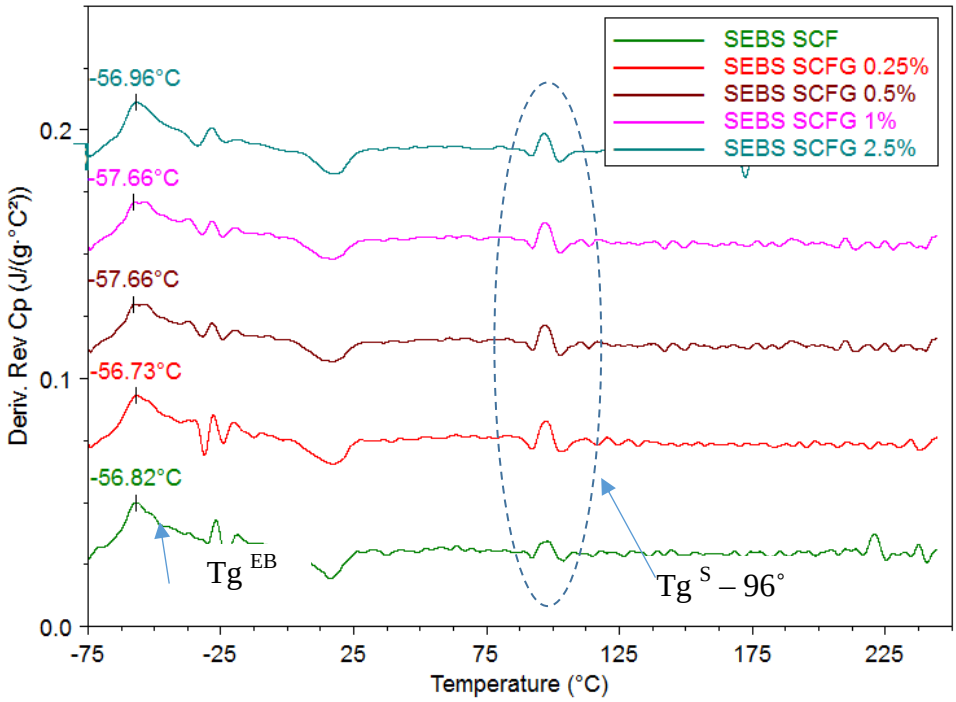

Figure 8.6 Derivative of reversing heat capacity thermogram for SEBS graphene composites with $scCO_2$

8.2.4 Dynamic Mechanical Thermal Analysis of SEBS Graphene Composites

The dynamic mechanical analysis was used to support the interpretation and analysis obtained using modulated DSC. Figure 8.7 to Figure 8.12 show storage modulus, loss modulus and tan delta of extruded SEBS graphene composites measured at a test frequency of 1Hz parallel direction to the axis of screw rotation.

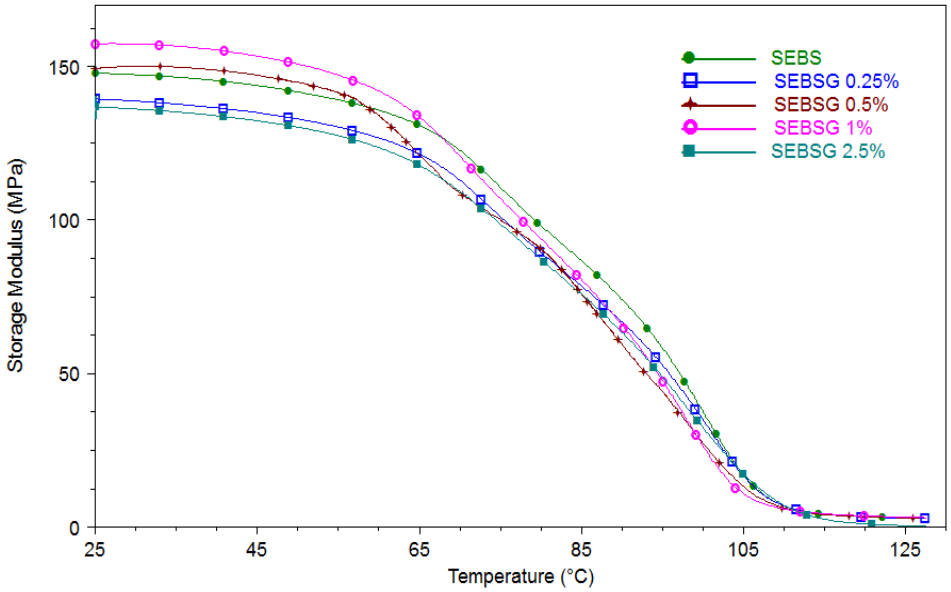

Figure 8.7 Storage modulus of SEBS graphene composites without $scCO_2$ measured at 1Hz

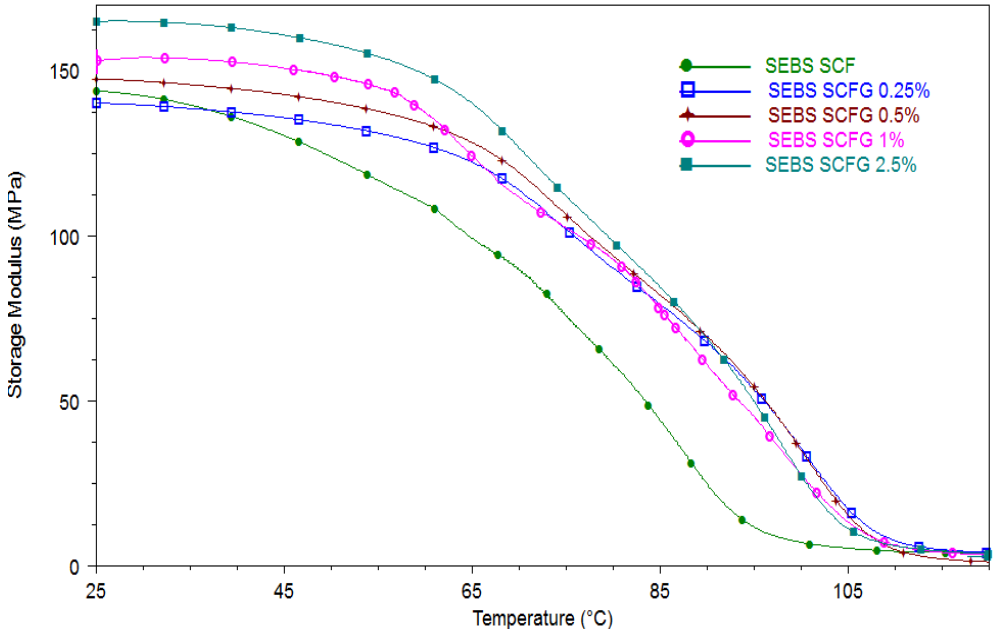

Figure 8.8 Storage modulus of SEBS graphene composites with $scCO_2$ measured at 1Hz

A large transition change in storage modulus was observed at 62.5 °C for virgin SEBS. It signifies that the material readily undergoes mechanical failure at this temperature, which is also the onset transition temperature of S-rich phase. Similar behaviour is observed for all the SEBS graphene composites. Similarly, a peak in the loss modulus was seen at 83.17 °C and is related to physical property changes ascribed to molecular motion processes and viscous transitions [198]. It may be due to the high segmental movement between styrene block and an ethylene-butylene block representing the viscous portion of the polymer. Both storage and loss modulus decrease upon addition of graphene, due to the presence of low shear stress along the axis of screw rotation during extrusion [199]. The storage modulus is highest at 160 MPa for 1% graphene loading and reduces to much lower values for 2.5% (80 MPa) compared to virgin SEBS. Such a reduction in the storage modulus with an increase in the graphene concentration usually occurs due to probable agglomeration of graphene particles within the SEBS polymer matrix and low alignment of additives along the axis of screw rotation because of increased viscosity during polymer processing.

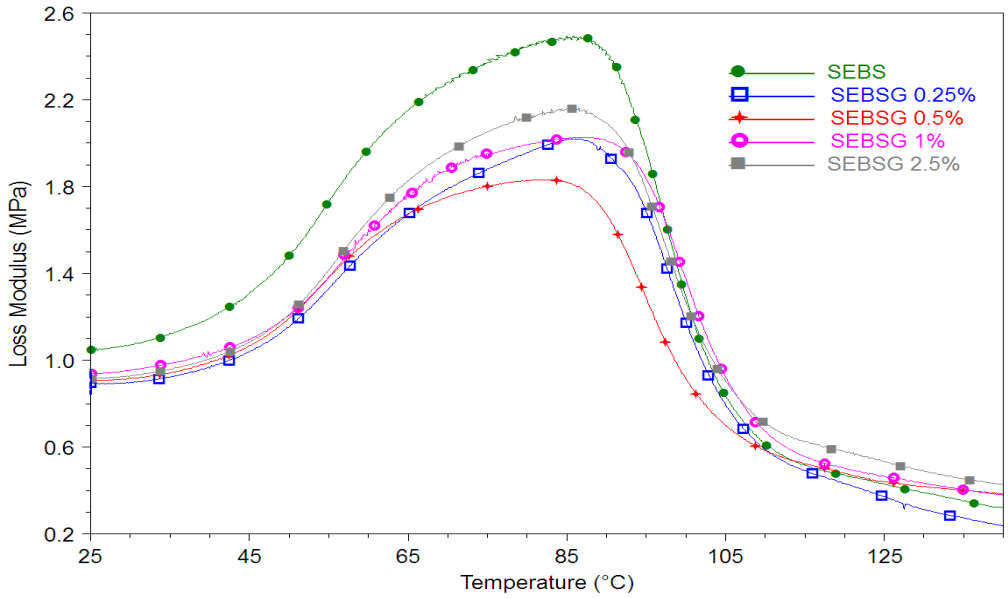

Figure 8.9 Loss modulus of SEBS graphene composites without $scCO_2$ measured at 1Hz

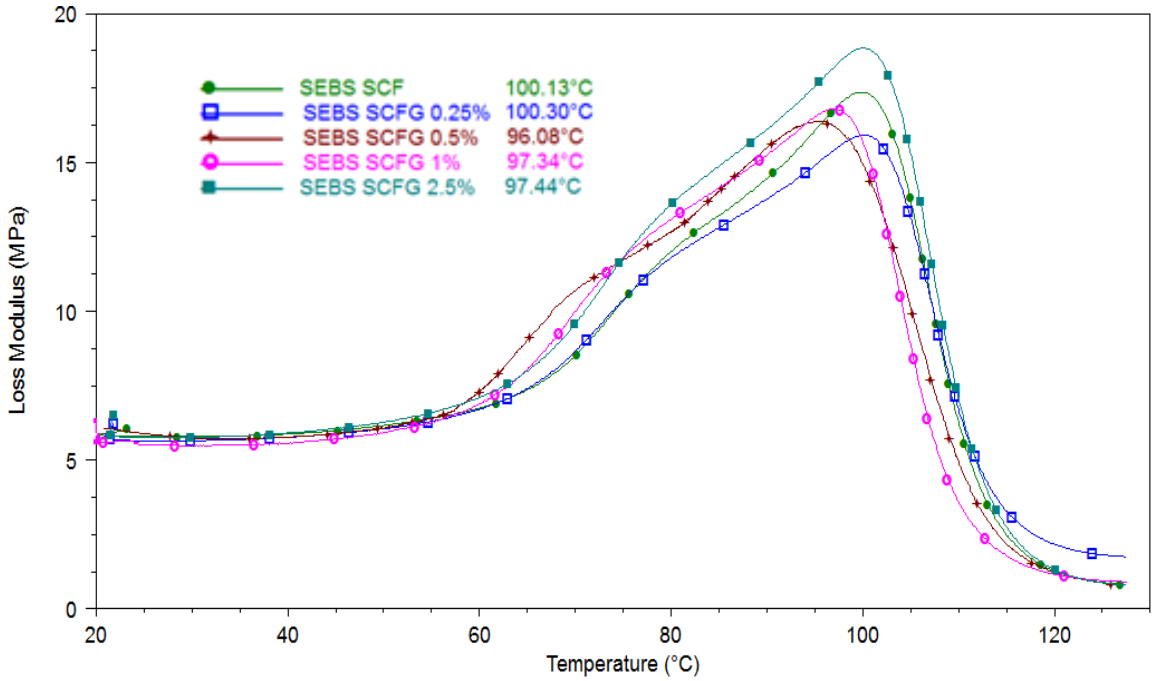

Figure 8.10 Loss modulus of SEBS graphene composites with $scCO_2$ measured at 1Hz

However, when the composite was processed with assisted $scCO_2$, the storage modulus for 2.5% graphene loading is highest at 175 MPa. In addition, the storage modulus is clearly enhanced even at lower loading concentrations. Such enhancement in storage modulus can be attributed to the probable $scCO_2$ ability to exfoliate and evenly disperse graphene particles without agglomerations. A similar trend can also be observed in the loss modulus curves. The peak of loss modulus indicates the accumulation of styrene block followed by glass transition temperature at around 96 °C for virgin SEBS graphene composites. When the composites are processed with $scCO_2$, the peak of loss modulus shifts to higher temperatures due to exfoliation and even dispersion of graphene particles within the SEBS matrix.

Tan delta is the ratio of viscous to elastic response of the polymer representing viscoelasticity; it is also known as damping factor. Therefore, the peak observed around 95.96 °C in the tan delta is due to the result of viscoelasticity representing the glass transition temperature of the styrene block.

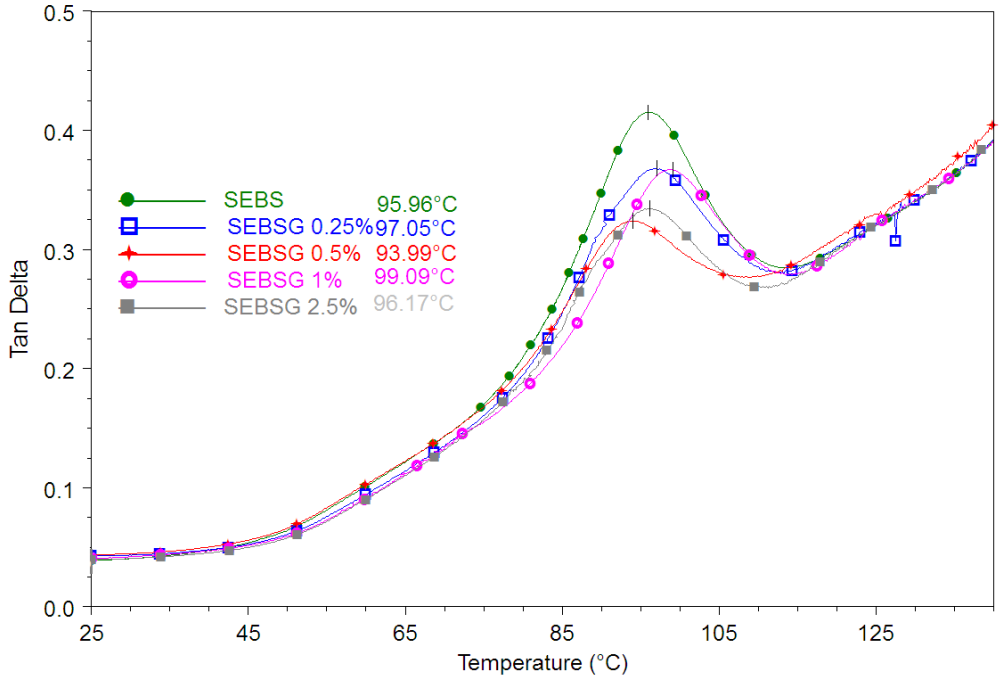

Figure 8.11 Tan delta of SEBS graphene composites without $scCO_2$ measured at 1Hz

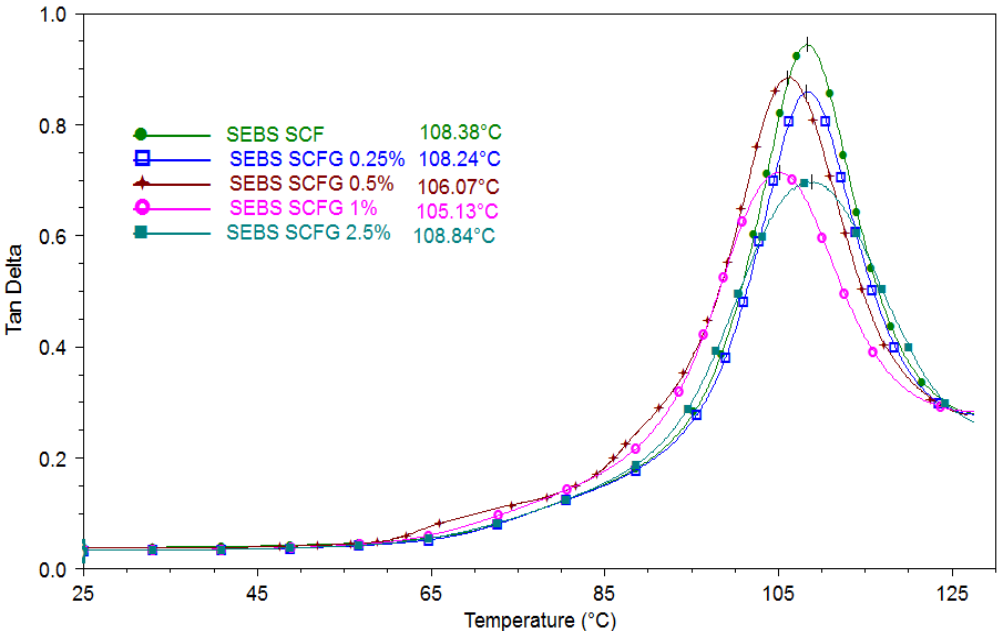

Figure 8.12 Tan delta of SEBS graphene composites with $scCO_2$ measured at 1Hz

It can be clearly seen the Tg represented by tan delta (Figure 8.12) curves shifts to higher temperatures when processed with assisted $scCO_2$, which is in agreement with the results obtained from the differential scanning calorimetry. Tan delta also indicates the energy dissipation mechanism mainly due to segmental motions or elastic response of the material, where the material changes from a rigid to an elastic state. With the addition of graphene filler,

the tan delta peak diminishes, due to the restrictions imposed by the graphene particles against the molecular motion of the polymer chain. This reduction and broadening of tan delta peak can be attributed to improved polymer chain interaction with the surface of particles which in turn leads to the formation of additional micro-domains with SEBS forming a heterogeneous network of SEBS and graphene composite [200, 201]. Where otherwise, increasing damping or tan delta illustrates poor interface adhesion, as in the case of virgin SEBS, where the chain segments can move easily, therefore, can easily break bonding at the interracial region resulting in mechanical failure.

8.2.5 Tensile Test of SEBS Graphene Composite

Figure 8.13 and Figure 8.14 shows the tensile test stress vs. strain curves of SEBS with various graphene ratios with and without $scCO_2$. It is evident from stress-strain curves that no significant change in resilience was observed upon addition of graphene, except for SEBSG 0.5% composite. This decrease in resilience can be attributed to the formation of more microstructures that has led to the heterogeneous composite network and less oriented molecules along the materials flow due to high viscosity along the direction of extrusion (also seen in tan delta curves of DMA - 8.2.4). As reported in the literature, due to the presence of a high shear force of corotating twin screw, additives are more aligned along the transverse direction of extrusion thereby increasing the stiffness in the transverse direction to extrusion [199, 202]. This heterogeneity or formation of microstructures is mainly dependent on the agglomeration and dispersion of additive particles that leads to different microstructures. However, when processed with assisted $scCO_2$, gradual enhancement in the modulus of resilience and toughness can be observed through all the graphene loading concentrations. The modulus of toughness increases upon addition of more than 1% graphene. This is mainly because the exfoliation of graphene which forms microstructures further blocks or restricts the easy dislocation motion, thereby increasing the toughness of the composites.

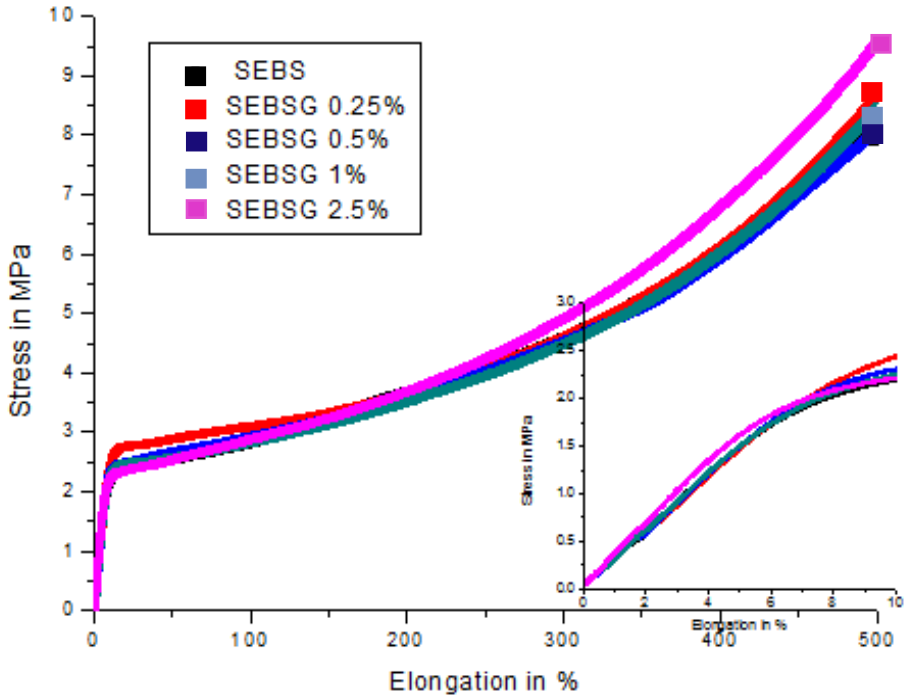

Figure 8.13 Stress vs. strain curve for SEBS graphene composites without $scCO_2$ measured at room temperature

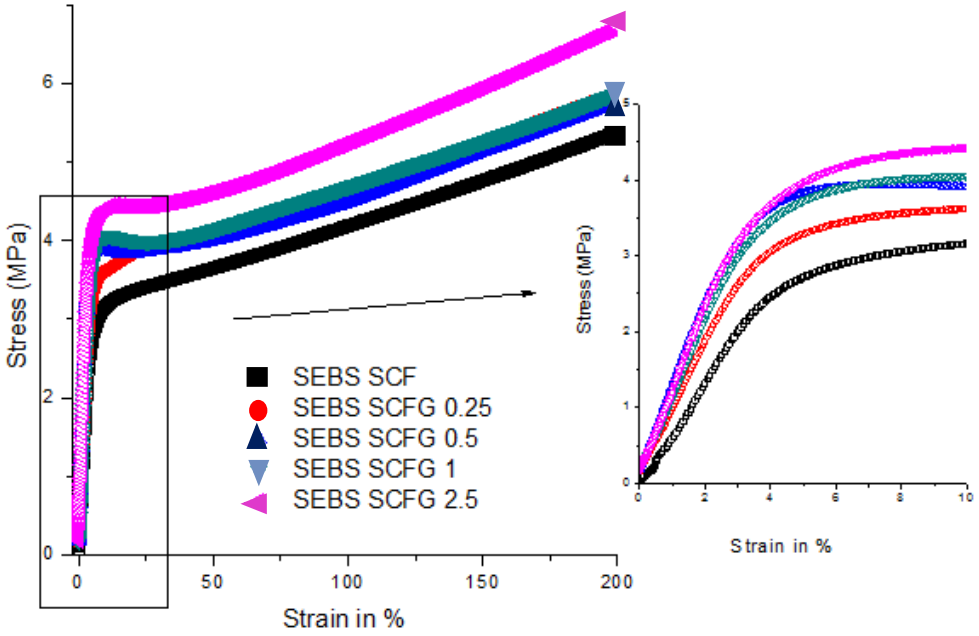

Figure 8.14 Stress vs. strain curve for SEBS graphene composites with $scCO_2$ measured at room temperature

Table 8.3 presents Young's modulus measured from the tangent slope obtained from 0.25 to 0.5% strain processed without $scCO_2$. The Young's modulus decreases at lower graphene concentrations and shows a gradual increase in graphene concentrations more than 1%. The

reason for such decrease in Young's modulus can be attributed to poor dispersion/low polymer chain alignment or poor or totally new unstable interphases created between the polymer chain and graphene making it an inhomogeneous material, thereby decreasing the modulus. However, at higher graphene concentration, the interaction may be higher, resulting in the stable formation of interphases, thereby gradually increasing the modulus.

Table 8.3 Young's modulus measured in MPa measured for all SEBS graphene composites at a tangent slope from 0.25% to 0.5% strain

Sample type	Young's Modulus (tangent slope obtained from 0.25 to 0.5 % strain)	
	Without $scCO_2$ MPa	With $scCO_2$ MPa
SEBS	61.08±6.6	64.01±1.6
SG0.25%	53.28±3.0	81.16±2.3
SG0.5%	55.40±4.8	110.21±2.6
SG1%	59.10±3.8	100.30±2.2
SG2.5%	64.00±3.4	122.60±3.8

8.2.6 Conductivity Test of SEBS Graphene Composites

Figure 8.15 and Figure 8.16 present the conductivity of SEBS graphene composites with and without $scCO_2$ respectively. The AC conductivity of all composites types except SEBS SCF G 2.5 wt.% remains linear with frequency suggesting the polarising ability of the composites under DC. Adding a conductive filler such as graphene does not result in enhancing the conductivity of the composites. This is mainly due to re-stacking of graphene fillers and forming agglomerates as discussed throughout this section. However, the conductivity increases for 1% and 2.5% due to the formation of the conductive network within the matrix, but, these conductive values are low making the material an insulator or dielectric. At and above 2.5% graphene when SEBS is extruded under $scCO_2$, the conductivity has two distinct features over frequency (i) the conductivity independent of frequency and (ii) the frequency dependent conductivity. The point of frequency at which the conductivity changes from independent to dependent on frequency is called the Maxwell-Wanger-Sillar (MWS) relaxation frequency. The transition/relaxation frequency at which AC current start to trigger is generally observed in conducting nanocomposites such as SEBS-SCFG 2.5 wt.% and is dependent on a different number of sites for conduction and polarisation [203]. MWS relaxation is the result of relaxation in the diffusion of charge carriers or electrons between charged particles in composites [204].

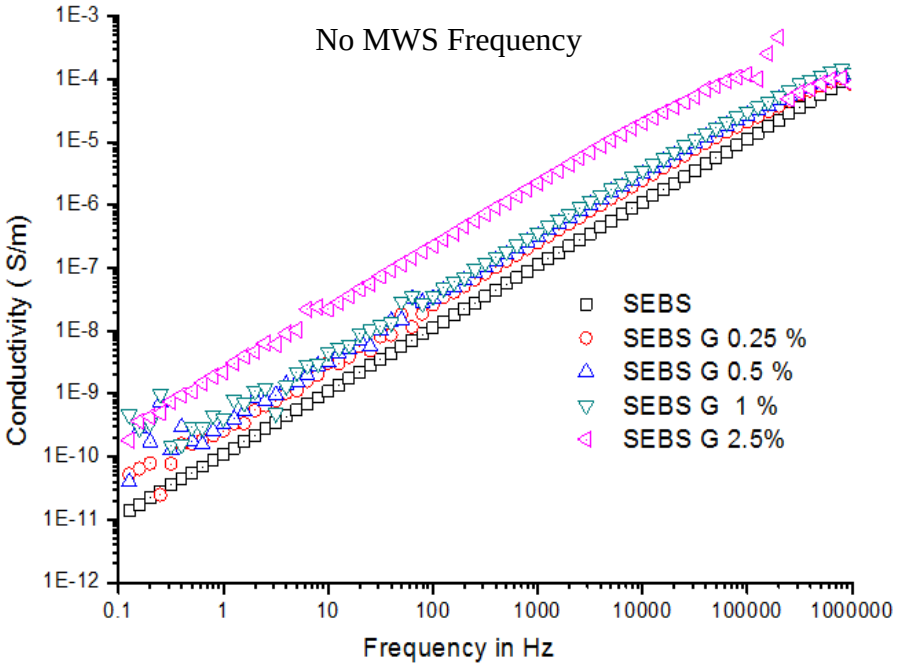

Figure 8.15 AC conductivity of SEBS graphene composites without $scCO_2$

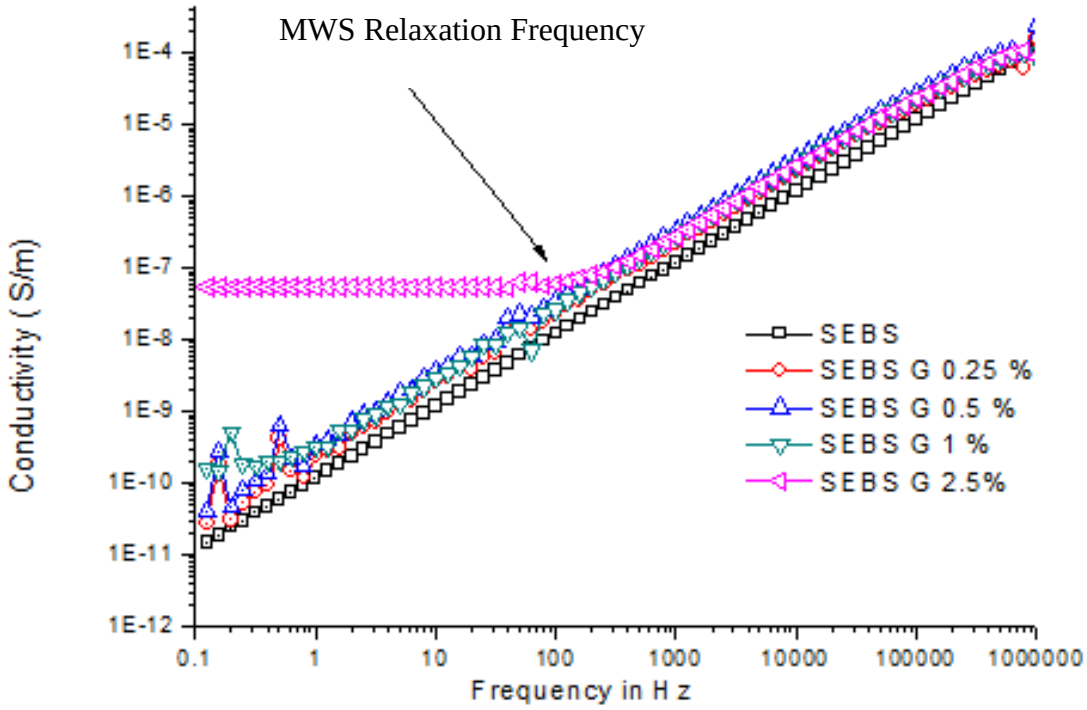

Figure 8.16 AC conductivity of SEBS graphene composites with $scCO_2$

These results suggest that the conductive percolation threshold for SEBS with graphene under SCF remains below 2.5% suggesting the DC conductivity with resistivity equivalent to 1/σ (conductivity before MWS frequency). However, the composite without SCF still remains dielectric when the graphene percentage is around 2.5%. The conductive percolation threshold

results in electron tunnelling effects between two graphene layers that exist between the polymer layers. Hence, homogenised mixing caused due to high dispersion of graphene during SCF processing leads to the formation of conductive composites at low percolation threshold.

8.2.7 Water Uptake Capacity of SEBS Graphene Composites

All the membranes were sulfonated to attach the polar SO_3^- moiety to facilitate proton transfer/ion-exchange ability. Table 8.4 presents the average water uptake capacity of sulfonated SEBS (sSEBS) graphene composites membranes that were immersed for 24 hours with distilled water. The water uptake did not vary considerably with the addition of graphene when processed with or without $scCO_2$ as the addition of graphene binds to styrene group of SEBS which in turn makes it difficult to graft the sulfonic acid group to styrene group. The average uptake remained almost constant at about 65% throughout.

Table 8.4 Average water uptake capacity of sSEBS graphene composites

Sample type	**Average water uptake capacity of sSEBS graphene composites**	
	Without SCF	With SCF
	%	%
sSEBS	65	66
sSG0.25%	63	66
sSG0.5%	66	63
sSG1%	62	65
sSG2.5%	64	63

8.2.8 Actuation Capabilities of SEBS Graphene Composites

All the membranes were immersed in distilled water and placed between two electrodes as shown in Figure 8.17(without $scCO_2$) and Figure 8.18 (with $scCO_2$). The bending degree and initial response times are presented in Table 8.5. A bending of 15° with initial movement of 15-20 sec was observed with sSEBS without $scCO_2$; and 18° with initial movement of a 5-7 sec for membranes with $scCO_2$. The reduction in initial response time suggests that membranes with $scCO_2$ were much faster in the transfer of charges upon application of the same stimuli (6.5V). Such reduced response times can be attributed to the supercritical ability to break down the microphases into smaller domains thereby enhancing styrene availability to sulfonation (suggesting even sulfonation). The addition of graphene particles enhances the electron conductivity at 6.5 volts where the membranes act as conductive strips with no sign of actuation.

Table 8.5 Actuation capabilities of sSEBS polymer matrix indicating the bending degree and initial response time with and without $scCO_2$

Sample Type	Actuation Capabilities of sSEBS Polymer Matrix			
	Without SCF		With SCF	
	Bending in Degrees	Initial Response Time for Actuation in sec	Bending in Degrees	Initial Response Time for Actuation in sec
sSEBS	15	15-20	18	5-7

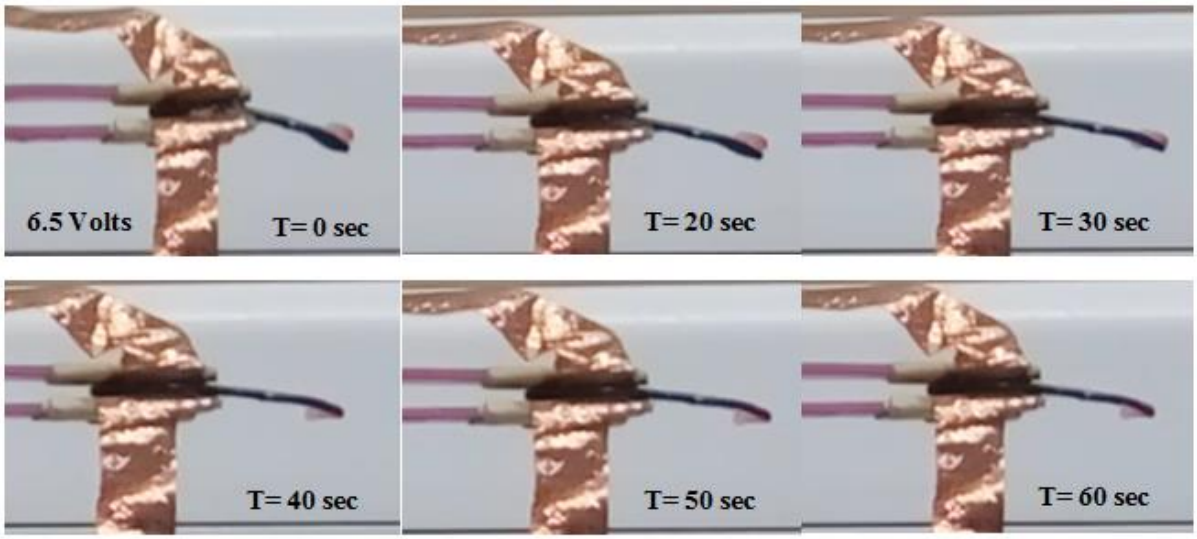

Figure 8.17 Bending capabilities of sulfonated SEBS without $scCO_2$

For these reasons, actuation capabilities of sSEBS graphene composites are not presented. Similar tip displacement of sSEBS has been reported by Wang et al [205] using LiCl solution with tip displacement of 0.2 mm (less than 3° displacement for actuator length and width of 4mm x 30mm with 100µm thick at 2V). Similar bending capability has also been reported by Immaudin et al [206] with tip displacement of 40mm for sSEBS (unknown thickness – HCl solution) against 23mm displacement for nafion membrane at 3V DC in both cases. The membrane used for actuation capabilities were around 0.5-0.6 mm thick and no additional ionic salts (distilled water was used) were used to enhance the ionic charge capacity, therefore higher actuation voltage was used (6.5V).

Figure 8.18 Bending capabilities of sulfonated SEBS with $scCO_2$

8.3 Key Points for Reprocessed SEBS Graphene Composites

Reprocessed SEBS graphene composites were investigated for thermal, mechanical and electrical properties for the various concentrations of graphene. The following are the observations made:

- The thermal degradation of SEBS increases by 25 °C upon addition of graphene. This showed that SEBS graphene composites increase the stability with respect to virgin SEBS due to graphene interaction with SEBS. The TGA thermogram analysis shows that the addition of graphene reduced the free flow or rearrangement of the EB block due to the formation of additional microphases. However, the use of $scCO_2$ reduced the degradation temperature by 10 °C compared to their composites counterparts because of high exfoliation thereby retaining the thermal behaviour of the polymer matrix.
- The $scCO_2$ processed composites show low relaxation phenomena in all domains of a triblock (EB block, interphase domain and S domain) and enhanced the microphase separation between soft and hard block compared to their counterparts.
- High exfoliation of graphene particles in the polymer matrix and low viscosity during processing when processed with $scCO_2$ led to (a) enhanced storage modulus and tan delta compared to their counterparts, and (b) improved Young's modulus in all composites
- In addition, better exfoliation of graphene led to low percolation threshold of graphene composites when extruded with an assistance of $scCO_2$. No FTIR spectra were attached in this chapter as the spectra measured when reprocessed did not show any significant changes.
- Bending capabilities between 15° to 18° for sSEBS can be observed for both with and without $scCO_2$. However, sSEBS membranes with $scCO_2$ tend to respond faster upon application of same voltage compared to untreated counterpart due to the suggested formation of addition interdomains when processed with $scCO_2$.

8.4 SEBS Graphene Oxide Composites

8.4.1 Throughput Test of SEBS GO Composites

Table 8.6 shows the average of 3 throughput reading for SEBS GO composites. The addition of fillers usually increases the viscosity when compared to a virgin polymer which in turn reduces the throughput of the extruder. However, the addition of $scCO_2$ increases the free volume fraction of the polymer melts and thus lowers their viscosities.

Table 8.6 Average weight of SEBS GO composite extruded for 1-minute

Sample type	**Average weight of SEBS based nanocomposite extruded for 1-minute**	
	Without SCF	With SCF
	g	g
SEBS	40.40±4.4	50.18±3.3
SEBSP	45.55±2.8	53.01±3.7
SEBS PGO 0.5%	46.96±4.9	52.77±3.5
SEBS PGO 1%	44.34±4.3	52.89±2.3
SEBS PGO 2.5%	43.33±2.2	53.28±4.1

8.4.2 Thermal Gravimetric Analysis of SEBS GO Composites

The Figure 8.19 show thermal degradation profile of SEBS GO composites with and without $scCO_2$. No significant differences can be observed with the maximum degradation temperature in the presence or absence of $scCO_2$ along with paraffin oil. A two-step degradation process can be observed in all the SEBS GO composites. The small peak at 320 °C arises mainly due to the addition of paraffin oil into virgin SEBS, where the paraffin oil degrades at 320 °C.

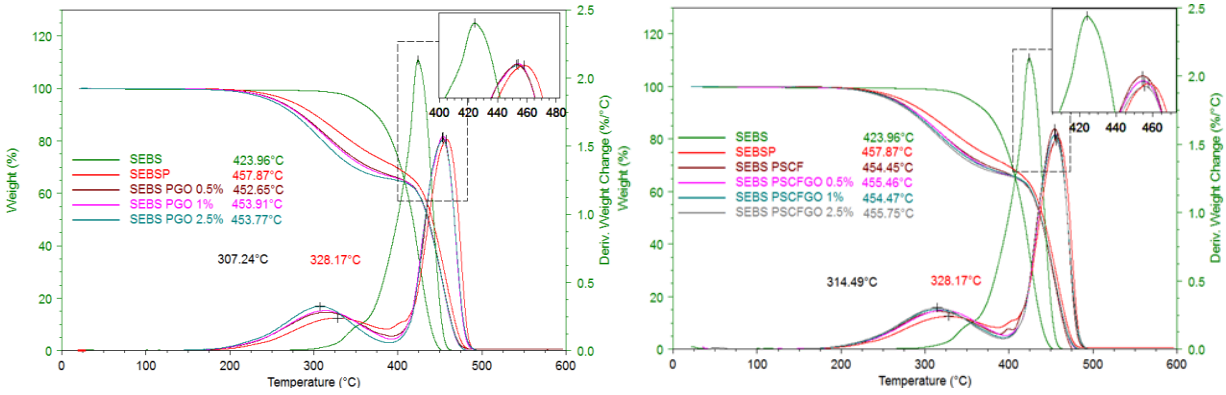

Figure 8.19 Thermal degradation profile of SEBS GO composites with and without $scCO_2$

Table 8.7 Maximum degradation temperature of SEBS GO composites with and without $scCO_2$

Sample type	Maximum degradation temperature of SEBS GO composites	
	Without SCF	With SCF
	° C	° C
SEBS	423.9	454.4
SEBSP	457.8	457.6
SEBS PGO 0.5%	452.6	455.4
SEBS PGO 1%	453.9	454.4
SEBS PGO 2.5%	453.7	455.7

8.4.3 Differential Scanning Calorimetry of SEBS GO Composites

The Figure 8.20 and Figure 8.21 show the heat flow thermogram of SEBS GO composite extrudates with and without $scCO_2$. The endothermic region found between -25 °C to 25 °C on all thermograms flattens with the addition of GO as GO particle interaction restricts the movement of EB block. The maximum endotherm almost remains constant around 1±1 °C in both the cases (with or without $scCO_2$). The glass transition temperature of the S-rich phase can be clearly seen (Tg^S – 95 °C) in both heat flow thermograms.

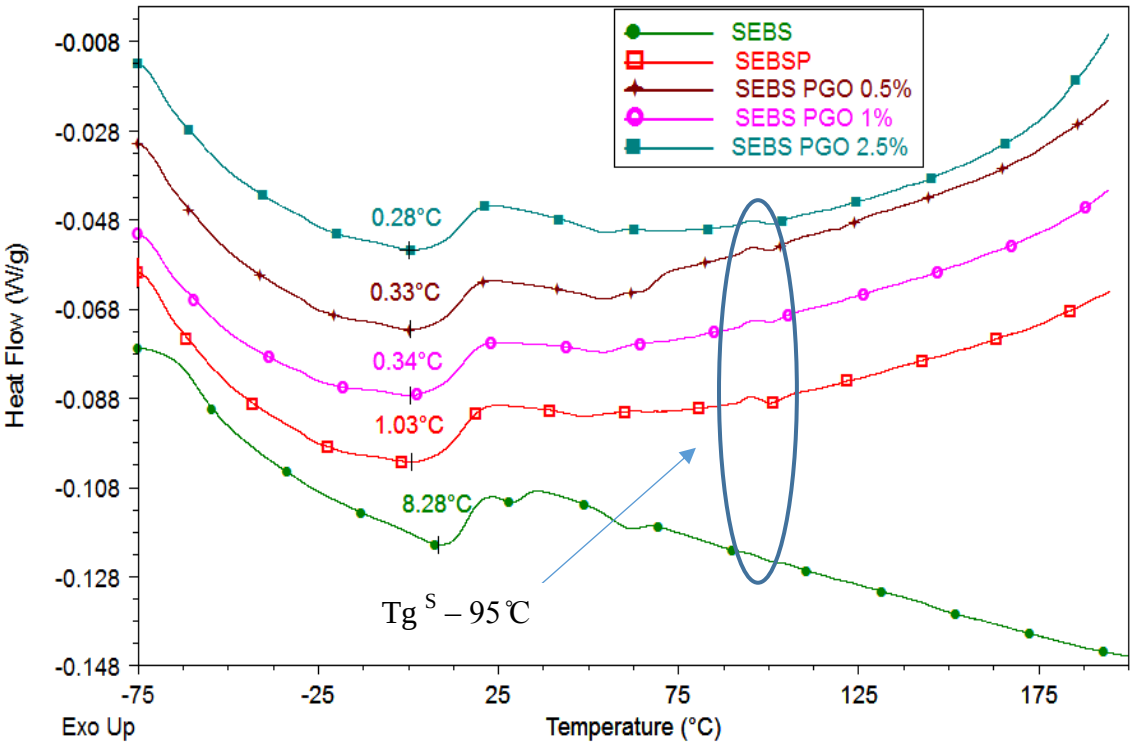

Figure 8.20 Heat flow thermogram of SEBS GO composites without $scCO_2$

The clear appearance of Tg S at 95 °C for virgin SEBSP extrudates signifies that the addition of paraffin oil provides or enhances easy movement of styrene rich phase within SEBS polymer

matrix. Figure 8.22 and Figure 8.23 presents the derivative reversing heat capacity thermogram of SEBS GO composites with and without $scCO_2$. A clear shift in Tg ^{EB} from -56 °C for virgin SEBS to -65 °C for virgin SEBSP (SEBS paraffin oil sample) can be observed in both with and without $scCO_2$ extrudates. In addition, Tg ^{S} is enhanced, these shifts in Tg suggests that addition of paraffin oil acts as a plasticiser. Paraffin oil is used in this section of study mainly to avoid degradation of GO during the process of extrusion. The combination of paraffin oil and $scCO_2$ allows extrusion of SEBS at very low temperatures (all the samples were extruded in the range of 100 °C to 125 °C). No significant changes can be observed when the samples were extruded with $scCO_2$.

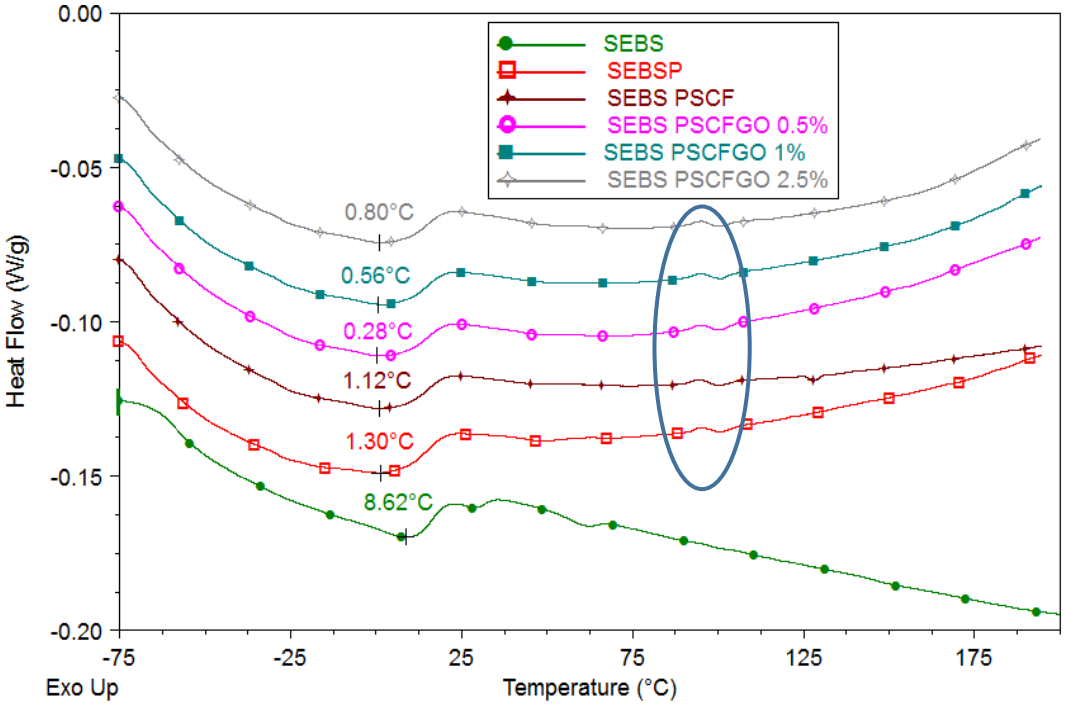

Figure 8.21 Heat flow thermogram of SEBS GO composites with $scCO_2$

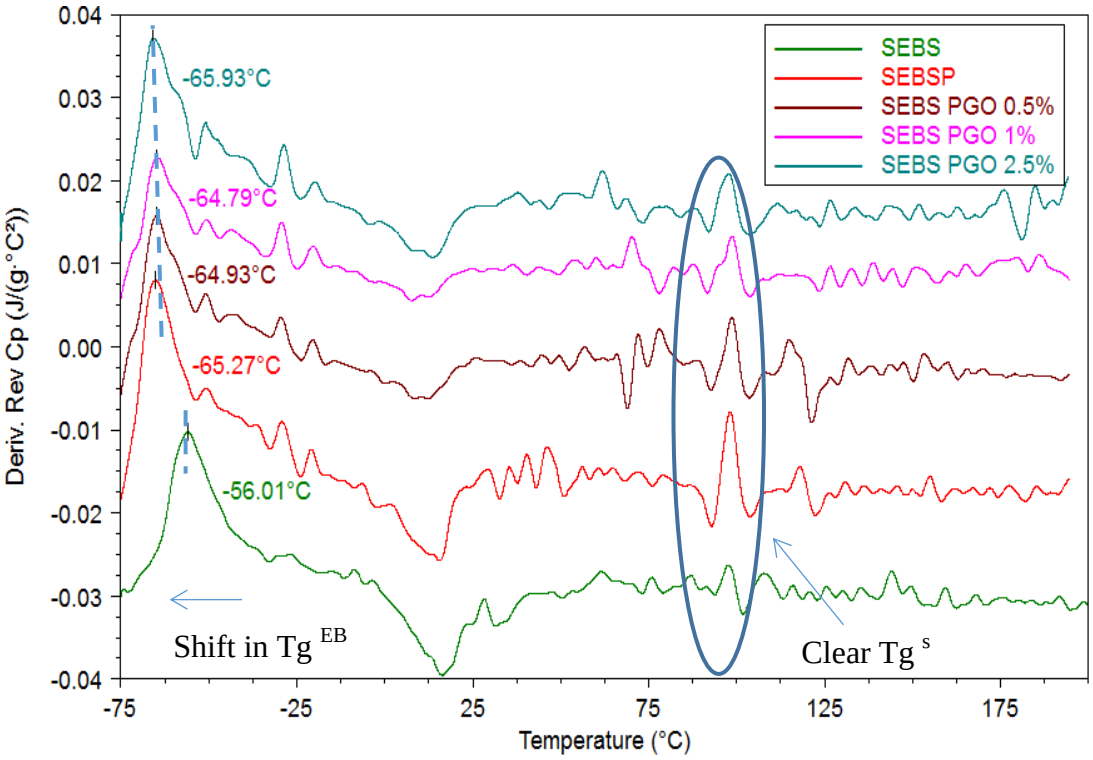

Figure 8.22 Derivative of reversing heat capacity thermogram of SEBS GO composites without $scCO_2$

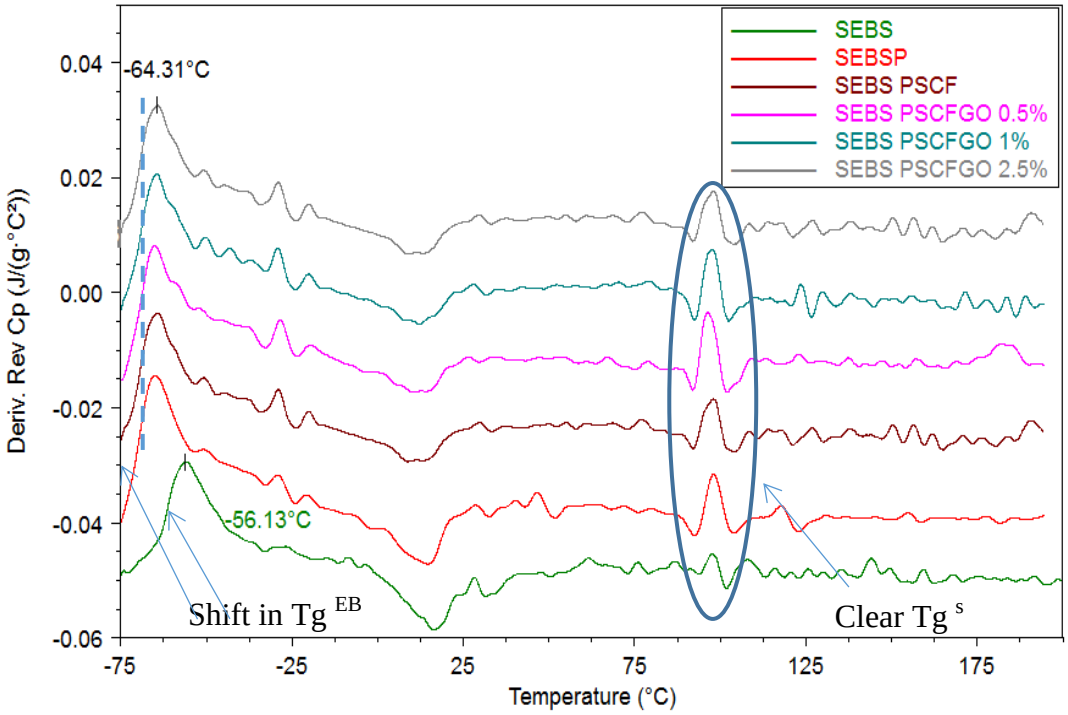

Figure 8.23 Derivative of reversing heat capacity thermogram of SEBS GO composites with $scCO_2$

8.4.4 Dynamic Mechanical Thermal Analysis of SEBS GO Composites

The Figure 8.24 presents the storage modulus of SEBS GO composites with and with $scCO_2$. The storage modulus was highest for 0.5% GO loading while reduces and is lesser than the virgin SEBS when the loading concentration is increased to 1% and 2.5%. However, the storage modulus continues to increase even at higher loading such as 2.5%, when the SEBS GO composites were processed with $scCO_2$. Such an increase in storage modulus when treated with $scCO_2$ suggests that $scCO_2$ processing at higher loading reduces the agglomeration of particles. Which otherwise, if agglomerated and not evenly dispersed results in reducing the mechanical properties of the composite (as seen in samples there were not processed with $scCO_2$). Similar results were also observed with SEBS graphene composite.

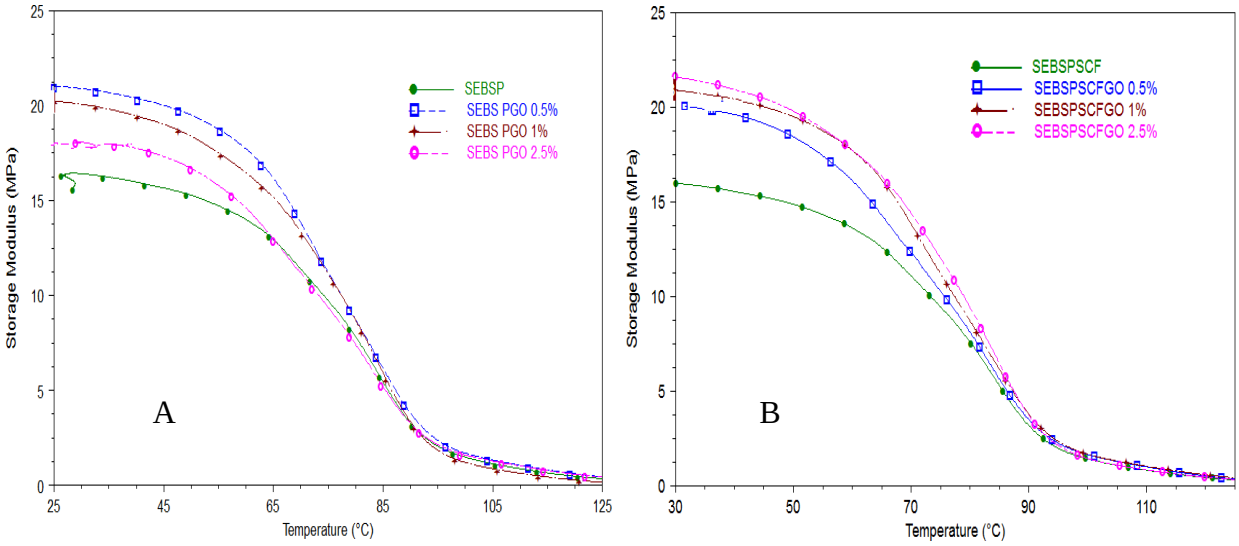

Figure 8.24 Storage modulus of SEBS GO composites (B)with and (A)without $scCO_2$

The loss modulus as seen in Figure 8.25 also follows the storage modulus, where the loss modulus is seen to be increasing for composites which were processed without $scCO_2$. Clearly, the loss modulus reduces at 2.5% loading proposing that the GO particles within the polymer matrix would have not evenly dispersed suggesting a low interaction between the polymer matrix and the filler particle. When such filler particles have a good interaction with the polymer matrix, they will usually result in enhancing the loss modulus as the interacted site restricts the relaxation of the polymer chain.

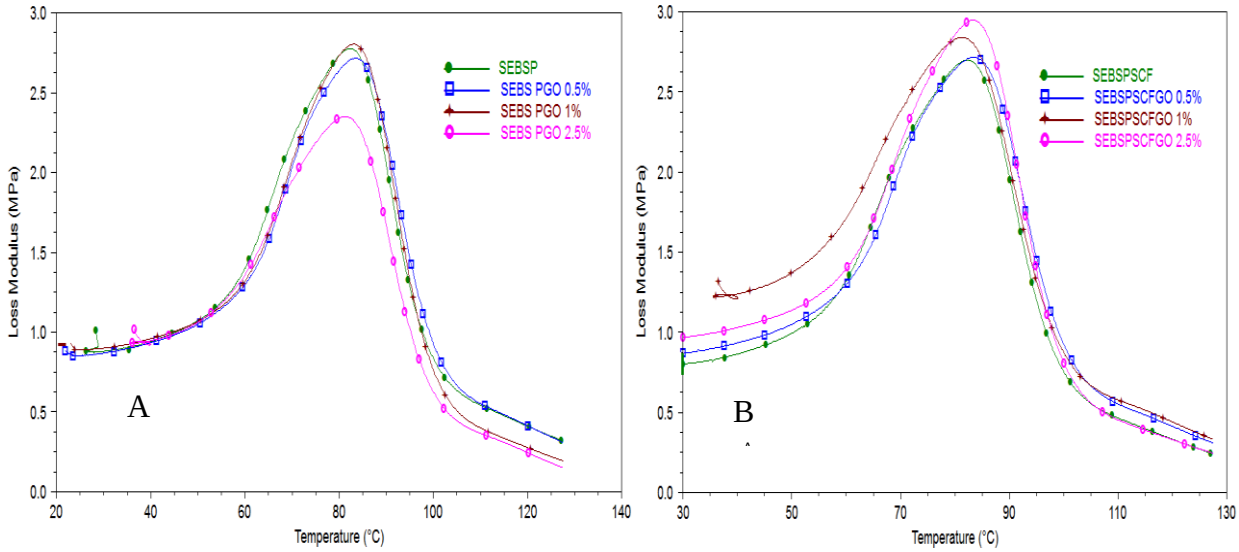

Figure 8.25 Loss modulus of SEBS GO composites (B)with and (A)without $scCO_2$

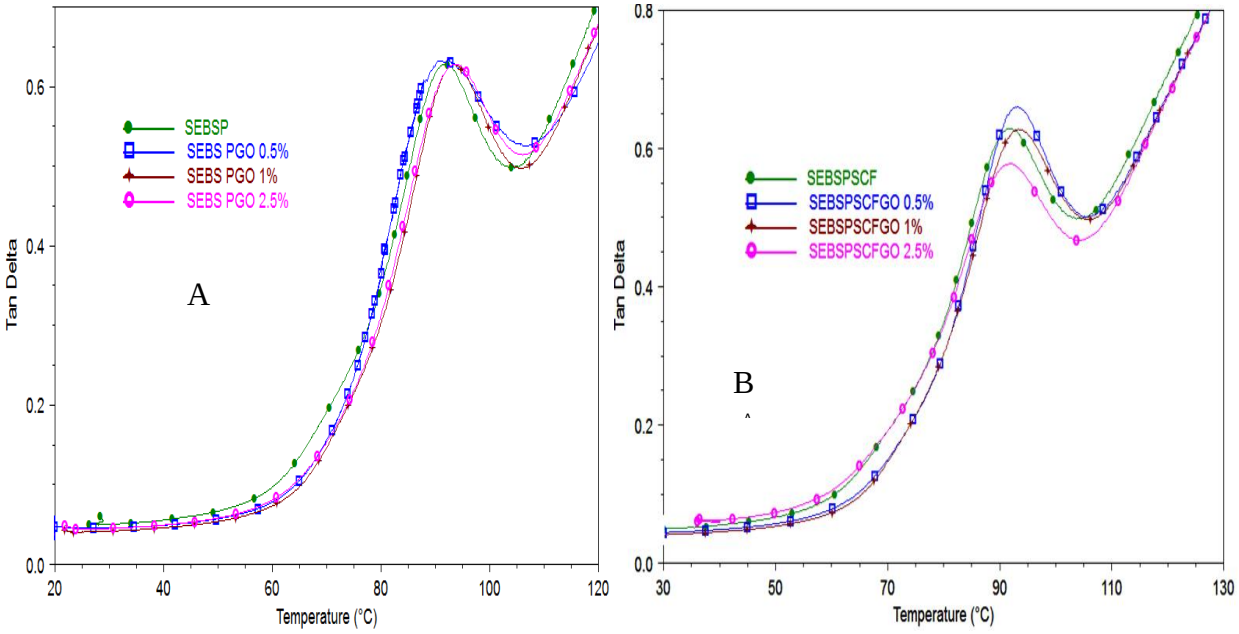

Figure 8.26 Tan delta of SEBS GO composites (A)with and (B)without $scCO_2$

Similar results can also be observed from the tan delta curves, where the loss due to heat dissipation is highest without $scCO_2$. However, when processed with $scCO_2$, the tan delta reduces with increasing loading concentration, suggesting good interaction and even dispersion of GO within the SEBS polymer matrix.

8.4.5 Tensile Test of SEBS GO Composite

Figure 8.27 and Figure 8.28 show the stress vs. strain curves of SEBS GO with and without $scCO_2$. Both the modulus of resilience and toughness are found to be highest for GO 0.5% loading without $scCO_2$.

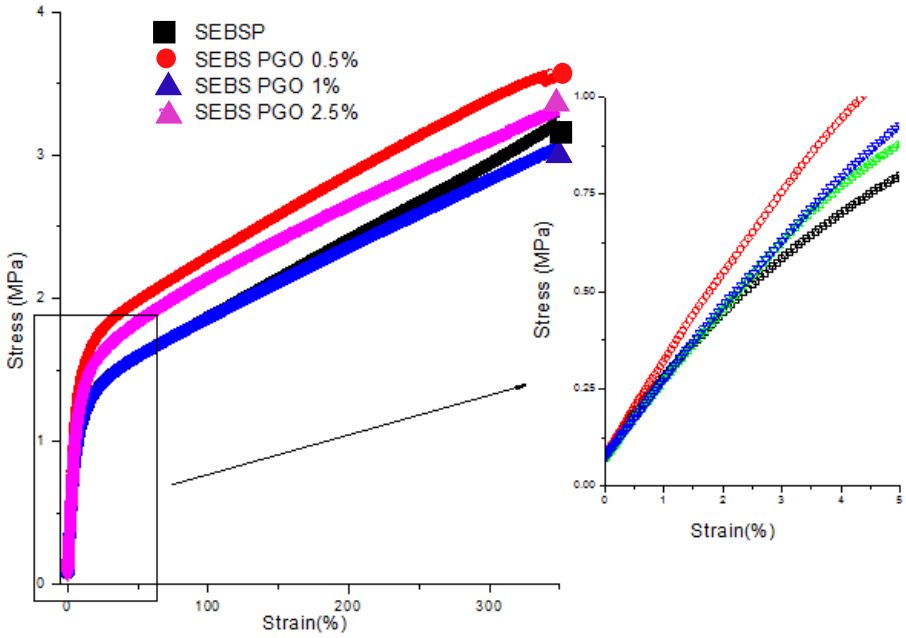

Figure 8.27 Stress vs. strain curves of SEBS GO composites without $scCO_2$

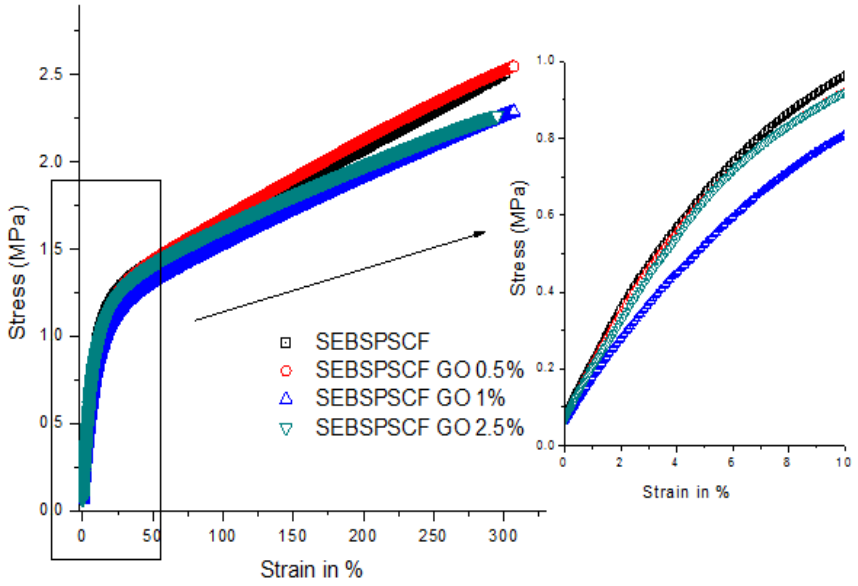

Figure 8.28 Stress vs. strain curves of SEBS GO composites with $scCO_2$

Table 8.8 Young's Modulus (tangent slope obtained from 0.25 to 0.5 % strain) for SEBSGO composites with and without $scCO_2$

Sample type	Young's Modulus (tangent slope obtained from 0.25 to 0.5 % strain)	
	Without $scCO_2$ MPa	With $scCO_2$ MPa
SEBS	61.08±3.4	64.01±1.6
SEBSP	15.20±4.3	13.90±3.3
SEBSP GO 0.5%	23.90±5.6	14.01±5.8
SEBSP GO 1%	18.88±2.8	12.14±2.2
SEBSP GO 2.5%	20.07±3.9	13.23 ±2.0

Similar results have also been reported in the DMA analysis (refer to Section 8.4.4), indicating that the GO particles at 0.5% reach the threshold beyond which the particles tend to agglomerate affecting the mechanical properties. When the composite was processed with $scCO_2$, the resilience and toughness decreased with respect to the untreated.

8.4.6 Electrical Testing of SEBS GO Composites

Figure 8.29 and Figure 8.30 present the conductivity of SEBS GO (GO) composites extruded with and without $scCO_2$ respectively. The relation of the conductivity of SEBS and SEBS GO 0.5% with/without $scCO_2$ with frequency range were found to be linear suggesting only the polarising effect of SEBS and SEBS GO 0.5%. Composites remain completely dielectric and do not pass direct current at the dry condition as no transfer of charge takes place between graphene layers. However, SEBS with GO 0.5 wt. % showed improved polarising capability as conductivity is higher than virgin SEBS. When the percentage of graphene oxide was increased to 1%, the conductivity remains constant over the period of frequency and changes linearly with the change in frequency in log scale showing Maxwell-Wagner-Sillar (MWS) relaxation frequency.

The transition/relaxation frequency at which AC current starts to trigger can be generally observed from conducting composites such as SEBS GO 1 wt. % and is dependent on a different number of sites for conduction and polarisation [207]. The conductive percolation threshold results in electron tunnelling effects between two graphene layers (reduced graphene layers during the extrusion process) that exist between polymer layers. Early MWS relaxation occurs in SEBS GO with 1% and 2.5 % composites without $scCO_2$ compared to their counterparts due to the result of agglomeration of GO as they provide a lower number of conductive sites than non-dispersed GO.

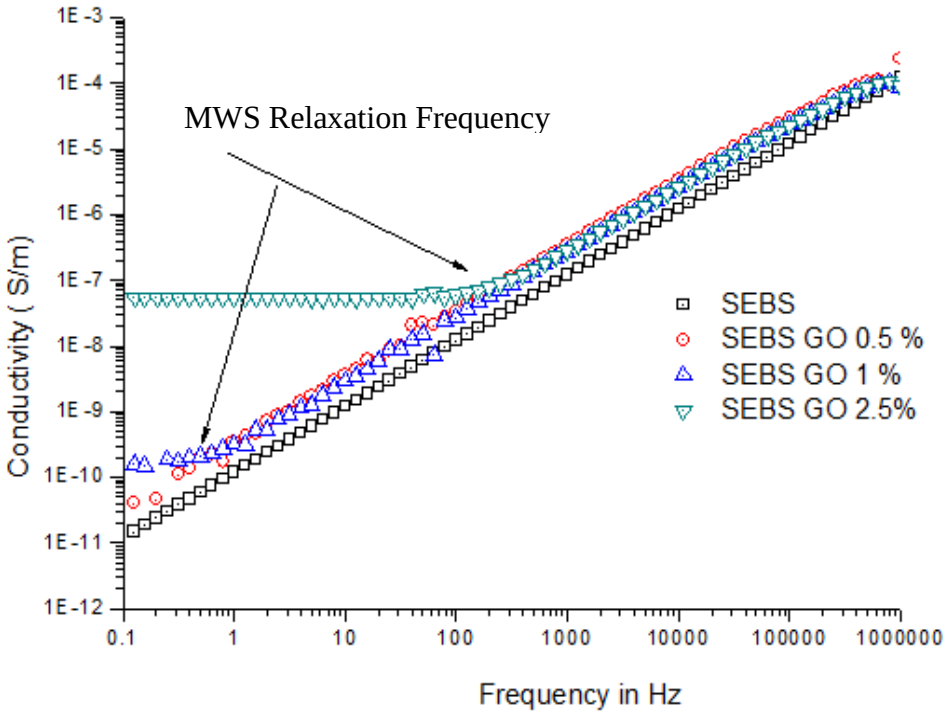

Figure 8.29 AC conductivity at various frequencies for SEBS GO composites without $scCO_2$

.

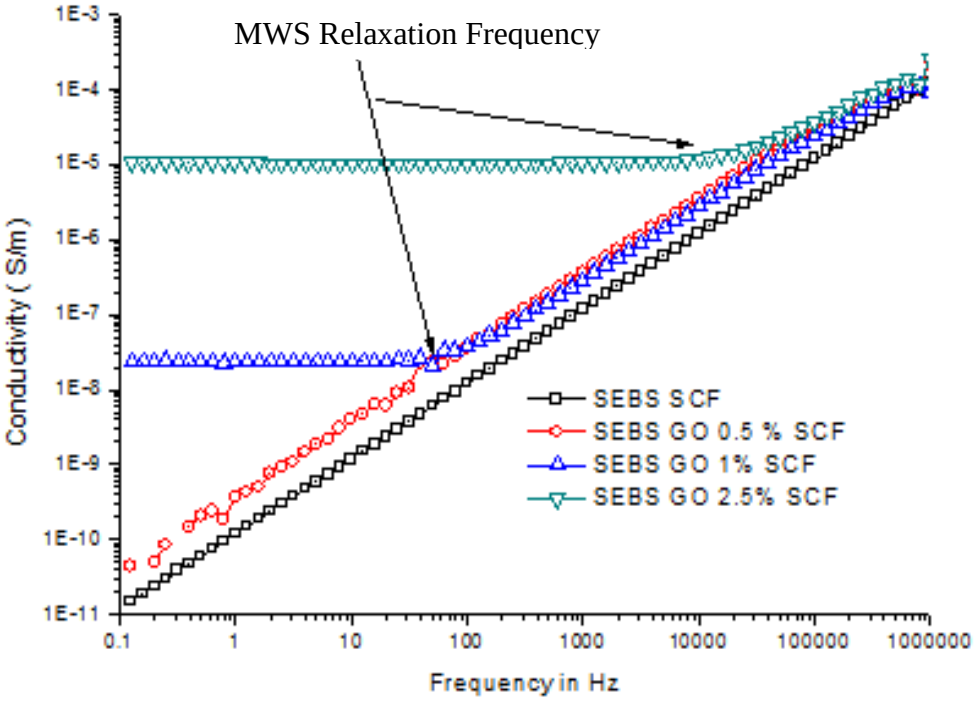

Figure 8.30 AC conductivity at various frequencies for SEBS GO composites with $scCO_2$

The use of $scCO_2$ provides better dispersion leading to high exfoliation of GO, thereby leading to improved DC conduction behaviour even at higher frequencies as highly dispersed GO conducts electricity as particles disperse more evenly than agglomerates in the polymer matrix. The DC Conductivity was also enhanced when the percentage of GO changes from 1 wt. % to 2.5 wt. %. GO as SEBSGO 2.5 wt. % has more conducting sites compared to SEBS-SCFGO 1 wt. %.

For bending actuation applications, highly polarising polymers (under dry condition) with low heating effects are preferred. However, under wet condition, polymeric materials need to be conductive through proton carriers for effective bending. Usually agglomerated GO polymeric composites when operated under electric field produces high heating effect leading to high loss and failure of the material under electric field in actuation like applications. Similarly, DC conductivity through electrons based composites demonstrate very low or no actuation properties as an electron can easily pass through polymer layers before the ions move from one point to another causing no actuation. Hence, it is suggested that a low percentage of the highly exfoliated GO-based polymer will enhance the bending performance of ionic actuators.

8.4.7 Water Uptake Capacity of SEBS GO composites

Table 8.9 shows the average water uptake capacity in percentage for sulfonated SEBS GO composites with and without $scCO_2$ which were immersed in distilled water for 24 hours. The water uptake capacity gradually increased upon addition of GO with and without $scCO_2$. However, the uptake capacity is much higher in scCO2 treated composites when compared to its untreated counterpart. Such increase in water uptake is mainly due to increase in the ionic polar nature of the sulfonic group and oxygen-rich polar GO surface, which enhances hydrophilicity and uptake capacity.

Table 8.9 Average water uptake capacity for sSEBS GO composites

Sample type	**Average water uptake capacity for sSEBS GO composites**	
	Without $scCO_2$	With $scCO_2$
	%	%
sSEBS	66	66
sSEBSP	60	63
sSEBS PGO 0.5%	**69**	**82(16)**
sSEBS PGO 1%	**77**	**86(10)**
sSEBS PGO 2.5%	71	79(8.9)

The uptake capacity is highest for 1% and reduces for 2.5% in case of without $scCO_2$ samples, due to suggested agglomeration. GO loading of 0.5%, 1% and 2.5% shows an increase of 16%, 10% and 8.9% compared to composites without $scCO_2$. Considerable improvements can be seen on the composites processed with $scCO_2$; due to the ability $scCO_2$ to exfoliate and evenly disperse GO particles within the matrix (similar improvements have been discussed in this chapter).

8.4.8 Actuation Capabilities of SEBS GO composites

In order to evaluate the actuation capabilities, sSEBS PGO loading of 0.5% with and without $scCO_2$ was chosen as higher GO loading will result in higher electron conductivity and agglomeration. Actuation capabilities of sSEBS membrane have been discussed in Section 8.2.8 and the bending degree remained the same when paraffin oil was added (sSEBSP samples). All the membranes were immersed in distilled water before the test. As seen from Table 8.10, the bending degree increased for membranes which were treated with $scCO_2$ (27°) compared to the untreated counterpart (22°). The bending degree of GO 0.5% membranes was higher when compared to sSEBS membranes (around 18°), due to suggested polar nature oxygen-rich GO surface. The initial response time for sSEBS PGO 0.5% without was 5 sec and 15 sec for membrane processed with $scCO_2$. The reason for the increase in initial response time can be attributed to exfoliation of GO particles as discussed throughout this chapter; as exfoliation of GO, particles creates higher ion interactive sites (higher water uptake) requiring additional water molecules to transfer upon excitation. Figure 8.31 and Figure 8.32 presents the bending capabilities for sSEBS GO 0.5% with and without $scCO_2$ at various input voltage and times.

Table 8.10 Actuation capabilities of sSEBS GO 0.5% GO composites with and without $scCO_2$

Sample Type	**Actuation Capabilities of sSEBS PGO 0.5% Composites**			
	Without SCF		With SCF	
	Bending in Degrees	Initial Response Time for Actuation in sec	Bending in Degrees	Initial Response Time for Actuation in sec
sSEBS PGO 0.5%	22	05	27	12-15

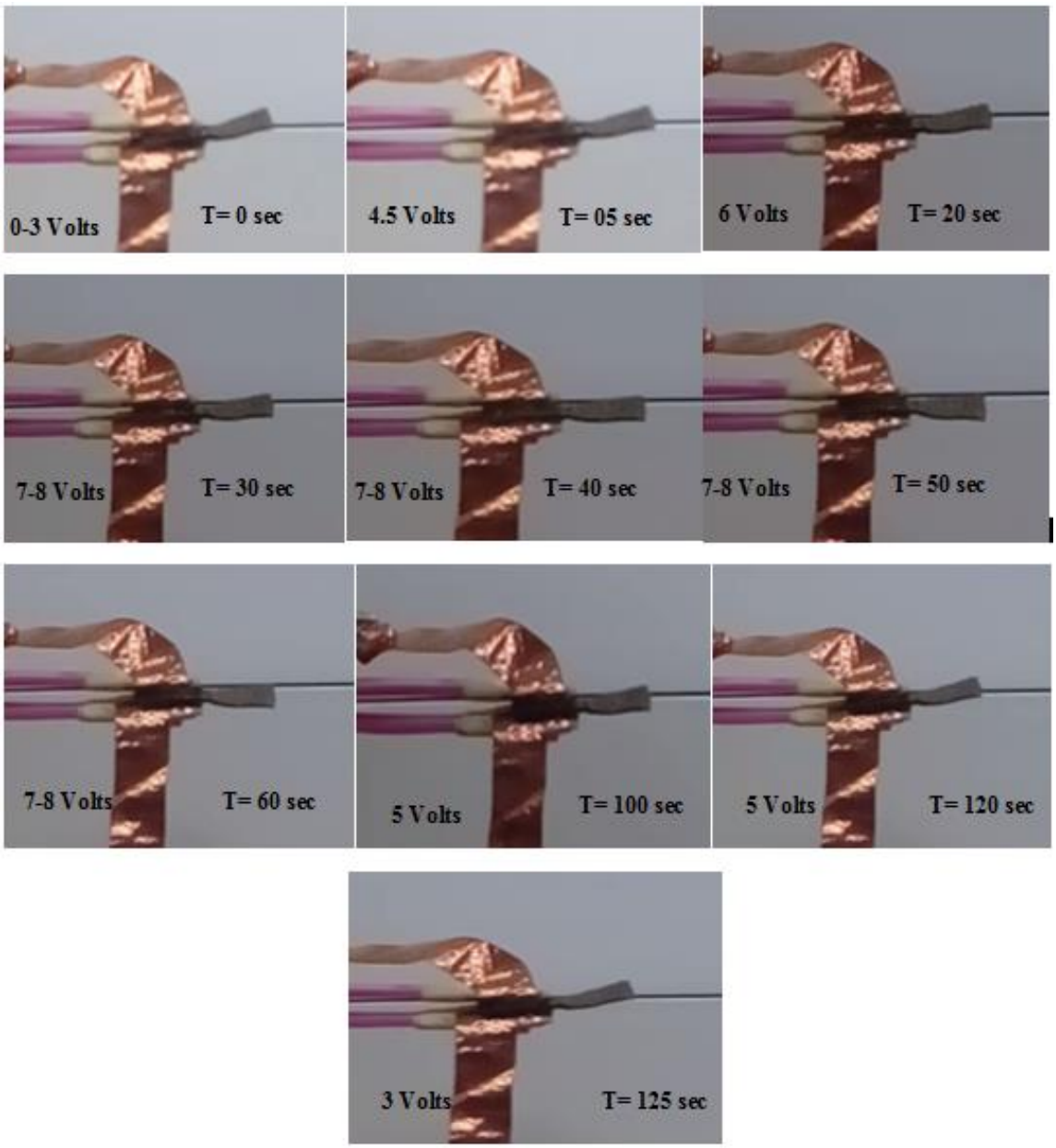

Figure 8.31 Bending capabilities of sSEBS GO 0.5% membranes without $scCO_2$

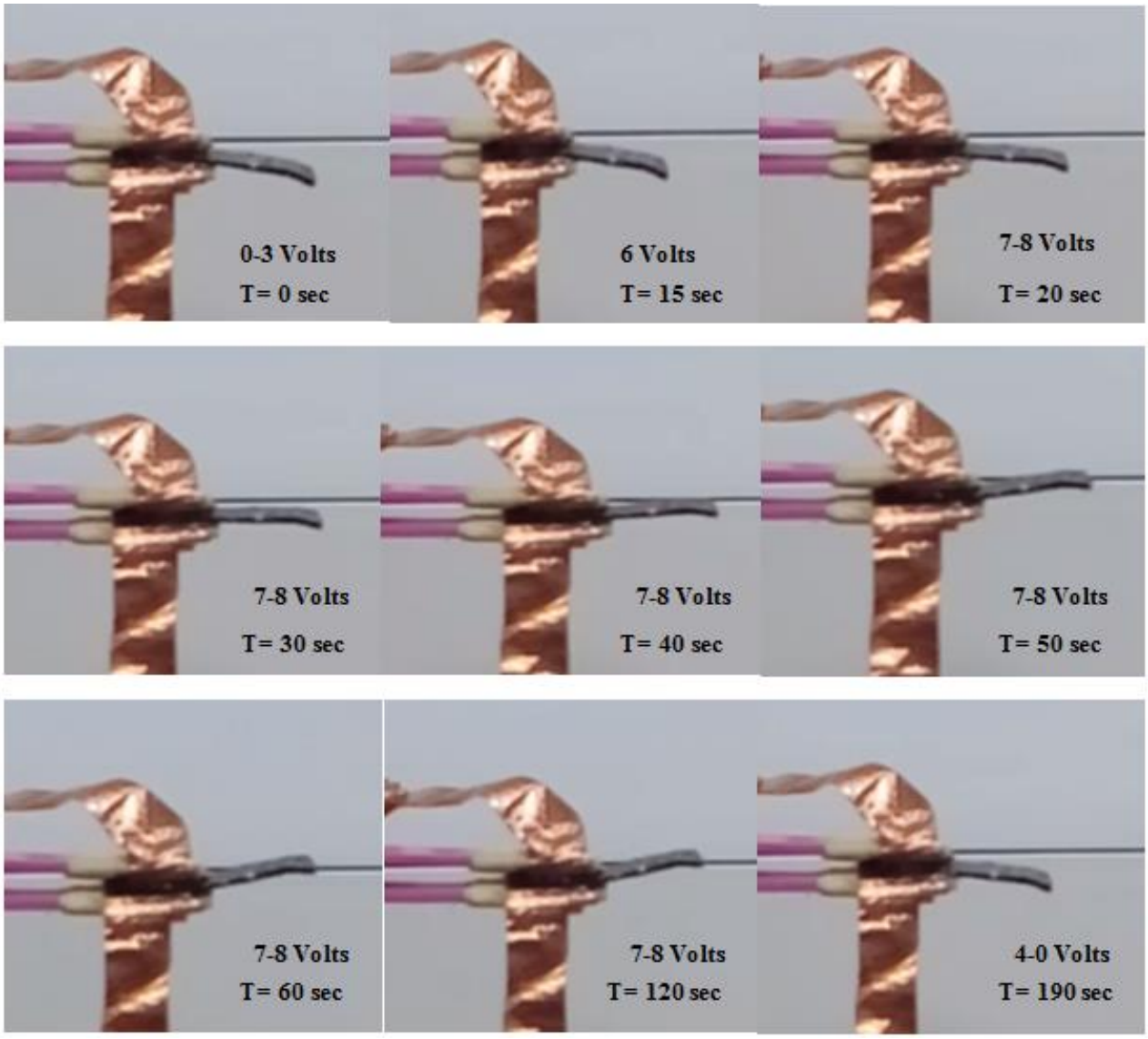

Figure 8.32 Bending capabilities of sSEBS GO 0.5% membranes with $scCO_2$

8.5 Key Points for Reprocessed SEBS GO Composites

Reprocessed SEBS GO composites were investigated for thermal, mechanical and electrical properties for the various compositions of GO. The following are the observations made:

- The throughput of the SEBS GO composites increased by 20% when processed with assisted $scCO_2$. No significant differences can be observed with the maximum degradation temperature in the presence or absence of $scCO_2$.
- The Tg ^{EB} block shifts from 56˚C in case of virgin SEBS to 65˚C for virgin SEBSP (SEBS paraffin oil sample) in both with and without $scCO_2$ extrudates. In addition, Tg ^{S} is enhanced, these shifts in Tg suggest that the addition of paraffin oil acts as a

plasticiser. The endothermic relaxation occurring in the Tg^{EB} block tends to flatten upon addition of GO in the case of both with and without $scCO_2$.

- The storage modulus increased upon addition of GO loading of (0.5%). However, the storage modulus gradually decreased with loading greater than 0.5%. When processed with $scCO_2$, the storage modulus increased gradually until 2.5% GO loading due to exfoliation. Similar results can also be observed in the tensile test results. The tan delta peak at 95.6 °C gradually reduced and broadened upon increasing concentration of GO percentage, which is indicative of improved polymer chain interaction when processed with $scCO_2$.

8.6 Conclusions for Reprocessed SEBS Graphene-Based Composites

SEBS graphene/GO composites were investigated to understand the effects of $scCO_2$ on the thermal, mechanical and electrical characteristics. In addition, the manufactured composites were evaluated for their ability as bending actuators. The throughput increased by around 25% for SEBS graphene composites and 20% in the case of GO composites when processed with $scCO_2$. In both the cases of graphene and GO, the TGA thermograms demonstrate the restriction imposed due to the addition of filler. The DSC results did not show any shifts in the peak of Tg upon addition of graphene or GO, however, the endothermic relaxation due to EB block flattened due to increase in viscosity upon addition of GO particles. The storage modulus without assisted $scCO_2$ increased beyond 1% loading in case of graphene, while highest at 0.5% loading in case of GO. However, when the composites were processed with $scCO_2$, the storage modulus increased gradually until 2.5% (highest storage modulus at 2.5%) in both the cases of graphene and GO. This clearly shows the $scCO_2$ ability to exfoliate and evenly disperse graphene base filler material within the polymer matrix. The water uptake capacity remained constant with and without $scCO_2$, even with the addition of graphene. In the case of GO, the water uptake increases by 10% compared to graphene and further increased with $scCO_2$ which is indicative of exfoliation and an oxygen-rich surface. The sSEBS membranes demonstrated bending degree of around 18° with or without $scCO_2$ and no actuation capabilities were observed with graphene composites. However, GO loading of 0.5% demonstrated a higher bending degree of 22° without $scCO_2$ and 27° with $scCO_2$. In addition, the response time decreased (faster actuation) for sSEBS membrane when treated with $scCO_2$ due to the suggested formation of smaller domains. The response time was lower for untreated GO 0.5% compared to treated counterpart due to an increase in polar groups.

9 Conclusions and Future Work

Electroactive polymers (EAPs), sometimes referred to as smart polymers, have garnered attention due to their promising applications in biomedical, tissue engineering, the automobile industry and even in electronics systems. A lot of research and commercial systems have already proved the efficacy of smart materials in our day-to-day products. However, in-depth understanding of electroactive/thermal/mechanical property of polymers/filler material and their ability to engineer their behaviour with existing industry standard processing techniques still stands as a barrier towards their complete industrial transition. One possible solution at the material selection/design stage is the use of thermoplastic elastomers (TPEs), which are multi-functional with properties of recyclability and possess thermoplastic processability and elasticity similar to vulcanised rubber. In addition, the desire to make materials smart, where it responds to external stimuli or change in environment by use of additional active filler material to the base polymer has led to increased complexity and cost. Hence, this research attempts to bridge the gap, by providing an in-depth understanding of their thermal, electrical and mechanical behaviours using industrial standard polymer processing techniques. This research emphasises and provides a thorough insight into the enhancement of polymer graphene-based composites using a supercritical fluid assisted polymer processing technique. Therefore, semi-crystalline Pebax and amorphous SEBS as base thermoplastic elastomer; and graphene and GO as filler materials were chosen for this research.

Preliminary work from this research focused on the effects of processing Pebax and SEBS at sub-critical, supercritical and beyond critical pressures on the thermal and mechanical properties. These investigations were helpful in creating new understandings on how phase separated materials, as in the case of TPEs (consisting of hard and soft phase), struggle to show their homogeneity in terms of their thermal and mechanical properties. Supercritical fluid processing is well documented in terms of viscosity reduction resulting in low-temperature processing conditions. However, this initial work (Chapter 4) demonstrated the supercritical fluid ability to break down the large microphase to smaller phase-separated structures, which enhanced the homogeneity of TPEs. The polymer processing method uses a conventional twin-screw extruder, with a simple supercritical fluid set up using syringe pump and CO_2 cylinder (CO_2 was not recycled at the end of the mixing zone of the extruder) resulting in foamed polymer matrices upon increasing critical pressure. This work was followed-up by investigating the effects of using graphene and GO as additive/filler material limited at low concentrations ($\leq$ 2.5 wt. %). In both the case of Pebax and SEBS (Chapter 5 and Chapter 6), GO as a filler material

demonstrated improved interaction and mechanical properties. The effect of agglomeration upon increasing the graphene-based filler beyond 1 wt. % was evident throughout Pebax and SEBS work.

In order to obtain a non-porous polymer matrix and also to compare the effects of supercritical fluid with respect to polymer matrix processed without assisted supercritical fluid, a major part of the thesis focused on reprocessing Pebax and SEBS graphene-based composites (Chapter 7 and 8). The supercritical fluid processing of polymer composites enhanced the thermal, mechanical and electrical characteristics due to the rearrangement of polymer chains into kinetically favourable conditions allowing exfoliation/even dispersion of graphene particles. In addition, supercritical processing tends to act as a cushion while manufacturing with temperature sensitive filler materials such as GO, where the intrinsic property of GO was maintained while improving the exfoliation and dispersion of the composite. The Pebax graphene composites acted as a conductor while the Pebax GO composites demonstrated sensitivity to temperatures. The indicative Tg of nylon increased to around 80 °C with $scCO_2$ upon addition of graphene and shifted down to 50 °C with GO. This clear appearance of phase change would suggest enhancing the applications of Pebax composites as thermally activated actuators rather than electroactive actuation. Such thermally sensitive Pebax GO composite not only enhances the mechanical properties but can be a huge platform for steerable catheters under thermal activation. In addition, improvements (as observed in this research work) in mechanical properties and meeting the needs of a material design requiring sufficient mechanical stiffness while maintaining the flexibility of Pebax overcomes the current industry need of complex catheter design thereby reducing cost.

In the case of SEBS, the supercritical treated SEBS composites at 0.5 wt. % GO improved water uptake capacity and showed ionic bending actuation capabilities of 27 degrees (greater than virgin SEBS which was about 15-18 degrees). However, repeatability was a major concern, where the bending actuation capabilities were not similar due to hydrolysis of the polymer matrix.

Future Work

This research presents the capability of supercritical carbon dioxide processing in terms of enhancement of/or balancing of the thermodynamic differences within the virgin thermoplastic elastomer. In addition, this research work also draws interest in composite processing where, SCF processing results in exfoliation/even dispersion, improving the characteristic property of a given composite. The following observation forms the basis for future work:

- This research work mainly shows the effects of supercritical carbon dioxide assisted processing using basic extrusion systems resulting in foamed polymer matrices. Similar work can be carried out with an additional set up where the carbon dioxide can be vented out or recycled at the end of mixing zone of the extruder resulting in a non-porous polymer matrix (adapt additional elongation flow on the die).
- The work done in this research demonstrates enhancement of mechanical properties when processed with a supercritical fluid, however, with the use of active GO particles, the chances of reducing the coefficient of friction is still unknown. Specifically, such evaluation of reduced coefficient of friction can be helpful in terms of catheter design, where the current PTFE layering can be altered.
- A number of studies have shown the ability of nylon to act as temperature sensitive actuators. The ability to change/engineer the shift in Tg of using Pebax with supercritical processing upon the use of GO was investigated and proved during the course of this research. Such shifts in the Tg has to be evaluated as temperature sensitive actuators and compared the state of art to draw a conclusion if any enhancement in the actuation can be observed.
- Enhanced mechanical, thermal and electric properties of SEBS/GO composites manufactured using $scCO_2$ to achieve enhanced improved performance in actuation as well as higher actuation cyclic phenomena (by lowering the value of tan delta). This will require a major long-term study for real applications.
- Finally, in order to produce repeatable and higher actuation capability in the case of SEBS composites, controlled sulfonation process, appropriate current selection and the use of polar salts (to enhance the ionic capacity) need to be investigated.

List of Publications

Papers currently accepted/in press by the Journal:

1. Effects of Supercritical Carbon Dioxide Assisted Processing on the Crystallization Kinetics of Pebax Graphene Composite Matrix ----Accepted with corrections - Polymer Engineering and Science

The following are the accepted papers:

[1] N. Karode, L. Fitzhenry, A. Poudel, P. Walsh, S. Matthews, A. Coffey, Performance enhancement of PEBAX using supercritical fluid extrusion for biomedical applications, Society of Plastic Engineers, ANTEC, 2016 (*Conference Proceedings*)

[2] N. Karode, L. Fitzhenry, S. Matthews, P. Walsh, A. Coffey, Enhancement of the Mechanical Properties of PEBAX Graphene Nanocomposite Using Supercritical Fluid Assisted Extrusion Polymer Processing Technique, Materials Science Forum, Trans Tech Publ, 2017, pp. 75-84

[3] A. Poudel, N. Karode, L. Fitzhenry, J. Kennedy, S. Matthews, P. Walsh, K. Thomas, A. Coffey, Investigation of the thermal, mechanical, electrical and morphological properties of supercritical carbon dioxide assisted extrusion of microphase-separated poly (styrene-ethylene/butylene-styrene), Journal of Supercritical Fluids, 130 (2017) 1-9

[4] N.S. Karode, A. Poudel, L. Fitzhenry, S. Matthews, P.R. Walsh, A.B. Coffey, Evaluation of interfacial region of microphase-separated SEBS using modulated differential scanning calorimetry and dynamic mechanical thermal analysis, Polymer Testing, 62 (2017) 268-277

[5] N. Karode, L. Fitzhenry, S. Matthews, P. Walsh, A. Coffey , Supercritical Carbon Dioxide Assisted Extrusion of Graphene Nanofiller Reinforced Polymers for Biomedical Applications, Society of Plastic Engineers, ANTEC, 2018 (*Conference Proceedings*)

[6] N. Karode, L. Fitzhenry, S. Matthews, P. Walsh, Wynette R, A. Coffey, Crystallisation Behaviour of Pebax Graphene Composite Matrix With and Without Supercritical Carbon Dioxide Assisted Polymer Processing Technique, May 2018, Crystal Growth and Design

References

1. *EAP history, current status, and infrastructure* in *Electroactive Polymer (EAP) Actuators as Artificial Muscles: Reality, Potential and Challenges*, Y. Bar-Cohen, Editor. 2004, SPIE Press: Bellingham.
2. Price, A.D., Berndt, C. S., Deluca, J. M., Farra, N., Gillies, A. G., Kopec, M. O. and Naguib, H. E. . *Synthesis and evaluation of ionic electroactive polyme ractuators*. in *10th International Workshop on Smart Materials and Structures*. 2007. Proceedings of Cansmart.
3. Heydt, R.D.K.R.P.H.P.R. *Electroactive polymers: an emerging technology for MEMS*. in *MEMS/MOEMS Components and Their Applications*. 2004. SPIE.
4. Wax, S., and R. Sands, *Electroactive polymer actuators and devices," in Smart Structures and Materials* Vol. 3669. 1999: Proc. SPIE
5. Madden, P.G.A., J.D.W. Madden, P.A. Anquetil, N.A. Vandesteeg, and I.W. Hunter, *The relation of conducting polymer actuator material properties to performance.* Oceanic Engineering, IEEE Journal of, 2004. 29(3): p. 696-705.
6. Kim, K.J. and M. Shahinpoor, *Ionic polymer–metal composites: II. Manufacturing techniques.* Smart Materials and Structures, 2003. 12(1): p. 65.
7. Park, I.-S., K. Jung, D. Kim, S.-M. Kim, and K.J. Kim, *Physical Principles of Ionic Polymer–Metal Composites as Electroactive Actuators and Sensors.* MRS Bulletin, 2008. 33(03): p. 190-195.
8. Bhandari, B., G.-Y. Lee, and S.-H. Ahn, *A review on IPMC material as actuators and sensors: fabrications, characteristics and applications.* International journal of precision engineering and manufacturing, 2012. 13(1): p. 141-163.
9. Hunter, I.W. and S. Lafontaine. *A comparison of muscle with artificial actuators*. in *Solid-State Sensor and Actuator Workshop, 1992. 5th Technical Digest., IEEE*. 1992.
10. Oguro, K., Kawami, Y. & Takenaka, H., *Bending of an ion-conducting polymer film-electrode composite by an electric stimulus at low voltage.* J. Micromach. Soc., 1992. 5: p. 27–30.
11. Kim, K.J., *Biomimetic Robotic Artificial Muscles*. 2013, Singapore, SGP: World Scientific & Imperial College Press.
12. Lu, J., S.-G. Kim, S. Lee, and I.-K. Oh, *Fabrication and actuation of electro-active polymer actuator based on PSMI-incorporated PVDF.* Smart Materials and Structures, 2008. 17(4): p. 045002.
13. SCF, I., *What are supercriticalfluids*. 2014.
14. Jo, C., D. Pugal, I.-K. Oh, K.J. Kim, and K. Asaka, *Recent advances in ionic polymer–metal composite actuators and their modeling and applications.* Progress in Polymer Science, 2013. 38(7): p. 1037-1066.
15. Bernat, J. and J. Kolota, *Adaptive observer-based control for an IPMC actuator under varying humidity conditions.* Smart Materials and Structures, 2018. 27(5): p. 055004.
16. Guo, D.-J., R. Liu, Y.-k. Li, W.H. Elliott, J.-P. Du, H. Zhang, Y. Ding, W. Tan, and S.-M. Fang, *Polymer actuators of fluorene derivatives with enhanced inner channels and mechanical performance.* Sensors and Actuators B: Chemical, 2018. 255: p. 791-799.
17. Vincenzini, P., Y. Bar-Cohen, and C. Federico, *Advances in Science and Technology, Volume 61 : Artificial Muscle Actuators using Electroactive Polymers : CIMTEC 2008*. 2009, Durnten, Zurich, CHE: Trans Tech Publications.
18. Berche, B.H., Malte; Kenna, Ralph *Critical phenomena: 150 years since Cagniard de la Tour.* Journal of Physical Studies 2009. 13(3).
19. Marre, S.R., Y.; Aymonier, C, *Supercritical microfluidics: Opportunities in flow-through chemistry and materials science.* . J. Supercrit. Fluids, 2011.
20. Kzarian, S.G., *Polymer Processing with Supercritical Fluids.* Polymer Science, 2009. Vol-42: p. 78-101.
21. Capuzzo, A., M.E. Maffei, and A. Occhipinti, *Supercritical fluid extraction of plant flavors and fragrances.* Molecules, 2013. 18(6): p. 7194-7238.

22. Goodship, V. and E. Ogur, *Polymer Processing with Supercritical Fluids*. 2004, Shrewsbury, GBR: Smithers Rapra.
23. Kazarian, S., *Polymer processing with supercritical fluids.* Polymer Science, 2000. 42(1): p. 78-101.
24. Hyatt, J.A., *Liquid and supercritical carbon dioxide as organic solvents.* The Journal of Organic Chemistry, 1984. 49(26): p. 5097-5101.
25. Fleming, O.S. and S.G. Kazarian, *Polymer Processing with Supercritical Fluids*, in *Supercritical Carbon Dioxide*. 2006, Wiley-VCH Verlag GmbH & Co. KGaA. p. 205-238.
26. Nalawade, S.P., F. Picchioni, and L.P.B.M. Janssen, *Supercritical carbon dioxide as a green solvent for processing polymer melts: Processing aspects and applications.* Progress in Polymer Science, 2006. 31(1): p. 19-43.
27. Cooper, A.I., *Polymer synthesis and processing using supercritical carbon dioxide.* Journal of Materials Chemistry, 2000. 10(2): p. 207-234.
28. Wang, W.-C.V., E.J. Kramer, and W.H. Sachse, *Effects of high-pressure CO2 on the glass transition temperature and mechanical properties of polystyrene.* Journal of Polymer Science: Polymer Physics Edition, 1982. 20(8): p. 1371-1384.
29. Wissinger, R.G. and M.E. Paulaitis, *Swelling and sorption in polymer–CO2 mixtures at elevated pressures.* Journal of Polymer Science Part B: Polymer Physics, 1987. 25(12): p. 2497-2510.
30. Compton, O.C. and S.T. Nguyen, *Graphene Oxide, Highly Reduced Graphene Oxide, and Graphene: Versatile Building Blocks for Carbon-Based Materials.* small, 2010. 6(6): p. 711-723.
31. Dreyer, D.R., S. Park, C.W. Bielawski, and R.S. Ruoff, *The chemistry of graphene oxide.* Chemical Society Reviews, 2010. 39(1): p. 228-240.
32. Seo, M., D. Yoon, K.S. Hwang, J.W. Kang, and J. Kim, *Supercritical alcohols as solvents and reducing agents for the synthesis of reduced graphene oxide.* Carbon, 2013. 64: p. 207-218.
33. Zhao, D., J. Ren, Y. Qiu, H. Li, K. Hua, X. Li, and M. Deng, *Effect of graphene oxide on the behavior of poly(amide-6-b-ethylene oxide)/graphene oxide mixed-matrix membranes in the permeation process.* Journal of Applied Polymer Science, 2015. 132(41): p. n/a-n/a.
34. Zhu, Y., S. Murali, W. Cai, X. Li, J.W. Suk, J.R. Potts, and R.S. Ruoff, *Graphene and graphene oxide: synthesis, properties, and applications.* Advanced materials, 2010. 22(35): p. 3906-3924.
35. Li, L., X. Zheng, J. Wang, Q. Sun, and Q. Xu, *Solvent-exfoliated and functionalized graphene with assistance of supercritical carbon dioxide.* ACS Sustainable Chemistry & Engineering, 2012. 1(1): p. 144-151.
36. Padmajan Sasikala, S., P. Poulin, and C. Aymonier, *Prospects of Supercritical Fluids in Realizing Graphene-Based Functional Materials.* Advanced Materials, 2016. 28(14): p. 2663-2691.
37. Aymonier, C., A. Loppinet-Serani, H. Reverón, Y. Garrabos, and F. Cansell, *Review of supercritical fluids in inorganic materials science.* The Journal of Supercritical Fluids, 2006. 38(2): p. 242-251.
38. Cansell, F., C. Aymonier, and A. Loppinet-Serani, *Review on materials science and supercritical fluids.* Current Opinion in Solid State and Materials Science, 2003. 7(4–5): p. 331-340.
39. Pu, N.-W., C.-A. Wang, Y. Sung, Y.-M. Liu, and M.-D. Ger, *Production of few-layer graphene by supercritical CO2 exfoliation of graphite.* Materials Letters, 2009. 63(23): p. 1987-1989.
40. Liu, C., G. Hu, and H. Gao, *Preparation of few-layer and single-layer graphene by exfoliation of expandable graphite in supercritical N, N-dimethylformamide.* The Journal of Supercritical Fluids, 2012. 63: p. 99-104.
41. Rangappa, D., K. Sone, M. Wang, U.K. Gautam, D. Golberg, H. Itoh, M. Ichihara, and I. Honma, *Rapid and Direct Conversion of Graphite Crystals into High-Yielding, Good-Quality Graphene by Supercritical Fluid Exfoliation.* Chemistry – A European Journal, 2010. 16(22): p. 6488-6494.
42. Zheng, X., Q. Xu, J. Li, L. Li, and J. Wei, *High-throughput, direct exfoliation of graphite to graphene via a cooperation of supercritical CO 2 and pyrene-polymers.* RSC Advances, 2012. 2(28): p. 10632-10638.

43. Jang, J.-H., D. Rangappa, Y.-U. Kwon, and I. Honma, *Direct preparation of 1-PSA modified graphene nanosheets by supercritical fluidic exfoliation and its electrochemical properties.* Journal of Materials Chemistry, 2011. 21(10): p. 3462-3466.
44. Horibe, T., H. Kondo, K. Ishikawa, H. Kano, M. Sekine, M. Hiramatsu, and M. Hori, *Supercritical Fluid Deposition of High-Density Nanoparticles of Photocatalytic TiO2 on Carbon Nanowalls.* Applied Physics Express, 2013. 6(4): p. 045103.
45. Meng, Y., F. Su, and Y. Chen, *Supercritical Fluid Synthesis and Tribological Applications of Silver Nanoparticle-decorated Graphene in Engine Oil Nanofluid.* Scientific Reports, 2016. 6: p. 31246.
46. Tewari, P.H., A.J. Hunt, and K.D. Lofftus, *Ambient-temperature supercritical drying of transparent silica aerogels.* Materials Letters, 1985. 3(9): p. 363-367.
47. De Cicco, F., P. Russo, E. Reverchon, C.A. García-González, R.P. Aquino, and P. Del Gaudio, *Prilling and supercritical drying: A successful duo to produce core-shell polysaccharide aerogel beads for wound healing.* Carbohydrate polymers, 2016. 147: p. 482-489.
48. Tabata, M., I. Adachi, Y. Hatakeyama, H. Kawai, T. Morita, and T. Sumiyoshi, *Large-area silica aerogel for use as Cherenkov radiators with high refractive index, developed by supercritical carbon dioxide drying.* The Journal of Supercritical Fluids, 2016. 110: p. 183-192.
49. Kong, Y., X. Shen, S. Cui, and M. Fan, *Facile synthesis of an amine hybrid aerogel with high adsorption efficiency and regenerability for air capture via a solvothermal-assisted sol–gel process and supercritical drying.* Green Chemistry, 2015. 17(6): p. 3436-3445.
50. Yang, G., J. Su, J. Gao, X. Hu, C. Geng, and Q. Fu, *Fabrication of well-controlled porous foams of graphene oxide modified poly (propylene-carbonate) using supercritical carbon dioxide and its potential tissue engineering applications.* The Journal of Supercritical Fluids, 2013. 73: p. 1-9.
51. Tayton, E., M. Purcell, A. Aarvold, J.O. Smith, S. Kalra, A. Briscoe, K. Shakesheff, S.M. Howdle, D.G. Dunlop, and R.O.C. Oreffo, *Supercritical CO2 fluid-foaming of polymers to increase porosity: A method to improve the mechanical and biocompatibility characteristics for use as a potential alternative to allografts in impaction bone grafting?* Acta Biomaterialia, 2012. 8(5): p. 1918-1927.
52. Gao, H. and G. Hu, *Graphene production via supercritical fluids.* RSC Advances, 2016. 6(12): p. 10132-10143.
53. Zheng, X., Q. Xu, L. He, N. Yu, S. Wang, Z. Chen, and J. Fu, *Modification of graphene oxide with amphiphilic double-crystalline block copolymer polyethylene-b-poly (ethylene oxide) with assistance of supercritical CO2 and its further functionalization.* The Journal of Physical Chemistry B, 2011. 115(19): p. 5815-5826.
54. Yu, N., X. Zheng, Q. Xu, and L. He, *Controllable-induced crystallization of PE-b-PEO on carbon nanotubes with assistance of supercritical CO2: effect of solvent.* Macromolecules, 2011. 44(10): p. 3958-3965.
55. Xu, G., N. Wang, J. Wei, L. Lv, J. Zhang, Z. Chen, and Q. Xu, *Preparation of graphene oxide/polyaniline nanocomposite with assistance of supercritical carbon dioxide for supercapacitor electrodes.* Industrial & Engineering Chemistry Research, 2012. 51(44): p. 14390-14398.
56. Gui, D., C. Liu, F. Chen, and J. Liu, *Preparation of polyaniline/graphene oxide nanocomposite for the application of supercapacitor.* Applied Surface Science, 2014. 307: p. 172-177.
57. Wu, Q., Y. Xu, Z. Yao, A. Liu, and G. Shi, *Supercapacitors based on flexible graphene/polyaniline nanofiber composite films.* ACS nano, 2010. 4(4): p. 1963-1970.
58. Xu, S., H. Yang, K. Wang, B. Wang, and Q. Xu, *Effect of supercritical CO 2 on fabrication of free-standing hierarchical graphene oxide/carbon nanofiber/polypyrrole film and its electrochemical property.* Physical Chemistry Chemical Physics, 2014. 16(16): p. 7350-7357.
59. Montjovent, M.-O., L. Mathieu, B. Hinz, L.L. Applegate, P.-E. Bourban, P.-Y. Zambelli, J.-A. Månson, and D.P. Pioletti, *Biocompatibility of bioresorbable poly (L-lactic acid) composite scaffolds obtained by supercritical gas foaming with human fetal bone cells.* Tissue engineering, 2005. 11(11-12): p. 1640-1649.

60. Yang, J., M. Wu, F. Chen, Z. Fei, and M. Zhong, *Preparation, characterization, and supercritical carbon dioxide foaming of polystyrene/graphene oxide composites.* The Journal of Supercritical Fluids, 2011. 56(2): p. 201-207.
61. Langer, R., *Perspectives and challenges in tissue engineering and regenerative medicine.* Advanced Materials, 2009. 21(32-33): p. 3235-3236.
62. Gedler, G., M. Antunes, V. Realinho, and J. Velasco, *Thermal stability of polycarbonate-graphene nanocomposite foams.* Polymer degradation and stability, 2012. 97(8): p. 1297-1304.
63. Antunes, M., G. Gedler, and J.I. Velasco, *Multifunctional nanocomposite foams based on polypropylene with carbon nanofillers.* Journal of Cellular Plastics, 2013. 49(3): p. 259-279.
64. Gedler, G., M. Antunes, J.I. Velasco, and R. Ozisik, *Enhanced electromagnetic interference shielding effectiveness of polycarbonate/graphene nanocomposites foamed via 1-step supercritical carbon dioxide process.* Materials & Design, 2016. 90: p. 906-914.
65. Kuang, T.-R., H.-Y. Mi, D.-J. Fu, X. Jing, B.-y. Chen, W.-J. Mou, and X.-F. Peng, *Fabrication of poly (lactic acid)/graphene oxide foams with highly oriented and elongated cell structure via unidirectional foaming using supercritical carbon dioxide.* Industrial & Engineering Chemistry Research, 2015. 54(2): p. 758-768.
66. Li, C., G. Yang, H. Deng, K. Wang, Q. Zhang, F. Chen, and Q. Fu, *The preparation and properties of polystyrene/functionalized graphene nanocomposite foams using supercritical carbon dioxide.* Polymer International, 2013. 62(7): p. 1077-1084.
67. Panwar, V., K. Cha, J.-O. Park, and S. Park, *High actuation response of PVDF/PVP/PSSA based ionic polymer metal composites actuator.* Sensors and Actuators B: Chemical, 2012. 161(1): p. 460-470.
68. Shahinpoor, M. and K.J. Kim, *Ionic polymer-metal composites: I. Fundamentals.* Smart Materials and Structures, 2001. 10(4): p. 819.
69. Kim, K.J. and M. Shahinpoor, *A novel method of manufacturing three-dimensional ionic polymer–metal composites (IPMCs) biomimetic sensors, actuators and artificial muscles.* Polymer, 2002. 43(3): p. 797-802.
70. Shahinpoor, M. and K.J. Kim, *Ionic polymer–metal composites: III. Modeling and simulation as biomimetic sensors, actuators, transducers, and artificial muscles.* Smart Materials and Structures, 2004. 13(6): p. 1362.
71. Shahinpoor, M. and K.J. Kim, *Ionic polymer–metal composites: IV. Industrial and medical applications.* Smart Materials and Structures, 2005. 14(1): p. 197.
72. Moghadam, A.A.A., A. Kouzani, K. Torabi, A. Kaynak, and M. Shahinpoor, *Development of a novel soft parallel robot equipped with polymeric artificial muscles.* Smart Materials and Structures, 2015. 24(3): p. 035017.
73. Lara-Est¨vez, J.C.I., L.A.n.S.d.A. Prado, K. Schulte, and E. Bucio, *PEBAXTM-Silanized Al2O3Composite. Synthesis and Characterization.* Open Journal of Polymer Chemistry, 2012. Vol.02No.02: p. 7.
74. Wang, Z.F., B. Wang, N. Qi, X.M. Ding, and J.L. Hu, *Free volume and water vapor permeability properties in polyurethane membranes studied by positrons.* Materials Chemistry and Physics, 2004. 88(1): p. 212-216.
75. Kear, K.E., *Developments in Thermoplastic Elastomers*. 2003, Shrewsbury, GBR: Smithers Rapra.
76. Müller, F., C.A. Ferreira, L. Franco, J. Puiggalí, C. Alemán, and E. Armelin, *New Sulfonated Polystyrene and Styrene–Ethylene/Butylene–Styrene Block Copolymers for Applications in Electrodialysis.* The Journal of Physical Chemistry B, 2012. 116(38): p. 11767-11779.
77. Mokrini, A., M.A. Huneault, Z. Shi, Z. Xie, and S. Holdcroft, *Non-fluorinated proton-exchange membranes based on melt extruded SEBS/HDPE blends.* Journal of Membrane Science, 2008. 325(2): p. 749-757.
78. Mokrini, A. and M.A. Huneault, *Proton exchange membranes based on PVDF/SEBS blends.* Journal of Power Sources, 2006. 154(1): p. 51-58.

79. Mokrini, A., R. Del, amp, x, C. o, and J.L. Acosta, *Synthesis and characterization of new ion conductors based on butadiene styrene copolymers.* Solid State Ionics, 2004. 166(3–4): p. 375-381.
80. Ehrenberg, S.G., J. Serpico, G.E. Wnek, and J.N. Rider, *Fuel cell incorporating novel ion-conducting membrane*. 1995, Google Patents.
81. Ehrenberg, S.G., J.M. Serpico, G.E. Wnek, and J.N. Rider, *Fuel cell incorporating novel ion-conducting membrane*. 1997, Google Patents.
82. Brownson, D.A.C. and C.E. Banks, *Graphene electrochemistry: an overview of potential applications.* Analyst, 2010. 135(11): p. 2768-2778.
83. Chan, H.E., *Graphene and Graphite Materials*. 2010, Hauppauge, NY, USA: Nova Science Publishers, Inc.
84. chemistry, T.n.p.i. *The Nobel Prize in Chemistry 2000*. 2000 [cited 2014 5th DEC 2014]; Available from: http://www.nobelprize.org/nobel_prizes/chemistry/laureates/2000/.
85. Geim, A.K. and K.S. Novoselov, *The rise of graphene.* Nat Mater, 2007. 6(3): p. 183-191.
86. Kim, H., Y. Miura, and C.W. Macosko, *Graphene/polyurethane nanocomposites for improved gas barrier and electrical conductivity.* Chemistry of Materials, 2010. 22(11): p. 3441-3450.
87. Morozov, S.V., K.S. Novoselov, F. Schedin, D. Jiang, A.A. Firsov, and A.K. Geim, *Two-dimensional electron and hole gases at the surface of graphite.* Physical Review B, 2005. 72(20): p. 201401.
88. Kim, H., A.A. Abdala, and C.W. Macosko, *Graphene/polymer nanocomposites.* Macromolecules, 2010. 43(16): p. 6515-6530.
89. Lim, Y., Y.P. Tan, H.N. Lim, W.T. Tan, M. Mahnaz, Z.A. Talib, N.M. Huang, A. Kassim, and M.A. Yarmo, *Polypyrrole/graphene composite films synthesized via potentiostatic deposition.* Journal of Applied Polymer Science, 2013. 128(1): p. 224-229.
90. Potts, J.R., D.R. Dreyer, C.W. Bielawski, and R.S. Ruoff, *Graphene-based polymer nanocomposites.* Polymer, 2011. 52(1): p. 5-25.
91. Dong, X., X. Wang, L. Wang, H. Song, H. Zhang, W. Huang, and P. Chen, *3D graphene foam as a monolithic and macroporous carbon electrode for electrochemical sensing.* ACS applied materials & interfaces, 2012. 4(6): p. 3129-3133.
92. Wallace, P.R., *The Band Theory of Graphite.* Physical Review, 1947. 71(9): p. 622-634.
93. Xing, G., H. Guo, X. Zhang, T.C. Sum, and C.H.A. Huan, *The physics of ultrafast saturable absorption in graphene.* Optics express, 2010. 18(5): p. 4564-4573.
94. Kazarian, S.G., M.F. Vincent, F.V. Bright, C.L. Liotta, and C.A. Eckert, *Specific Intermolecular Interaction of Carbon Dioxide with Polymers.* Journal of the American Chemical Society, 1996. 118(7): p. 1729-1736.
95. Kazarian, S.G., *Polymer Processing with Supercritical Fluids.* Polymer Science, Ser. C, 2000. 42(1): p. 78–101.
96. Serhatkulu, G.K., C. Dilek, and E. Gulari, *Supercritical CO2 intercalation of layered silicates.* Journal of Supercritical Fluids, 2006. 39(2): p. 264-270.
97. Chen, J., B. Yao, C. Li, and G. Shi, *An improved Hummers method for eco-friendly synthesis of graphene oxide.* Carbon, 2013. 64: p. 225-229.
98. Hummers Jr, W.S. and R.E. Offeman, *Preparation of graphitic oxide.* Journal of the American Chemical Society, 1958. 80(6): p. 1339-1339.
99. Paulchamy, B., G. Arthi, and B. Lignesh, *A simple approach to stepwise synthesis of graphene oxide nanomaterial.* Journal of Nanomedicine & Nanotechnology, 2015. 6(1): p. 1.
100. Nojima, S., K. Kato, S. Yamamoto, and T. Ashida, *Crystallization of block copolymers. 1. Small-angle x-ray scattering study of a .epsilon.-caprolactone-butadiene diblock copolymer.* Macromolecules, 1992. 25(8): p. 2237-2242.
101. Rangarajan, P., R.A. Register, and L.J. Fetters, *Morphology of semicrystalline block copolymers of ethylene-(ethylene-alt-propylene).* Macromolecules, 1993. 26(17): p. 4640-4645.

102. Begenir, A., S. Michielsen, and B. Pourdeyhimi, *Crystallization behavior of elastomeric block copolymers: Thermoplastic polyurethane and polyether-block-amide.* Journal of Applied Polymer Science, 2009. 111(3): p. 1246-1256.
103. Avrami, M., *Kinetics of phase change. I General theory.* The Journal of Chemical Physics, 1939. 7(12): p. 1103-1112.
104. Avrami, M., *Kinetics of phase change. II Transformation-time relations for random distribution of nuclei.* The Journal of Chemical Physics, 1940. 8(2): p. 212-224.
105. Avrami, M., *Granulation, phase change, and microstructure kinetics of phase change. III.* The Journal of chemical physics, 1941. 9(2): p. 177-184.
106. Piorkowska, E., A. Galeski, and J.-M. Haudin, *Critical assessment of overall crystallization kinetics theories and predictions.* Progress in polymer science, 2006. 31(6): p. 549-575.
107. Bianchi, O., R.V.B. Oliveira, R. Fiorio, J.D.N. Martins, A.J. Zattera, and L.B. Canto, *Assessment of Avrami, Ozawa and Avrami–Ozawa equations for determination of EVA crosslinking kinetics from DSC measurements.* Polymer Testing, 2008. 27(6): p. 722-729.
108. Jeziorny, A., *Parameters characterizing the kinetics of the non-isothermal crystallization of poly (ethylene terephthalate) determined by DSC.* Polymer, 1978. 19(10): p. 1142-1144.
109. Ozawa, T., *Kinetics of non-isothermal crystallization.* Polymer, 1971. 12(3): p. 150-158.
110. Evans, U.R., *The laws of expanding circles and spheres in relation to the lateral growth of surface films and the grain-size of metals.* Transactions of the Faraday Society, 1945. 41(0): p. 365-374.
111. Liu, T., Z. Mo, S. Wang, and H. Zhang, *Nonisothermal melt and cold crystallization kinetics of poly(aryl ether ether ketone ketone).* Polymer Engineering & Science, 1997. 37(3): p. 568-575.
112. Kissinger, H.E., *Variation of peak temperature with heating rate in differential thermal analysis.* Journal of research of the National Bureau of Standards, 1956. 57(4): p. 217-221.
113. Langford, J.I. and A. Wilson, *Scherrer after sixty years: a survey and some new results in the determination of crystallite size.* Journal of Applied Crystallography, 1978. 11(2): p. 102-113.
114. Scherrer, P., *Bestimmung der Grosse und der inneren Struktur von Kolloidteilchen mittels Rontgenstrahlen (1918) in: X-ray Diffraction Methods in Polymer Science, Ed. LE Alexander.* LE Alexander, 1969.
115. Jenkins, M.J., Y. Cao, and S.N. Kukureka, *The effect of molecular weight on the crystallization kinetics and equilibrium melting temperature of poly(tetramethylene ether glycol).* Polymers for Advanced Technologies, 2006. 17(1): p. 1-5.
116. Armstrong, S., B. Freeman, A. Hiltner, and E. Baer, *Gas permeability of melt-processed poly(ether block amide) copolymers and the effects of orientation.* Polymer, 2012. 53(6): p. 1383-1392.
117. Richards, D.H., *Poly(tetrahydrofuran), polymer monographs no. 8: P. Dreyfuss Gordon & Breach, 1981.* Polymer, 1983. 24(4): p. 499.
118. Bernardo, P., J.C. Jansen, F. Bazzarelli, F. Tasselli, A. Fuoco, K. Friess, P. Izák, V. Jarmarová, M. Kačírková, and G. Clarizia, *Gas transport properties of Pebax®/room temperature ionic liquid gel membranes.* Separation and Purification Technology, 2012. 97(0): p. 73-82.
119. Kaplan, D.S., *Structure–property relationships in copolymers to composites: Molecular interpretation of the glass transition phenomenon.* Journal of Applied Polymer Science, 1976. 20(10): p. 2615-2629.
120. Hourston, D.J., M. Song, A. Hammiche, H.M. Pollock, and M. Reading, *Modulated differential scanning calorimetry: 6. Thermal characterization of multicomponent polymers and interfaces.* Polymer, 1997. 38(1): p. 1-7.
121. Hourston, D.J., F.-U. Schäfer, M.H.S. Gradwell, and M. Song, *TMXDI-based poly(ether urethane)/polystyrene interpenetrating polymer networks: 2. Tg behaviour, mechanical properties and modulus-composition studies.* Polymer, 1998. 39(23): p. 5609-5617.
122. Halim, K.A.A., J.E. Kennedy, and J.B. Farrell, *Preparation and characterisation of polyether-block-amide/montmorillonite (MMT) nanocomposites for use in angioplasty balloon applications.* 2011.
123. Mark, E.J., *Polymer Data Handbook*. 1999, New York Oxford University Press.

124. Bondar, V., B. Freeman, and I. Pinnau, *Gas sorption and characterization of poly (ether-b-amide) segmented block copolymers.* Journal of Polymer Science Part B: Polymer Physics, 1999. 37(17): p. 2463-2475.
125. Zhai, W., Y. Ko, W. Zhu, A. Wong, and C.B. Park, *A study of the crystallization, melting, and foaming behaviors of polylactic acid in compressed CO2.* International journal of molecular sciences, 2009. 10(12): p. 5381-5397.
126. Tena, A., S. Shishatskiy, and V. Filiz, *Poly(ether-amide) vs. poly(ether-imide) copolymers for post-combustion membrane separation processes.* RSC Advances, 2015. 5(29): p. 22310-22318.
127. Colonna, M., M. Nicotra, and M. Moncalero, *Materials, designs and standards used in ski-boots for alpine skiing.* Sports, 2013. 1(4): p. 78-113.
128. Nibbering, E.T., J. Dreyer, O. Kühn, J. Bredenbeck, P. Hamm, and T. Elsaesser, *Vibrational dynamics of hydrogen bonds*, in *Analysis and control of ultrafast photoinduced reactions*. 2007, Springer. p. 619-687.
129. Cao, H., F. Qi, R. Liu, F. Wang, C. Zhang, X. Zhang, Y. Chai, and L. Zhai, *The influence of hydrogen bonding on N-methyldiethanolamine-extended polyurethane solid-solid phase change materials for energy storage.* RSC Advances, 2017. 7(19): p. 11244-11252.
130. Marcos-Fernández, A., A.E. Lozano, L. González, and A. Rodríguez, *Hydrogen Bonding in Copoly(ether–urea)s and Its Relationship with the Physical Properties.* Macromolecules, 1997. 30(12): p. 3584-3592.
131. Cogswell, F.N., *Polymer melt rheology: a guide for industrial practice*. 1981: Elsevier.
132. Vlachopoulos, J. and D. Strutt. *The role of rheology in polymer extrusion*. in *New Technology for Extrusion Conference. Milan, Italy. Nov*. 2003.
133. Shirkavand, M.J., H. Azizi, I. Ghasemi, M. Karrabi, and R. Rashedi, *A correlation between microstructure and rheological properties of broad MWD high-density polyethylene.* Iranian Polymer Journal, 2015. 24(11): p. 953-963.
134. Costello, B., *Use of rheology to determine the molecular weight distribution of polymers.*
135. Thomas, S. and G. Zaikov, *Recent advances in polymer nanocomposites*. 2009: CRC Press.
136. Jeske, H., A. Schirp, and F. Cornelius, *Development of a thermogravimetric analysis (TGA) method for quantitative analysis of wood flour and polypropylene in wood plastic composites (WPC).* Thermochimica Acta, 2012. 543: p. 165-171.
137. Overney, R., C. Buenviaje, R. Luginbuehl, and F. Dinelli, *Glass and structural transitions measured at polymer surfaces on the nanoscale.* Journal of thermal analysis and calorimetry, 2000. 59(1-2): p. 205-225.
138. Spaans, R.D., M. Muhammad, and M.C. Williams, *Probing the interfacial region of microphase-separated block copolymers by differential scanning calorimetry.* Journal of Polymer Science Part B: Polymer physics, 1999. 37(4): p. 267-274.
139. Kennedy, J.E. and C.L. Higginbotham, *Synthesis and characterisation of styrene butadiene styrene based grafted copolymers for use in potential biomedical applications*. 2011: INTECH Open Access Publisher.
140. Cantournet, S., R. Desmorat, and J. Besson, *Mullins effect and cyclic stress softening of filled elastomers by internal sliding and friction thermodynamics model.* International Journal of Solids and Structures, 2009. 46(11): p. 2255-2264.
141. Avram, M. and G.D. Mateescu, *Infrared spectroscopy: applications in organic chemistry*. 1978: Krieger Pub Co.
142. Nalawade, S.P., F. Picchioni, J.H. Marsman, and L. Janssen, *The FT-IR studies of the interactions of CO 2 and polymers having different chain groups.* The Journal of supercritical fluids, 2006. 36(3): p. 236-244.
143. Lorenzo, A.T., M.L. Arnal, J. Albuerne, and A.J. Müller, *DSC isothermal polymer crystallization kinetics measurements and the use of the Avrami equation to fit the data: Guidelines to avoid common problems.* Polymer Testing, 2007. 26(2): p. 222-231.

144. McFerran, N.L.A., C.G. Armstrong, and T. McNally, *Nonisothermal and isothermal crystallization kinetics of nylon-12.* Journal of Applied Polymer Science, 2008. 110(2): p. 1043-1058.
145. Zhang, F., X. Peng, W. Yan, Z. Peng, and Y. Shen, *Nonisothermal crystallization kinetics of in situ nylon 6/graphene composites by differential scanning calorimetry.* Journal of Polymer Science Part B: Polymer Physics, 2011. 49(19): p. 1381-1388.
146. Krikorian, V. and D.J. Pochan, *Unusual Crystallization Behavior of Organoclay Reinforced Poly(l-lactic acid) Nanocomposites.* Macromolecules, 2004. 37(17): p. 6480-6491.
147. Guo, B., Q. Zou, Y. Lei, M. Du, M. Liu, and D. Jia, *Crystallization behavior of polyamide 6/halloysite nanotubes nanocomposites.* Thermochimica Acta, 2009. 484(1): p. 48-56.
148. Kuo, M., J. Huang, and M. Chen, *Non-isothermal crystallization kinetic behavior of alumina nanoparticle filled poly (ether ether ketone).* Materials Chemistry and Physics, 2006. 99(2): p. 258-268.
149. Torrens-Serra, J., S. Venkataraman, M. Stoica, U. Kuehn, S. Roth, and J. Eckert, *Non-isothermal kinetic analysis of the crystallization of metallic glasses using the master curve method.* Materials, 2011. 4(12): p. 2231-2243.
150. Zhou, W.Y., B. Duan, M. Wang, and W.L. Cheung, *Isothermal and Non-isothermal Crystallization Kinetics of Poly (L-Lactide)/Carbonated Hydroxyapatite Nanocomposite Microspheres*, in *Advances in Diverse Industrial Applications of Nanocomposites*. 2011, InTech.
151. Huang, H., L. Gu, and Y. Ozaki, *Non-isothermal crystallization and thermal transitions of a biodegradable, partially hydrolyzed poly (vinyl alcohol).* Polymer, 2006. 47(11): p. 3935-3945.
152. Jung, J.-Y. and I.-K. Oh, *Novel nanocomposite actuator based on sulfonated poly (styrene-b-ethylene-co-butylene-b-styrene) polymer.* Journal of nanoscience and nanotechnology, 2007. 7(11): p. 3740-3743.
153. Stoyanov, H., G. Kofod, and R. Gerhard. *A co-axial dielectric elastomer actuator*. in *Advances in Science and Technology*. 2008. Trans Tech Publ.
154. Latko, P., M. Bielecki, R. Kozera, and A. Boczkowska, *Relationship between processing and electrical properties in SEBS/CNT nanocomposites.* Journal of Elastomers & Plastics, 2017. 49(4): p. 356-367.
155. Karode, N.S., A. Poudel, L. Fitzhenry, S. Matthews, P.R. Walsh, and A.B. Coffey, *Evaluation of interfacial region of microphase-separated SEBS using modulated differential scanning calorimetry and dynamic mechanical thermal analysis.* Polymer Testing, 2017. 62: p. 268-277.
156. Panaitescu, D., R. Gabor, C. Nicolae, A. Parau, C. Vitelaru, V. Raditoiu, and M. Chipara, *Block Copolymer Elastomer with Graphite Filler: Effect of Processing Conditions and Silane Coupling Agent on the Composite Properties.* Polymers, 2018. 10(1): p. 46.
157. Liu, Y.-T., X.-M. Xie, and X.-Y. Ye, *High-concentration organic solutions of poly(styrene-co-butadiene-co-styrene)-modified graphene sheets exfoliated from graphite.* Carbon, 2011. 49(11): p. 3529-3537.
158. Song, P., Z. Cao, Y. Cai, L. Zhao, Z. Fang, and S. Fu, *Fabrication of exfoliated graphene-based polypropylene nanocomposites with enhanced mechanical and thermal properties.* Polymer, 2011. 52(18): p. 4001-4010.
159. Ramanathan, T., A. Abdala, S. Stankovich, D. Dikin, M. Herrera-Alonso, R. Piner, D. Adamson, H. Schniepp, X. Chen, and R. Ruoff, *Functionalized graphene sheets for polymer nanocomposites.* Nature nanotechnology, 2008. 3(6): p. 327-331.
160. Jian, Z., *Recent advances in graphene based polymer composites [J].* New Chemical Materials, 2012. 8: p. 004.
161. Kuilla, T., S. Bhadra, D. Yao, N.H. Kim, S. Bose, and J.H. Lee, *Recent advances in graphene based polymer composites.* Progress in polymer science, 2010. 35(11): p. 1350-1375.
162. Shi, N. and Q. Dou, *Crystallization behavior, morphology, and mechanical properties of poly (lactic acid)/tributyl citrate/treated calcium carbonate composites.* Polymer Composites, 2014. 35(8): p. 1570-1582.

163. Schulz, E., *B. Wunderlich. Macromolecular physics, vol. 2 crystal nucleation, growth, annealing. Academic Press New York 1976, Preis $ 46, 50.* Kristall und Technik, 1977. 12(1): p. K11-K12.
164. Butler, G.B., *Polymers: Structure and bulk properties (Meares, Patrick).* Journal of Chemical Education, 1966. 43(7): p. 396.
165. McFerran, N.L., C.G. Armstrong, and T. McNally, *Nonisothermal and isothermal crystallization kinetics of nylon-12.* Journal of applied polymer science, 2008. 110(2): p. 1043-1058.
166. Stankovich, S., D.A. Dikin, G.H. Dommett, K.M. Kohlhaas, E.J. Zimney, E.A. Stach, R.D. Piner, S.T. Nguyen, and R.S. Ruoff, *Graphene-based composite materials.* nature, 2006. 442(7100): p. 282-286.
167. Noël, A., J. Faucheu, J.-M. Chenal, J.-P. Viricelle, and E. Bourgeat-Lami, *Electrical and mechanical percolation in graphene-latex nanocomposites.* Polymer, 2014. 55(20): p. 5140-5145.
168. Combes, J.R., S. Kumar, L.S. Smith, H.K. Mahabadi, and P.G. Odell, *Supercritical fluid processes*. 2000, Google Patents.
169. Elkovitch, M.D. and D.L. Tomasko, *Effect of supercritical carbon dioxide on morphology development during polymer blending.* Polymer Engineering & Science, 2000. 40(8): p. 1850-1861.
170. Elkovitch, M.D., D.L. Tomasko, and L.J. Lee, *Supercritical carbon dioxide assisted blending of polystyrene and poly (methyl methyacrylate).* Polymer Engineering & Science, 1999. 39(10): p. 2075-2084.
171. McNally, T. and P. Pötschke, *Polymer-carbon nanotube composites: Preparation, properties and applications*. 2011: Elsevier.
172. Rosato, D.V. and M.G. Rosato, *Injection molding handbook*. 2012: Springer Science & Business Media.
173. Wang, R.-X., L.-F. Huang, and X.-Y. Tian, *Understanding the protonation of polyaniline and polyaniline–graphene interaction.* The Journal of Physical Chemistry C, 2012. 116(24): p. 13120-13126.
174. Al-Mashat, L., K. Shin, K. Kalantar-Zadeh, J.D. Plessis, S.H. Han, R.W. Kojima, R.B. Kaner, D. Li, X. Gou, and S.J. Ippolito, *Graphene/polyaniline nanocomposite for hydrogen sensing.* The Journal of Physical Chemistry C, 2010. 114(39): p. 16168-16173.
175. Khanam, P.N., D. Ponnamma, and M. AL-Madeed, *Electrical Properties of Graphene Polymer Nanocomposites*, in *Graphene-Based Polymer Nanocomposites in Electronics*. 2015, Springer. p. 25-47.
176. Krikorian, V. and D.J. Pochan, *Crystallization behavior of poly (L-lactic acid) nanocomposites: nucleation and growth probed by infrared spectroscopy.* Macromolecules, 2005. 38(15): p. 6520-6527.
177. Ornaghi, H.L., A.S. Bolner, R. Fiorio, A.J. Zattera, and S.C. Amico, *Mechanical and dynamic mechanical analysis of hybrid composites molded by resin transfer molding.* Journal of Applied Polymer Science, 2010. 118(2): p. 887-896.
178. Wu, Z.-S., W. Ren, L. Gao, B. Liu, C. Jiang, and H.-M. Cheng, *Synthesis of high-quality graphene with a pre-determined number of layers.* Carbon, 2009. 47(2): p. 493-499.
179. Pati, M.K., P. Pattojoshi, and G.S. Roy, *Fabrication and Characterization of Graphene Based Nanocomposite for Electrical Properties.* Advances in Materials Physics and Chemistry, 2015. 5(01): p. 22.
180. Ratna, D., S. Divekar, A.B. Samui, B.C. Chakraborty, and A.K. Banthia, *Poly(ethylene oxide)/clay nanocomposite: Thermomechanical properties and morphology.* Polymer, 2006. 47(11): p. 4068-4074.
181. Xu, C., X. Shi, A. Ji, L. Shi, C. Zhou, and Y. Cui, *Fabrication and Characteristics of Reduced Graphene Oxide Produced with Different Green Reductants.* PloS one, 2015. 10(12): p. e0144842.
182. Liaros, N., K. Iliopoulos, M. Stylianakis, E. Koudoumas, and S. Couris, *Optical limiting action of few layered graphene oxide dispersed in different solvents.* Optical Materials, 2013. 36(1): p. 112-117.

183. Kumar, A.S.K. and S.-J. Jiang, *Preparation and characterization of exfoliated graphene oxide–l-cystine as an effective adsorbent of Hg (ii) adsorption.* RSC Advances, 2015. 5(9): p. 6294-6304.
184. Sreeprasad, T. and V. Berry, *How do the electrical properties of graphene change with its functionalization?* Small, 2013. 9(3): p. 341-350.
185. Mao, S., H. Pu, and J. Chen, *Graphene oxide and its reduction: modeling and experimental progress.* Rsc Advances, 2012. 2(7): p. 2643-2662.
186. Shankar, R., T.K. Ghosh, and R.J. Spontak, *Dielectric elastomers as next-generation polymeric actuators.* Soft Matter, 2007. 3(9): p. 1116-1129.
187. Koo, C.M., *Electroactive Thermoplastic Dielectric Elastomers as a New Generation Polymer Actuators*. 2012: INTECH Open Access Publisher.
188. Jeon, J.-H. and I.-K. Oh, *Introduction to Ionic Polymer-Metal Composite Actuators and Their Applications.* Journal of the Korean Society for Precision Engineering, 2011. 28(11): p. 1242-1250.
189. Palmre, V., D. Pugal, K.J. Kim, K.K. Leang, K. Asaka, and A. Aabloo, *Nanothorn electrodes for ionic polymer-metal composite artificial muscles.* Sci. Rep., 2014. 4.
190. Martín, Z., I. Jimenez, M.A. Gomez, H. Ade, and D.A. Kilcoyne, *Interfacial interactions in PP/MMT/SEBS nanocomposites.* Macromolecules, 2009. 43(1): p. 448-453.
191. Tjong, S., S. Bao, and G. Liang, *Polypropylene/montmorillonite nanocomposites toughened with SEBS-g-MA: Structure–property relationship.* Journal of Polymer Science Part B: Polymer Physics, 2005. 43(21): p. 3112-3126.
192. Rath, T. and Y. Li, *Nanocomposites based on polystyrene-b-poly (ethylene-r-butylene)-b-polystyrene and exfoliated graphite nanoplates: effect of nanoplatelet loading on morphology and mechanical properties.* Composites Part A: Applied Science and Manufacturing, 2011. 42(12): p. 1995-2002.
193. Ganguly, A., A.K. Bhowmick, and Y. Li, *Insights into montmorillonite nanoclay based ex situ nanocomposites from SEBS and modified SEBS by small-angle X-ray scattering and modulated DSC studies.* Macromolecules, 2008. 41(16): p. 6246-6253.
194. Vuluga, Z., D. Panaitescu, C. Radovici, C. Nicolae, and M. Iorga, *Effect of SEBS on morphology, thermal, and mechanical properties of PP/organoclay nanocomposites.* Polymer Bulletin, 2012. 69(9): p. 1073-1091.
195. Visakh, P. and O.B. Nazarenko, *Thermal Degradation of Polymer Blends, Composites and Nanocomposites*, in *Thermal Degradation of Polymer Blends, Composites and Nanocomposites*. 2015, Springer. p. 1-16.
196. Inuwa, I., A. Hassan, and S. Shamsudin, *THERMAL PROPERTIES, STRUCTURE AND MORPHOLOGY OF GRAPHENE REINFORCED POLYETHYLENE TEREPHTHALATE/POLYPROPYLENE NANOCOMPOSITES.* Malaysian Journal of Analytical Sciences, 2014. 18(2): p. 466-477.
197. Hourston, D., M. Song, A. Hammiche, H. Pollock, and M. Reading, *Modulated differential scanning calorimetry: 6. Thermal characterization of multicomponent polymers and interfaces.* Polymer, 1997. 38(1): p. 1-7.
198. Klempner, D., *Advances in interpenetrating polymer networks*. Vol. 4. 1994: CRC Press.
199. Poudel, A., P. Walsh, J. Kennedy, K. Thomas, J.G. Lyons, and A. Coffey, *Thermal, mechanical, dielectric, and morphological study of dielectric filler–based thermoplastic nanocomposites for electromechanical applications.* Journal of Thermoplastic Composite Materials, 2018: p. 0892705717751017.
200. Szczepanski, C.R., C.S. Pfeifer, and J.W. Stansbury, *A new approach to network heterogeneity: Polymerization Induced Phase Separation in photo-initiated, free-radical methacrylic systems.* Polymer, 2012. 53(21): p. 4694-4701.
201. Pothan, L.A., Z. Oommen, and S. Thomas, *Dynamic mechanical analysis of banana fiber reinforced polyester composites.* Composites Science and Technology, 2003. 63(2): p. 283-293.
202. Poudel, A., N. Karode, L. Fitzhenry, J. Kennedy, S. Matthews, P. Walsh, K. Thomas, and A. Coffey, *Investigation of the thermal, mechanical, electrical and morphological properties of supercritical*

carbon dioxide assisted extrusion of microphase-separated poly(styrene-ethylene/butylene-styrene). The Journal of Supercritical Fluids, 2017. 130: p. 1-9.
203. Ma, P.-C., M.-Y. Liu, H. Zhang, S.-Q. Wang, R. Wang, K. Wang, Y.-K. Wong, B.-Z. Tang, S.-H. Hong, and K.-W. Paik, *Enhanced electrical conductivity of nanocomposites containing hybrid fillers of carbon nanotubes and carbon black.* ACS applied materials & interfaces, 2009. 1(5): p. 1090-1096.
204. Psarras, G., E. Manolakaki, and G. Tsangaris, *Electrical relaxations in polymeric particulate composites of epoxy resin and metal particles.* Composites Part A: Applied Science and Manufacturing, 2002. 33(3): p. 375-384.
205. Wang, X.-L., I.-K. Oh, J. Lu, J.-H. Ju, and S.-W. Lee. *Ionic polymer-metal composite actuators employing sulfonated poly (styrene-ethylene-butylene-styrene) as ionic-exchange membranes*. in *International Conference on Smart Materials and Nanotechnology in Engineering*. 2007. SPIE.
206. Inamuddin, A. Khan, M. Luqman, and A. Dutta, *Kraton based ionic polymer metal composite (IPMC) actuator.* Sensors and Actuators A: Physical, 2014. 216: p. 295-300.
207. Ma, P.-C., M.-Y. Liu, H. Zhang, S.-Q. Wang, R. Wang, K. Wang, Y.-K. Wong, B.-Z. Tang, S.-H. Hong, K.-W. Paik, and J.-K. Kim, *Enhanced Electrical Conductivity of Nanocomposites Containing Hybrid Fillers of Carbon Nanotubes and Carbon Black.* ACS Applied Materials & Interfaces, 2009. 1(5): p. 1090-1096.